Dissertation

Mid-Infrared Spectroscopy and Porous Oxides:

From Trace Analysis to Interactions at Surfaces

A thesis submitted for the degree of

Doctor of Technical Sciences (Dr. techn.)

at

Technische Universität Wien

Faculty of Technical Chemistry

Institute of Chemical Technologies and Analytics

under supervision of

Univ. Prof. Dr. Bernhard Lendl

defended by

DI Bettina Baumgartner

Mat.Nr. 01026089

Vienna, November 2019

Die approbierte gedruckte Originalversion dieser Dissertation ist an der TU Wien Bibliothek verfügbar.
The approved original version of this doctoral thesis is available in print at TU Wien Bibliothek.

TU Bibliothek WIEN Your knowledge hub

Die approbierte gedruckte Originalversion dieser Dissertation ist an der TU Wien Bibliothek verfügbar.
The approved original version of this doctoral thesis is available in print at TU Wien Bibliothek.

„Science makes people reach selflessly for truth and objectivity; it teaches people to accept reality, with wonder and admiration, not to mention the deep awe and joy that the natural order of things brings to the true scientist.“

\- Lise Meitner

Die approbierte gedruckte Originalversion dieser Dissertation ist an der TU Wien Bibliothek verfügbar.
The approved original version of this doctoral thesis is available in print at TU Wien Bibliothek.
TU Bibliothek Your knowledge hub WIEN

TU Bibliothek Your knowledge hub WIEN
Die approbierte gedruckte Originalversion dieser Dissertation ist an der TU Wien Bibliothek verfügbar.
The approved original version of this doctoral thesis is available in print at TU Wien Bibliothek.

Abstract

This thesis focused on the combination of mesoporous silica with attenuated total reflection Fourier transform (ATR-FTIR) spectroscopy. ATR crystals coated with thin mesoporous silica films were investigated as a means to preconcentrate target analytes on the ATR crystal and thus to significantly enhance sensitivity and selectivity of mid-infrared based sensing schemes. ATR-FTIR spectroscopy was further used to characterize the porous material itself and for investigation of chemical and physical processes within these materials. Apart from FTIR spectroscopy, the combination of mesoporous silica films with novel IR light sources, light guiding schemes and detectors is outlined as well.

The synthesis and functionalization of silica films with different pore sizes and pore periodicity are described, including characterization via FTIR spectroscopy, X-ray diffraction, transmission electron microscopy, porosimetry and contact angle measurements. The obtained films were coated on ATR crystals (20 mm× 10 mm× 0.5 mm) cut from low-cost silicon and germanium wafers. In contrast to commercial ATR prisms, these crystals allow for fast and flexible screening of enrichment layers without the need to recover the blank ATR crystal between experiments. A dedicated optical setup compatible with commercial FTIR spectrometers was designed to house the ATR crystals.

For sensing, the enrichment of target molecules in ordered mesoporous silica films was studied. The influence of chemical functionalization, pore size and pore periodicity on the sensing performance of organic contaminants in water and in gas phase was investigated. Aromatic and aliphatic hydrocarbons were enriched in hydrophobic films, while the matrix, water or water vapor, was excluded from the volume probed by the evanescent field. Thereby enrichment factors for aromatic hydrocarbons of up to 1800 from aqueous phase and up to 32000 from gas phase could be achieved. Adsorption into and desorption from the porous films was fast, resulting in response times to changes in sample concentration of a few seconds and fast regeneration of the films after adsorption. Moreover, by changing the organic moiety in the mesoporous film, an ion exchange functionality was introduced allowing for sensing nitrate at drinking water levels between 1 mg L^{-1} to 50 mg L^{-1}. To quantify the mass of adsorbed pollutant in films, the relevant equations for ATR spectroscopy were derived and experimentally verified for adsorption into mesoporous films.

The porous materials were characterized by taking advantage of the molecular specific information of IR spectroscopy when measuring mesoporous silica films exposed to well-defined analyte concentrations. To this end, the adsorption of water into the mesoporous films was followed by ATR spectroscopy while changing the humidity of the gas above the film. Quantitative analysis of the obtained spectra facilitated the retrieval of porosity and pore size distribution of the mesoporous film. The results agreed well with porosimetry measurements based on established ellipsometric porosimetry. In addition, the absorption bands of adsorbed water were carefully analyzed to retrieve information on the structure of adsorbed water at different stages of pore filling. The identification of different states of

Die approbierte gedruckte Originalversion dieser Dissertation ist an der TU Wien Bibliothek verfügbar.
The approved original version of this doctoral thesis is available in print at TU Wien Bibliothek.
TU Bibliothek Your knowledge hub WIEN

hydrogen bonding of the water molecules visible in the IR spectra enabled to differentiate quantitatively between the first layers of surface-induced ordered water, similar to the structure in ice crystals, and bulk water situated at larger distance to the pore surface.

The methodology and optical setup developed for coated ATR-crystals from Si wafers was further used to investigate photocatalytic reactions of Pt loaded TiO_2. A UV-top irradiated, liquid phase ATR spectroscopy setup allowed simultaneous, time resolved investigations of both, Pt particle growth during their *in situ* photodeposition via monitoring of the Pt^0–CO_{ads} band, and of the photooxidation of methanol in an aqueous environment. Thereby, different reaction pathways of the photooxidation of methanol to CO and CO_2 for different Pt loadings at otherwise fixed reaction conditions could be observed *in situ* for the first time.

Finally, efforts toward new instrumentation for ATR spectroscopy making use of 3D printing are shown. A 3D-printed twin of the optical setup built from aluminum optomechanical components and its characterization are summarized. Moreover, a 3D-printed mini-spectrometer with the dimension of 12 × 9 × 8 cm including a pulsed emitter and a tunable Fabry-Pérot filter is presented.

Keywords: Infrared Spectroscopy • Porous Materials • Sensing • Adsorption • Functional Coating • Reaction Monitoring

Die approbierte gedruckte Originalversion dieser Dissertation ist an der TU Wien Bibliothek verfügbar.
The approved original version of this doctoral thesis is available in print at TU Wien Bibliothek.
TU Bibliothek WIEN Your knowledge hub

Kurzfassung

Diese Doktorarbeit befasste sich mit der Kombination von mesoporösem Siliziumdioxid mit Fourier-Transform Infrarot (FTIR) Spektroskopie in abgeschwächter Totalreflexion (ATR). Dünne, mesopörose Siliziumdioxidschichten wurden auf ATR Kristalle aufgebracht um Zielanalyten direkt am Kristall anzureichern. Dadurch konnte die Sensitivität und Selektivität IR-basierter Sensorsysteme signifikant erhöht werden. ATR-FTIR Spektroskopie wurde ebenso zur Charakterisierung der porösen Materialien selbst sowie der Untersuchung chemischer und physikalischer Prozesse an der Oberfläche dieser Materialien eingesetzt. Abgesehen von FTIR Spektroskopie wurden mesoporöse Siliziumdioxidschichten mit neuen IR-Lichtquellen, Lichtwellenleitersystemen und Detektoren kombiniert.

Die Synthese und Funktionalisierung von Siliziumdioxidschichten mit unterschiedlichem Porendurchmesser und variierender Porenanordnung wird vorgestellt und deren Charakterisierung mit FTIR Spektroskopie, Röntgendiffraktion, Transmissionselektronenmikroskopie, Kontaktwinkelmessungen und Porosimetrie wird beschrieben. Die erzielten Schichten wurden auf ATR Kristallen (20 mm × 10 mm × 0.5 mm), welche aus Germanium oder Silizium Wafern geschnitten wurden, aufgebracht. Im Gegensatz zu kommeriziellen ATR Prismen ermöglichen diese Kristalle schnelle und flexible Untersuchungen einer Vielzahl verschiedener Anreicherungsschichten ohne die Notwendigkeit, den unbeschichteten Kristall wiederherzustellen. Diese ATR Kristalle wurden in einem für sie zugeschnittenen optischen Aufbau untergebracht, der den Einbau in kommerzielle FTIR Spektrometer ermöglichte.

Zur quantitativen Analyse wurde die Anreichung von Zielmolekülen in mesoporöse Siliziumdioxidschichten untersucht. Der Einfluss von chemischer Funktionalisierung, Porengröße und Porenanordnung auf die Sensoreigenschaften hinsichtlich der Messung organischer Verunreinigungen in wässriger und gasförmiger Matrix wurde erforscht. Aromatische und aliphatische Kohlenwasserstofffe wurden in hydrophobe Schichten angereichert, während die Wassermatrix vom Messvolumen des evaneszenten Feldes ausgeschlossen wurde. Hierdurch konnten für aromatische Kohlenwasserstoffe Anreicherungsfaktoren von bis zu 1800 aus wässriger Lösung und bis zu 32000 aus der Gasphase erreicht werden. Die Adsorption in und Desorption aus den porösen Schichten findet schnell statt, woraus sich Ansprechzeiten auf veränderte Probenkonzentrationen von wenigen Sekunden ergaben. Ebenso schnell wurde die vollständige Regeneration der Schichten erreicht. Des Weiteren konnte durch die Änderung der organischen funktionellen Gruppe in der mesoporösen Schicht eine Ionentauscherfunktion eingebracht werden. Diese ermöglichte die Analyse von Nitratkonzentrationen auf Trinkwasserniveau zwischen 1 mg L^{-1} bis 50 mg L^{-1}. Grundlegende mathematische Zusammenhänge der ATR Spektroskopie wurden heranzegogen um die Adsorbatmasse in der mesoporösen Siliziumdioxidschicht zu bestimmen.

Mit Hilfe der molekülspezifischen Informationen des IR Spektrums und durch Aufgabe definierter Analytkonzentrationen konnte das poröse Material selbst charakterisiert werden. Zu diesem Zweck wurde bei variierender Luftfeuchtigkeit die Adsorption von Wasserdampf in

Die approbierte gedruckte Originalversion dieser Dissertation ist an der TU Wien Bibliothek verfügbar.
The approved original version of this doctoral thesis is available in print at TU Wien Bibliothek.
TU Bibliothek Your knowledge hub WIEN

die mesoprösen Siliziumdioxidschichten verfolgt. Die quantitative Anaylse der gewonnen Spektren ermöglichte die Ableitung von Porosität sowie Porengrößenverteilung der mesopörosen Schichten. Die Ergebnisse stimmten gut mit Messungen der etablierten ellipsometrischen Porosimetrie überein. Zusätzlich konnte durch tiefergreifende Studie der Wasserabsorptionsbanden die Struktur von Wasser im Verlauf der Porenfüllung bestimmt werden. Verschiedene Strukturen sowie die involvierten Wasserstoffbrückenbindungen konnten im IR Spektrum unterschieden werden. Dies ermöglichte die quantitative Differenzierung zwischen den ersten Monolagen von oberflächeninduziert-geordnetem Wasser - ähnlich zu Eiskristallen - und weniger geordnetem Wasser in größerem Abstand zur Oberfläche, dessen Spektrum flüssigem Wasser ähnelt.

Die Vorgehensweise und der optische Aufbau, die für beschichtete Silizium ATR Krstialle entwickelt wurden, konnten auch angewandt werden, um photokatalytische Reaktionen an Pt-beladenen TiO_2 Partikeln zu studieren. Hierzu wurde der optische Aufbau für UV-Bestrahlung adapiert. Dies ermölgichte die zeitaufgelöste Beobachtung des Pt-Partikelwachstums während der Photoabscheidung anhand der Pt^0–CO_{ads} Absorptionsbande, sowie, simultan dazu, der Photooxidation von Methanol in wässrigen Lösungen. Auf diese Weise konnten erstmals *in situ* die Reaktionsschritte der Methanolphotooxidation zu CO und CO_2 sowie deren Abhängigkeit von der Pt-Beladung untersucht werden.

Zuletzt werden die Fortschritte, die im Bereich neuer Instrumentierung der ATR Spektroskopie in Kombination mit 3D Druck erzielt wurden, präsentiert. Ein 3D-gedruckter Zwilling des aus optomechnischen Aluminiumbauteilen bestehenden optischen Aufbaus wurde angefertigt und charakterisiert. Weiters wird ein 3D-gedrucktes Mini-Spektrometer mit den Abmessungen $12 \times 9 \times 8$ cm, das sich aus einer gepulsten IR-Quelle und einem Fabry-Pérot Filter zusammensetzt, vorgestellt.

Schlagworte: Infrarotspektroskopie • Poröse Materialien • Sensoren • Adsorption • Funktionelle Beschichtungen • Reaktionsüberwachung

Die approbierte gedruckte Originalversion dieser Dissertation ist an der TU Wien Bibliothek verfügbar.
The approved original version of this doctoral thesis is available in print at TU Wien Bibliothek.
TU Bibliothek WIEN Your knowledge hub

Acknowledgements

Generally, science is quite rational and unemotional, and we often do not have the opportunity or neglect to show gratitude. So, I hope with the following words I can express how grateful I feel for all the support I experienced in the course of my thesis.

First of all, I would like to thank my supervisor Bernhard Lendl for creating and providing the scientific environment that allowed me to pursue this thesis. He supported me whenever it was necessary in the last three years and offered me a lot of freedom in my scientific work. Thank you for giving me the opportunity to attend international conferences and summer schools.

I also would like to thank David Grosso and Erwin Rosenberg for taking the time reading and evaluating this thesis.

I very much thank David Grosso a second time for allowing me to work in his lab and explore new approaches for material synthesis. Thank you, Jerome Loizillon, for endless discussions on water adsorption and pore filling, our shared projects and your great support during my stay in Marseille and beyond.

After changing my research field rather drastically from polymer chemistry to IR spectroscopy, I was and still am very grateful for all the support, discussions and valuable advices I obtained from the former and present colleagues in our working group. Especially, I would like to thank Christoph Gasser, Karin Wieland and Andreas Schwaighofer for always taking the time, sharing your scientific knowledge and listen to all kind of problems. Thank you, Harald Moser, for always finding the correct gas adapter, even if three different were needed in between! I want to thank Dette Kirchsteiger for all her insights into ion exchange mechanism and her great spirit. Finally, I want to thank my ATR-buddy, Stephan Freitag, for sharing my love for reaction monitoring, 3D-printing and dirty jokes! Your cheerfulness and your constant (non-)scientific input supported me significantly during this thesis!

It was and still is a great pleasure for me to work on shared projects and I would like to thank all of my collaboration partners: Nuria Teigell Beneitez and Jeroen Missinne (both IMEC/Uni Ghent) for our work within the Aquarius project on Ge waveguides; Haolan Zhao, Anton Vasiliev, and Giuseppe Antonacci (all IMEC/Uni Ghent) for their interest in combining mesoporous materials with integrated optics; Greta Haselmann (Institute of Materials Chemistry, TU Wien) for her stamina and good spirits throughout our work on photocatalysis combined with ATR spectroscopy (and the 22 versions of our resulting manuscript); Florian Pilat and Borislav Hinkov (Institute of Photonics, TU Wien) for our shared efforts toward reaction monitoring with monolithic integrated optics; Michael Stöger-Pollach and Johannes

Die approbierte gedruckte Originalversion dieser Dissertation ist an der TU Wien Bibliothek verfügbar.
The approved original version of this doctoral thesis is available in print at TU Wien Bibliothek.
TU Bibliothek Your knowledge hub WIEN

Bernardi (USTEM, TU Wien) for TEM measurements; Werner Artner (XRC, TU Wien) for constant support with XRD and GISAXS measurements; and Thomas Konegger (CTA, TU Wien) for allowing me to use his oven.

Thank you to all my friends for their understanding and enriching moments during these demanding years.

I want to thank my brother, Julius, and my mother, Eva, for their loving and everlasting support throughout this thesis and my studies. Thank you, Mama, for always encouraging me to make my way and being a role model in so many aspects. This work is dedicated to you!

I would like to express my deepest gratitude to Jakob Hayden, who provided me with unwavering support, encouragement, love and patience throughout the duration of this thesis. Our countless scientific discussions and shared projects gave me great pleasure, contributed to the quality of this work and enriched my way of targeting analytical questions. I am glad that you have accompanied me during my studies and to have you in my life.

Finally, financial support should not go unmentioned: This work is part of the AQUARIUS project, which has received funding from the European Union's Horizon 2020 research and innovation program under grant agreement No. 73146. This project is an initiative of the Photonics Public Private Partnership.

Die approbierte gedruckte Originalversion dieser Dissertation ist an der TU Wien Bibliothek verfügbar.
The approved original version of this doctoral thesis is available in print at TU Wien Bibliothek.
TU Bibliothek Your knowledge hub WIEN

Content

Abstract ..... *v*
Kurzfassung ..... *vii*
Acknowledgements ..... *ix*
Content ..... *xi*
Abbreviations ..... *xv*
Symbols ..... *xvii*

Introduction 1
Chapter 1 Fundamentals on Enrichment-Based Mid-Infrared Sensing 3

1.1 Mid-Infrared Spectroscopy 3

1.1.1 Fundamentals of IR Spectroscopy 3
1.1.2 Absorption Measurements in Transmission Configuration 6
1.1.3 Absorption Measurements in Total Internal Reflection Configuration 8
1.1.4 Instrumentation for MIR Spectroscopy 12

1.2 Synthesis of Mesoporous Films 16

1.2.1 Sol-Gel Process 16
1.2.2 Thin Film Templating by Evaporation Induced Self-Assembly 17
1.2.3 Surface Functionalization 19

1.3 Adsorption Mechanisms in Mesoporous Materials 21

1.3.1 General Aspects of the Adsorption Mechanism 21
1.3.2 Special Aspects of Adsorption from Liquid Phase 25
1.3.3 Mass transfer in Pores 27

1.4 Enrichment-Based Sensing Schemes Related to this Work 29

1.4.1 State-of-the-Art of Enrichment Coatings 29
1.4.2 Mesoporous Materials for Sensing Applications 37
1.4.3 Conclusion on Enrichment Materials for Mid-IR sensing 38

Chapter 2 Experimental Details 39

2.1 FTIR Spectrometer Setup 39

2.1.1 Preparation of ATR Crystals 40
2.1.2 Home-built ATR Mount aka *Clipsi* 40
2.1.3 Flow Cell Designs 41
2.1.4 Design and 3D-Printing of ATR Instrumentation 42
2.1.5 Spectroscopic Performance of Silicon and Germanium ATR Crystals 43

2.2 Sample Preparation 44

2.2.1 Liquid Sample Handling 44
2.2.2 Liquid Sample Characterization 45
2.2.3 Gas Sample Handling 45

2.3 Synthesis and Methods 47

2.3.1 Chemicals 47
2.3.2 Characterization of Mesoporous Materials 47
2.3.3 Synthesis of Mesoporous Films 48
2.3.4 Surface Functionalization 50
2.3.5 Synthesis of Mesoporous TiO_2 50

Die approbierte gedruckte Originalversion dieser Dissertation ist an der TU Wien Bibliothek verfügbar.
The approved original version of this doctoral thesis is available in print at TU Wien Bibliothek.
TU Bibliothek WIEN Your knowledge hub

2.3.6 Nanoimprinting 51

Chapter 3 Synthesis and Characterization of Mesoporous Films 53

3.1 Optimization of Synthesis of Mesoporous Silica Films 53

3.1.1 Template Removal of Mesoporous Silica Films 57
3.1.2 Multilayer Deposition 57

3.2 Characterization of Mesoporous Silica on Planar Surfaces 59

3.2.1 IR Spectra of Mesoporous Films 59
3.2.2 X-ray Diffraction of Mesoporous Films 59
3.2.3 Transmission Electron Microscopy 62
3.2.4 Characterization of Film Thickness 62
3.2.5 Porosity and Pore Size Distribution 63
3.2.6 Wettability and Stability of Mesoporous Films in Water 64

3.3 Coating of Integrated Optics 66

3.3.1 Ge and Si Waveguides - Aquarius Project 66
3.3.2 IOCs for Photothermal Spectroscopy 68
3.3.3 IOCs for Raman Spectroscopy 69
3.3.4 Coating of Monolithic Laser Chips 70

3.4 Nanoimprinting 71

3.4.1 Considerations for Porous Waveguides 71
3.4.2 Experimental Results 72

Chapter 4 Mesoporous Films coated on ATR Crystals for Quantitative Analysis 75

4.1 Determination of the Effective Path Length of the Blank Si ATR Crystal 75

4.1.1 Theoretical Evaluation of the Effective Path Length within the Mesoporous Film 76
4.1.2 Experimental Verification of the Effective Path Length 77
4.1.3 Retrieval of Analyte Concentrations inside the Mesoporous Films 78

4.2 Enrichment of Hydrocarbons from Aqueous Phase 79

4.2.1 Discrimination of Hydrocarbons in the IR Spectra 79
4.2.2 Proof-of-Principle using Benzonitrile and Valeronitrile 80
4.2.3 Different Surface Functionalization 85
4.2.4 Enrichment of Aliphatic Hydrocarbons 86
4.2.5 Enrichment of Aromatic Hydrocarbons 87
4.2.6 Conclusion 90

4.3 Enrichment of Anions 92

4.3.1 Introduction of an Ion Exchange Moiety into Mesoporous Silica 92
4.3.2 Proof-of-Principle using a P123 Film 93
4.3.3 TMAC Functionalized CTAB Film 95

4.4 Enrichment from Gas Phase 96

4.4.1 Adsorption of Single BTEX Molecules 96
4.4.2 Adsorption of BTEX Gas Mixtures 99
4.4.3 Conclusion 101

Chapter 5 *In Situ* Monitoring of Process at Interfaces 103

5.1 Porosity, Pore Size Distribution and Investigations of Structure of Water in the Pore... 103

Die approbierte gedruckte Originalversion dieser Dissertation ist an der TU Wien Bibliothek verfügbar.
The approved original version of this doctoral thesis is available in print at TU Wien Bibliothek.
TU Bibliothek WIEN Your knowledge hub

5.1.1 Monitoring Water Adsorption and Desorption in Mesoporous Silica 104
5.1.2 Retrieval of Adsorbed Water Concentration and Porosity 106
5.1.3 Pore Size Distribution 108
5.1.4 Structure of Confined Water during Adsorption 110
5.1.5 Calculation of Surface-Induced Ordered Water Monolayers 114
5.1.6 Conclusion 117

5.2 Desorption under Cavitation for Different Solvents 119
5.3 Photocatalytic Reactions Monitored by ATR-FTIR Spectroscopy 123

5.3.1 Experimental Procedures 124
5.3.2 Characterization of Pt-loaded TiO_2 Thin Films 127
5.3.3 Reaction Monitoring under UV Irradiation with ATR-FTIR Spectroscopy 129
5.3.4 Spectroscopic Investigations of CO Adsorbed on Pt 131
5.3.5 Photocatalytic Decomposition of Methanol 135
5.3.6 Temporal Correlation between Pt^0-$CO_{(ads)}$ Bands and Photooxidation Products using MCR-ALS Analysis 139
5.3.7 Conclusion 143

Chapter 6 Advances in Instrumentation for ATR Spectroscopy 145

6.1 Characterization of a 3D-printed ATR Module 145

6.1.1 Characterization and Iterative Optimization of the 3D-Printed ATR Unit 146
6.1.2 Exemplary Use Cases 148
6.1.3 Conclusion and Costs 151

6.2 3D-Printed Mini ATR-IR Spectrometer 152

6.2.1 Design of a Mini ATR-IR Spectrometer 152
6.2.2 Noise Characterization 153
6.2.3 Show-Case Application: Determination of Nitrate in Water 153

Chapter 7 Summary and Outlook 155

7.1 Mesoporous Silica Cladding on Ge-based Integrated Optics 156

Bibliography 159
Appendix 176

A. Abstract of Published Works 176

Publication I 176
Publication II 176
Publication III 177
Publication IV 178
Publication V 178
Publication VI 179
Publication VII 179
Publication VIII 180
Publication IX 181
Publication X 181
Publication XI 182

B. MATLAB scripts 183

B.1 Porosimetry and PSD 183
B.2 Gauss Fitting for Water Bands 185

Die approbierte gedruckte Originalversion dieser Dissertation ist an der TU Wien Bibliothek verfügbar.
The approved original version of this doctoral thesis is available in print at TU Wien Bibliothek.
TU Bibliothek Your knowledge hub WIEN

B.3 *Bruggeman* Effective Medium Approximation 190
B.4 BTEX Gas Phase Fitting 193
B.4 Cavitation Pressure 195

C. Construction Drawings *197*

C.1 ATR Crystal Cartridge 197
C.2 Liquid Flow Cell 198
C.3 Gas Flow Cell 199
C.4 Flow Cell for Photocatalysis 200

D. Curriculum Vitae *201*

Die approbierte gedruckte Originalversion dieser Dissertation ist an der TU Wien Bibliothek verfügbar.
The approved original version of this doctoral thesis is available in print at TU Wien Bibliothek.
TU Bibliothek Your knowledge hub WIEN

Abbreviations

(low-density) polyethylene	(LD)PE
absorption unit	A.U.
attenuated total reflection	ATR
Bruggeman effective medium approximation	BEMA
benzene, ethylbenzene, toluene, xylenes (naphtalenes)	BETX(N)
chlorinated hydrocarbons	CHC
critical micelle concentration	CMC
Complementary metal–oxide–semiconductor	CMOS
cetyltrimethylammonium bromide	CTAB
external cavity	EC
evaporation induced self-assembly	EISA
electromagnetic	EM
ellipsometric porosimetry	EP
ethyltriethoxy silane	ETES
fiber evanescent wave spectroscopy	FEWS
dt. Fluorkautschuk (fluoroelastomer)	FKM
focused ion beam	FIB
Fabry-Pérot	FP
Fourier transform	FT
Gracing incidence small angle x-ray scattering	GI-SAXS
graphical user interface	GUI
Hydrocarbon	HC
high-density	HD
hexamethyldisilazane	HMDS
interband cascade laser	ICL
integrated optical circuit	IOC
infrared	IR
internal reflection element	IRE
International Union of Pure and Applied Chemistry	IUPAC
low-density	LD
limit of detection	LOD
mobil composition of matter	MCM
mercury-cadmium-telluride	MCT
Mach-Zehnder interferometer	MZI
micro-electro-mechanical system	MEMS
methyl triethoxysilane	MTES
methyltrichlorosilane	MTCS
molecular weight	MW
nuclear magnetic resonance	NMR
polyacrylnitrile-co-butadiene	PAB
polyacrylnitrile	PAN
pore condensation	PC

Die approbierte gedruckte Originalversion dieser Dissertation ist an der TU Wien Bibliothek verfügbar.
The approved original version of this doctoral thesis is available in print at TU Wien Bibliothek.
TU Bibliothek Your knowledge hub WIEN

poly ethylene oxide	PEO
poly(methyl methacrylate)	PMMA
poly propylene	PP
polypropylene oxide	PPO
polystyrene	PS
polystyrene-co-butadiene	PSB
pore size distribution	PSD
phenyltriethoxy silane	PTES
polytetrafluoroethylene	PTFE
polyvinylchloride	PVC
quantum cascade laser	QCL
relative humidity	RH
refractive index	RI
root-mean-square	RMS
room temperature	RT
Santa Barbara amorphous type material	SBA
signal to noise ratio	SNR
surface plasmon resonance	SPR
1,1,2,2-tetrachloroethane	TeCE
transmission electron microscopy	TEM
tetraethoxysilane	TEOS
tetramethoxysilane	TMOS
ultra violet	UV
visible	VIS
volatile organic compound	VOC
X-ray diffraction	XRD
X-ray photoelectron spectroscopy	XPS

Die approbierte gedruckte Originalversion dieser Dissertation ist an der TU Wien Bibliothek verfügbar.
The approved original version of this doctoral thesis is available in print at TU Wien Bibliothek.
TU Bibliothek Your knowledge hub WIEN

Symbols

absorbance	A
absorption coefficient	α
spectral radiance per unit wavenumber	$B(\tilde{\nu})$
concentration	c
speed of light in vacuum	c_0
anharmonicity constant	χ
path length	d
diffusivity	$D(q)$
effective path length	d_e
Tolman length	δ
depth of penetration	d_p
electrical field	$\boldsymbol{E}$
photon energy	E
allowed energy levels	E_n
energy barrier	E_b
enrichment factor	EF
vacuum permittivity	ε_0
geometric factor	G
surface energy per unit surface area at the liquid-vapor interface	γ_{lv}
number of formed cavitation bubbles per unit time and per unit volume	Γ
attempt frequency for bubble formation per unit time	Γ_0
Planck constant h $= 6.6261 \cdot 10^{-34}$ m^2 kg / s	h
Intensity	I
component	i
diffusion flux	J
wave vector	$\boldsymbol{k}$
Freundlich affinity coefficient	K_F
Langmuir constant	K_L
imaginary part of refractive index	κ
Boltzmann constant $k_b = 1.3806 \cdot 10^{-23}$ J K^{-1}	k_B
length	l
wavelength of radiation	λ
vacuum wavenumber	λ_0
molar mass	M_W
refractive index	n
number of atoms	N_{atom}
number of bounces of an ATR element	N
Freundlich linearity index	n_F
adsorbed amount at surface	n^a
complex refractive index	$\hat{n}$
surface excess amount	n_i^σ
vacuum wavenumber	$\tilde{\nu}$
vibrational quantum number	v_i

Die approbierte gedruckte Originalversion dieser Dissertation ist an der TU Wien Bibliothek verfügbar.
The approved original version of this doctoral thesis is available in print at TU Wien Bibliothek.
TU Bibliothek Your knowledge hub WIEN

pressure	p
porosity	P
cavitation pressure	p_l^{cav}
saturation pressure	p_0
geometric factor	q
amount of adsorbed analyte	q_e
maximum adsorption capacity	q_m
reflectivity	R
gas constant	R_g
critical bubble radius	r_c
Kelvin radius	r_K
pore radius	r_p
amplitude reflection coefficients	$r_\parallel$, $r_\perp$
equilibrium position	r_c
density	ρ
fraction of intensity of the evanescent field within the film thickness	s
kinetic molecular diameter	σ
temperature	T
time	t
transmission	T
glass transition temperature	T_g
film thickness	th
angle of incidence	θ
critical angle of incidence	θ_c
contact angle	θ_{CA}
volume	V
pore volume	V_{pore}
molecular volume	V_m
molar fraction	x
frequency	υ

Vectors such as electric field $\boldsymbol{E}$ are given in bold font, while scalar values such as time t are given in italic font.

Die approbierte gedruckte Originalversion dieser Dissertation ist an der TU Wien Bibliothek verfügbar.
The approved original version of this doctoral thesis is available in print at TU Wien Bibliothek.
TU Bibliothek Your knowledge hub WIEN

Introduction

Chemical and physical processes at interfaces are ubiquitous and facilitate numerous applications in science and industry. Examples include separation processes used in waste water treatments or chromatography, and heterogeneous catalysis, *e.g. Haber-Bosch* process or *Ziegler-Natta* polymerization among other fields of application. All these have in common that they rely on accessible surface that can be increased by porosity. Porous materials offer inherent advantages such as high-surface area and defined pore size and pore size distribution that determine their mechanical, physical and chemical properties. These paved their way to an impressive range of applications. Across all of them, the basic working principle relies on the fundamental process of adsorption, by IUPAC definition "*the increase in the concentration of a substance at the interface of a condensed and a liquid or gaseous layer owing to the operation of surface forces*". Thus, deepening the understanding of adsorbent–adsorbate interactions is key to exploiting the full potential of these fascinating materials.

However, *in situ* monitoring and thus obtaining real-time information about adsorbent-adsorbate interactions at conditions similar to practical applications are difficult to access with established experimental approaches. Mid-infrared spectroscopy is ideally suited for quantitative analysis of adsorbed analytes and for studying adsorption processes qualitatively. This is because the recorded absorptions are directly proportional to the concentration of adsorbed molecules allowing quantification of single and multiple analytes. Furthermore, the probed molecular vibrations are highly sensitive to the molecular fingerprint and intra- and intermolecular interactions, which allows for directly accessing qualitative information.

This thesis aspired to combine infrared spectroscopy with chemically and structurally tailored porous materials to address challenges in analytical and physical chemistry. Building upon the adsorption of analytes into mesoporous silica films coated on attenuated total reflection (ATR) crystals, chemical sensors for gaseous and liquid samples were developed, chemical and physical processes at the surface were studied and the porous materials themselves were characterized.

In **Chapter 1** the fundamentals for infrared (IR) spectroscopy with special focus on ATR infrared spectroscopy, synthesis of mesoporous films and adsorption processes into porous materials are summarized. In addition, a detailed overview of the state-of-the-art in enrichment-based sensing is given. The experimental details on the dedicated optical setup for ATR crystals obtained from double-side polished silicon and germanium wafers, their fabrication procedure, the flow cell designs for different analytical purposes, as well as the

Die approbierte gedruckte Originalversion dieser Dissertation ist an der TU Wien Bibliothek verfügbar.
The approved original version of this doctoral thesis is available in print at TU Wien Bibliothek.
TU Bibliothek Your knowledge hub WIEN

synthetic procedures for mesoporous films are given in **Chapter 2**. The characterization of mesoporous silica films on planar and structured surfaces of different integrated optics is given in **Chapter 3** and comprises infrared spectroscopy, X-ray diffraction, electron microscopy, contact angle measurements, and porosimetry. Within **Chapter 4**, the effective path length within the coating was retrieved from fundamentals of ATR IR spectroscopy and experimentally verified, allowing for quantitative analysis. Analytes at low concentrations were adsorbed into mesoporous films with different pore sizes and pore arrangements from aqueous solutions and gas phase. The sensing applications benefit from high enrichment factors of up to 1800 from aqueous phase and up to 32000 from gas, while excluding the strong infrared absorber water from the probed volume. Fast adsorption in less than 5 s and full recovery was observed in gas and liquid phase. Additionally, this chapter includes results on anion enrichment enabled by introduction of an ion exchange moiety into the mesoporous film. The high specificity of IR spectroscopy paired with the high surface sensitivity of multibounce ATR crystals are used in **Chapter 5** for qualitative analysis of processes at interfaces. Here, IR spectroscopy not just allowed for differentiating degradation products upon photooxidation of methanol by means of their spectral fingerprint, but also to discriminate different local structures of water upon adsorption into mesoporous silica. In addition to the water structure, the thereby obtained spectra also served for retrieving porosity and pore size distribution of the employed films. Finally, in **Chapter 6**, new instrumentation for ATR spectroscopy based on 3D-printing is presented. A 3D-printed ATR module compatible with commercial FTIR spectrometers was designed and the quality of recorded spectra regarding signal to noise ratio bears comparison with a similar setup built from commercial optomechanic components. The great versatility of the 3D-printed module is showcased for a variety of fields using a 3D-printed liquid compartment. Lastly, a Fabry-Pérot filter and a miniaturized thermal emitter were combined in a fully 3D-printed mini-spectrometer with a footprint of only 80 × 120 × 70 mm.

This work was performed within the framework of the H2020 project *Aquarius*, which aimed for inline and online IR-spectroscopic oil-in-water sensors. An external-cavity quantum-cascade laser-based spectrometer was realized by the project partners from *Fraunhofer IAF, Fraunhofer IPMS* (Germany), and *Vigo SA* (Poland). Together with the work package partners from *IMEC/Ghent University* (Belgium), we were responsible for the inline sensor, which comprised Ge-based integrated optical circuits for MIR evanescent field spectroscopy that were coated with mesoporous silica enrichment films.

This thesis was written as monograph to have the opportunity to discuss the obtained results in a broader context compared to the scientific publications that have already resulted from this thesis.[1–3] The abstracts of these publications and already submitted authored and co-authored manuscripts written in the course of this thesis are summarized in the Appendix.

Die approbierte gedruckte Originalversion dieser Dissertation ist an der TU Wien Bibliothek verfügbar.
The approved original version of this doctoral thesis is available in print at TU Wien Bibliothek.
TU Bibliothek WIEN Your knowledge hub

Die approbierte gedruckte Originalversion dieser Dissertation ist an der TU Wien Bibliothek verfügbar.
The approved original version of this doctoral thesis is available in print at TU Wien Bibliothek.

Chapter 1 Fundamentals on Enrichment-Based Mid-Infrared Sensing

This thesis is based on diverse principles which are introduced in this chapter and are divided into four main subjects: **Section 1.1** summarizes the basics on infrared spectroscopy and its instrumentation and focuses on fundamentals on evanescent field spectroscopy. The basics of sol-gel chemistry and the soft-templating approach toward ordered mesoporous materials are discussed in **section 1.2**. The fundamental adsorption processes that take place in porous materials and in particular in mesoporous materials from gas as well as in the special situation from aqueous phase are given in **section 1.3**. Finally, **section 1.4** gives an overview of the state-of-the-art in enrichment-based sensing schemes using ATR spectroscopy and related techniques based on integrated optics.

1.1 Mid-Infrared Spectroscopy

Mid-Infrared spectroscopy is an analytical technique providing molecule-specific qualitative and quantitative information of gaseous, liquid, and solid samples in a label-free and non-destructive manner. In this introductory section, only an overview of this technique will be given and the interested reader is referred to Ref. [4] and [5] for more detailed information. Based on these references, the most relevant basics of this technique are summarized in **sections 1.1.1** and **1.1.2**. **Section 1.1.3** summarizes the fundamentals of attenuated total reflection (ATR) spectroscopy. Additionally, state-of-the-art in instrumentation as well as emerging MIR sensing schemes toward miniaturization are discussed in **section 1.1.4**.

1.1.1 Fundamentals of IR Spectroscopy

Spectroscopic techniques in general are based on the interaction of matter with electromagnetic (EM) radiation to probe physical and chemical properties. The energy of the EM radiation can be transferred to the matter by absorption or scattering processes. Absorption can take place if the energy of the radiation matches the resonant frequency of a respective transition of the molecule or atom. The frequency ν of this radiation is directly

linked to its wavelength λ and energy E via the *Einstein-Planck* relation:

$$E = h \cdot \nu = h \cdot \frac{c_0}{\lambda_0} = h \cdot c_0 \cdot \tilde{\nu}_0 \tag{1.1}$$

with the *Planck* constant h, the speed of light in vacuum c_0 and the vacuum wavenumber $\tilde{\nu}_0$. The latter is given in the unit inverse centimeter cm^{-1}, the commonly used measure of energy in vibrational spectroscopy. Wavelength and wavenumber depend on refractive index and are related via:

$$\lambda = \frac{1}{\tilde{\nu}} = \lambda_0 \cdot n \quad \text{with} \quad n = \frac{c_0}{c_m} \tag{1.2}$$

with the speed of light in the respective medium c_m.

Depending on the wavelength, different transitions, *i.e.,* the resonance between two different quantum states, can be exited:

- Gamma radiation (λ_0 = 1 - 100 pm) probes changes in the energy levels of an atomic nucleus, as *e.g.* in Mößbauer spectroscopy
- X-ray radiation (λ_0 = 10 - 0.1 nm) induces changes in the states of core electrons, as in *e.g.* Auger-electron spectroscopy, x-ray spectroscopy
- Ultraviolet and visible radiation (λ_0 = 10 - 1000 nm) excites electronic transitions of valance electrons, as probed in *e.g.* Fluorescence spectroscopy, UV/Vis spectroscopy
- Infrared radiation (λ_0 = 0.7 µm - 100 µm) induces vibrational transitions of the molecule, as used in *e.g.* IR spectroscopy
- Terahertz radiation (λ_0 = 0.1 mm - 1 mm) probes rotational movements of the molecule in the gas phase or lattice vibrations in crystals, as probed in *e.g.* rotational spectroscopy
- Microwaves (λ_0 = 1 cm - 100 cm) excite electron spins, as used in *e.g.* electron paramagnetic resonance (EPR)
- Radio waves (λ_0 = 1 m - 100 m) induce changes in spins of atomic nuclei, as used in *e.g.* nuclear magnetic resonance (NMR) spectroscopy

For this thesis the infrared region is of special interest. This region is further divided into: near IR radiation (NIR, λ_0 = 0.75 µm - 2.5 µm/ $\tilde{\nu}_0$ = 13 300 cm^{-1} - 4000 cm^{-1}) that probes overtone transitions and combination vibrations; mid IR (MIR, λ_0 = 2.5 µm - 25 µm/ $\tilde{\nu}_0$ = 4000 cm^{-1} - 400 cm^{-1}) radiation that induces transitions of fundamental vibrational modes; and far IR (FIR, also called Terahertz radiation, λ_0 = 25 µm - 1000 µm/ $\tilde{\nu}_0$ = 400 cm^{-1} - 10 cm^{-1}) radiation is mainly used to probe rotational transitions or lattice vibrations.

The number of vibrational transitions induced by MIR radiation present in molecules, and the number of different ways a molecule can vibrate such as bending, rocking or stretching vibrations, is determined by the structure of the molecule and the number of atoms N_{atom}, it is composed of. The maximum number of vibrational modes in a linear molecule equals to $3 \cdot N_{atom}$ - 5 and to $3 \cdot N_{atom}$ - 6 for non-linear molecules. In a first approximation, the

Die approbierte gedruckte Originalversion dieser Dissertation ist an der TU Wien Bibliothek verfügbar.
The approved original version of this doctoral thesis is available in print at TU Wien Bibliothek.
TU Bibliothek Your knowledge hub WIEN

vibration, hence the displacement of the atoms from the equilibrium position r_e, can be described as a harmonic oscillator, where the atoms vibrate at a characteristic frequency ν_i at each mode i (see **Figure 1.1**). The potential energy of the oscillator is quantized and the allowed energy levels E_n, are described by **equation (1.3)**:

$$E_n = h \cdot \nu_i \cdot \left(\upsilon_i + \frac{1}{2}\right) \tag{1.3}$$

where ν_i is the fundamental frequency of the i-th mode, and each vibrational state is associated with a vibrational quantum number υ_i (i = 0, 1, 2, …). The harmonic oscillator model yields the selection rule of $\Delta\upsilon_i = \pm 1$ for electric dipole transitions that can be observed in IR spectroscopy. However, the approximation of the harmonic oscillator is typically only valid for low υ_i, hence, for fundamental vibrations. Higher vibrational states, *i.e.*, vibrations associated with a larger displacement of the involved atoms, are described more accurately using the anharmonic *Morse* potential that expands equation (1.3) by an anharmonic term and the anharmonicity constant χ_i:

$$E_n = h \cdot \nu_i \cdot \left(\upsilon_i + \frac{1}{2}\right) - h \cdot \nu_i \cdot \chi_i \cdot \left(\upsilon_i + \frac{1}{2}\right)^2 \tag{1.4}$$

In this model, transitions of $|\Delta\upsilon_i|>1$ are allowed, hence, also overtone bands and combination transitions, although less probable and thus less intense than fundamental vibrations, are possible. In contrast to the harmonic oscillator, the energy difference of adjacent vibrational states is not constant but decreases with υ_i.

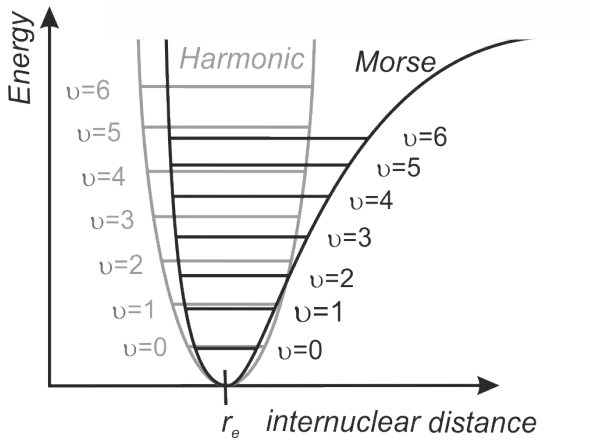

Figure 1.1: Model of harmonic and *Morse*-type (anharmonic) oscillator with vibrational energy levels $\upsilon_i = 1 - 6$.

In IR spectra of gases, a vibrational transition is usually accompanied by rotational transitions giving rise to a large number of ro-vibrational absorption lines for a single vibrational mode, known as the P-, Q- and R-branches. For larger molecules, typically > 5 atoms, the individual ro-vibrations are not resolved due to the small difference in energy between them. In condensed phase bands of vibrational transitions are broadened due to intermolecular interactions.

Not all theoretically possible transitions between different vibrational states are dipole allowed and they must fulfill a basic prerequisite to be IR active: The vibrational mode needs to lead

Die approbierte gedruckte Originalversion dieser Dissertation ist an der TU Wien Bibliothek verfügbar.
The approved original version of this doctoral thesis is available in print at TU Wien Bibliothek.
TU Bibliothek Your knowledge hub WIEN

to a change in dipole moment of the molecule. Except for symmetric, diatomic molecules, *e.g.* H_2 or N_2, that thus cannot be excited by MIR radiation, the majority of molecules can be probed by IR spectroscopy. Since the vibrational frequency is affected by molecular mass and bond strength and the intensity of the absorption depends on the change in dipole moment during vibration, every molecule has its characteristic absorption spectrum.

The MIR region provides access to the group frequency vibrations of functional groups, *e.g.* -OH, C=O, -NH_2, that are not or only slightly affected by the rest of the molecule. In contrast, vibrations resulting from movement of the entire molecule (skeletal vibrations) are typically located between 1600 cm^{-1} to 500 cm^{-1} and yield absorption bands characteristic for the respective molecule. As this region allows for differentiation between organic molecules of similar structure and with similar functional groups, it is referred to as *fingerprint region*. In this thesis different hydrocarbons were investigated for sensing applications (see section 4.2 and 4.4 for further details) and photooxidation products of methanol (see section 5.2) were differentiated using this characteristic region. In addition, bands in the IR spectrum of condensed phase molecules are influenced by the chemical environment of the molecule, *i.e.*, if the molecule is in liquid or solid state or associated to a surface. Within this thesis, the high sensitivity of IR spectroscopy for changes in the H-bonding of water in silica mesopores is exploited to study the structure of water adsorbed to the pore surface (in section 5.1). In addition, the band of CO adsorbed to Pt nanoparticles is strongly affected by the site on the particle, *e.g.* terraces or corners, which was used to monitor the growth of Pt nanoparticles during photodeposition (see section 5.3.4)

Besides qualitative information, IR spectra can be evaluated quantitatively as will be discussed in the subsequent section.

1.1.2 Absorption Measurements in Transmission Configuration

The EM radiation propagating in a medium with refractive index n in direction x, can be described by a plane wave:

$$\boldsymbol{E}(x,t) = \boldsymbol{E}_0 \cdot e^{i(k \cdot x - \omega \cdot t)} \tag{1.5}$$

$$|k| = \frac{2 \cdot \pi \cdot n}{\lambda_0} \tag{1.6}$$

with the wave vector k, position x, the angular frequency ω and time t. The wave vector k depends on the vacuum wavelength λ_0 and is given by **equation (1.6)**. **Equation (1.5)** is extended if attenuation takes place within the medium, which is described by the complex refractive index $\hat{n} = n + i\kappa$:

$$\boldsymbol{E}(x,t) = \boldsymbol{E}_0 \cdot e^{i(k \cdot x - \omega \cdot t)} \cdot e^{-\frac{2 \cdot \pi \cdot \kappa}{\lambda_0} x} \tag{1.7}$$

The imaginary part κ of the refractive index is known as absorption index, thus, describes the absorption within the medium. It is proportional to the linear absorption coefficient α:

$$\kappa = \frac{\alpha}{4 \cdot \pi \cdot \tilde{\nu}_0} \tag{1.8}$$

Die approbierte gedruckte Originalversion dieser Dissertation ist an der TU Wien Bibliothek verfügbar.
The approved original version of this doctoral thesis is available in print at TU Wien Bibliothek.
TU Bibliothek Your knowledge hub WIEN

The electric field is not the physical quantity that is measured at the detector, but the intensity *I(x)* that is related to $\boldsymbol{E}$ via the vacuum permittivity ε_0 and the speed of light c_0:

$$I(x) = \frac{c_0 \cdot n \cdot \varepsilon_0}{2} \cdot \left| \boldsymbol{E}_0 \cdot e^{-\frac{2 \cdot \pi \cdot \kappa}{\lambda_0} x} \right|^2 \quad \textbf{(1.9)}$$

The ratio of this intensity before and after travelling through an absorbing medium is known as transmission $T = I/I_0$. Note that I_0 not necessarily is retrieved from an empty sample compartment but can also be recorded for the respective solvent without analyte. In this case, T only depends on the length of the passed medium $x = d$. The negative logarithm (base 10 is used throughout this thesis) of this ratio defines absorbance A. Using *Lambert-Beer's* law allows for quantitative analysis of bands in the IR spectrum. It relates the absorbance A of a certain vibration of the molecule with the respective molar decadic absorption coefficient $\varepsilon = \alpha/c$ (in L mol^{-1} cm^{-1}), the concentration c (mol L^{-1}) and the path length d (in cm) and holds true for low concentraitons:[6]

$$A = -\log\left(\frac{I(\tilde{\nu})}{I_0(\tilde{\nu})}\right) = \frac{4 \cdot \pi \cdot \log_{10}(e) \cdot \kappa}{\lambda_0} \cdot d = \varepsilon(\tilde{\nu}) \cdot c \cdot d \quad \textbf{(1.10)}$$

Experimentally, the absorbance is determined using the initial intensity $I_0(\tilde{\nu})$ reaching the detector without being attenuated by the sample and with attenuation of the sample $I(\tilde{\nu})$. Therefore, a spectrum is obtained from a background measurement probing the empty matrix, *e.g.* air or pure solvent of the analyte, which is referred to as background single beam spectrum $I_0(\tilde{\nu})$, and a measurement of the sample containing the analyte in the matrix $I(\tilde{\nu})$. This ratio allows for accounting for intensity loss caused by the pure solvent or reduced transmission through optical elements.

Since $\varepsilon(\tilde{\nu})$ is fixed in a direct measurement for an analytical problem, the absorbance, being the analytical signal, can only be enhanced by increasing c or d. The path length is increased in multi-pass cells for gas-phase measurements, increasing spacer thickness of a transmission flow cell for liquid samples, or increased number of active reflections in evanescent field spectroscopy or using waveguides (for further explanation see sections 1.1.3 and 1.1.3.1). However, in liquid-phase measurements, d is usually limited by the strong background absorption of the solvent. Especially, water is a strong IR absorber and allows only for path lengths up to < 10 µm for measurements performed in FTIR spectrometers at the bending vibration at 1640 cm^{-1}.[7] Another possibility is to perform a sample pretreatment and thus increase c, *e.g.* by liquid-liquid extraction or drying of a liquid sample. However, in these approaches the main advantages of IR spectroscopy - being non-destructive and fast - are lost. In fact, these benefits can be preserved if evanescent field spectroscopy is combined with enrichment layers, which is the main topic of this thesis and the state of the art of this approach will be discussed in detail in section 1.4.1, while the basics on evanescent field spectroscopy will be discussed in the following section.

Die approbierte gedruckte Originalversion dieser Dissertation ist an der TU Wien Bibliothek verfügbar.
The approved original version of this doctoral thesis is available in print at TU Wien Bibliothek.
TU Bibliothek Your knowledge hub WIEN

1.1.3 Absorption Measurements in Total Internal Reflection Configuration

The most prominent probing technique for the acquisition of IR spectra is in attenuated total reflection (ATR) configuration. It allows for quick and robust measurements of liquids, solids and pastes or other troublesome samples, and requires hardly any sample preparation.

The beam path in ATR configuration is illustrated in **Figure 1.2A** where a plane wave is refracted at two IR transparent dielectric media: The angle at which the plane wave is refracted when travelling from one medium to the other one with different refractive indices n_i is described by Snell's law:

$$n_1 \cdot \sin(\theta_1) = n_2 \cdot \sin(\theta_2) \tag{1.11}$$

with θ_1 and θ_2 being the angle of incidence and refraction with respect to the surface normal. This law is a consequence of the continuity condition of the x- and y- component of $\boldsymbol{E}$ at the boundary between both media derived from *Maxwell's* equations.[8,9] If the originating medium is optically denser, thus $n_1 > n_2$, θ_2 is always larger than the angle of incidence θ_1 (see Figure 1.2A, dashed line, note that this beam is partially reflected). Theoretically, when increasing θ_1 the refracted angle will at some point approach 90°, hence traveling parallel to the interface. This θ_1 is considered the critical angle θ_c. In fact, for $\theta_1 > \theta_c$ the beam is internally totally reflected at the interface of the medium with higher refractive index and no light is transmitted (see Figure 1.2A, solid line). The critical angle can be derived from **equation (1.11)** for $\theta_2 = 90°$:

$$\theta_c = \sin^{-1}\frac{n_2}{n_1} \tag{1.12}$$

As implied by **equation (1.12)**, materials with high refractive index are required to be used as internal reflection elements (IRE). In this thesis silicon and germanium were used for IREs, here, θ_c corresponds to $\theta_c(Si) = 23°$ and $\theta_c(Ge) = 19°$, for n_2(water)=1.32 and n_1(Si) = 3.42 or n_1(Ge) = 4.02, respectively, at 1640 cm^{-1}.[10,11]

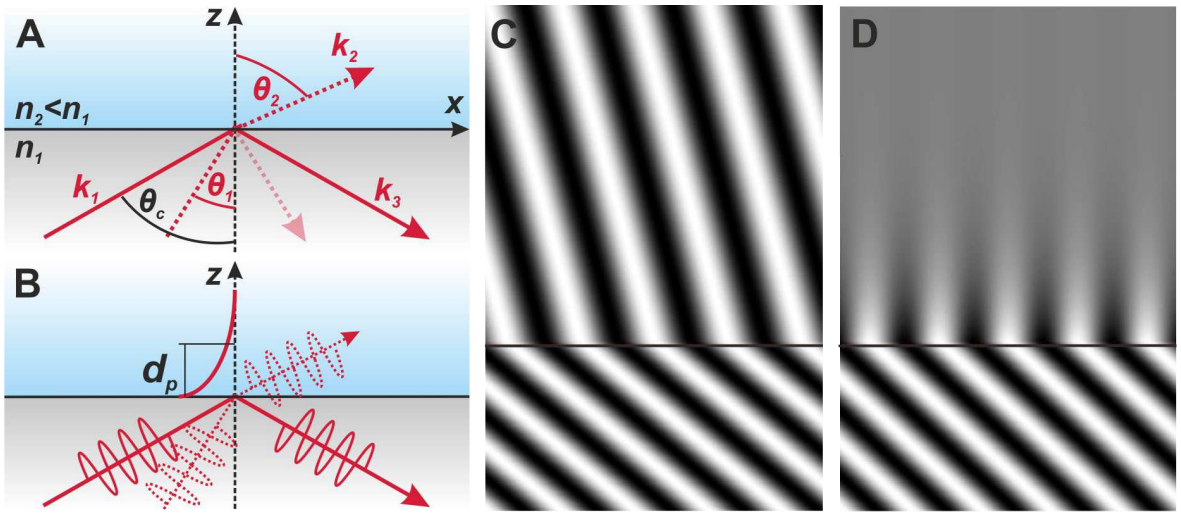

Figure 1.2: (A) Light is refracted (dotted line) and reflected (solid line) at the surface between two dielectric media with different refractive indices $n_1 > n_2$ depending on angle of incidence $\boldsymbol{\theta_1}$. (B) For $\boldsymbol{\theta_1 > \theta_c}$, total internal reflection occurs, and an evanescent wave is generated. (C-D) Representation of the refracted incident wave (C) and evanescent wave (D). Adapted from Ref. [12].

Die approbierte gedruckte Originalversion dieser Dissertation ist an der TU Wien Bibliothek verfügbar.
The approved original version of this doctoral thesis is available in print at TU Wien Bibliothek.
TU Bibliothek Your knowledge hub WIEN

When travelling waves undergo total internal reflection, an evanescent field is formed that extends from the interface into the optically thinner medium (see **Figure 1.2B**). The evanescent field is also a consequence of the continuity condition derived from *Maxwell's* equations (shown in Ref. [9]), and its exponential decay in the optically thin medium is described by the purely imaginary z-component of the wave vector:

$$\boldsymbol{E}(x,t) = \boldsymbol{E}_0 \cdot e^{i(k_x \cdot x + k_z \cdot z - \omega \cdot t)} \tag{1.13}$$

$$\boldsymbol{E}(x,t) = \boldsymbol{E}_0 \cdot e^{i \cdot x \cdot \frac{2 \cdot \pi \cdot n_1}{\lambda_0} \sin(\theta)} \cdot e^{-2 \cdot z \cdot \frac{2 \cdot \pi}{\lambda_0} \sqrt{n_1^2 \cdot \sin^2(\theta) - n_2^2}} \tag{1.14}$$

In **equation (1.14)**, the gray term corresponds to an oscillation parallel to the surface, while the blue term represents the exponential decay of the evanescent field in z direction. As soon as absorption occurs, n is replaced by $\hat{n}$ and this term will also have an oscillating characteristic. Note that both terms have no polarization dependency. The amplitude of the electric field at the surface $\boldsymbol{E}_0(z = 0)$ is however dependent on the polarization of incoming light, but as it only represents the starting point from which the evanescent wave decays, it does not affect the course of the decay. Returning to Figure 1.2, the evanescent field of s-polarized light will have the same extension as p-polarized light in z direction, but as the amplitude $\boldsymbol{E}_{0,\parallel} > \boldsymbol{E}_{0,\perp}$ is different at the interface this appears in a less "bright" evanescent field for s-polarized light.[5,13] As discussed below, this will also affect the effective path length d_e.

Harrick and *du Pre* defined the depth of penetration d_p, with the wavelength λ_1, the angle of incidence θ, and $n_{21} = n_2/n_1$, that determines the point where the $\boldsymbol{E}$ field falls to $1/e$ of $\boldsymbol{E}(d_p)/\boldsymbol{E}_0$, as an arbitrary parameter:[14]

$$d_p = \frac{\lambda_1}{2 \cdot \pi \cdot (n_1^2 \cdot \sin^2\theta - n_2^2)^{\frac{1}{2}}} \tag{1.15}$$

It should be noted that $\boldsymbol{E}$ is not zero at d_p, but $\boldsymbol{E}$ equals to 37 % of $\boldsymbol{E}_0$ at d_p.[15] In addition, the intensity is not proportional to $\boldsymbol{E}$, but to $I(\tilde{\nu}) \approx \boldsymbol{E}^2$ (compare equation (1.9)). If considering this, the remaining intensity at three times d_p corresponds to only 0.25 % of the initial intensity. Therefore, the major fraction of the probed volume is close to the surface up to $3 \cdot d_p$.

The calculations of the amplitude of the field $\boldsymbol{E}$ of the reflected wave using the continuity conditions derived from *Maxwell's* equations, yield the *Fresnel* equations (derivation not shown here, but can be found in Ref. [9]). These equations define the amplitude reflection coefficients r for both polarizations of light:

$$r_\parallel = \frac{n_2^2 \cdot \cos(\theta_1) - n_1 \sqrt{n_2^2 - n_1^2 \cdot \sin^2(\theta_1)}}{n_2^2 \cdot \cos(\theta_1) + n_1 \sqrt{n_2^2 - n_1^2 \cdot \sin^2(\theta_1)}} \tag{1.16}$$

$$r_\perp = \frac{n_1 \cdot \cos(\theta_1) - \sqrt{n_2^2 - n_1^2 \cdot \sin^2(\theta_1)}}{n_1 \cdot \cos(\theta_1) + \sqrt{n_2^2 - n_1^2 \cdot \sin^2(\theta_1)}} \tag{1.17}$$

Die approbierte gedruckte Originalversion dieser Dissertation ist an der TU Wien Bibliothek verfügbar.
The approved original version of this doctoral thesis is available in print at TU Wien Bibliothek.
TU Bibliothek Your knowledge hub WIEN

Analogous to equation (1.9), the ratio of the intensity of the incident and the reflected beam R equals to $R_\perp = |r_\perp|^2$ and $R_\parallel = |r_\parallel|^2$. For non-absorbing media ($\alpha = \kappa = 0$, hence the imaginary part of the refractive index is zero), light will be totally reflected for $\theta_1 > \theta_c$ and $R_\perp = R_\parallel = 1$ (compare **Figure 1.3** black curves).

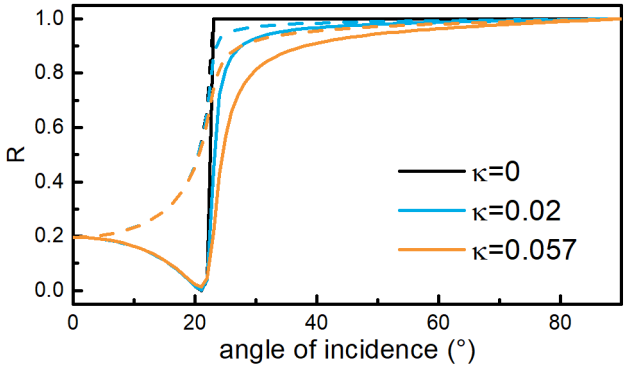

Figure 1.3: Reflection of light at an interface between optically denser and optically rarer medium. Reflectance was calculated for a Si ATR element ($n_1 = 3.42$) and water ($n_2 = 1.32$) as sample for different absorption indices. Here, pure water at 1640 cm^{-1} equals to a $\kappa = 0.057$. Full lines show $R_\parallel$ (parallel polarization), while dotted lines represent $R_\perp$ (orthogonal polarization).

As the probed medium in spectroscopy is inherently absorbing, equation (1.16) and (1.17) can be adapted by inserting the complex refractive index $n_2 = \hat{n}$.[16] The absorption index of the sample strongly influences R and for higher κ, no sharp critical angle exists anymore (Figure 1.3 blue and orange curve). For comparison, R was calculated for $\kappa = 0.057$ of pure water ($c = 55.6$ mol L^{-1}, $\tilde{\nu} = 1640$ cm^{-1}, $\varepsilon = 21.4$ L mol cm^{-1} inserted into equation (1.8), compare spectrum in Figure 3.11) as an example for a very strong IR absorber and is depicted in Figure 1.3. As transmission $= 1 - R$, 7 % and 4 % of the intensity of light for parallel and orthogonal polarization, respectively, is transmitted at an angle of incident of 45°, which is mainly used for ATR crystals in this thesis. Hence, not *total* reflection is taking place anymore, but *attenuated total* reflection (ATR) that is proportional to the absorption coefficient.

To compare the sampling depth of an ATR measurement with classical transmission measurements, the concept of the effective path length d_e was introduced.[13,15,17] For low absorption in transmission experiments, equation (1.10) can be written as

$$\frac{I}{I_0} \approx 1 - \alpha \cdot d \tag{1.18}$$

For internal reflection, the rarer medium can be treated in terms of intensity loss per reflectivity R, with the absorption coefficient α and the number of reflections N:

$$R = (1 - \alpha \cdot d_e)^N \tag{1.19}$$

By this definition, a transmission measurement through the sample with $d = d_e$ yields the same absorbance as the reflective losses for the same sample in ATR configuration for $N = 1$. Furthermore, d_e is related to the $\boldsymbol{E}$ field for a weak absorber via:[13]

$$d_e = \frac{n_{21}}{cos\theta} \int_0^{th} E^2 dz \tag{1.20}$$

with $n_{21} = n_2/n_1$ and the thickness of the absorbing rarer medium th. In the case of semi-infinite bulk film (absorbing film $th \to \infty$) $d_e = \frac{n_{21} \cdot E_0^2 \cdot d_p}{2 \cdot \cos(\theta)}$ and for the thin film case ($th << d_p$)

Die approbierte gedruckte Originalversion dieser Dissertation ist an der TU Wien Bibliothek verfügbar.
The approved original version of this doctoral thesis is available in print at TU Wien Bibliothek.
TU Bibliothek WIEN Your knowledge hub

$d_e = \frac{n_{21} \cdot th \cdot E_0^2}{\cos(\theta)}$. From the parameters for semi-infinite bulk films and the amplitude of the fields at the surface, d_e can be derived from the components of E_0:[13]

$$d_{e,\perp} = \frac{\lambda_0}{n_1} \cdot \frac{n_{21}\, cos(\theta)}{\pi\,(1 - n_{21}^2)[sin^2(\theta) - n_{21}^2]^{1/2}} \tag{1.21}$$

$$d_{e,\parallel} = \frac{\lambda_0}{n_1} \cdot \frac{n_{21}\cos(\theta)\,[2\,sin^2(\theta) - n_{21}^2]}{\pi\,(1 - n_{21}^2)[(1 + n_{21}^2)sin^2(\theta) - n_{21}^2][sin^2(\theta) - n_{21}^2\,]^{1/2}} \tag{1.22}$$

$$d_e = \frac{d_{e,\perp} + d_{e,\parallel}}{2} \tag{1.23}$$

For unpolarized light, d_e can be derived from equation (1.23). It was found that this approximation is only valid for weak absorbers and $\alpha \cdot d_e \ll 3$ and $\frac{\kappa \cdot d_e}{\lambda_1} < 0.1$.[17] If again using water as an example, for $d_e = 10$ µm at 1640 cm^{-1}, $\frac{\kappa \cdot d_e}{\lambda_1} = 0.09$, hence equations (1.21)-(1.23) are still valid.

Although the validity of d_e as analogue for the path length d in transmission experiments has been shown, there are distinct differences compared to transmission spectra:

i. d_e depends on the wavelength, therefore, bands with same absorption coefficient appear stronger at higher wavelengths,
ii. d_e and hence sensitivity can be tuned by the angle of incidence (compare section 6.1)
iii. Although the refractive index of ATR crystals is usually constant for the probed wavelength range, the refractive index of the sample changes, exhibiting anomalous dispersion close to absorption bands. This results in a lower d_e for the high-wavenumber edge of the absorption band, yielding a shift of the band observed in ATR spectra toward lower wavenumbers, compared to transmission spectra. The extent of this shift depends on the ratio of refractive indices n_{21}.
iv. d_e depends on the polarization of light. This should not be confused with the probed depth defined by the exponential decay with the decay constant d_p, which is independent from polarization.

1.1.3.1 Absorption Measurements in High-Index Waveguides

As the path length of ATR spectroscopy linearly increases with the number of active reflections, the sensitivity of ATR spectroscopy can be extended by using other light-guiding optics such as fibers or waveguides instead of the typical ATR crystals mainly in shape of a prism that offer solely a limited number of reflections. These waveguides also rely on high-contrast refractive index materials with low absorption coefficients that confine the EM radiation in one or more dimensions. For example, low index claddings of a high refractive index fiber in different geometries, typically silver halides, have been widely applied for MIR spectroscopy (referred to as fiber evanescent wave spectroscopy, FEWS).[18,19] Although this approach allows for increasing path lengths, it goes hand in hand with mechanically fragile fibers as thin as 100 µm, which typically limits their applicable physical length and hence the

Die approbierte gedruckte Originalversion dieser Dissertation ist an der TU Wien Bibliothek verfügbar.
The approved original version of this doctoral thesis is available in print at TU Wien Bibliothek.
TU Bibliothek Your knowledge hub WIEN

accumulated effective path length of a few tens of µm for liquid sensing. To further enhance the path length in hollow core waveguides, the use of more powerful light sources such as quantum cascade lasers (QCLs) are required and have been employed (see section 1.1.4 for more details).

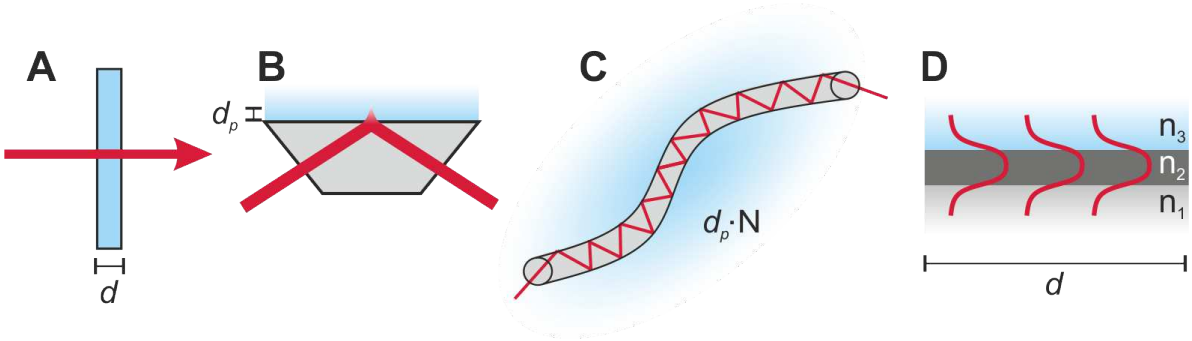

Figure 1.4: Basic configurations for mid-IR spectroscopy. (A) Conventional transmission spectroscopy, (B-D) evanescent field-base spectroscopy using (B) a single bounce ATR crystal, (C) an optical fiber, or (D) a waveguide with $n_2 > n_1 > n_3$.

Integrated MIR-waveguides as part of integrated optical circuits (IOCs) provide mechanical stability and decrease the footprint of IOC chips to a few mm^2 for path lengths in the range of optical fibers.[20,21] For this sensing scheme, light is confined and transmitted in a high index layer (*core*, n_2 in **Figure 1.4D**) with a thickness in the range of less than ten times the wavelength between two low index layers, called *cladding*. Light is totally reflected at the core-cladding interface. This configuration is called slab or planar waveguide. For sensing applications, the cladding is partially removed from the wave guiding layer allowing for interaction with the analyte. If the cross-section of the high-index material is restricted in a second dimension, the structure is called rectangular or strip waveguide. The light guided in the waveguide is described in terms of optical modes that depend on the thickness and the refractive index contrast. In the framework of the H2020 project Aquarius, germanium waveguides with a height between 2 - 4 µm were employed. The field distribution and hence the field extending outside the core, can be calculated (numerically) and is used to design waveguides.

1.1.4 Instrumentation for MIR Spectroscopy

Basically, every setup for direct absorption spectroscopy consists of three parts: a MIR light source, a wavelength discriminating element, either dispersive or interferometric, and a detector. Here, different light sources and the function of a FTIR spectrometer will be outlined.

1.1.4.1 IR Light Sources

The most widely used continuous light sources for the MIR region are black-body emitters. The radiation emitted by these light-sources is described by the *Planck* equation that relates the spectral radiance per unit wavenumber $B(\tilde{\nu}, T_0)$ to the temperature of the black-body T_0:

Die approbierte gedruckte Originalversion dieser Dissertation ist an der TU Wien Bibliothek verfügbar.
The approved original version of this doctoral thesis is available in print at TU Wien Bibliothek.
TU Bibliothek Your knowledge hub WIEN

$$B(\tilde{\nu}, T_0) = 2 \cdot h \cdot c^2 \cdot \tilde{\nu}^3 \frac{1}{e^{\frac{hc\tilde{\nu}}{k_B T_0}} - 1} \quad (1.24)$$

with the Boltzmann constant k_B. The integration of the spectral radiance over the radiating surface, radiating angle and frequency yields the spectral power in W usually given for light sources. An increase in temperature is accompanied by a shift of the maximum toward higher wavenumbers. With respect to the signal-to-noise ratio (SNR) of the spectrum, radiation and hence temperature should be as high and constant over time as possible, however, the black-body has to be operational at ambient conditions (unlike tungsten in a lightbulb), which limits the selection of materials. Silicon carbide has prevailed as material and is most widely used in spectrometers, commercially known as *Globar*, operated at 1300 K emitting typically irradiation over the entire MIR region providing 30 - 40 mW inside a sample compartment of a typical FTIR spectrometer.[22]

In contrast to bulky Globar rods that emit continuously, thin films of different alloys of metals or semiconductors with very low heat capacity allow for pulsed operation at low electrical power consumption.[23] These films can be further tuned in terms of spectral radiance and intensity using lithography,[24] and are widely applied in non-dispersive IR spectroscopy applications.[25] Their small size (fit in TO-39 case with a diameter of 10 mm), pulsed operation without the need of mechanical parts and low power consumption make them an ideal light source for compact sensing systems.[26] Within this thesis, their features were also exploited to build a miniature ATR spectrometer (see section 6.2 for details).

Besides broadband thermal emitters, laser based IR sources such as solid-state lasers,[27,28] quantum cascade lasers (QCLs),[29,30] and interband cascade lasers (ICLs)[31,32] have emerged. Semiconductor laser diodes generate MIR radiation via electron-hole recombination between the conduction and the valence band of appropriate semiconductors or semiconductor mixtures. In contrast to that, QCLs and ICLs emit from cascaded structures of alternating ultra-thin layers of band gap III-V materials, *i.e.*, quantum well heterostructures, utilizing sub-band or interband transitions, respectively. Tuning of this layer structure and used materials allows for tailoring the emission wavelength and lasing condition *i.e.,* pulsed or continuous wave (cw) operation. Although QCLs and ICLs are available in a broad wavelength regime, their tuning range itself is limited. The combination of QCLs with an external cavity (EC) and moveable gratings enables extending the spectral range to over several hundred wavenumbers, whilst emitting at high power of typically 10 – 250 mW.

1.1.4.2 FTIR Spectroscopy

The Fourier-Transform infrared spectrometer is the most commonly employed IR spectrometer design and was also mainly used in this thesis. The design of the two-beam interferometer was outlined by Michelson in 1891.[33] As illustrated in **Figure 1.5**, the interferometer consists of two perpendicular plane mirrors, of which one is fixed and the other is movable along an axis perpendicular to its plane. IR radiation from a broadband emitter is

Die approbierte gedruckte Originalversion dieser Dissertation ist an der TU Wien Bibliothek verfügbar.
The approved original version of this doctoral thesis is available in print at TU Wien Bibliothek.
TU Bibliothek Your knowledge hub WIEN

partially reflected at the beam splitter to the fixed mirror and partially transmitted to the movable mirror. The retro-reflected beams are again partially reflected and transmitted at the beam splitter and the recombined partial-beams interfere. The path difference introduced by the moving mirror Δl leads to a phase difference between the waves reflected off the fixed mirror and that reflected off the moving mirror.

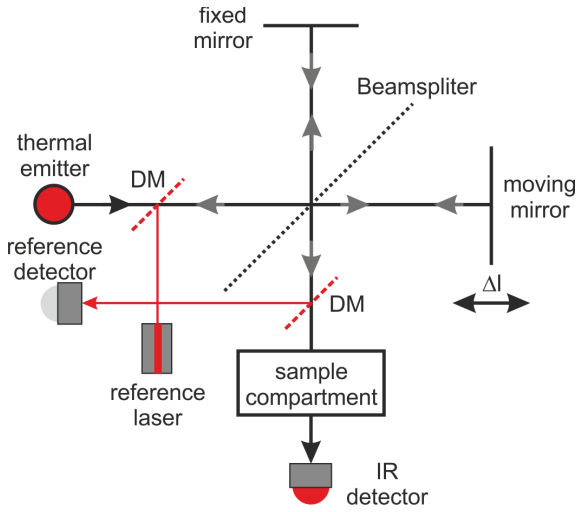

Figure 1.5: Working principle of a FTIR spectrometer. DM… dichroic mirror.

The beams interfere either constructively or destructively, depending on the wavelength and the path length difference Δl, which leads to an intensity variation $I(\Delta l)$ at the output arm (= detector) of the interferometer. The so called interferogram $I(\Delta l)$ is given by the cosine Fourier transform of the input light spectrum $I_0(\tilde{\nu})$:

$$I(\Delta l) = \frac{1}{2} \int_{-\infty}^{\infty} I_0(\tilde{\nu}) \cos(2 \cdot \pi \cdot \tilde{\nu} \cdot \Delta l)\, d\tilde{\nu} \qquad (1.25)$$

with the signal $I(\Delta l)$ as a function of relative mirror position and wavenumber. This signal is then mathematically transformed into the desired single beam spectrum using the inverse Fourier transform. This spectrometer design provides several advantages over dispersive systems: (i) In contrast to dispersive systems, all contribute to the intensity measured at all Δl. This allows for measuring a spectrum with M data points, M times faster compared to a dispersive system, or for achieving the same signal to noise ratio (SNR) the measurement time will be $\sqrt{M}$ times shorter (multiplex or *Fellgett* advantage). (ii) As FTIR instruments accept circular beam shapes in contrast to slits that are required for dispersive systems, a higher optical throughput is achieved (throughput or *Jacquinot* advantages). (iii) A reference laser (compare Figure 1.5) allows for precisely measuring the moving mirror position and hence for increasing the precision of the wavelength axis (Precision or *Connes* advantage).

1.1.4.3 Miniaturization of IR Sensors

Although FTIR spectrometers are still considered the *gold standard* and are available with a footprint of only 22 cm x 30 cm as specified for the *Bruker Alpha II* spectrometer, the great

Die approbierte gedruckte Originalversion dieser Dissertation ist an der TU Wien Bibliothek verfügbar.
The approved original version of this doctoral thesis is available in print at TU Wien Bibliothek.
TU Bibliothek WIEN Your knowledge hub

advances in the field of **integrated optics** of the past decades hold promise to achieve the functionality and advantages of conventional IR spectroscopic chemical sensing, but at a drastically reduced foot-print and lower cost due to CMOS-fabrication.[34] Fully functional spectrometers have been reported with the size of a few cm^2, with interaction path lengths ($\approx$ 50 µm) comparable with silver halide fibers.[35–39] Different integrated sensing schemes based on micro-cavity resonators,[40] MIR spectroscopy[41], MIR dual comb spectroscopy,[42] Raman spectroscopy,[43,44] or photothermal spectroscopy[45] have been demonstrated. Despite their impressive integration of functionality, achieving effective optical path lengths of several meters as routinely used in spectroscopic gas sensing is challenging in the NIR and even harder in the MIR. Here, the path length is limited by the waveguide losses that are still >1 dB/cm for Ge-on-SOI or graded GeSi waveguides suitable for the MIR.[46–49] Despite the shorter path length and in contrast to multi-pass cells, sensitivity can be increased using enrichment claddings that attract and hence concentrate the analyte within the volume probed by the evanescent wave. In addition, these claddings can introduce additional selectivity *e.g.* hydrophobicity to exclude the strong IR absorber water. This concept of coating waveguides for sensing applications was pursued in the H2020 AUQARIUS project and also with other collaboration partners of IMEC. The results obtained of mesoporous coatings on different integrated optics are summarized in section 3.3.
In addition, further examples found in literature for this approach are given in section 1.4.

A second, compared to the Michelson-interferometer rather young sensing scheme based on interference filters, so called **filtometers**, was exploited in the framework of this thesis to reduce size and cost for MIR sensing. In contrast to interferometers and dispersive elements, wavelength discrimination is achieved by the use of optical band pass filters.[50] Here, layers of two dielectric materials with different refractive indices, so called Bragg-reflectors, are alternatingly deposited on an IR-transparent material. Depending on the wavelength, internal reflection from these layers will vary from constructive to destructive interference, which defines the band of radiation transmitting through the filter. In many filtometers, these layered materials are used as window of a pyroelectric detector. In addition to fixed-wavelength Bragg-reflectors, *Fabry-Pérot* (FP) filter designs have emerged in the 1990s that discriminate the transmitted wavelength by the distance d between two coplanar reflective surfaces and the refractive index between these surfaces.[51] By changing d, the filter can be spectrally tuned and the spectral resolution varies between 55 nm up to 220 nm/20 cm^{-1} up to 50 cm^{-1}, depending on the wavelength range.[52] A micro-electro-mechanical system (MEMS)-based MIR filter using a FP air resonator combined with a pyroelectric detector was first reported in 2003 and is now commercially distributed by *InfraTec* for < 500 € in several MIR wavelength ranges.[53,54] Paired with pulsed thermal emitters *e.g.* from *Axetrix* for 80 € an ATR spectroscopy module that houses FP filter, light source and ATR crystal was designed and tested (see section 6.2).

Die approbierte gedruckte Originalversion dieser Dissertation ist an der TU Wien Bibliothek verfügbar.
The approved original version of this doctoral thesis is available in print at TU Wien Bibliothek.
TU Bibliothek WIEN Your knowledge hub

1.2 Synthesis of Mesoporous Films

Since the discovery of mesoporous silica in 1990,[55,a] much attention has been given to these high-surface area (>1000 $m^2\ g^{-1}$) and structurally well-defined materials.[56–58] Large, accessible pore volumes, versatile surface chemistry, hence, manifold possibilities of functionalization, and tunable regular pore sizes within the mesoporous regime (2-50 nm)[59] of (organo-)silica have been exploited in various fields such as catalysis,[60–62] membranes and separation,[63] electrochemistry,[64] sensors,[65] optics,[66] and environmental technologies.[67]

In this section, the basic principles of sol-gel chemistry (based on Ref. [68]), the combination of sol-gel chemistry with surfactants yielding the evaporation induced self-assembly (EISA) process to form mesoporous silica films and different film deposition techniques will be discussed.

1.2.1 Sol-Gel Process

Sol-gel chemistry allows for creating oxide networks from molecular precursors at ambient conditions in a two-stage process: In a first step, a stable suspension of colloidal solid particles, the so-called *sol*, is formed by hydrolysis and subsequent condensation and gelation of the precursors yields the network structure. By subsequent solvent removal, an oxide material is obtained. Synthesis conditions as well as drying parameters effect structure and type of the produced materials *e.g.* aerogels or xerogel.

Silica gels are well-investigated and are obtained from alkoxysilanes $Si(OR)_4$ *e.g.* tetraethoxysilane (TEOS) or tetramethoxysilane (TMOS), which are hydrolyzed and further condensed to an interconnected three-dimensional network with siloxane Si-O-Si bonds (compare **Figure 1.6**).

Hydrolysis

$$\equiv Si{-}OR + H_2O \rightleftharpoons \equiv Si{-}OH + ROH$$

Condensation

$$\equiv Si{-}OR + \equiv Si{-}OH \overset{-ROH}{\rightleftharpoons} \equiv Si{-}O{-}Si\equiv$$

$$\equiv Si{-}OH + \equiv Si{-}OH \overset{-H_2O}{\rightleftharpoons} \equiv Si{-}O{-}Si\equiv$$

Figure 1.6: Hydrolysis and condensation reactions of an alkoxysilane to SiO_2 via sol-gel process.

Hydrolysis and condensation reactions are affected by many factors, such as used alkoxysilane precursor, types and concentration of solvents, and temperature. Furthermore, the point of zero charge for the Si-OH containing species is between pH = 1.5 to 4.5 (the higher the degree of condensation the lower the point of zero charge). Therefore, the reaction mechanism of the initial hydrolysis is governed by the pH, hence can be catalyzed via acidic or basic conditions: At pH < 3, the protonated oxygen of the Si-OH or Si-OR group acts as a good leaving group (H_2O or ROH) making the silicon atom more accessible for reactions with water (= hydrolysis) or silanol groups (= condensation). For basic catalyzed hydrolysis (pH > 3), the silicon atom is attacked either by an OH^- (= hydrolysis) or $Si\text{-}O^-$ (= condensation) ion in

[a] Note that in a patent filed in 1969 mesoporous silica was already produced but not noticed.[368]

Die approbierte gedruckte Originalversion dieser Dissertation ist an der TU Wien Bibliothek verfügbar.
The approved original version of this doctoral thesis is available in print at TU Wien Bibliothek.
TU Bibliothek Your knowledge hub WIEN

a S_N2-type substitution mechanism. Besides the difference in reaction mechanism forming the siloxane bond, the reversibility of the condensation reaction is also pH dependent. While the basic catalyzed reaction has a reversible character, the reaction at low pH is considered irreversible. Furthermore, the structural development of the resulting silica gel is governed by the pH as it also affects the reaction rate for hydrolysis and condensation. For low pH, hydrolysis proceeds faster leading to three-dimensional gel networks, while faster rates for condensation at high pH give highly condensed networks in particles. The proceeding condensation and pH dependent structural differences are depicted in **Figure 1.7**.

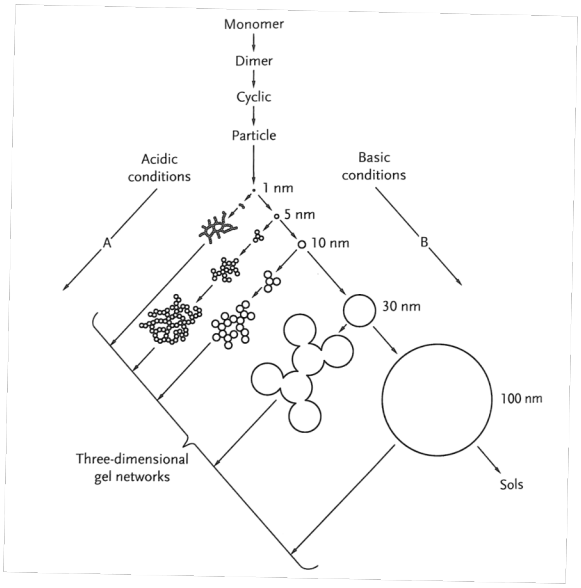

Figure 1.7: The structural development of silica gels is governed by type of catalysis: 3d-networks are formed under acidic conditions and highly condensed particles are obtained under basic conditions.[68]

As the condensation reaction proceeds, at a certain point *gelation* occurs. Note that after gelation, the solvent still remains in the wet-gel network and it still contains unbounded clusters that can further undergo structural rearrangements. These rearrangements are defined as the *aging* process, which takes place until all liquid is completely removed. This is performed by drying, which can be performed by *e.g.* increasing temperature or decreasing pressure. During this last process step the network becomes increasingly stiffer as well as shrinkage occurs yielding a xerogel. Special drying techniques have been developed to impede shrinkage, *e.g.* supercritical drying, and the obtained materials are called aerogels.

Sol-gel chemistry offers different processing routes leading to a variety of materials, where gelation occurs before or after casting the sol. Thin films are prepared by standard coating techniques such as dip or spin coating. Porosity in sol-gel materials is influenced by the size and structure of the particles formed initially by condensation reactions and the collapse of the gel while drying.[69] However, classical sol-gel chemistry provides usually microporous materials (< 2 nm) and lacks of control over pore size and distribution. The subsequent section gives an overview of possibilities to control pore size and pore arrangement.

1.2.2 Thin Film Templating by Evaporation Induced Self-Assembly

Ordered periodic mesoporous materials with controlled pore size were firstly synthesized in

Die approbierte gedruckte Originalversion dieser Dissertation ist an der TU Wien Bibliothek verfügbar.
The approved original version of this doctoral thesis is available in print at TU Wien Bibliothek.
TU Bibliothek Your knowledge hub WIEN

1990, by using surfactants as sacrificial template.[55,70] Ever since, many different templates *e.g.* soft templates such as surfactants or amphiphilic block copolymers were used to generate materials with different pore sizes up to 60 nm.[71]

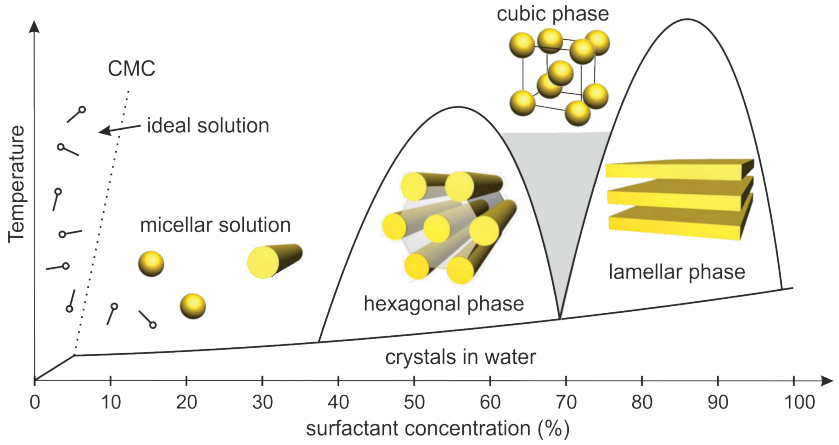

Figure 1.8: Schematic phase diagram of CTAB. Above the critical micelle concentration (CMC), different mesophases are formed.

The soft-templating approach relies on the driving forces of interactions between hydrophilic head groups and hydrophobic tails of the surfactants. These driving forces lead to the assembling of discrete spherical or cylindrical micelles that further aggregate into 2d or 3d ordered mesostructures of liquid crystalline phases with long-range order at higher concentrations.[72] These so-called mesophases are an intermediate between liquid and solid and form above the critical micelle concentration (CMC). An exemplary phase diagram of the ionic surfactant cetyltrimethylammonium bromide (CTAB) is given in **Figure 1.8**.

The proposed mechanism for the formation of ordered mesostructures in the presence of a sol is called cooperative self-assembly. Based on this mechanism, solvent evaporation induced self-assembly (EISA) was developed as powerful tool to synthesize mesostructured thin films with large, accessible pores.[70,72,73] In this context, thin films are commonly deposited via two methods: (i) spin coating and dip coating.[74] In dip coating, the substrate is immersed in the coating solution and removed with a defined velocity that allows for film thickness adjustment. In spin coating, the solution is deposited on a rotating substrate and through rotation a thin film is formed. Both methods in combination with EISA are depicted in **Figure 1.9**.

While for dip coating, the substrate is immersed in the isotropic solution containing sol and surfactants, for spin coating a certain amount (typically few tens of µL) are applied to the substrate. With the start of dipping or spinning, respectively, the film forms and the solvent begins to evaporate. Thereby the surfactant concentration of the solution increases and as well the silica condensation further proceeds. As soon as the CMC is exceeded, the liquid-crystalline phase is formed. At the same time, the silica network further condenses and hence stabilizes the formed mesophase. The precursor and the surfactant contribute both to the assembly (= cooperative self-assembly). However, the kinetics of the formation of highly ordered films are influenced by many factors such as used solvent, spinning or dipping speed, used silanes, *etc.* It was found that by controlling the relative humidity (RH) during

Die approbierte gedruckte Originalversion dieser Dissertation ist an der TU Wien Bibliothek verfügbar.
The approved original version of this doctoral thesis is available in print at TU Wien Bibliothek.
TU Bibliothek Your knowledge hub WIEN

deposition, the evaporation rate of the solvent as well as the condensation rate of the silica can be influenced.[75] Thereby, highly ordered mesoporous films can be achieved. In particular for ionic-surfactants *e.g.* CTAB, monitoring RH during film deposition is essential to control the final structure of silica films.[75] Besides ionic surfactants, non-ionic, amphiphilic triblock copolymers are widely applied for the synthesis of mesoporous films.[76] Here, mainly polyoxamers consisting of poly ethylene oxide (PEO) and poly propylene oxide (PPO) blocks with variable block chain length and variable molecular weight *e.g.* P123 (MW = 5 800 g mol^{-1}) or F127 (MW = 12 600 g mol^{-1}) were used in this thesis. Polymeric surfactants allow for increasing the pore size to up to 60 nm and for tuning microporosity.[77-79]

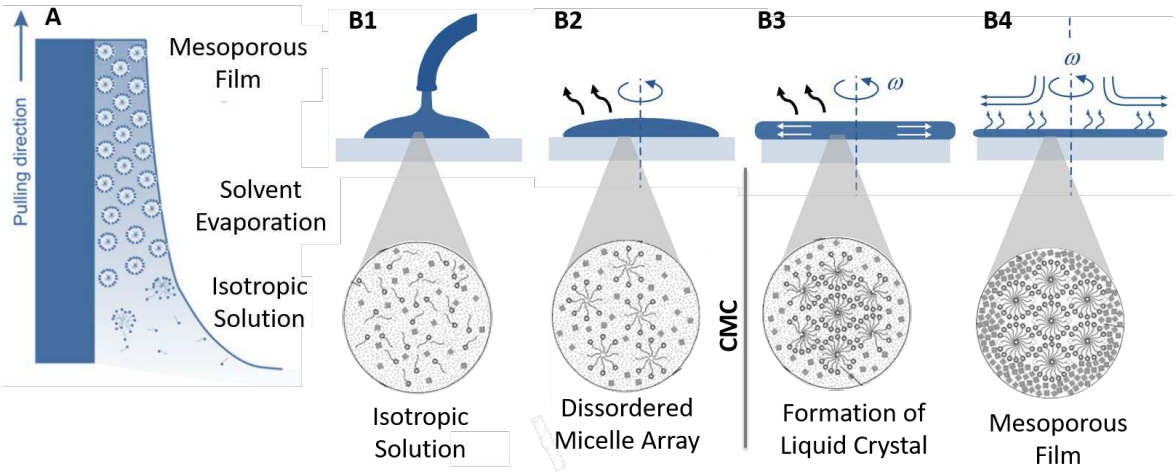

Figure 1.9: Scheme of dip (A) and spin (B) coating of a sol for the formation of mesoporous silica films via EISA. B1) Application of sol on substrate surface B2) rotation of substrate, spreading of the sol and evaporation of solvent, B3) micellar structures form B4) silica further condenses to a network. Adapted from Ref. [80] and [73].

After film deposition, the surfactants are removed by calcination (> 300 °C), extraction or UV/ozone treatments leading to highly ordered mesostructured materials.[77] The variation of used surfactant and precursor/surfactant ratio can lead to many different pore mesophases, *e.g.* 2d hexagonal, 3d hexagonal and 3d cubic.

In addition to structural variability, the rich chemistry of silica allows for tuning the surface properties, which will be discussed in the following section.

1.2.3 Surface Functionalization

(Mesoporous) Silica is an attractive material for many applications because it offers a wide range of different surface modification methods and hence many possibilities for tailoring surface properties. Organic functional groups R' can be either introduced by co-condensation (so-called ormosils; pre-functionalization, **Figure 1.10**) or grafted to silanol groups at the surface of porous silica (post-functionalization) via covalent linkage formed through the reaction of silica species with *e.g.* organoalkoxysilanes (R-Si(OR')$_3$). Typically, organosilanes such as 3-aminopropyltrimethoxysilane, 3-mercaptopropyl trimethoxysilane, octyltrimethoxy-silane, hexamethyldisilazane (HMDS) or trichloromethyl silane (TCMS) are used, but as the same chemistry is widely applied for modification of chromatography columns, a broad range

Die approbierte gedruckte Originalversion dieser Dissertation ist an der TU Wien Bibliothek verfügbar.
The approved original version of this doctoral thesis is available in print at TU Wien Bibliothek.
TU Bibliothek Your knowledge hub WIEN

of different silanes are commercially available. These include amino- and sulfo- functionalized organotrialkoxysilanes as well as more complex organoalkoxysilanes with *e.g.* crown ether or porphyrin moieties among others.

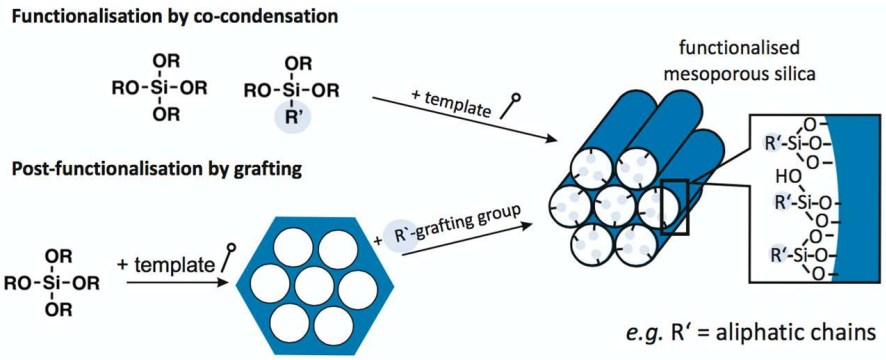

Figure 1.10: Surface modification of mesoporous sol-gel materials: A) Pre-functionalization by co-condensation, B) Post-functionalization by grafting. Adapted from Ref. [58].

In the co-condensation pathway, the silica network is formed through hydrolysis and subsequent condensation of an organotrialkoxysilane *e.g.* methyltriethoxysilane (MTES) and tetraalkoxysilane *e.g.* tetraethoxysilane (TEOS) (see **Figure 1.11A**). As the organic functionality is directly inserted into the material during its synthesis, the degree of functionalization, *e.g.* methylation for MTES, is directly dependent on the initial sol composition. However, high concentration of organotrialkoxysilanes as well as sterically demanding R' moieties, may disrupt the self-assembly of mesopores during the EISA process.[81] Furthermore, post processing of the film via heat treatment may remove the organic functionalities, which limits this functionalization pathway.

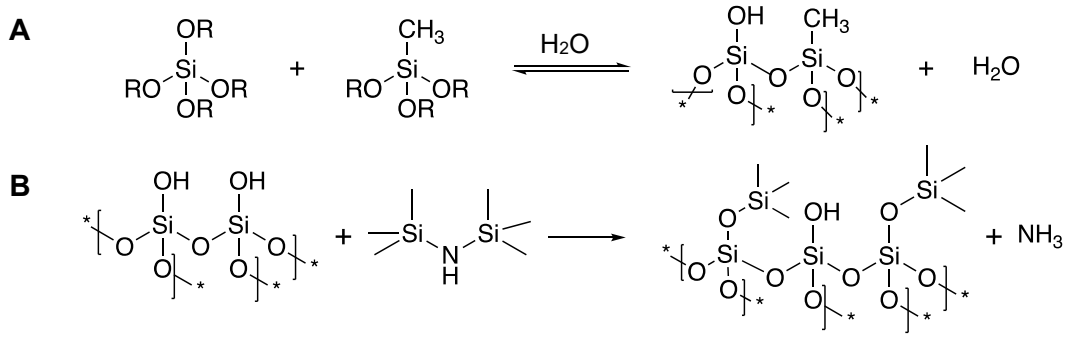

Figure 1.11: Scheme of the co-condensation (A) and post-functionalization (B) with R= -C_2H_5, or -H depending on the degree of hydrolysis. A) TEOS and MTES forming a silicon dioxide network functionalized with methyl groups. B) Silica is post-functionalized using hexamethyldisilazane.

Therefore, the post-functionalization pathway is a good alternative for introducing demanding organic groups using alkoxysilanes (R-Si(OR')$_3$), chlorosilanes (R-$SiCl_3$) or other silazanes. Depending on reaction conditions and silylation agent, the properties of the functionalized mesoporous materials can be largely affected.[82] An example for post-functionalization using HMDS is depicted in **Figure 1.11B.**

Die approbierte gedruckte Originalversion dieser Dissertation ist an der TU Wien Bibliothek verfügbar.
The approved original version of this doctoral thesis is available in print at TU Wien Bibliothek.
TU Bibliothek Your knowledge hub WIEN

1.3 Adsorption Mechanisms in Mesoporous Materials

This section deals with the fundamental processes of adsorption into porous materials and the mass transfer within them. It is based on the Handbook of Porous Solids (Ref. [83]) and the International Union of Pure and Applied Chemistry (IUPAC) technical report on physisorption of gases (Ref. [84]).

1.3.1 General Aspects of the Adsorption Mechanism

Generally, *adsorption* is defined as the increase in concentration or density of one or more gaseous components in the vicinity of a gas-solid interface.[85] In contrast to adsorption, *absorption* occurs if the adsorptive penetrates the surface layer and enters the bulk structure. If a clean solid (= *adsorbent*) is brought in contact with an adsorbable gas (= *adsorbate* or *adsorptive*) it is called *physisorption*. Unlike in *chemisorption*, there are no chemical bonds, *i.e.,* ionic or covalent bonds, to the surface, thus the adsorbate is not influenced by the adsorption itself and the interaction relies on attractive dispersion forces, short range repulsive forces, and specific molecular interactions such as polarization, or field-dipole interactions. These forces occur as a result of particular geometric and electronic properties of the adsorbate and adsorbent. Even though, adsorption energies for physisorption are lower compared to chemisorption, they can be enhanced when a molecule enters a pore of molecular dimensions. Although factors such as pore shape influence the adsorption mechanism, it is mainly governed by the pore size. The IUPAC defines three pore size regimes: (i) macroporous: diameter ≥ 50 nm, (ii) mesoporous: 2 - 50 nm, (iii) microporous: ≤ 2 nm.[59] This categorization is based on the three distinctive adsorption processes depending on the pore size: monolayer-multilayer adsorption in macropores, capillary condensation in mesopores, and micropore filling in micropores.

The adsorption mechanism in mesopores takes place in three stages: (i) *monolayer adsorption* = all adsorbed molecules are in contact with the surface of the adsorbent; (ii) *multilayer adsorption* = more than one layer of molecules so that not all the adsorbed molecules are in direct contact with the pore surface of the adsorbate; (iii) followed by *pore condensation*. During pore or capillary condensation, a gas condenses to a liquid-like phase in a pore at a pressure p below the saturation pressure p_0 of the bulk liquid (this term cannot be applied for micropore filling as this process does not involve a vapor-liquid transition).

1.3.1.1 Physisorption Isotherms

The adsorption process can be described quantitatively using the total adsorbed amount n^a:

$$n^a = \int_0^{V^a} c \, dV \tag{1.26}$$

with the local adsorbate concentration c and the volume of the adsorbed phase V^a. However, this approach requires knowledge of either V^a (implying a known density of the adsorbate) or

Die approbierte gedruckte Originalversion dieser Dissertation ist an der TU Wien Bibliothek verfügbar.
The approved original version of this doctoral thesis is available in print at TU Wien Bibliothek.
TU Bibliothek Your knowledge hub WIEN

the local concentration as a function of the distance to the surface, which is usually not available. *Gibbs* tried to overcome this problem by replacing n^a by the intermediate quantity called surface excess amount n^σ. It assumes the gas concentration to be totally 2-dimensional ($V^a = 0$) and at which n^σ is located on a notional surface ("Gibbs dividing surface"). n^σ and n^a are only identical for small p/p_0. Note that this is not an adsorption model, but just allows to describe the experimental data.

The pressure above the adsorbent at constant temperature as a function of the amount adsorbed per unit mass of solid adsorbent n^a is known as *adsorption isotherm*. If the adsorption takes place at a temperature below the critical temperature of the gas (= the temperature at which a substance cannot exist as liquid independent of the applied pressure), the pressure is expressed as fraction of pressure p and saturation pressure p_0 of the adsorbate at temperature T:

$$n = f\left(\frac{p}{p_0}\right) \tag{1.27}$$

Depending on the structure of the adsorbent, six different isotherms are classified by IUPAC, which are depicted in **Figure 1.12**.

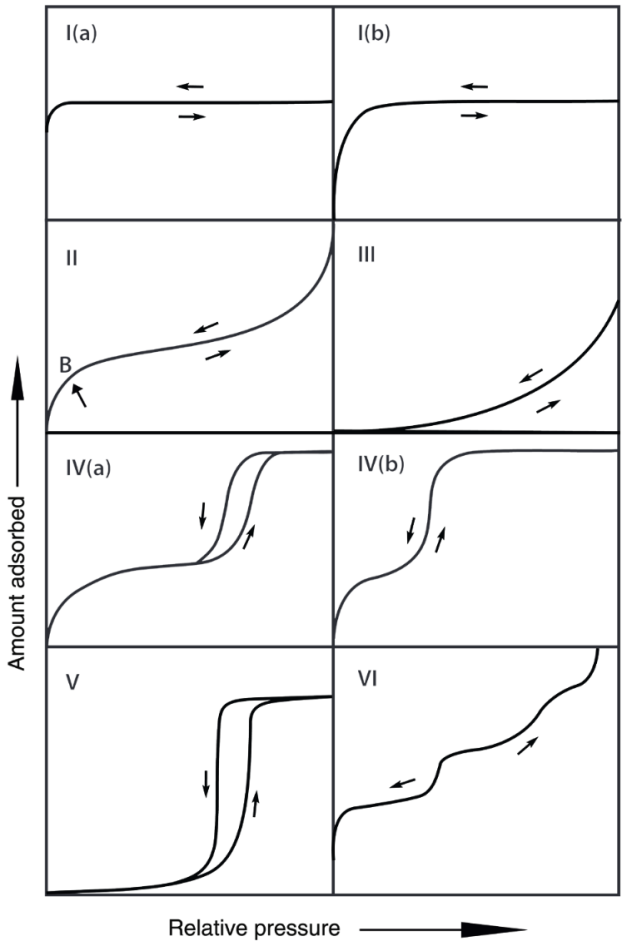

Figure 1.12: IUPAC classified physisorption isotherms.[84] See text for further explanation.

Reversible *Type I* isotherms show a long saturation plateau and are given by microporous solids with relatively small external surfaces such as zeolites. The steep increase at low p/p_0

Die approbierte gedruckte Originalversion dieser Dissertation ist an der TU Wien Bibliothek verfügbar.
The approved original version of this doctoral thesis is available in print at TU Wien Bibliothek.
TU Bibliothek Your knowledge hub WIEN

is due to enhanced adsorption energy in narrow pores, resulting in fast micropore filling. The narrower the pore size distribution, the faster the plateau is reached (compare I(a) for narrow and I(b) for broad size distribution). Reversible *type II* isotherms are obtained from most gases adsorbed on nonporous or macroporous solids that underlie an unrestricted monolayer-multilayer adsorption process up to high p/p_0. The knee in the isotherm (II, B in **Figure 1.12**) usually corresponds to the completion of a monolayer coverage.[b] In contrast, for *type III* isotherms, the adsorbent-adsorbate interactions are comparably weak yielding rather clusters than a complete monolayer which result in no distinct feature upon monolayer completion. *Type IV* isotherms obtained for by mesoporous adsorbents and are a combination of monolayer formation at the pore walls as in type II paired with pore condensation. They are typically characterized by a final saturation plateau. Depending on the pore shape and size, type IV isotherms are accompanied by a hysteresis, called IV(a), or are completely reversible as in IV(b), which is the case for small pores, pores with conical or cylindrical shape.[86] Combining weak interactions as described in type III isotherms with pore filling gives *type V* isotherms that are typically observed for water adsorption on hydrophobic surfaces. Reversible *type VI* isotherms are obtained from layer-by-layer adsorption on a highly uniform nonporous surface.

1.3.1.2 Adsorption Hysteresis

Reproducible hysteresis loops located in the multilayer range of the isotherm are usually associated with capillary condensation. In mesopores, the number of *van der Waals* interactions between adsorbate/adsorbent are increased to such an extent that a liquid-vapor transition below the saturation pressure p_0 of the respective bulk liquid takes place. The condensed liquid forms a meniscus depending on surface tension of the liquid and the shape of the capillary (corresponding to *Young-Laplace* equation). This meniscus allows for establishing an equilibrium of the filled pores below p_0 that causes a delayed desorption, thus the hysteresis loop.

In the case of more complex pore structures, the desorption path is often further influenced by different forms of pore blocking. The latter is defined as a pore structure with pores that are connected to an external surface only through narrow necks *e.g.* ink bottle pore shape. As liquid condensed in the narrow necks desorbs at lower pressures compared to the wider pore itself, the pores remain filled upon desorption. If emptying of the bottle-neck pores takes places in equilibrium the desorption branch of the hysteresis can provide information on the size of interconnections. For N_2 sorption at 77 K, this critical neck diameter was found theoretically and experimentally to be around 5 nm.[86,87] Below this interconnection diameter, desorption is assumed to occur via cavitation *i.e.,* spontaneous change of a liquid to a small vapor-filled cavity. In contrast to desorption under equilibrium conditions, desorption under cavitation does not allow for the retrieval of geometric information and pore size distribution.

The hysteresis of the isotherm is further affected by the width of the pore size- and neck size

[b] Note that this knee corresponds to the completion of three monolayers in the case of water.

Die approbierte gedruckte Originalversion dieser Dissertation ist an der TU Wien Bibliothek verfügbar.
The approved original version of this doctoral thesis is available in print at TU Wien Bibliothek.
TU Bibliothek Your knowledge hub WIEN

distribution. Here, narrow distributions correspond to a steep, step-like increase for the adsorption and desorption branch.

1.3.1.3 Analysis of Mesoporous Materials

The type IV isotherm of mesoporous material without macropores is nearly horizontal for high p/p_0 after pore condensation. At this stage, usually at $p/p_0 = 0.95$, the pore volume V_p is derived. This assumes that the adsorbate in the porous material has the same molar volume as in bulk (*Gurvich* rule). While this holds true to a great extent for N_2 sorption *e.g.* the volume and other properties of water are effected by confinement,[88–90] which was also studied in this thesis and results are given in section 5.1.

The porosity $P = \frac{V_p}{V}$ is defined as ratio of pore volume V_p and apparent volume V of the adsorbent. If the surface area SA is available, *e.g.* from N_2 sorption measurements, [c] one possibility to derive a pore radius is by $r = V_p/SA$. In the ideal case of mesoporous silica with open-ended, cylindrical pores as found in MCM-41, this radius is defined as $2\,V_p/SA$.

However, methods based on the *Kelvin* equation are mainly used to derive the pore size distribution of mesoporous materials.[91–94] The *Kelvin* equation describes the relation between the difference of equilibrium pressure p of the meniscus and saturation pressure p_0 of bulk liquid for liquid-vapor interfaces involving a meniscus with radius r_K

$$\ln\left(\frac{p}{p_0}\right) = -\frac{2 \cdot \gamma_{lv} \cdot V_m}{R_g \cdot T \cdot r_K} \tag{1.28}$$

with the surface tension of the bulk fluid γ_{lv}, the gas constant R_g and the molar liquid volume V_m. The *Kelvin* equation solely relates the curvature r_K of a pure liquid-vapor interface to the equilibrium relative pressure. It does not consider monolayer-multilayer adsorption preceding to pore condensation. The actual pore radius r_p does not equal to $r_K \neq r_p$ and needs to be extended by the thickness of the adsorbed layer t and the contact angle θ_{CA} (method of *Barrett*, *Joyner* and *Halenda*, BJH):[95]

$$\ln\left(\frac{p}{p_0}\right) = -\frac{\gamma_{lv} \cdot V_m \cdot \cos(\theta_{CA}) \cdot G}{R_g \cdot T \cdot (r_K + t)} \tag{1.29}$$

For N_2 sorption, t is derived empirically, *e.g.* by the *Halsey* equation,[96] from the isotherm,[97] or by applying microscopic methods based on molecular simulations or density functional theory.[87] However, for the adsorbate water, these calculations are much more difficult as it is not an inert molecule but strongly interacts with itself and the surface.

Furthermore, a geometric factor G is introduced to consider different pore shapes. Here, $G = 1$ for cylindrical and $G = 2$ for spherical pores is applied. As in the case for mesoporous films, surfactant removal is always accompanied with contraction perpendicular to the surface

[c] Surface area determinations using BET-model are questionable for other adsorbates than N_2 at 77 K, which was not used in this thesis. Therefore, it is not discusses here and the interested reader is referred to *e.g.* Ref. [83].

Die approbierte gedruckte Originalversion dieser Dissertation ist an der TU Wien Bibliothek verfügbar.
The approved original version of this doctoral thesis is available in print at TU Wien Bibliothek.
TU Bibliothek Your knowledge hub WIEN

and even spherical pores are compressed along this axis yielding elliptical pores. This deformation and the corresponding G factor is derived from the inorganic pore contraction model,[91] yielding values between 1 and 2 depending on shrinkage induced anisotropy (see section 5.1 for further details).

In addition, γ_{vl} is a function of curvature and can be modified by the *Tolman* model with a fixed *Tolman* length δ, with δ being the molecular diameter of the adsorbate:[98,99]

$$\gamma_{vl} = \gamma_0 \left(\frac{1}{1 + \frac{G \cdot \delta}{r_K}} \right) \tag{1.30}$$

Even if considering for this, one has to keep in mind that the Kelvin equation has its limitation and depends mainly on the used film thickness t, which has to be estimated. Therefore, especially for water, further investigations are required.

1.3.2 Special Aspects of Adsorption from Liquid Phase

Many industrial or natural processes involve a liquid/solid interface *e.g.* heterogeneous catalysis, purification of liquids by activated charcoal or zeolites, stationary phases for liquid chromatography, or ion exchange membranes.

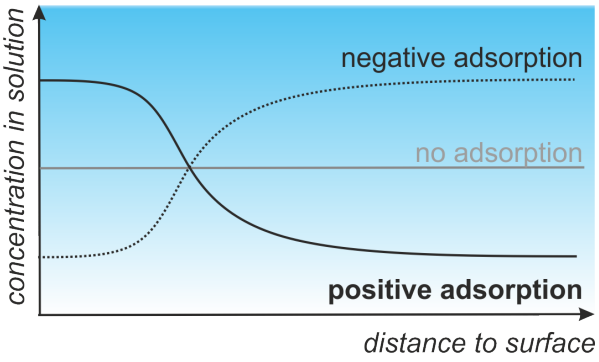

Figure 1.13: Concentration profile of a solution near an interface. If no adsorption occurs, the concentration profile is flat. For (positive) adsorption, the concentration of the solution is lower with increasing distance from the surface. For negative adsorption it is reversed.

However, the description of phenomena occurring on this interface is difficult, as adsorption is always a competitive process, and in contrast to gas sorption, non-inert molecules interact with the surface and are typically higher in complexity.

Here, the surface chemistry, *e.g.* wettability, can differ significantly to gas/solid interfaces. As schematically represented in **Figure 1.13**, adsorption causes the formation of a concentration gradient near the surface. This picture is idealized and in reality, these profiles are oscillating. Experimentally, the concentration can only be measured at a large distance from the surface, defined as c_i^l. The surface excess amount n_i^σ of component i is the difference between introduced amount n_i and the amount obtained from the concentration c_i^l measured fare away from the surface and volume $V^{l,0}$ of the liquid introduced into the system:

$$n_i^\sigma = n_i - c_i^l \cdot V^{l,0} \tag{1.31}$$

As for gas adsorption experiments, the adsorbed amount n^a equals n^σ only for low

Die approbierte gedruckte Originalversion dieser Dissertation ist an der TU Wien Bibliothek verfügbar.
The approved original version of this doctoral thesis is available in print at TU Wien Bibliothek.
TU Bibliothek WIEN Your knowledge hub

concentrations (lower than 10 mmol L^{-1}). Here, the concentration of the solvent is considered constant. For concentrated solutions or mixtures, it can be shown that the relative surface excess of compound 2 with respect to compound 1 equals

$$n_i^{\sigma(1)} = n_2 - n_1 \cdot \frac{x_2^l}{x_1^l} \tag{1.32}$$

where x corresponds to the molar fractions.

Analogous to Figure 1.12 for gas phase adsorption, adsorption isotherms - plotted as amount adsorbed against the concentration of external phase - can be used to describe the adsorption process. Here, the isotherm is a result of the balance between the solute/solute, solute/solvent, solute/surface, and solvent/surface interactions. Typically, these adsorption isotherms are obtained via batch experiments. In this approach, a certain amount of adsorbent is added to the liquid containing the solute. After some time (minutes up to hours) or after equilibrium has been reached, the adsorbent is filtered off and the concentration of the remaining solute is determined, *e.g.*, by liquid or gas chromatography coupled to a UV/Vis detector.[100–103]

Note that besides solute/surface interactions, adsorption may also occur as a consequence of rejection of the solute by the solvent *e.g.* due to low solubility.

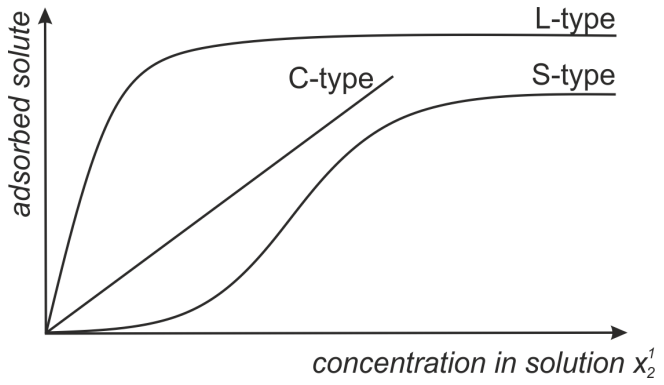

Figure 1.14: System of isotherm classification for adsorption from dilute solutions.

The affinity of the solute to the adsorbent is reflected in the initial slope of the isotherm (compare **Figure 1.14**): (i) L-type isotherms following the *Langmuir* model have a concave slope toward the x-axis, and no lateral interactions between the adsorbate molecules take place.[104] (ii) S-type isotherms underlie a more complex model, taking into account lateral interactions between molecules. These interactions are typically reflected in a change in concavity of the isotherm as adsorption progresses. Again, as for gas sorption, concavity directing toward the y-axis corresponds to strong adsorbate interaction, *i.e.,* capillary condensation. (iii) A linear isotherm is obtained for constant partition, *i.e.,* C-type isotherm.[105] Most of experimentally obtained isotherms are often modeled as a combination of these "ideal" isotherm types.

In contrast to gas sorption experiments, where typically inert gases like N_2 or Ar are used, for adsorption from solutions the interactions are specific for each (class of) material. For example, iodine or methylene blue are typically employed to probe the adsorption capacity for charcoal. Interaction that are strongly dependent on various properties such as surface charge, hence

Die approbierte gedruckte Originalversion dieser Dissertation ist an der TU Wien Bibliothek verfügbar.
The approved original version of this doctoral thesis is available in print at TU Wien Bibliothek.
TU Bibliothek Your knowledge hub WIEN

polarity, used solvent, pH, *etc.*, limit the applicability of adsorption from solution for surface area determinations. However, due to the wide range of molecules that can be applied, adsorption from solution allows for probing other properties such as percentage of surface which can be considered, polar/non-polar, acidic/basic *e.g.* determination of polar surface cites in silica using calorimetry.[106]

Furthermore, the use of molecules of different sizes allows for pore size analysis. If the size of the molecule is in the range of the pore, a molecular sieving effect may occur. The most prominent example in this context is the separation of *o*-xylene from *p*-xylene using zeolites. Besides size selection, affinity effects that enhance diffusion if pore size and adsorbate size are in the same order can take place, which will be discussed in more detail in the following section.

1.3.3 Mass transfer in Pores

In general, diffusion is described by *Fick's* first law, which describes the diffusivity $D(q)$ as a function of the adsorbed phase concentration q:

$$J = -D(q)\frac{\partial q}{\partial z} \tag{1.33}$$

With the diffusion flux J and position z. The diffusivity is defined as the rate of transport of sorbate under a given concentration gradient. D largely depends on the pore diameter (compare **Figure 1.15)**:[107] (i) Activated diffusion (also referred to as configurational or surface diffusion) dominates in the microporous regime if the molecule is of similar size as the pore. This regime is common in microporous solids (such as zeolites) and diffusivity is low typically $< 10^{-8}$ m^2 s^{-1}, owing to the fact that the surface interactions are very strong and the molecule "sticks" to the surface. In contrast, Knudsen and molecular diffusion are 2 - 3 orders of magnitude higher and govern the mesoporous and macroporous regime, respectively. If the mean free path l of the molecule is much smaller than the pore diameter $D_{pore} >> l$, molecule-molecule collisions are more probable than molecule-pore wall collisions. Therefore, the dominant diffusion mechanism for macroporous materials is molecular diffusion. If the number of molecule-pore wall collisions exceeds the molecule-molecule collisions (which is the case for $l/D_{pore} > 1$), the mass transport occurs by Knudsen diffusion, where the molecule bounces from wall to wall.

Die approbierte gedruckte Originalversion dieser Dissertation ist an der TU Wien Bibliothek verfügbar.
The approved original version of this doctoral thesis is available in print at TU Wien Bibliothek.
TU Bibliothek Your knowledge hub WIEN

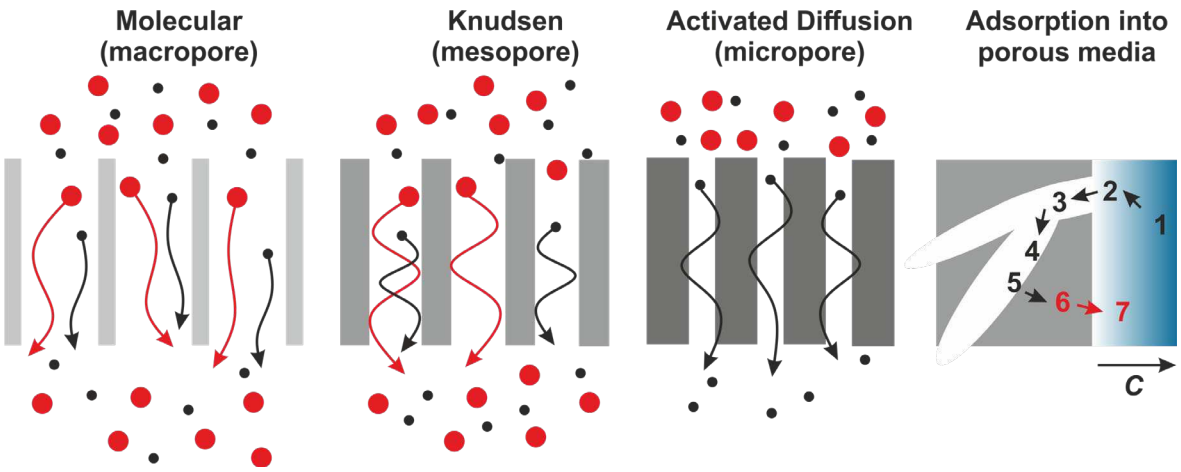

Figure 1.15: Illustration of the diffusion of large (red) and small (black) molecules in macroporous, mesoporous and microporous materials. (Right) Adsorption into a porous material.

The concentration gradient (that causes a mass transfer) between solid and solution can be described in several steps (compare **Figure 1.15, right**):

1. The dissolved molecule diffuses to the external surface of the porous material by bulk diffusion.
2. Mass transfer at the external surface occurs through the high-concentration layer around the adsorbent.
3. Diffusion into the porous volume takes place and the diffusion coefficient is a function of the pore diameter. Depending on the ratio between pore size and molecule size, Knudsen diffusion may occur.
4. Fast and exothermic adsorption at the solid surface takes place (depending on the system, reaction energies between 0 - 60 kJ mol^{-1} arise).
5. Surface diffusion is comparably slow (ca. 10 000 times smaller diffusivity than the pore diffusion coefficient) and thus limits the global kinetics of adsorption.
6. The exothermic reaction (step 4) causes heat that is dissipated via the material to the solid-liquid interface.
7. Thermal conduction through the solution takes place. For adsorption from gas phase, the high thermal capacity of water causes no change in temperature is found, however, for VOC adsorption a significant temperature change can be noted due to their lower thermal capacity.[108]

Die approbierte gedruckte Originalversion dieser Dissertation ist an der TU Wien Bibliothek verfügbar.
The approved original version of this doctoral thesis is available in print at TU Wien Bibliothek.
TU Bibliothek Your knowledge hub WIEN

1.4 Enrichment-Based Sensing Schemes Related to this Work

Although the combination of ordered mesoporous silica films with ATR spectroscopy to, on the one hand, characterize the film itself, and on the other hand, to use it for different sensing applications can be considered a scientific achievement of this work, neither the use of coated ATR crystals for sensing, nor mesoporous materials for adsorption are new concepts. This section summarizes the state of the art of these neighboring disciplines. Different materials have been used for enrichment films and were coated on internal reflection elements ranging from ATR crystals to optical fibers and waveguides (**section 1.4.1**). The use of mesoporous silica in different sensing schemes will be summarized in **section 1.4.2**. Finally, in **section 1.4.3,** parameters required for enrichment films on ATR crystals will be discussed.

1.4.1 State-of-the-Art of Enrichment Coatings

In January 2017 - at the beginning of this thesis - I was confronted with the task of finding an appropriate enrichment material in the framework of the H2020 project Aquarius. This project aimed for an oil-in-water sensor, based on Ge waveguides coated with a functional enrichment layer. In this context, several requirements for this enrichment layer were defined:

- high affinity toward apolar compounds
- high selectivity (enabling oil type discrimination/identification)
- fast enrichment < 30 s (low ppm), 10 min (low to mid ppb)
- IR-transparency between 1300 – 1500 cm^{-1}
- adhesion on Waveguide (preferably by covalent bonding)
- film thickness $> d_p$ to exclude the matrix water
- porosity to facilitate fast diffusion of the analytes
- robustness (chemical as well as mechanical)

A thorough literature search for functional coatings on MIR waveguides used for sensing hydrocarbons in water (ATR crystals, optical fibers and waveguides) was performed. All coating materials were assessed regarding their applicability (matrix, analytes) and their properties were compared (thickness, enrichment equilibrium time, spectral transmission window). By doing so the coatings were grouped on the one hand into first-, second- and third-generation waveguides (conventional internal reflection elements as ‘‘first generation’’ waveguide, MIR-transparent optical fibers as ‘‘second generation’’ waveguides and integrated optics as “third generation”, as coined by *Mizaikoff et al.*[19]) and on the other hand by type of material (organic polymers, fluorinated polymers and sol-gel materials).
Furthermore, the model substances for all three waveguide generations and all materials can be categorized

- BETX(N) and derivatives: benzene, ethylbenzene, toluene, xylenes, naphthalenes (typical detection region 1000 – 700 cm^{-1})
- CHCs: aliphatic or aromatic chlorinated hydrocarbons *e.g.* tetrachloroethylene or dichlorobenzenes (typical detection region 1000 – 800 cm^{-1})

Die approbierte gedruckte Originalversion dieser Dissertation ist an der TU Wien Bibliothek verfügbar.
The approved original version of this doctoral thesis is available in print at TU Wien Bibliothek.
TU Bibliothek Your knowledge hub WIEN

- pesticides *e.g.* Alachlor, Atrazine, DDT (typical detection region 1700 – 1100 cm^{-1})
- organic solvents *e.g.* tetrahydrofuran, ethanol, acetonitrile

In general, detection and quantification in first- and second-generation waveguides relies in most cases on either strong C-Cl stretching vibration of organic chlorine compounds (800 – 500 cm^{-1}) or C-H vibrations out of the plane of aromatic rings (1000 – 700 cm^{-1}). There is no report for sensing contaminants in the fingerprint region between 1800 and 1300 cm^{-1}. This is most likely due to the used materials that show strong absorptions within this range *e.g.* PE or PP.

1.4.1.1 First Generation Waveguides: Coated ATR crystals

Organic Polymers. (low density) Polyethylene (LDPE), polypropylene (PP), polyethylene-polypropylene copolymer (co-PE/PP), polyvinylchloride (PVC), polystyrene (PS), polyisobutylene (PIB), polyacrylnitrile (PAN), polyacrylnitrile-co-butadiene (PAB), and polystyrene-co-butadiene (PSB) were used as coating materials (compare **Table 1.1**). The shortest times of only a few minutes until the enrichment equilibrium is reached are reported for co-PE/PP coatings.[109–111] Films with thicknesses ranging from 0.12 to 20 µm were used and for most reports film thicknesses of three times the depth of penetration of the evanescent wave d_p were targeted (compare section 1.1.3, where the intensity of the evanescent wave at $3 \cdot d_p$ corresponds to 0.25 % of the initial intensity). In general, higher film thickness led to longer enrichment times. LODs ranging from low ppb to low ppm are reported.

Fluorinated Polymers. Since fluorinated polymers such as polytetrafluoroethylene (PTFE, Teflon) and its co-polymers do not consist of–CH_2- and –CH_3 groups, they show no absorptions between 1300 – 3000 cm^{-1}. Therefore, they are an attractive enrichment material for many analytes such as hydrocarbons, CHCs and others. The main drawback of PTFE is its processability: PTFE is neither meltable nor soluble in any solvents, therefore, processing of enrichment layers is only achieved via detours (*e.g.* plasma deposition). Alternatively, PTFE co-polymers such as AF1600 and AF2400 (the main difference of both are their glass transition temperatures) can easily be processed and were used quiet successfully for CHCs. By using films with a thickness of 5-8 µm, enrichment times below 20 min and LODs of less than 115 ppm were reported in literature (compare **Table 1.2**).[112–114]

Sol-Gel-Based Materials. Different chemically modified sol-gel-based materials have been used until now. Typically, organosilica materials were prepared from classical sol-gel precursors (tetraethoxysilane, TEOS, or tetramethoxysilane, TMOS) with organically modified precursors (ethyltrimethoxysilane, ETES, phenyltrimethoxysilane, PTES, methyltrimethoxysilane, MTES). In some cases, an additional surface functionalization treatment was performed with ocyltrichlorosilane, trichloromethylsilane (TCMS) or hexamethyldisilazane (HMDS).

Die approbierte gedruckte Originalversion dieser Dissertation ist an der TU Wien Bibliothek verfügbar.
The approved original version of this doctoral thesis is available in print at TU Wien Bibliothek.
TU Bibliothek Your knowledge hub WIEN

Sol-gel materials in Ref. [115,116] reach the enrichment equilibrium after 10 s, which is most likely due to their porosity (20 – 40 % porosity is reported). Sol-gel materials used in Ref. [117] and [118] show inferior performance, because just silica gels (without calcination or other treatments) instead of oxides were used.

Die approbierte gedruckte Originalversion dieser Dissertation ist an der TU Wien Bibliothek verfügbar.
The approved original version of this doctoral thesis is available in print at TU Wien Bibliothek.
TU Bibliothek Your knowledge hub WIEN

Die approbierte gedruckte Originalversion dieser Dissertation ist an der TU Wien Bibliothek verfügbar.
The approved original version of this doctoral thesis is available in print at TU Wien Bibliothek.

Table 1.1: Literature overview of organic polymer-based enrichment films on ATR crystals.

Ref.	Analyte	LOD	ATR material	Coating Material	coating thickness	Equilibrium time	Regeneration time	Flow rate ml min^{-1}	Spectra range
[119]	BTEX	50 ppb	ZnSe	co-PE/PP	4.2 µm	20 min		3	
[110]	pesticides	2ppm	ZnSe	PVC with chloroparaffine, PBD, PIB, co-PE/PP	<5 µm	10 min	5 min	SF *	
[109]	BTEX, CHC	23-1850 ppb	ZnSe	co-PE/PP, co-PE/PP/5-methylene-3-norbornene	5-20 µm	4-30 min	30 min	5-42	1600 - 600
[120]	CHC	20-300 ppb	ZnSe	co-PE/PP	0.12-10 µm	10 min	2 min	SF*	
[121]	BTEX		ZnSe	Alkylated PS	4 µm	60 min		4	
[122]	BTEX	40-60 ppb	ZnSe	co-PE/PP	5 µm	20 min		5	800-600
[111]	CHC	1.5-2 ppm	ZnSe	LDPE, PIB, co-PE/PP, co-PE/V, PEox, PECl, PMP, PBD	10-40µm (22µm)	8-40 min			1000-700
[123]	CHC	<200 ppb	ZnSe	PIB, PVC, PA, PS, PAB and PSB	$> d_p$	20 min (80%)	>20 min		1550-900
[124]	CHC	2-3 ppm	ZnSe	LDPE, PIB	6-19µm	20-30 min		SF*	1000-700
[125]	F-HC	23 - 79 ppb	ZnSe	co-PE/PP, PIB	1-10 µm	>20 min		1-5	1040-840
[126]	BTEX	50 - 700 ppb	diamond	co-PE/PP, PIB	2.5 µm	8 min	10 min	1-4	850 - 650
[127]	Cl-Phenols, Cl-Aniline	0.03-700 ppm	ZnSe	PIB, PDMS, ABS, SB				2	1485-760
[128]	BTEX, naphtalenes	low ppm	ZnSe	PIB	4.5 - 8.4 µm	5-60 min	20-60 min	1.5	820 - 655

BTEX = Benzene, Toluene, CHC = chlorinated hydrocarbon; Ethylbenzene, Xylenes; co-PE/PP = 60 % polyethylene / 40 % polypropylene copolymer, PVC = polyvinylchloride; PBD = polybutadiene; PS = polystyrene; LDPE = low density polyethylene; PIB = polyisobutylene; PDMS= polydimethylsiloxane; ABS = Acrylonitrile butadiene styrene; SB = styrene-butadiene rubber

Die approbierte gedruckte Originalversion dieser Dissertation ist an der TU Wien Bibliothek verfügbar.
The approved original version of this doctoral thesis is available in print at TU Wien Bibliothek.

Table 1.2: Literature overview of fluorinated polymer-based enrichment films on ATR crystals.

Ref.	Analyte	LOD	ATR material	Coating Material	coating thickness	Equilibrium time	Regeneration time	Flow rate ml min^{-1}	Spectra range
112	THF, EtOH, ACN, Toluene	27-115 ppm	ZnSe	Teflon AF2400, poly(acrylonitrile-co-butadiene), PDMS, poly(styrene-co-butadiene)	5-7 µm	2-20 min		5	
113	CHC	10-100 ppm	ZnSe	Teflon AF2400	5.1 µm	5-10 min		5	980-3030
129	CHC		ZnSe	Teflon AF 2400	5.3 µm	10 min		5	800-1000
130	TCE	300 ppb	ZnSe	PTFE-films, plasma-deposited	0.6 µm	>30 min	>30min	5	1100-680
131	CHC			Teflon AF2400	5 µm	2-15 min		5	
114	CHC	10-20 ppm	ZnSe	Teflon AF 1600 (Tg=160°C) and 2400 (Tg=240°C)	5-7 µm	5-15 min		5	780-1500

Die approbierte gedruckte Originalversion dieser Dissertation ist an der TU Wien Bibliothek verfügbar.
The approved original version of this doctoral thesis is available in print at TU Wien Bibliothek.

Table 1.3: Literature overview of silica-based enrichment films on ATR crystals.

Ref.	Analyte	LOD	ATR material	Coating Material	coating thickness	Equilibrium time	Regeneration time	Flow rate ml min^{-1}	Spectra range
[115]	Benzene		Si	TEOS + ETES with trimethylchlorosilane, 29 Å pore diameter, 30% porosity	0.38 µm	6 s	6 s	-	
[132]	benzonitrile	350 ppb	Si	1:1 TEOS: ETES + octyltrichlorosilane	0.39 µm	6 s	6 s	-	1100-2700
[116]	Acetone, IPA	1.5 - 26 ppm	Si	SiO_2 (TEOS, TMOS) +HMDS	0.25 µm	10 s	<10 s	-	
[133]	nitrobenzene	1-5 ppm	Ge (100Å Si-layer)	SiO_2 (TEOS, TMOS)	0.54 µm				1100-3000
[117]	pesticides	sub ppm-ppm	ZnSe	PTMOS and TMOS mixture	1.7 µm	20-200 min		3	
[118]	*p*-Xylene, nitro chlorobenzene	700 ppm	ZnSe	organosilica (-CH_3, -Ph) from sol-gel	2-6 µm	120 min		5	

[a] Sol was deposited but not calcined; *SF = stopped flow; TEOS = tetraethoxysilane; ETES = ethyltriethxoysilane; TMOS = tetramethoxysilane; PTMOS = phenyltrimethoxysilane; MTES = methyltrimethoxysilane;

1.4.1.2 Second Generation Waveguides: Fibers

Similar coating materials were used with optical fibers as waveguide. The same trends found for ATR crystals are seen for optical fibers: co-PE/PP seems to be the best choice regarding LODs and equilibrium time for the tested analytes

Table 1.4: Literature overview of enrichment films on optical fibers.

Coating material	Analyte	LOD	Fiber material	d_{film} [µm]	t_{eq}	Ref
LDPE, PIB, co-PE/PP	CHCs	1 ppm	$AgCl_xBr_{1-x}$	10-20	15 min	[134]
PIB, co-PE/PP	CHCs			2.5	5 min	[135]
co-PE/PP	CHCs	300 ppb	$AgCl_xBr_{1-x}$	10	18 min	[136]
co-PE/PP	Aromatic CHCs	5 ppb	flattened $AgCl_xBr_{1-x}$	2.9	30 min	[137]
co-PE/PP	BTEX	5 ppb	flattened $AgCl_xBr_{1-x}$	7.6	5 min	[138]
co-PE/PP or PIB	CHC, Toluene	80 ppb	$AgCl_xBr_{1-x}$	5-15	10-45 min	[139]
PVC, PIB, co-PE/PP, PE	Alachlor, CHCs	5 ppm	$AgCl_xBr_{1-x}$	10-20	40 min	[140]
poly(acrylonitrile-co-butadiene), co-PE/PP	TCE	900 ppb	$AgCl_xBr_{1-x}$	10-20	5-30 min	[141]
PVC	BTEX	500 ppm	Ag halide	1.1	3 min	[142]
Organosilane (PTMOS +TMOS)	Nitrobenzene and parathion	9 ppm	$AgCl_xBr_{1-x}$	4-10	25 min	[143]
PDMS	aliphatic HCs	13 ppm	sapphire	1.3/2.9	15-30 min	[144]
LDPE	TCEs	5 ppm	$AgCl_xBr_{1-x}$	15	10 min	[148, 149]
silicone	TeCE Toluene	22-29 ppm	silica core	-	20 min	[147]
PAN	water		$AgCl_xBr_{1-x}$	7		[148]
polysulfone, PS	blood serum		$AgCl_xBr_{1-x}$	2-3		[149]
Teflon AF 160	TeCE	1 ppm	$AgCl_xBr_{1-x}$	1-3	2 min	[150]
Teflon	TeCE	1 ppm	fluoride optical	-	26 min	[151]

1.4.1.3 Third Generation Waveguides: Integrated Optics

In this literature overview, the definition of third generation of waveguides was applied widely ranging from sensing schemes based on straight waveguides, Mach-Zehnder interferometers[d],

[d] As for the Michelson interferometer, the beam of the light source is divided using a beam splitter, both beams are recombined on a second beam splitter at which both arms interfere. Both outputs are detected.

Die approbierte gedruckte Originalversion dieser Dissertation ist an der TU Wien Bibliothek verfügbar.
The approved original version of this doctoral thesis is available in print at TU Wien Bibliothek.
TU Bibliothek Your knowledge hub WIEN

surface-plasmon resonance (SPR)[e] or photonic crystal (PC) waveguide[f]. Furthermore, the wavelength range - as for the surveys above - is not limited to the mid-IR region. However, all of them have a cladding for sensitivity enhancement in common. As visible from **Table 1.5**, similar materials have been employed as for the first- and second-generation waveguides *e.g.* PDMS or Teflon. Furthermore, macrocyclic molecules such as cyclodextrins or cryptophanes have been used for trapping different analytes.

Table 1.5: Literature overview of enrichment films on integrated optics.

Coating material	Analyte	LOD	method	Fiber material	Light source	Ref.
Teflon AF 1600	BTX in water	100-360 ppb	RI change	Single mode SiO_2/SiN_x waveguide	laser diode (660 nm)	152
Teflon AF 1600	BTX in water	55- 200 ppb	RI change	Near-IR SPR	broadband near-IR source	153
styrene-acrylonitrile film incorporating cryptophane-A	methane	17 ppm	Phase shift	Si_3N_4 rib waveguide IO-MZI	solid-state laser (785 nm)	154
HMDS plasma polymerized thin film	water, isopropanol, hexane vapors	-	Phase shift	200 nm Si_3N_4 film IO-MZI	HeNe laser (632 nm)	155
Cryptophane-A-6Me in poly(acrylic acid)-carbon nanotubes/ polypropylene amine hydrochloride nanofilm	methane	0.18 %	RI change	PC fiber long-period grating	CO_2–laser	156
γ-cyclodextrin	naphthalene in solvent vapor	500 ppb	RI change	planar Bragg grating	Tunable laser (1555 - 1590 nm)	157
immobilized *b*-cyclodextrin	adamantane carboxylic acid, butylbenzoic acid and methyl orange	-	Phase shift	IO-MZI on glass slide	He-Ne laser	158
PDMS (VP 1529 and Silgel 604)	HCs, FHC	10- 100 ppm	RI change	IO-MZI	laser diode (790 nm)	159
PDMS (Sylgard Elastomer 184)	xylene in water	100 ppb	trans	SI PC slot waveguide	Broadband NIR-source (1665 - 1745 nm)	160

[e] Surface plasmons (conducting electrons of a thin metal film) are excited with polarized light in total reflection configuration using a prism. Upon adsorption on the metal film, the refractive index changes and hence the angel of the reflected light, which is detected.

[f] Microstructures with periodic dielectric constant that allow to control and manipulate the light-matter interaction for excessing a "forbidden" frequency range=photonic band gap, otherwise not possible.[369]

Die approbierte gedruckte Originalversion dieser Dissertation ist an der TU Wien Bibliothek verfügbar.
The approved original version of this doctoral thesis is available in print at TU Wien Bibliothek.
TU Bibliothek Your knowledge hub WIEN

ZrO_2, TiO_2 nanostructured thin films (nanowires)	CO_2	-	Phase shift	Si_3N_4 waveguide IO-MZI	tunable laser source	[161]
zeolite	Toluene vapor	200 ppb	RI change	Period Fiber Grating	CO_2-laser	[162]

OI-MZI = Integrated optic -Mach-Zehnder interferometer, trans = transmission, PC = photonic crystal, SPR = surface plasmon resonance, FHC = fluorinated hydrocarbons

Only a few reports are available on mesoporous claddings or even mesoporous wave guiding layers. Topics discussed in literature include TiO_2 waveguide films,[163] mesoporous thin film as enrichment films on SPR sensor for metal cation detection,[164] ppm-level NH_3 sensor using mesoporous TiO_2-P_2O_5 film waveguides at 633 nm,[165] long period grating sensor with powder mesoporous silica films for sensing porphyrins in water,[166] or sensing of VOCs at telecom wavelength using microfiber coupler coated with mesoporous silica.[167]

1.4.2 Mesoporous Materials for Sensing Applications

Giving a complete overview over mesoporous materials used in analytical science would be too ambitious and is far beyond the scope of this section. However, it is intended to give an idea of the plethora of sensing applications these materials have been employed for and by doing so to show their versatility.

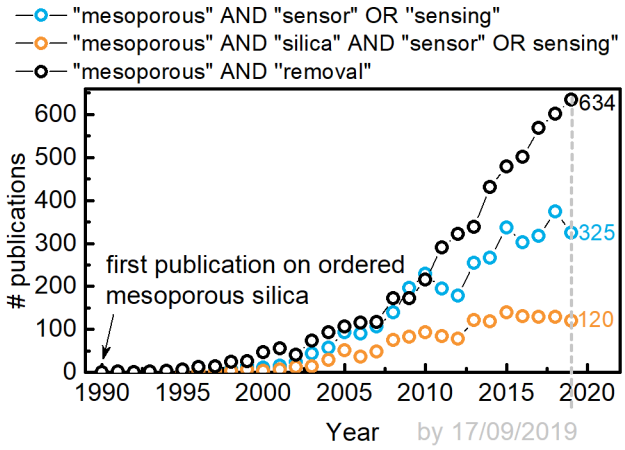

Figure 1.16: Result of Scopus literature search at 17/09/2019. Total number of publications on "mesoporous" AND "sensor" OR "sensing" = 3603; "mesoporous" AND "removal" = 5487.

A literature search in Scopus using the keywords "mesoporous" and "sensing"/"sensor" for either title or abstract gave a total number of 3606 publications over the last 30 years, and the temporal progression is given in **Figure 1.16, blue curve**. The search was refined, and the term "silica" was added. The corresponding orange data points in Figure 1.16 clearly show, that the major fraction of mesoporous sensors is based on silica. Besides in sensing applications, mesoporous materials are vastly employed for pollution removal and water remediation, which is reflected in an even higher number of 5487 publications containing "mesoporous" and "removal" (**Figure 1.16, black curve**).

On these topics, great reviews are available *e.g.* Ref. [63,168–174]. To very briefly sum up these

Die approbierte gedruckte Originalversion dieser Dissertation ist an der TU Wien Bibliothek verfügbar.
The approved original version of this doctoral thesis is available in print at TU Wien Bibliothek.
TU Bibliothek Your knowledge hub WIEN

reviews: Mesoporous materials are used for capacitive and resistive gas sensors (mainly mesoporous ZnO), optical sensors (including photoluminescence, absorption, reflection), gravimetric sensors (mainly based on quartz-crystal microbalances, QCM), metal cation sensors (*e.g.* Hg^{2+}, Cd^{2+}, Ni^{2+}, Cu^{2+}, Co^{2+}, *etc.*), or electrochemical sensing, to name the main categories.

A very recent review on the influence of porosity and pore structure on the sensing performance also concludes that pore structure *e.g.* 2d hexagonal versus 3d porous structures, strongly influences the sensing properties.[175]

1.4.3 Conclusion on Enrichment Materials for Mid-IR sensing

After conducting the literature search summarized in the previous sections, organically modified silica from sol-gel processes clearly stood out especially regarding their **speed of diffusion**. The porous structure enables faster enrichment (< 10 s) compared to various polymers (> 5 min), which were used as bulk materials. Sol-gel coatings reached LODs of as low as 350 ppb after several seconds from aqueous solutions on ATR crystals,[132] while other coatings based on organic polymers reached similar values only after more than 5 min. These long enrichment and recovery times, due to the diffusion resistance of bulk polymers, limit their practical applications for *in situ* monitoring. Compared to microporous materials such as zeolites or activated carbon, mesoporous silica allows **fast regeneration** without the need of harsh treatments *e.g.* heat treatment > 200 °C.[172,176] The significantly faster diffusion into porous silica compared to polymer coatings can be attributed to different enrichment mechanisms. While porous silica films rely on adsorption into the pores (compare section 1.3), diffusion into polymer materials can be rather compared with a dissolution of the analyte in the bulk material, hence absorption takes place. This difference is also reflected in the calibration curves: Here, bulk diffusion into polymers yields linear calibration functions, in contrast to mesoporous materials for which **calibration curves are non-linear** and follow, depending on the mechanism of adsorption a *Langmuir* or *Freundlich* equation (compare section 4.2.2.2). In fact, these functions are beneficial for sensing purposes due to their high slope at low concentrations.

Besides high-surface areas and fast diffusion, mesoporous materials are **low refractive index materials** (between n = 1.03 - 1.3, tunable by functionalization and porosity),[177,178] which is a highly demanded feature for claddings of integrated optics as the refractive index contrast determines the light confinement within a waveguide.[179] Other benefits of sol-gel materials are (i) the versatility regarding pore size, pore shape, introduction of organic functionalities (see section 1.2 for details) and (ii) no absorption in the fingerprint region (see Chapter 3 for representative IR spectrum). Lastly, in contrast to polymers that are prone to swelling in the presence of water and thus also are reported to frequently in the end detach from the sensor surface, silica allows for **covalent bonding to an oxide surface**.

Die approbierte gedruckte Originalversion dieser Dissertation ist an der TU Wien Bibliothek verfügbar.
The approved original version of this doctoral thesis is available in print at TU Wien Bibliothek.
TU Bibliothek Your knowledge hub WIEN

Die approbierte gedruckte Originalversion dieser Dissertation ist an der TU Wien Bibliothek verfügbar.
The approved original version of this doctoral thesis is available in print at TU Wien Bibliothek.

Chapter 2 Experimental Details

In the first section the optical setup and the flow cells designed and used in this thesis are explained. The preparation and characterization of Si and Ge ATR crystals are described in **section 2.1.1** and **2.1.5**. Details on data acquisition are also given in **section 2.1**. Furthermore, the preparation and handling of liquid and gaseous samples is described in **section 2.2**. Finally, experimental details on the synthesis and characterization of mesoporous films are given in **section 2.3**.

2.1 FTIR Spectrometer Setup

All FTIR spectra if not otherwise stated were recorded using a Vertex 80v spectrometer (*Bruker*, Germany) equipped with a liquid nitrogen cooled mercury–cadmium–telluride (MCT) detector (*InfraRed Associates*, USA, D* = 4×10^{10} cm $Hz^{0.5}$ W^{-1} at 9.2 µm). IR spectra were acquired with a spectral resolution of 4 cm^{-1}, and a total of 8–32 scans (1-4 s, double-sided, backward forward acquisition mode) were averaged per spectrum. The beam diameter was optimized for maximum signal at the MCT detector and minimal noise, resulting in an optimal beam aperture of 8 mm. In this configuration, the detector signal accounted for 2000 - 4000 counts in OPUS (no signal gain). Spectra analysis was performed using the software package OPUS 7.5 (*Bruker*, Germany) and a MATLAB (*MathWorks*, USA) script was used for linear baseline subtraction and integration of absorption bands.

Due to the size and weight of standard ATR crystals spin and dip coating can only be performed with difficulties. Therefore and also because of high cost of standard ATR crystals it was necessary to design an ATR unit with disposable, light-weight and cheap ATR crystals. In this thesis, following the work of *Karabudak et al*,[180] 20 × 10 × 0.525 mm^3 ATR crystals from double-side polished Si and Ge wafers were prepared. These custom-made ATR crystals required for a dedicated mount for the FTIR spectrometer - to this end *Clipsi* was designed: This optical setup comprised an adapter plate, optical components, the ATR crystals prepared from double-side polished Si or Ge wafers, respectively, that were inserted into home-built

flow cells and a home-built ATR cartridge. This setup allowed for fast exchange of the ATR crystals without the need for realignment and was designed to fit in Bruker FTIR spectrometers. Every component and the characterization of the system performance including noise are discussed in detail in the following sections.

2.1.1 Preparation of ATR Crystals

10 mm × 20 mm silicon ATR crystals were cut with a dicing machine from standard ~525 µm thick, double-side polished CZ Si or Germanium wafers (adapted from *Karabudak et al.*[180]). Dicing was done at IMEC/Uni Ghent. The narrow facets were polished to a defined angle of 55° or 45°. To achieve this, 20 × 10 mm Ge or Si pieces were attached to angled aluminum holders with an acetone-dissolvable glue. Subsequently, diamond or Al_2O_3 polishing plates with 30 µm, 9 µm, 3 µm, 1 µm and 0.1 µm grain size were used for polishing. The obtained ATR crystals were cleaned with acetone in ultrasonic bath. ATR crystal polishing was performed in the sample preparation lab of USTEM (TU Wien).

2.1.2 Home-built ATR Mount aka *Clipsi*

On a standard transmission-cell Bruker adapter plate, a 2.5 cm thick aluminum spacer plate was mounted. On top, two breadboards were fixed, which built the basis for all further optical components. Two gold mirrors glued on rotation mounts on a dovetail rail directed the IR beam onto the angled facets of the ATR crystal and further to the detector (see **Figure 2.1**).

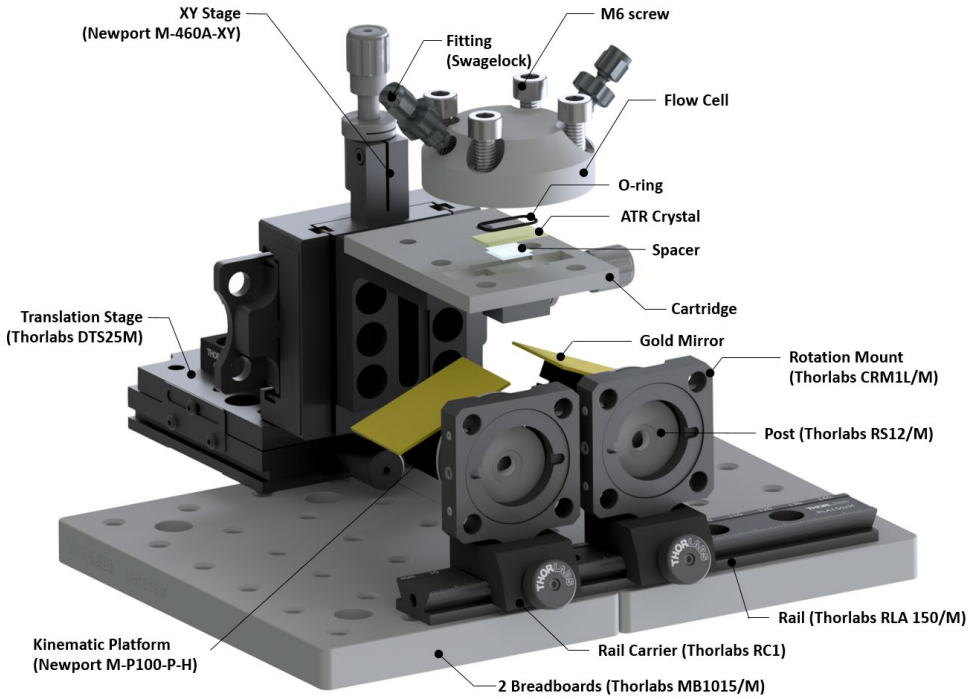

Figure 2.1: 3D explosion drawing of *Clipsi*. See text for details.

The rotation mounts were adjusted by firstly setting them to 0° (= parallel to table) with the help of a bubble level and subsequently rotated to $\theta/2$ *e.g.* 22.5° for 45° angle of incidence. An aluminum cartridge (see Appendix for construction drawing) that houses the ATR crystals

Die approbierte gedruckte Originalversion dieser Dissertation ist an der TU Wien Bibliothek verfügbar.
The approved original version of this doctoral thesis is available in print at TU Wien Bibliothek.
TU Bibliothek WIEN Your knowledge hub

was mounted on an x-y-z stage. The flow cells were fixed to the cartridge using four M6 screws. A piece of a glass microscope slide was used as spacer that prevents the ATR crystal to get in contact with the aluminum cartridge.

2.1.3 Flow Cell Designs

Throughout this thesis, different experiments demanded for customized flow cells. A 13 × 1 mm FKM O-ring (*Persicaner*, Austria) that formed a watertight seal around the edges of the ATR crystals built the basis of every flow cell design. The flow cells were fixed finger-tightly with four M6 screws to the ATR crystal cartridge as given in section 2.1.2**.**

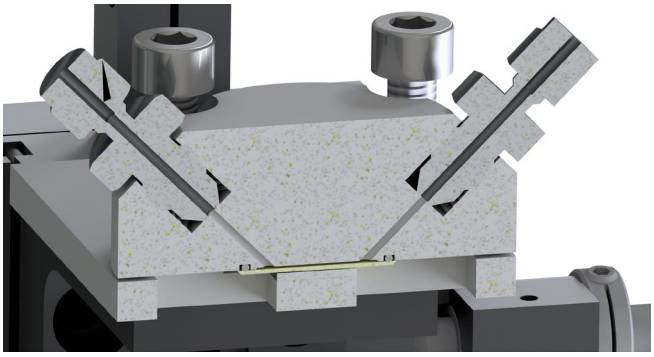

Figure 2.2: Flow cell for liquid samples. See text for details.

Aqueous sample application and especially hydrocarbons-in-water measurements were performed using an aluminum flow cell. Aluminum and not polymers were chosen to prevent analyte diffusion into the flow cell material. A small dead-volume allowed for fast liquid sample exchange and, facilitated testing the response times of 'ATR sensors based on mesoporous silica films. The flow cell is shown in **Figure 2.2** and has a volume of 20 µL. Two low-dead volume SS-100-6-2AN fittings (*Swagelok*, USA) were used to connect with stainless steel tubing (1/16'', 0.75 mm I.D.) to the rest of the flow system. The construction drawing is given in the Appendix and following these blueprints, the flow cell and the ATR crystal cartridge were manufactured by *Protolabs* (USA).

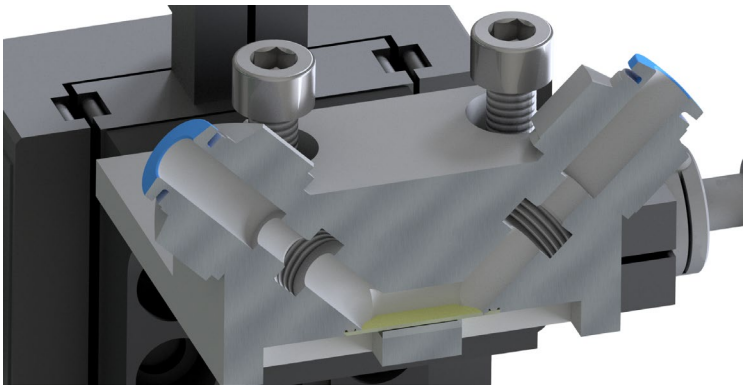

Figure 2.3: Flow cell for gaseous samples. See text for details.

Gas enrichment experiments required a flow cell with minimum pressure drop. Therefore, a cell with larger bore I.D. of the tubing and flow cell volume was designed. This flow cell allowed for reliable gas flow application using the gas mixer. To this end, the liquid handling

Die approbierte gedruckte Originalversion dieser Dissertation ist an der TU Wien Bibliothek verfügbar.
The approved original version of this doctoral thesis is available in print at TU Wien Bibliothek.
TU Bibliothek WIEN Your knowledge hub

flow cell was adapted to a flow cell volume of 4 cm^3 as shown in **Figure 2.3** with wider input channels. The flow cell was connected with 6 mm O.D. tubing using Festo adapters with G 1/8" threads. The construction drawing is given in the Appendix and following these blueprints the flow cell was manufactured by *Protolabs* (USA).

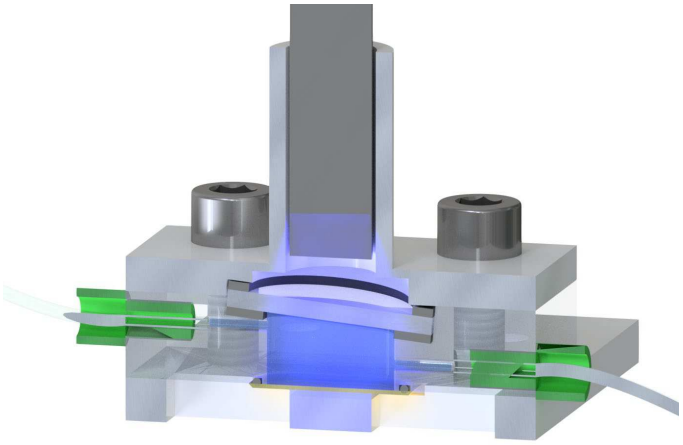

Figure 2.4: Flow cell (PMMA) with beveled volume and duct for UV fiber for photocatalysis experiments.

To allow for monitoring **photocatalytic reactions** using ATR-FTIR spectroscopy (see section 5.3 for details), several requirements were considered and implemented in the dedicated setup: (i) The flow cell design and the optical fiber duct allowed for uniform UV illumination. (ii) Gas accumulation that occurs upon photooxidation of methanol was avoided by the beveled flow cell volume to ease gas bubble removal from the probed volume (see **Figure 2.4**). (iii) Exhaust heat produced by the UV lamp was dissipated using a 10 × 10 cm computer fan placed above the flow cell unit. Photocatalysis experiments were performed using a PMMA flow cell with 0.7 mL volume sealed on top with a Viton® flat gasket and 2 mm sapphire window allowing for UV top-illumination. The construction drawing of the flow cell is given in the Appendix and following these blueprints the flow cell was manufactured by *Protolabs* (USA).

2.1.4 Design and 3D-Printing of ATR Instrumentation

The 3D-printed ATR setup is fixed with two M2 countersunk screws and nuts sunk into the ATR body, to fit on a commercial spectrometer adapter plate (universal transmission unit, *Bruker*, Germany) allowing to be embedded into the beam path of any Bruker spectrometer. The 3D-printed body with a footprint of length × width × height = 70 × 70 × 105 mm^3 was designed to be printed in one piece and is equipped with dove-tail rails with 10 mm width allowing for adjustment of the mirror mounts. The mirror mounts have triangular holes that allow their fixture using M3 screws. Gold-sputtered microscope slides, attached to the mirror mount using double-sided tape, were used to direct the IR beam to the facets of the ATR crystal. The groove (21 × 11 × 0.4 mm^3) on the top of the body allows to reproducibly exchange the ATR crystals. A 14 × 1 mm FKM O-ring sealed the ATR crystal and the fixture mounted with four M6 screws (the holes on top of the body are designed to easily cut

Die approbierte gedruckte Originalversion dieser Dissertation ist an der TU Wien Bibliothek verfügbar.
The approved original version of this doctoral thesis is available in print at TU Wien Bibliothek.
TU Bibliothek Your knowledge hub WIEN

the M6 thread into the PLA material). In addition, a small adapter was designed to host the IRUBIS ATR crystals (*IRUBIS GmbH*, Germany, 11 × 9 mm) in the same body.

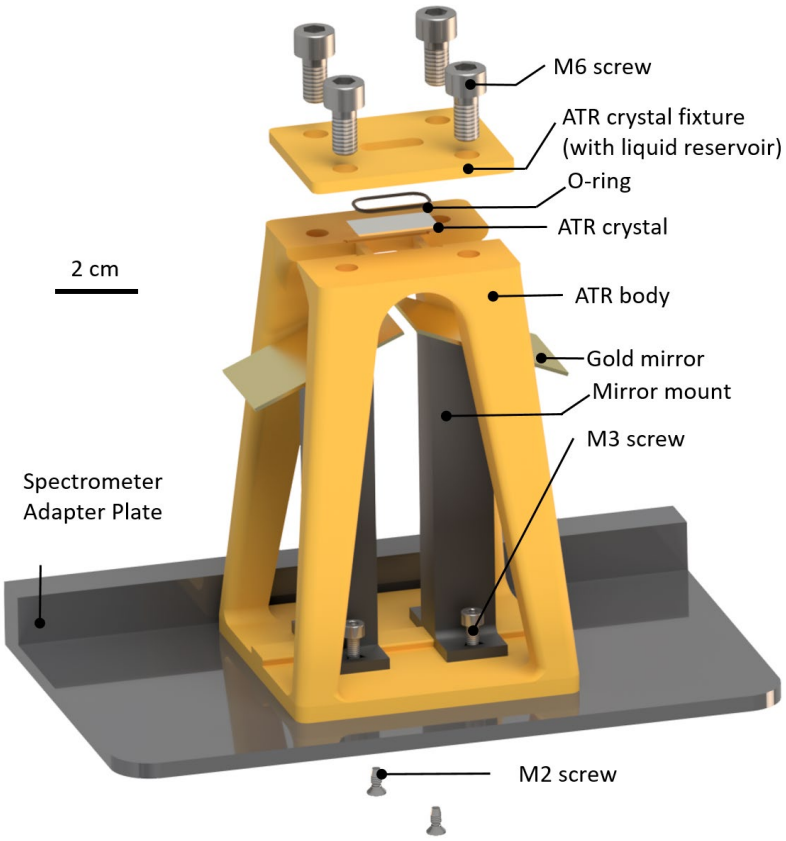

Figure 2.5: 3D-exploded-view drawing of 3D-printed ATR module mounted on the spectrometer adapter plate using custom-built ATR elements.

Following the blueprints developed in Inventor Professional 2017 (*Autodesk*, USA) the components were sliced using Slic3er Prusa Edition v1.40.1 software (*Prusa Research*, Czech Republic). A Prusa i3 MK3 3D printer (*Prusa Research*, Czech Republic) was used for additive manufacturing. The hotend of the extruder was equipped with a 0.4 mm brass nozzle. PLA with a diameter of 1.75 mm sourced from Prusa (*Prusa Research*, Czech Republic) was printed at 200 °C (first layer: 220 °C). The layer height was set to 0.15 mm (0.2 mm for the first layer). Lifting of the Z axis, when filament retraction is triggered was set to zero to avoid stringing, therefore post-processing of the printed ATR module was mainly required for visual impression. The infill was set to 20 % using a honeycomb pattern. No support structures were used. Further printing parameters were chosen as suggested by Slic3r for Prusa PLA. The overall printing time for the ATR module including the mirror mounts was 10.5 h with the proposed settings using ~27 m filament. The print of the mini-spectrometer took 5 h and used 16 m filament.

2.1.5 Spectroscopic Performance of Silicon and Germanium ATR Crystals

Single Channel spectra of uncoated ATR are given in **Figure 2.6, left**. The transmission of blank Si starts decreasing below 1500 cm^{-1} and it is not transparent below 1250 cm^{-1}. Bands at 1447 cm^{-1}, 1385 cm^{-1} and 1296 cm^{-1} are associated with phonons in silicon.[181] Ge with thin

Die approbierte gedruckte Originalversion dieser Dissertation ist an der TU Wien Bibliothek verfügbar.
The approved original version of this doctoral thesis is available in print at TU Wien Bibliothek.
TU Bibliothek WIEN Your knowledge hub

SiO2 film is transparent until 800 cm^{-1}. The strong Si-O-Si bands of the film are located between 1250 and 1000 cm^{-1}, hence transmission of the coated Ge and Si ATR crystals are limited to wavenumbers higher than 1250 cm^{-1} (Figure 2.6, right).

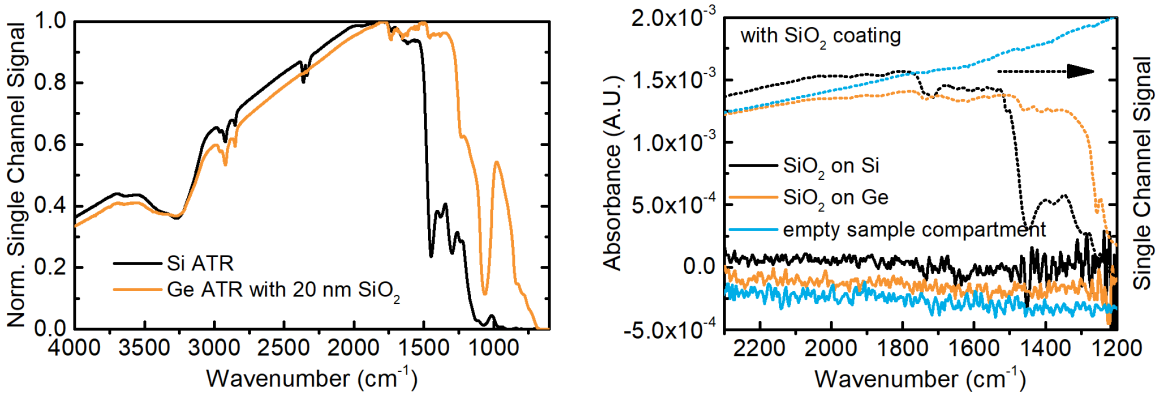

Figure 2.6: (Left) Single channel spectra of used Ge and Si ATR crystals. (Right) FTIR spectra of 100% lines of different ATR crystal materials coated with mesoporous silica to illustrate the noise floor.

The noise level was evaluated as the RMS noise of 100% lines, which were obtained by calculating the absorbance spectrum of two subsequent single-channel spectra of the same sample under identical conditions. The decrease in transmission of the Si ATR crystal is reflected in the noise that increased below 1500 cm^{-1}. The noise increased in this region to 10^{-4} A.U (RMS noise of 100 % lines, 64 scans, 8 s, 1300 – 1500 cm^{-1}, resolution 4 cm^{-1}), while being 2-3 $\cdot 10^{-5}$ A.U (64 scans, 8 s, 1500 – 2000 cm^{-1}, resolution 4 cm^{-1}). In contrast, Ge is transparent down to 800 cm^{-1} ($3 \cdot 10^{-5}$ A.U. RMS noise, 32 scans, 4 s, 1200 – 2000 cm^{-1}, resolution 4 cm^{-1}) and transmission is only limited by absorption of the SiO_2 film (absorbance at 1000 – 1200 cm^{-1}). Furthermore, the RMS noise for the empty sample compartment of the spectrometer, with reduced aperture to obtain the same intensity at the detector as with ATR crystals was recorded and yielded the same RMS noise values as for Ge ATR crystals.

2.2 Sample Preparation

2.2.1 Liquid Sample Handling

An automated flow system enabled reproducible sample application. The system consisted of a 10-way selection valve (*Valco Instruments Co. Inc.*, Switzerland), a peristaltic pump (*Ismatec*, Germany), and 1/16-in. stainless steel tubing with 0.75 mm inner diameter.

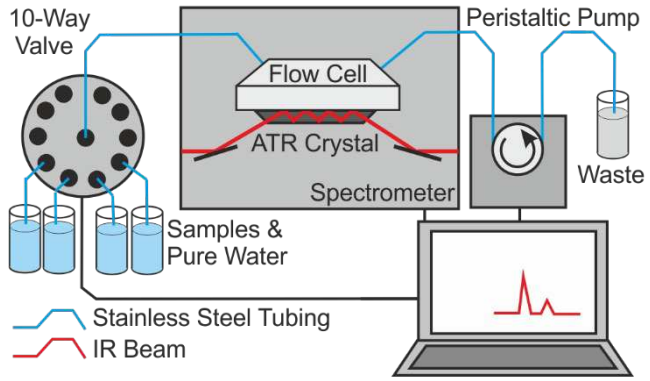

Figure 2.7: Optical setup consisting of a flow cell placed on a Si ATR crystal within a commercial FTIR spectrometer. The sample is supplied by an automated flow system comprising a peristaltic pump and a selection valve.

Die approbierte gedruckte Originalversion dieser Dissertation ist an der TU Wien Bibliothek verfügbar.
The approved original version of this doctoral thesis is available in print at TU Wien Bibliothek.

The distance between selection valve and flow cell was 30 cm. Stainless steel tubing was used instead of tubing made of polymers to avoid possible absorptions of the apolar analytes into the polymer tubing walls. A LabView-based GUI (*National Instruments*, USA) with server-client program structure controlled the system.[182] Analyte solutions were applied at a flow rate between 0.5 - 2 mL min^{-1}.

2.2.2 Liquid Sample Characterization

IR transmission spectra were recorded on a Bruker Tensor 27 or 37 FTIR spectrometer. Experiments were performed with a custom-made liquid cell comprising two 2 mm-thick CaF_2 windows separated by PTFE spacers with different thicknesses.

UV/VIS spectra were recorded on a Cary 50 Bio UV/Vis spectrophotometer (*Agilent Technologies*, USA) in quartz cuvettes with $d = 1$ cm filled with 1.5 mL analyte solution between 190 - 600 nm.

2.2.3 Gas Sample Handling

Depending on the targeted analyte, vapors were prepared either (i) by bubbling through the respective solution or (ii) mixing the liquid phase analyte with N_2 in a gas container. Method (i) was used for preparing samples with defined humidity and high concentration of VOC vapors (> 1000 ppmv), while low concentrations (< 1000 ppmv) are accessible via method (ii). This method was used for preparation of BTEX gas samples.

2.2.3.1 Water Vapor and High VOC Vapor Concentrations

Samples of defined water vapor pressures were generated by mixing a dry N_2 flow with a moistened N_2 flow obtained from bubbling through water at 50 °C by means of mass flow controllers (controlled using LabView, *National Instruments*, USA). The water temperature was achieved by placing a 500 mL Schott glass filled half with water into a thermostat (*Julabo*, Germany). Lower thermostat temperatures were tested but did not allow to reach a relative humidity range > 85 %. The total flux (dry and humid N_2) was fixed to 2 L min^{-1}. All vessels and the flow cell were connected by 6 mm O.D. PUN tubing. The actual water relative vapor pressure was determined by transmission IR spectroscopy in a 4 cm transmission cell with ZnSe windows. Bands between 1800 – 1600 cm^{-1} were integrated and calibrated to the spectrum obtained from the PNNL database.

For methanol, isopropanol and toluene vapors at high concentrations, the thermostat temperature was set to 20 °C. Vapor concentrations were calibrated to spectra obtained from the PNNL database.

2.2.3.2 Low BTEX Vapors Concentrations

Gas samples were prepared by injecting 200 - 500 µL of liquid VOC into a 10 cm long tubing

Die approbierte gedruckte Originalversion dieser Dissertation ist an der TU Wien Bibliothek verfügbar.
The approved original version of this doctoral thesis is available in print at TU Wien Bibliothek.
TU Bibliothek Your knowledge hub WIEN

(6 mm O.D.) enclosed with two manual valves connected to an evacuated pressure vessel (2 x 10 L, *Festo*, Germany, CRVZS Series, interconnected with stainless steel tubing, see **Figure 2.8,** note that for liquid application the system right to the reducing valve is disconnected). The required liquid volumes were derived from the ideal gas law *e.g.* If inserted for 500 µL toluene with $n = 2.5 \cdot 10^{-3}$ mol, $R = 8.314$ J K^{-1} mol^{-1}, $T = 298$ K, $V = 0.02$ $m^3 \cdot 9 = 0.18$ m^3, this yields a toluene partial pressure of 34 Pa or 850 ppmv, which roughly corresponds to the measured concentration. The reservoir was filled with N_2 to 9 bar alternating through the VOC-filled tubing g as well as a second tubing connected to the second vessel to ensure good gas mixing. The reservoir was then connected to a mass flow controller (MFC, *Voegtlin AG*, Switzerland) using a reducing valve. A second mass flow controller was used for N_2 and both streams were mixed to yield a flow of 1 L min^{-1}. Both MFCs were controlled using LabView. All tubing were PUN or PTFE tubing (6 mm O.D.). As VOCs diffuse into the tubing and to avoid the carryover of VOCs, the point of mixing both streams was kept as short as possible and was ca. 30 cm. In addition, standard calibration of VOCs in transmission measurements was performed with increasing concentration as well as in random order. For both methods the same concentrations were found, hence, no contamination due to carryover or tubing diffusion is assumed.

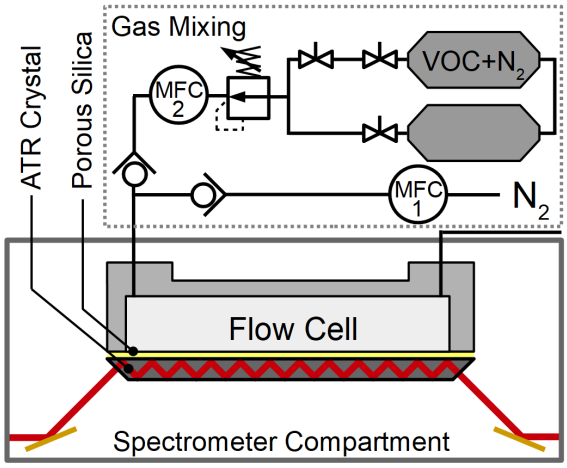

Figure 2.8: Optical setup with gas mixing and conditioning unit.

Concentrations of the applied VOC vapors were determined from IR transmission measurements. Although concentrations could be derived from the injected liquid volume as well as the gas volume and applied pressure, this approach was found to be less accurate than IR spectroscopy (no precise pressure gauge was available, and VOCs were injected with varying losses). A gas cell with ZnSe windows and a path length of 4 cm was used for transmission measurements. For calibration of VOCs concentrations, transmission spectra of each VOC (standards prepared as explained below) were integrated in the C-H stretching region between 3100 cm^{-1} - 2800 cm^{-1}. Concentrations were obtained from the band areas using reference spectra of 1 ppm/m VOC from the PNNL database. Since a reference spectrum of 1,2,4-trimethylbenzene was not available, the spectrum of 1,2,3-trimethylbenzene was used, assuming very similar integrated absorptivity in the analyzed spectral region. The

Die approbierte gedruckte Originalversion dieser Dissertation ist an der TU Wien Bibliothek verfügbar.
The approved original version of this doctoral thesis is available in print at TU Wien Bibliothek.
TU Bibliothek Your knowledge hub WIEN

concentration of the gas mixture obtained from 200 µL toluene and *p*-xylene and 100 µL 1,2,4-trimethylbenzene was calculated from band areas at 728 cm^{-1}, 795 cm^{-1} and 805 cm^{-1} for toluene, *p*-xylene and trimethylbenzene, respectively.

2.3 Synthesis and Methods

2.3.1 Chemicals

Tetraethoxysilane (TEOS, *Sigma Aldrich* 99.5 %), abs. ethanol (*Fisher*, 99.6 %), hydrochloric acid (*VWR*, 37 %), hexamethyldisilazane (HMDS, *TCI*, >96.0 %), cetyltrimethylammonium bromide (CTAB, *Sigma Aldrich*, 99 %), Pluronic P123 (*Sigma Aldrich*, average M~5800 g mol^{-1}), Pluronic F127 (*Sigma*, BioReagent), sodium thiocyanate (*Fluka*, p.a.), abs. acetone (*Sigma Aldrich*, 99.8 %) was dried over molecular sieves. Abs. toluene (*Sigma Aldrich*, 99.9 %) was used as received in a sealed bottle. Methyltriethoxysilane (MTES, *Sigma Aldrich*, >98 %), octyltriethoxysilane (*TCI,* >98 %), phenyltriethoxysilane (*TCI*, >98 %), N-[3-(trimethoxysilyl) propyl]-N,N,N-trimethylammonium chloride (TMAC, *Sigma Aldrich*, 50 % in methanol), (3-mercaptopropyl)trimethoxysilane (MPTMS, *Fluka,* 95 %), 3-aminopropyltriethoxysilane (APTES, *TCI*, >98 %) were used as received.
Cyclohexane (*Sigma-Aldrich*, 99.9 %), heptane (*Merck*, for chromatography), *p*-xylene (*Aldrich*, 98 %), 1,2,4-trimethylbenzene (*Aldrich*, 98 %) methanol (*VWR*, 99.9 %), isopropanol (*VWR*, 99.6 %), benzonitrile (*Sigma Aldrich*, 99 %), and valeronitrile (*Sigma Aldrich*, 99%) were used as received. Bovine Serum Albumin (99 %, *Sigma Aldrich*) was used as received and dissolved in deionized water. *Escherichia coli (E.coli)* pellets were a gift from *Consiglio Nazionale delle Ricerche*, Italy. Nitrile rubber gloves were obtained from VWR. Superglue (Loctite 495) was purchased from RS components. Two-component epoxy resin (*Polytec PT*, Germany) was mixed in 10:1 ratio and subsequently applied on a Si ATR crystal by spin coating using a spin velocity of 4000 rpm.

2.3.2 Characterization of Mesoporous Materials

Low Angle X-ray diffraction and Gracing Incidence Small Angle X-ray scattering data was collected with an Empyrean (*PANanalytical*, USA) multipurpose diffractometer in Bragg-Brentano geometry operating with a Cu anode (Cu K_α λ= 1.5406 Å) at 45 kV and 40 mA; a GalliPix detector was used. For low angle XRD patterns, a 10 mm mask, 1/8 soll slit and 1/2 antiscatter slit was inserted into the BBHD mirror. Samples were placed on the silicon single crystal sample holder and fixed with a small amount of Vaseline. The diffraction patterns were recorded at room temperature between 1° and 6° (2θ) at a rate of 100 s/step and a step size of 0.01°. The sample holder was rotated during measurements at a rate of 4 s/turn.
IR transmission spectra were recorded on a Bruker Tensor 27 or 37 FTIR spectrometer. For transmission spectra of silica films on Si pieces, the background spectrum was recorded using a blank Si piece fixed with tape in an aperture usually used for KBr pellets and placed

Die approbierte gedruckte Originalversion dieser Dissertation ist an der TU Wien Bibliothek verfügbar.
The approved original version of this doctoral thesis is available in print at TU Wien Bibliothek.
TU Bibliothek Your knowledge hub WIEN

in the beam path.

Contact angles were measured on a DSA 30 contact angle goniometer (*Krüss*, Germany) equipped with a video camera. Static contact angles were obtained with the tangent method of the instrument software from 10 µL water droplets that were placed onto the surface of the sample.

Transmission electron microscopy (TEM) of cross-section specimens was performed on a Tecnai G20 (*FEI*, USA) operating at 200 keV. Samples were prepared in several steps: 1) two cleaved ca. 5 mm × 10 mm pieces were glued together film-to-film, 2) cutting of this piece into two ca. 2 mm × 5 mm pieces using a band saw with SiC particles, 3) an acetone soluble glue was used to fix the cross-section of the sample on a glass sample holder. 4) The first cross section was polished using diamond plates with 30 µm, 9 µm, 3 µm, 1 µm and 0.1 µm grain size. 5) The sample was released in acetone and the polished side was glued to the sample holder. 6) Using the same diamond polishing plates, the second side was polished down to 10 µm sample thickness, which was checked with a height profile calibrated microscope. 8) The thinned samples were released using acetone and glued to a 3 mm Cu ring. 9) Argon-ion milling until a hole in the center of the sample is formed.

Film thickness was determined via a Dektak XTL Stylus (*Bruker*, Germany) **profilometer** by measuring five scratches distributed over the entire film for several coatings. The variation of the thickness within a single film as well as the film-to-film variation was ±10 nm (*e.g.*, for different 3D hexagonal films: 425, 441, 425, 426, and 424 nm) except for the 1 mm rims, which based on the flow cell design are not in contact with the sample.

Films were analyzed by **spectroscopic ellipsometry** with a UV-visible variable angle spectroscopic ellipsometer (M2000, *J.A. Woolam*, USA) equipped with a controlled atmospheric cell. Refractive index dispersions and film thicknesses were extracted from conventional Ψ and Δ fitting (where Ψ and Δ are the ratio of the amplitude diminutions and the phase difference induced by the reflection) using a Cauchy model (CompleteEASE software, *J.A. Woolam,* USA) and measured under dry atmosphere. The porosities were calculated from the refractive index of the coatings using Bruggeman effective medium approximation. Water isotherms were obtained from ellipsometric porosimetry investigations performed on the films just after desorption at 200°C for 30 min to remove adsorbed VOCs. The H_2O relative vapor pressure was adjusted using mass flow controllers (ACEflow, *Solgelway*, France). The flux was set at 5 L min^{-1}.

2.3.3 Synthesis of Mesoporous Films

Films were spin coated with a KW-4A (*Chemat Scientific*, USA) or SPIN150i-NPP (*SPS-Europe GmbH*, Germany). Mixing a humidified and dry air stream using two rotameters controlled the relative humidity in the spinning chamber. The humidified air was obtained by bubbling through a gas-washing bottle placed in thermostat at a constant temperature of 25 °C. The humidity was controlled using a hygrometer (635, *Testo GmbH*, Austria).

Die approbierte gedruckte Originalversion dieser Dissertation ist an der TU Wien Bibliothek verfügbar.
The approved original version of this doctoral thesis is available in print at TU Wien Bibliothek.
TU Bibliothek Your knowledge hub WIEN

Prior to every film deposition series, the substrates were cleaned with ethanol for 15 min in an ultrasonic bath, rinsed with ethanol and subsequently dried in a dry air flow.

2.3.3.1 Films prepared using CTAB

The synthesis of mesoporous surface-modified silica was adapted from the literature.[183–185] The sol was prepared by the addition of 0.9 mL water (pH = 1.25 adjusted with HCl, 0.056 M) to 2.08 g TEOS diluted in 2.2 mL ethanol. The mixture was stirred at 40 °C for 3 h. For 3d hexagonal structures and for cubic structures, 0.12 eq. and 0.16 eq. CTAB (0.041 g or 0.054 g), respectively, were dissolved in 0.5 mL ethanol, followed by addition of 0.5 mL sol, leading to a final molar ratio of 1:13:5:5 · 10^{-3}:0.12–0.16 for TEOS:EtOH:H_2O:HCl:CTAB. The mixture was stirred for 5 min and spin coated onto the Si ATR crystals with a spinner velocity of 2000 rpm and for 30 s. 30 µL of solution (for 2 × 1 cm^2 pieces) were applied on the spinning substrate. The RH of the spinner chamber was controlled and adjusted to 50% for the 3d hexagonal structures and to 65% for the cubic structures. After deposition, the samples were pretreated at 110 °C overnight, followed by either (i) surface functionalization with simultaneous surfactant removal or (ii) calcination.

2.3.3.2 Films prepared using F127

F127 film was prepared by stirring of ethanol, TEOS, water and 0.1 M HCl (molar ratio TEOS:EtOH:H_2O:HCl = 1:8.7:10.3:0.01) at room temperature for 20 min. A polymer solution was added to the sol giving a final molar ratio of TEOS:EtOH:F127:H_2O:HCl = 1:16:0.01:16.3:0.015 and the mixture was stirred for 3 h at room temperature. Films were spin coated with a spinner velocity of 2000 rpm and subsequently calcined at 400 °C for 12 h with a heating ramp of 1 K min^{-1}.

2.3.3.3 Films prepared using P123

P123 film was prepared by stirring of ethanol, TEOS, water and 0.1 M HCl (molar ratio TEOS:EtOH:H_2O:HCl = 1:5.2:6:0.01) at room temperature for 20 min. A polymer solution was added to the sol giving a final molar ratio of TEOS:EtOH:P123:H_2O:HCl = 1:14.6:0.009:6:0.01 and the mixture was stirred for 3 h at room temperature. All films were spin coated with a spinner velocity of 2000 rpm and subsequently calcined at 400 °C for 12 h with a heating ramp of 1 K min^{-1}.

2.3.3.4 Synthesis non-ordered CTAB Films

For dip coating experiments performed in the lab of Prof. Grosso in Marseille, solutions of ethanol, 1.69 g TEOS, 1.45 g MTES, 0.73 g H_2O, 0.73 g 0.1 M HCl and 0.83 g CTAB with a total ratio of TEOS:MTES:EtOH:H_2O:HCl:CTAB = 0.5:0.5:10:15:0.026:0.14 were mixed together in a closed flask and heated to 70 °C for 30 - 60 min. Subsequently, the solution was filled into PTFE containers and transferred into the humidity-controlled chamber of a dip coater (ACEdip, *Solgelway*) and film deposition on Si or Ge pieces was performed with 0.15 -

Die approbierte gedruckte Originalversion dieser Dissertation ist an der TU Wien Bibliothek verfügbar.
The approved original version of this doctoral thesis is available in print at TU Wien Bibliothek.
TU Bibliothek WIEN Your knowledge hub

10 mm/s dipping speed. Films were calcined at 450°C for 10 min under IR lamps (home-made system).

The obtained films were analyzed by ellipsometry and had a film thickness ranging from 500 - 1500 nm and a refractive index of 1.21 at 700 nm.

2.3.4 Surface Functionalization

Note that for all functionalization reactions, no stirring bar was used to prevent damage of the chips.

Functionalization with HMDS. For simultaneous surfactant removal and surface modification (only used for CTAB), films were dried *en vacuu* at 150 °C for 2 h in a three-neck flask. 20 mL abs. acetone and 0.5 mL HMDS were added to the ATR crystals under inert atmosphere and the mixture was heated to reflux temperature for different reaction times. The modified films were thoroughly washed with acetone and dried at 110 °C overnight.

Functionalization with chlorosilanes or organoalkoxysilanes. If films were not directly placed in the flask after calcination (films were removed from the oven when still hot and placed in the flask), films were dried *en vacuu* at 150 °C for 2 h in a three-neck flask. Under inert atmosphere, 20 mL abs. toluene and 50 - 200 µL of respective silane (depending on the number of films) were added and heated to reflux temperature for 6 - 8 h. After cooling back to RT, films were rinsed with toluene and acetone and dried at 60 °C to remove unreacted silane.

Introducing a trimethyl ammonium moiety.[186] Films were placed in a 3-neck flask and 15 mL methanol and 0.5 mL TMAC solution were added. The solution was heated to reflux temperature for 8 h. Subsequently, films were rinsed with acetone and heated to 60 °C in the oven over night.

Introducing a sulfonic acid moiety. According to literature,[187] films were firstly functionalized with (3-mercaptopropyl)trimethoxysilane (MPTMS): 20 mL abs. toluene and 100 µL MPTMS were added to the freshly calcined films into a three-neck flask under inert atmosphere. The reaction mixture was heated to reflux temperature for 6 h. The films were rinsed with toluene and acetone and placed in the oven at 60 °C over night. Subsequently, films were added to a mixture of 10 mL methanol and 10 mL 30 % hydrogen peroxide solution and heated to reflux temperature for 6 h. After cooling back to room temperature, 10 mL 0.1 M H_2SO_4 were added and stirring was continued for 4 h at room temperature. Films were rinsed with acetone and placed in the oven at 60 °C over night.

As functionalization with TMAC and MPTMS not fully saturate free Si-OH groups, these were functionalized a second time using HMDS as described above.

2.3.5 Synthesis of Mesoporous TiO_2

For dip coating experiments performed in the lab of Prof. Grosso in Marseille, solutions of

Die approbierte gedruckte Originalversion dieser Dissertation ist an der TU Wien Bibliothek verfügbar.
The approved original version of this doctoral thesis is available in print at TU Wien Bibliothek.
TU Bibliothek Your knowledge hub WIEN

2.7 g Ti5E, 10 g Ethanol, 2 g H_2O and 0.44 g F127 with a total ratio of Ti:EtOH:H2O:F127 = $1:33:17:3 \cdot 10^{-3}$ were mixed for 30 min at RT. This solution yielded films of ca. 200 nm after calcination at 450 °C and a refractive index of 1.78.
Ti5E is a stock solution prepared form 1 eq. $TiCl_4$ and 5 eq. EtOH.

2.3.6 Nanoimprinting

For nanoimprinting experiments, PDMS molds were supplied by IMEC with rectangular shapes with 5 - 100 µm width and 2 cm length with either 790 nm or 1550 nm depth (was measured using the profilometer at TU Wien). All experiments were performed at Prof. Grosso's lab at the University of Marseille.
Prior to all experiments, PDMS molds were evacuated in a desiccator for at least 15 min. An exemplary soft-NIL experiment included the following steps:[188]

1. Dip coating at RH = 0 % with the silica solution described in section 2.3.3.4 at 4 mm s^{-1}
2. Immediately removing the film from the dip coater and placing it in a home-made box flushed with regulated humidified air at maximum humidity *i.e.* 90 %
3. Removal of the PDMS mold from the desiccator and placing it on the film, here, the evacuated mold absorbs remaining air bubbles
4. Leave the film for 1 min at high humidity
5. Thermal treatment of film including PDMS mold at 50 °C for 30 min
6. Removal of the PDMS mold
7. Thermal treatment of the casted material for 5 min at 200 °C, following by 10 min at 450 °C

Micro-transfer-molding *i.e.,* filled PDMS molds are removed from film and transferred on a blank substrate, was also tested and involved the following procedure:

1.-3. As described above
4. Change to ca. 10 % low humidity
5. After 1 min, removal of the PDMS mold
6. Increasing the humidity to 70-80 % with the PDMS mold still in the box
7. Application of the PDMS mold to the new substrate and holding time of 1 min
8. Thermal treatment at 70 °C for 1 min

Die approbierte gedruckte Originalversion dieser Dissertation ist an der TU Wien Bibliothek verfügbar.
The approved original version of this doctoral thesis is available in print at TU Wien Bibliothek.

Die approbierte gedruckte Originalversion dieser Dissertation ist an der TU Wien Bibliothek verfügbar.
The approved original version of this doctoral thesis is available in print at TU Wien Bibliothek.

Die approbierte gedruckte Originalversion dieser Dissertation ist an der TU Wien Bibliothek verfügbar.
The approved original version of this doctoral thesis is available in print at TU Wien Bibliothek.

Chapter 3 Synthesis and Characterization of Mesoporous Films

This chapter summarizes the efforts toward the synthesis of ordered mesoporous silica films (**section 3.1**) and their application on planar substrates (**section 3.2**) as well as results obtained with different integrated optics provided by cooperation partners at IMEC and TU Wien (**section 3.3**). Furthermore, first results on nanoimprinting of SiO_2 and TiO_2 obtained in cooperation with Aix-Marseille Université are given as well (**section 3.4**).

3.1 Optimization of Synthesis of Mesoporous Silica Films

Mesoporous silica films were obtained using the surfactant templating route (as described in section 1.2.2), using acidic hydrolysis and condensation of tetraethoxysilane (TEOS) in ethanol and cetyltrimethylammonium bromide (CTAB) or polyoxamers (P123 and F127) as surfactant.[73,183–185,189–192] The synthesis and deposition of films with each surfactant were optimized regarding their film thickness and periodicity and corresponding intensity of the reflections obtained from X-ray diffraction patterns.

First mesoporous films prepared in the course of this thesis were synthesized using CTAB following the procedure reported by *Besson et al.*[183,189,190] However, the films reported in the cited publications are thinner than 300 nm and therefore too thin for the targeted sensing application. In addition, experimental procedures for thin film synthesis are generally kept short in publications, most of the time they use dip coating and not spin coating and are sometimes hard to reproduce if new in the field.[193] Therefore, a video of my working procedure is available on the group sever (\\cavs-nas\CAVS Stuff\mesoporoous_silica_synthesis).

Firstly, a spin coater was adapted to allow controlling the relative humidity (RH). This was accomplished with two rotameters (4 – 50 L min^{-1} flux), a plastic bowl and a bubbler with an aquarium stone for bubble generation, placed in a thermostat at 25 °C as inspired by Ref. [194]. Humidity was controlled by hand using the two rotameters and a hygrometer that

was placed in the spinning chamber. RH was adjusted prior to every spin coating series. Studies with varying surfactant concentration, ethanol content and RH were conducted, and every sample was analyzed using XRD and profilometry. Thereby, three different pore arrangements were obtained as reported in literature:[184,185,191] a 3d hexagonal, a cubic and 2d hexagonal phase. XRD patterns are shown in **Figure 3.3**. The structural change with CTAB content and RH is summarized in **Table 3.1** and **Table 3.2**. Obtained film thicknesses ranged from 316 nm to 550 nm for a volumetric ratio of sol:EtOH = 1:1 and 260 nm to 385 nm for sol:EtOH = 1:2 and films were thicker for higher CTAB concentrations and lower EtOH content. Film thickness increased with decreasing relative humidity.

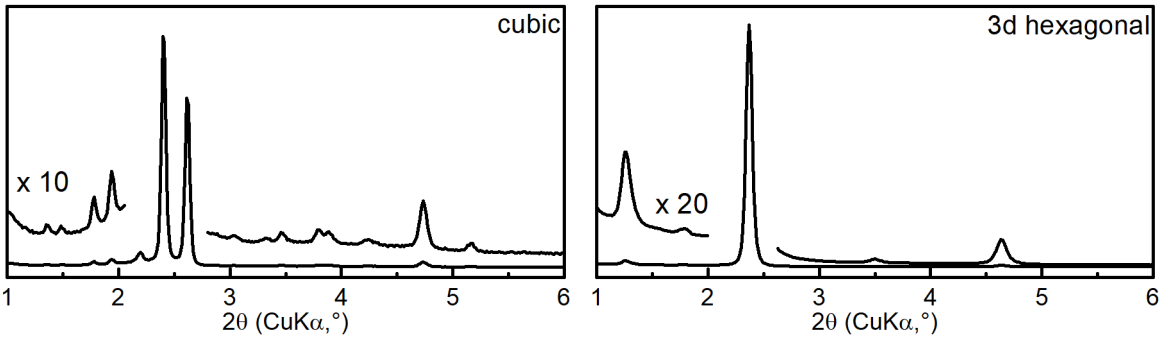

Figure 3.1: X-ray diffraction pattern of mesoporous silica films obtained using CTAB as surfactant.

From these results, optimal conditions for 3d hexagonal and cubic films were derived (as given in **Chapter 2**) to be at 0.12 and 0.16 eq. CTAB:TEOS, at 55 % and 65 % RH, respectively, yielding films of 425 nm and 500 nm thickness for a volumetric ratio of sol:EtOH=1:1 after template removal using acetone.

Table 3.1: Results of TEOS films obtained from dynamic spin coating at 2000 rpm with sol:EtOH = 1:1 for different CTAB ratios and relative humidity derived from XRD patterns. 3d hexagonal (3d), cubic and 2d hexagonal (2d) structures were obtained. XRD patterns with low intensity are given in brackets.

CTAB / RH %	0.10	0.12	0.14	0.16	0.18	0.20
80 %	-	-	-	-	-	-
70 %	(3d)	3d	cubic	cubic	-	2d
60 %	(3d)	3d	cubic	cubic	-	2d
50 %	3d	(3d)	(cubic)	(cubic)	-	2d

Table 3.2: Results of TEOS films obtained from dynamic spin coating at 2000 rpm with 1 sol:EtOH = 1:2. See Table 3.1 caption for further explanation.

CTAB / RH %	0.10	0.12	0.14	0.16	0.18	0.20
80 %	-	(3d)	-	-	-	-
70 %	(3d)	3d	-	-	-	-
60 %	3d	3d	-	-	-	2d
50 %	3d	-	(cubic)	-	-	2d

Die approbierte gedruckte Originalversion dieser Dissertation ist an der TU Wien Bibliothek verfügbar.
The approved original version of this doctoral thesis is available in print at TU Wien Bibliothek.
TU Bibliothek Your knowledge hub WIEN

Die approbierte gedruckte Originalversion dieser Dissertation ist an der TU Wien Bibliothek verfügbar.
The approved original version of this doctoral thesis is available in print at TU Wien Bibliothek.

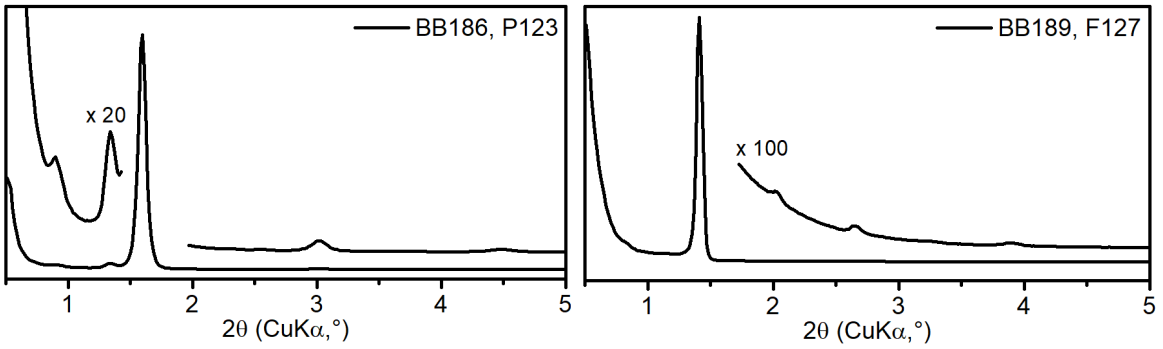

Figure 3.3: X-ray diffraction pattern of mesoporous silica films obtained using P123 and F127 as surfactant.

In a first attempt, P123 films were synthesized according to literature[192] using a home-made dip coater (samples BB172 - BB174 and BB177 - BB179). Here, lamellar and 2d hexagonal structures depending on P123 content (Φ = 64 % and Φ = 45 %, see below for explanation) were obtained (see **Figure 3.3** for 2d hexagonal and BB173 for lamellar structure) and the best results (in terms of intensity of the reflection in XRD patterns) were obtained for 30 %RH. This synthesis proofed to be very robust, and was easily transferred to spin coating, resulting in up to 400 nm thick films.

On the basis of the P123 synthesis, a sol composition for films using F127 as surfactant was derived. According to Ref. [192] the mass fraction Φ of the surfactant was calculated:

$$\Phi = \frac{V_{polymer}}{V_{polymer} + V_{SiO_2}} \tag{3.1}$$

where, V_{SiO2} corresponds to the non-volatile components in the solution and $V_{polymer} = m_{polymer}/\rho_{polymer}$ with a polymer density $\rho = 1.02$ g cm^{-3}. If considering full hydrolysis, V_{SiO2} is the sum of SiO_2 and four equivalents water:[192]

$$V_{SiO_2} = \frac{m_{SiO_2}}{\rho_{SiO_2}} + \frac{m_{H_2O}}{\rho_{H_2O}} \tag{3.2}$$

with ρ_{SiO_2} = 2.2 g cm^{-3} and ρ_{H_2O} = 1 g cm^{-3}.

As reported in Ref. [192] for P123, expected mesophases for polyoxamers can be roughly derived from the corresponding polymer-water phase diagram, *e.g.,* for F127 for Φ = 20-30 % a hexagonal phase, and for Φ = 35-80 % a cubic phase was observed.[76] In the case of silica film synthesis for films > 300 nm, it was found that Φ = 28 % is optimal to obtain cubic films (samples BB181 onwards, denoted F127BB) regardless RH. For higher F127 concentrations, *e.g.* Φ = 45 % for BB180, only broad reflections were found in the XRD pattern.

In addition, the synthesis was adapted for higher F127 fraction (Φ = 63 %), which was also found to be suitable for large pore synthesis with wormlike pore arrangement and with a film thickness of 600 nm (compare master thesis of Sophia Steinbacher, therefore this film is denoted F127SS).

Die approbierte gedruckte Originalversion dieser Dissertation ist an der TU Wien Bibliothek verfügbar.
The approved original version of this doctoral thesis is available in print at TU Wien Bibliothek.
TU Bibliothek Your knowledge hub WIEN

Die approbierte gedruckte Originalversion dieser Dissertation ist an der TU Wien Bibliothek verfügbar.
The approved original version of this doctoral thesis is available in print at TU Wien Bibliothek.

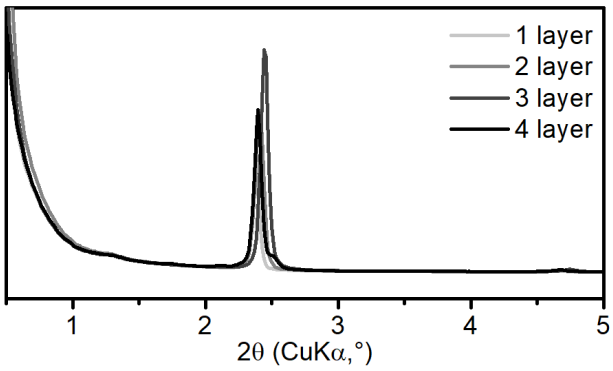

Figure 3.5: X-ray diffraction pattern of mesoporous silica films (CTAB, 3d hexagonal) obtained from multiple layer deposition.

The film thickness of subsequent layers was verified using profilometry and was found to scale, as expected, with the thickness of the first layer and the number of layers.

Die approbierte gedruckte Originalversion dieser Dissertation ist an der TU Wien Bibliothek verfügbar.
The approved original version of this doctoral thesis is available in print at TU Wien Bibliothek.
TU Bibliothek Your knowledge hub WIEN

3.2 Characterization of Mesoporous Silica on Planar Surfaces

This section summarizes the thorough characterization of all mesoporous films synthesized in this thesis.

3.2.1 IR Spectra of Mesoporous Films

The formation of silica and complete removal of the template was confirmed by FTIR measurements. The Si–O–Si stretching modes are found at ~1070 cm^{-1} in the IR transmission spectra (**Figure 3.6**). In addition, bands around 3200 cm^{-1} can be attributed to either remaining water in the film or Si-OH bands of not fully condensed silica. This band is significantly reduced after calcination. In addition, a weak band at 3745 cm^{-1} is visible after calcination corresponding to isolated Si-OH vibrations. Surfactants show characteristic bands associated with C-H vibrations that are also removed by calcination. IR absorption bands at 1259 cm^{-1} (on top of the strong Si-O-Si band) and several bands between 2800 - 3000 cm^{-1} are associated with the CH_3 deformation and C–H stretching modes, respectively, and stem from the organic moieties introduced by the surface functionalization using HMDS.

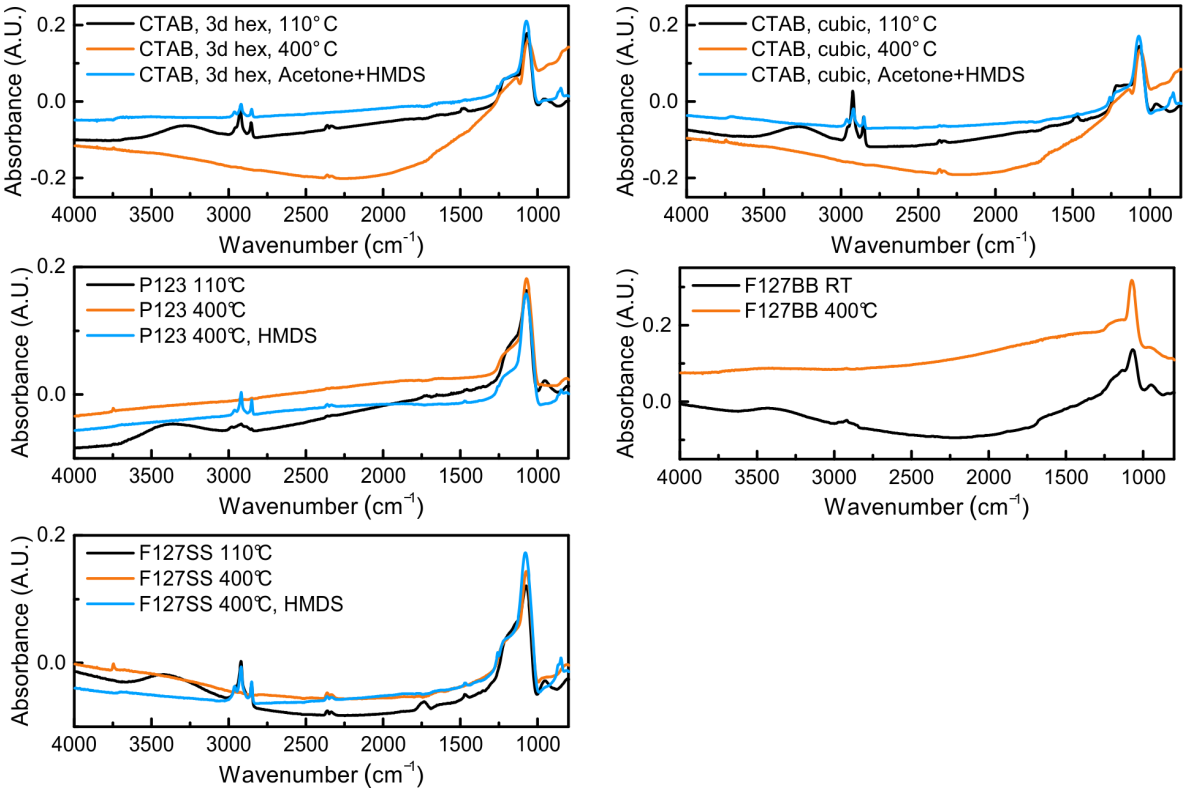

Figure 3.6: FTIR transmission spectra of mesoporous hybrid films deposited on Si substrates. Spectra were recorded with a blank Si piece as background, resulting in notable baseline shifts.

3.2.2 X-ray Diffraction of Mesoporous Films

X-ray diffraction proved the periodic arrangement of mesopores in the films (see **Figure 3.7**). For films treated at 400 °C, compared to films treated at 110 °C, the reflections show a shift

Die approbierte gedruckte Originalversion dieser Dissertation ist an der TU Wien Bibliothek verfügbar.
The approved original version of this doctoral thesis is available in print at TU Wien Bibliothek.
TU Bibliothek Your knowledge hub WIEN

toward higher 2θ values due to contraction (compare Table 3.4). Note the significant difference for the CTAB films obtained by calcination at 400 °C compared to functionalization and simultaneous surfactant removal with HMDS performed in acetone. Here, the films show a significantly smaller contraction.

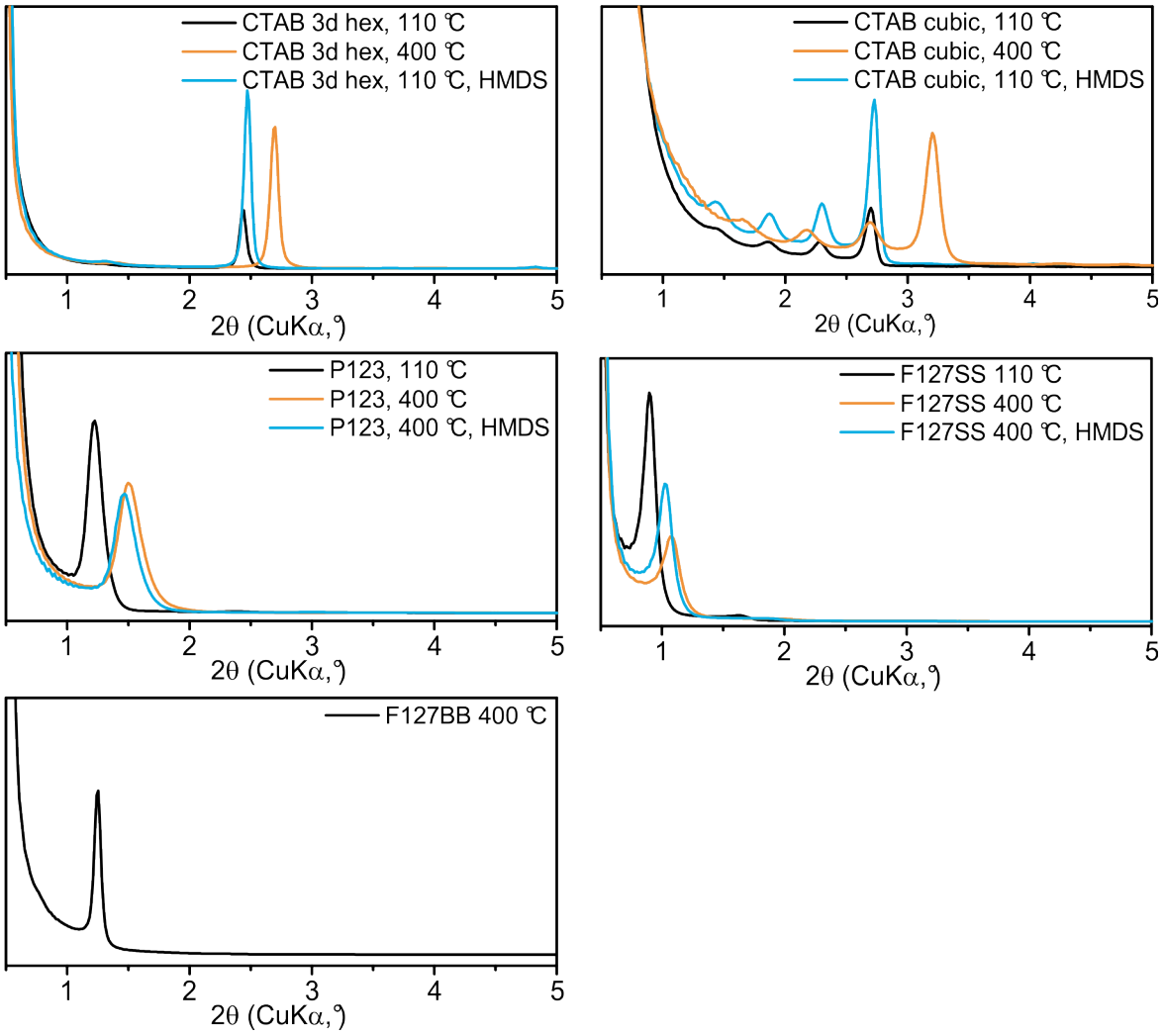

Figure 3.7: X-ray diffraction patterns of mesoporous films obtained in Bragg-Brentano geometry. Reflections are shifted toward higher $2\boldsymbol{\theta}$ values upon calcination at 400 °C.

All films were further characterized using grazing incidence small angle X-ray scattering (GI-SAXS, see **Figure 3.8**). Thereby, elliptical diffraction patterns were found for all samples. This is due to the anisotropic contraction upon shrinkage.[91] As both CTAB films were not calcined but only treated at 110 °C this asymmetry is less pronounced. Furthermore, all films except for the F127SS film show distinct reflections originating from a highly ordered film associated with cubic or hexagonal structures as found in literature.[78,183,195] In the case of F127SS no distinct features but continuous rings indicate that periodical domains are randomly orientated with respect to the surface.

Die approbierte gedruckte Originalversion dieser Dissertation ist an der TU Wien Bibliothek verfügbar.
The approved original version of this doctoral thesis is available in print at TU Wien Bibliothek.
TU Bibliothek Your knowledge hub WIEN

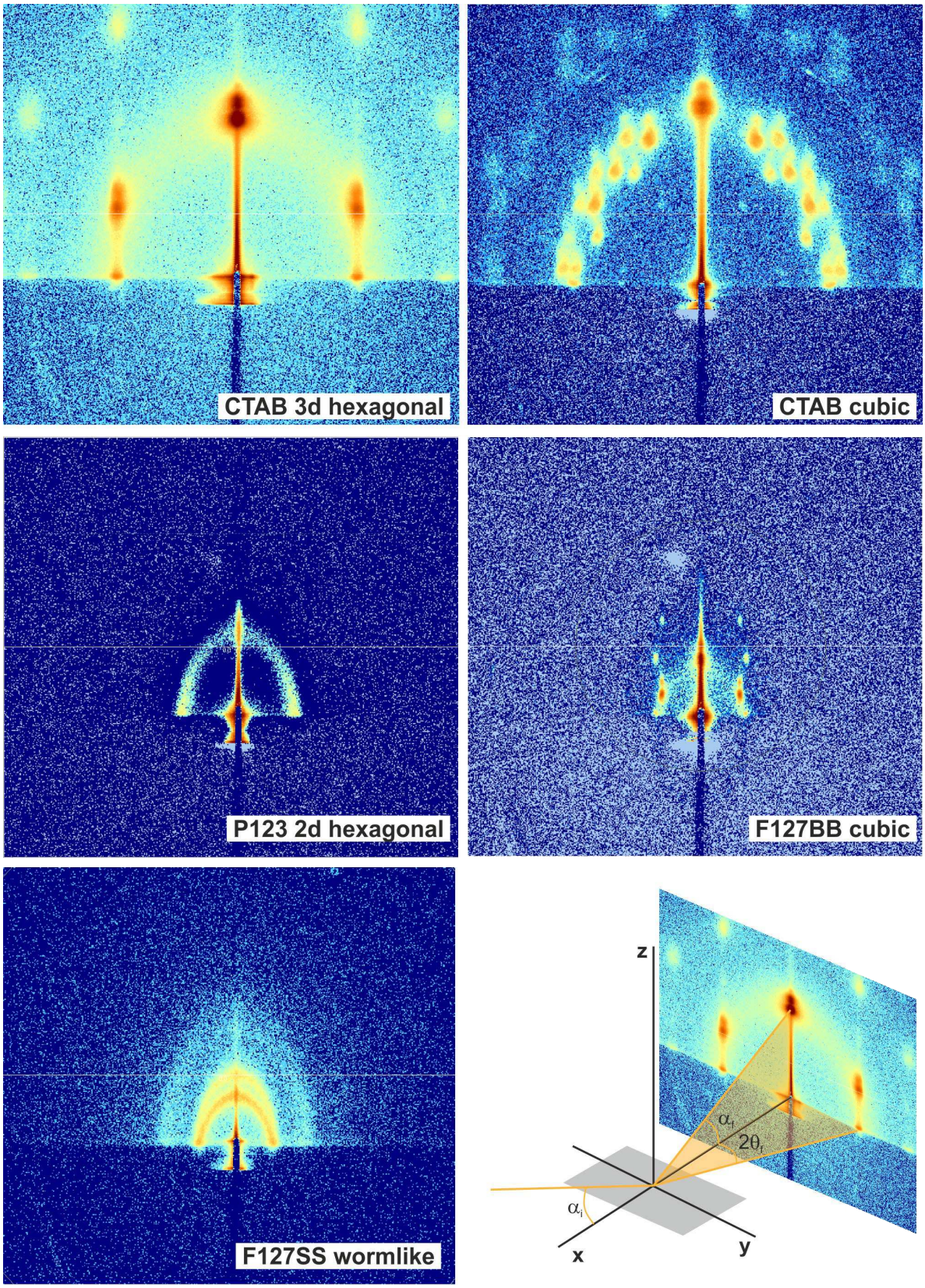

Figure 3.8: GI-SAXS patterns of mesoporous films and schematic representation of the measurement setup.

Die approbierte gedruckte Originalversion dieser Dissertation ist an der TU Wien Bibliothek verfügbar.
The approved original version of this doctoral thesis is available in print at TU Wien Bibliothek.
TU Bibliothek Your knowledge hub WIEN

3.2.3 Transmission Electron Microscopy

Transmission electron micrographs (**Figure 3.9**) prepared in cross-section, clearly show highly periodic pore structures throughout the entire CTAB films.

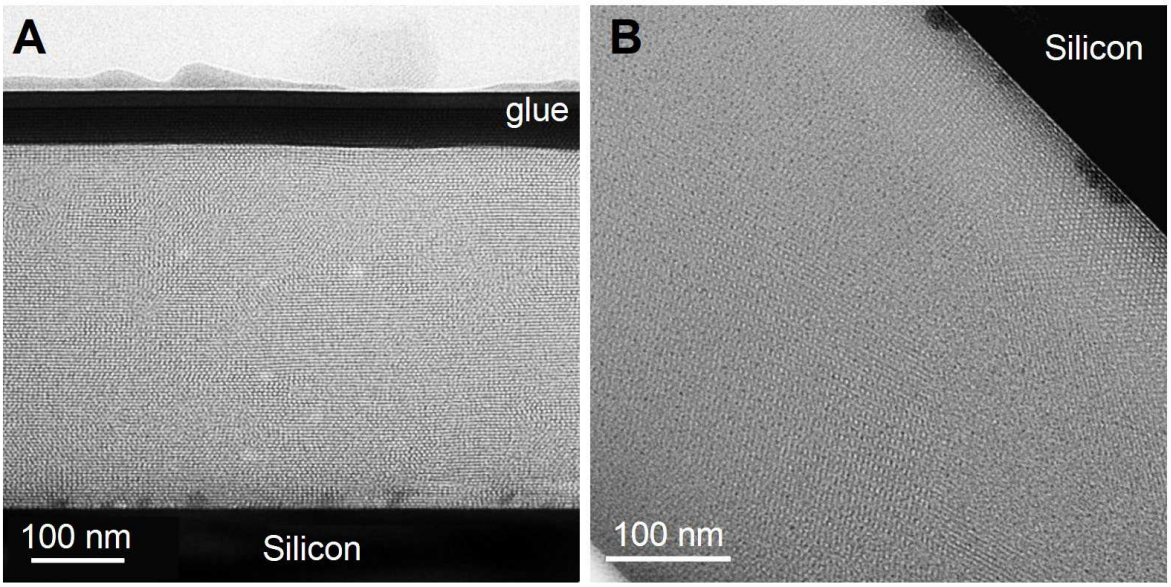

Figure 3.9: Cross-section transmission electron micrographs of functionalized (A) CTAB 3d hexagonal and (B) CTAB cubic mesoporous films.

3.2.4 Characterization of Film Thickness

The thicknesses of the untreated and calcined films were determined by profilometry and are summarized in Table 3.4. The pore anisotropy A_{pore} was calculated using **equation (3.3)**. The axis perpendicular to the surface experiences the main contraction. Due to this anisotropy the spherical pores deform after calcination into spheroids of long and short radii a and b, respectively. The determination of the degree of this deformation $A_{pore} = a/b$ obtained from the macroscopic film thickness contraction is proposed by the Isotropic Inorganic Pore Contraction model.[91] It assumes that the isotropic wall contraction of the mesoporous lattice is equal to the contraction of silica films without porogene to the power of 1/3:

$$A_{pore} = \frac{d_{mesoporous\ film,\ as\ deposited}}{d_{mesoporous\ film,\ 400\,°C}} \cdot \left(\frac{d_{silica\ reference,\ as\ deposited}}{d_{silica\ reference,\ 400\,°C}} \right)^{1/3} \qquad (3.3)$$

The found contraction is within the range, which is typically found for mesoporous films.[91]

Die approbierte gedruckte Originalversion dieser Dissertation ist an der TU Wien Bibliothek verfügbar.
The approved original version of this doctoral thesis is available in print at TU Wien Bibliothek.
TU Bibliothek Your knowledge hub WIEN

Table 3.4: Film thickness before and after heat treatment at 400 °C for 12 h and corresponding contraction

	$th_{film,\ as\ deposited}$ [nm]	$th_{film,after\ calcination}$ [nm]	Contraction [%]	Pore Anisotropy A_{pore}
CTAB 3d hexagonal	571	398	30.3	1.32
CTAB cubic	642	445	30.6	1.33
F127SS	998	602	39.7	1.53
F127BB	410	250	39.0	1.52
P123	490	340	30.6	1.33
Silica without template	135	105	22.2	

3.2.5 Porosity and Pore Size Distribution

Water vapor adsorption allows for retrieving porosity and pore size distribution of mesoporous films. This will be discussed and shown in section 5.1.3 in combination with ATR IR spectroscopy and compared to ellipsometric porosimetry (EP). P123 film and F127BB film were not characterized with water adsorption using ATR spectroscopy, but with ellipsometric porosimetry, and the resulting PSD are given in **Figure 3.10**, showing pore sizes of 6.5 nm and 6.8 nm for the P123 and F127BB film, respectively. From isotherms (not shown) porosities of 33 % and 50 %, respectively, were retrieved. **Table 3.5** summarizes the pore diameters (given as maximum of the PSD of the adsorption) and porosities of each film investigated in this thesis.

Table 3.5: Summary of porosity and maxima of the pore size distribution (PSD) of mesoporous films obtained from ellipsometric porosimetry.

	Porosity %	PSD adsorption [nm]	PSD desorption [nm]
CTAB 3d hex	51	4.8	3.5
CTAB cubic	55	4.9	3.5
F127SS	63	12.5	7.4
F127BB	33	6.5	4.1
P123	50	6.8	5.7

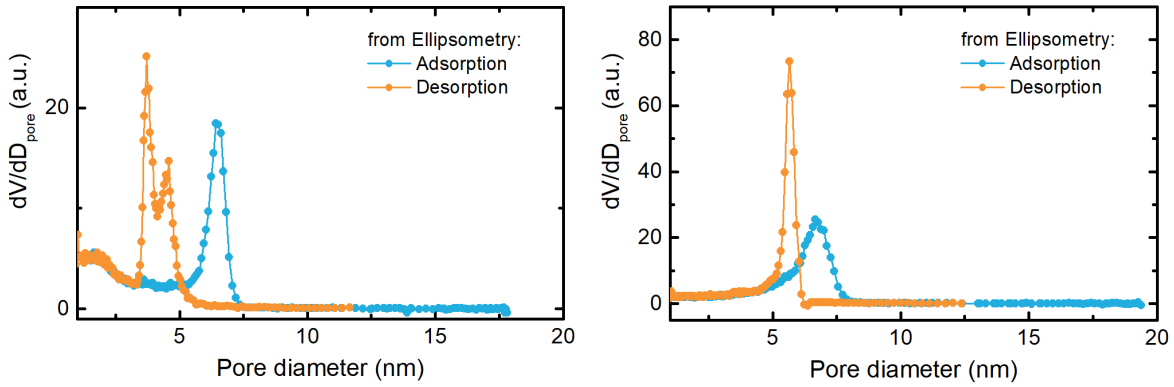

Figure 3.10: Pore size distribution obtained from ellipsometric porosimetry for F127BB (left) and P123 (right) films.

Die approbierte gedruckte Originalversion dieser Dissertation ist an der TU Wien Bibliothek verfügbar.
The approved original version of this doctoral thesis is available in print at TU Wien Bibliothek.
TU Bibliothek Your knowledge hub WIEN

3.2.6 Wettability and Stability of Mesoporous Films in Water

The surface wettability was characterized by static contact angle measurements. Surface modification led to an increase of the contact angle from 27° for pristine silica to 88° for HMDS functionalized silica films. The increased hydrophobicity of the sylilated silica film was further confirmed with ATR-IR spectra of water on coated and uncoated ATR crystals: As the films are not entirely covering the evanescent wave, a fraction of the absorbance of water is visible, although it is largely eliminated from the probed volume on coated ATR crystals compared to blank Si ATR crystals (see **Figure 3.11**).

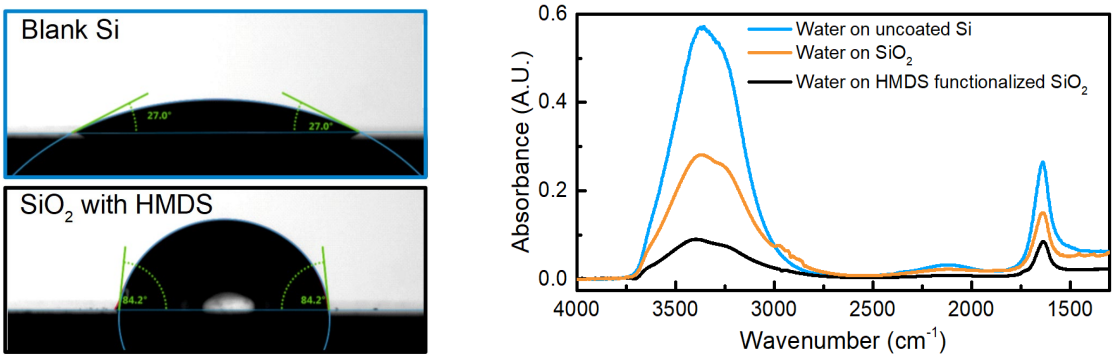

Figure 3.11: (Left) Photos of contact angle measurements of (top) uncoated Si and (bottom) surface-modified mesoporous silica films. Surface modification increased the contact angles to 85°.(Right) FTIR spectra of water on blank (black) and coated without surface functionalization (orange) and coated with HMDS functionalized (blue) Si ATR crystals: Organically modified mesoporous films repel water from the evanescent field, yielding strongly reduced IR absorption from water.

While for the functionalized film, water absorption takes place solely in the evanescent filed reaching beyond the film, unfunctionalized SiO_2 can be penetrated by water and a higher absorbance for water was found. The obtained absorbance at 1640 cm^{-1} corresponds to ca. 50 % of the absorbance for uncoated ATR crystals. This is related to the accessible pore volume, hence the porosity (compare section 5.1 for further details). Furthermore, the IR absorption bands of water in the spectra at 3400 cm^{-1} and 1640 cm^{-1} are less intense for spectra recorded with coated ATR crystals compared to blank Si crystals. Note that the change in relative intensity of the water bands is a result of the wavelength dependency of the depth of penetration d_p of the evanescent wave (see section 1.1.3).

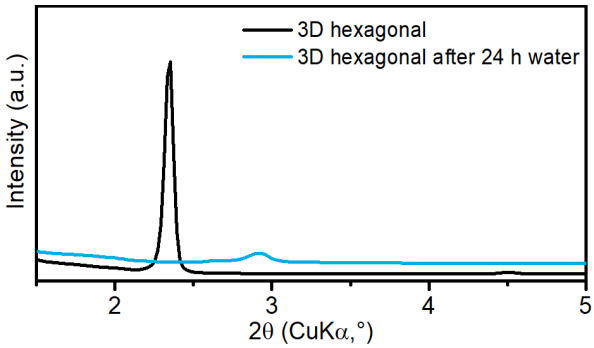

Figure 3.12: XRD pattern of a pristine 3d hexagonal film and after been 24 h of water flow.

Die approbierte gedruckte Originalversion dieser Dissertation ist an der TU Wien Bibliothek verfügbar.
The approved original version of this doctoral thesis is available in print at TU Wien Bibliothek.
TU Bibliothek Your knowledge hub WIEN

Pure silica films were not tested within this thesis for sensing (only for water adsorption experiments), because by this approach on the one hand the strong IR absorber water cannot be excluded from the evanescent field and on the other hand pure silica shows inferior stability in water compared to functionalized silica.

XRD measurements were performed on unfunctionalized SiO_2 prior and after 24 h hours of water flow application. Hereby, the flow cell was attached to a mesoporous film coated on a silicon piece and a water flow of 1 ml min^{-1} was applied using a peristaltic pump. It is clearly visible that the film had degraded and only a minor and shifted reflection is visible in the XRD pattern of the water treated film (**Figure 3.12**). These results correspond well with literature.[196,197] With HMDS functionalization no degradation was observed.

Die approbierte gedruckte Originalversion dieser Dissertation ist an der TU Wien Bibliothek verfügbar.
The approved original version of this doctoral thesis is available in print at TU Wien Bibliothek.
TU Bibliothek Your knowledge hub WIEN

3.3 Coating of Integrated Optics

As briefly introduced in **Chapter 1**, this thesis was performed within the framework of the H2020 project Aquarius, which aims for a MIR oil-in-water sensor using coated germanium waveguides and integrated optics. In the course of this thesis and after first promising results of mesoporous silica as enrichment layer on ATR crystals (see **Chapter 4**), further collaborations for coating other integrated optical circuit (IOC) chips were initiated. In contrast to planar surfaces as found on ATR crystals, integrated optics have structured surfaces with differences in height from a few hundreds of nm up to several µm and with different materials at the interface. In this section, the results of coating different IOCs are summarized.

3.3.1 Ge and Si Waveguides - Aquarius Project

The following results were obtained in collaboration with Nuria Teigell-Beneitez, IMEC/Ghent University and Prof. David Grosso and Jérôme Loizillon, Aix-Marseille Université.

Prior to coating fully functional IOCs, dummy Si and Ge waveguide structures were provided by IMEC. Here, different film deposition techniques were investigated: (i) spin coating, (ii) ambient temperature dip coating with (iii) different dipping speeds and (iv) variation of humidity (v) high temperature (60 °C) dip coating and (vi) multiple layers of coatings obtained by all these techniques. Furthermore, to enhance compatibility of the Ge and Si structures with the mesoporous silica films, IMEC provided Si and Ge waveguides with a 20 nm and 100 nm SiO_2 film. Coated samples were sent back to IMEC for (FIB-)SEM investigations. For structures wider than 5 µm, solely very thin mesoporous films on top of the structures were obtained (**Figure 3.13**, left).

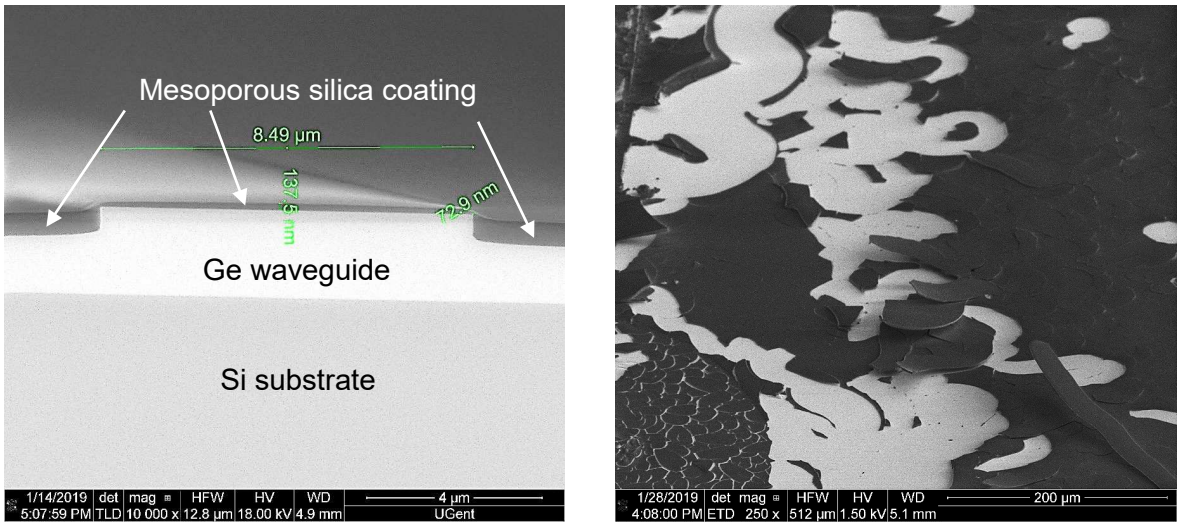

Figure 3.13: (Left) SEM cross-section images of coated waveguide structures. The mesoporous silica coating is clearly visible next to the Ge waveguide and only a thin film is observed on top of the waveguide. (Right) Cracks formed if films thicker than 1 µm are calcined.

Thickest films were obtained using high-temperature dip coating and several layer dip coating and spin coating. However, for film thicknesses > 1 µm, films started cracking and detaching

Die approbierte gedruckte Originalversion dieser Dissertation ist an der TU Wien Bibliothek verfügbar.
The approved original version of this doctoral thesis is available in print at TU Wien Bibliothek.
TU Bibliothek Your knowledge hub WIEN

off the chip (see **Figure 3.13**, right) if calcined at 400 °C. Therefore, surfactants removal solely with acetone and simultaneous HMDS functionalization was performed. Structures with different width were tested and it was shown that on wider waveguides (> 10 µm) the film thickness at the central part of the waveguide reached the thickness as found on planar substrates. However, wider waveguide structures were not preferred considering desired waveguide properties and narrower structures were thus targeted. Furthermore, it was found that coatings with 100 nm thick SiO_2 pre-deposited on the structures did not improve the coverage as compared to 20 nm of SiO_2.

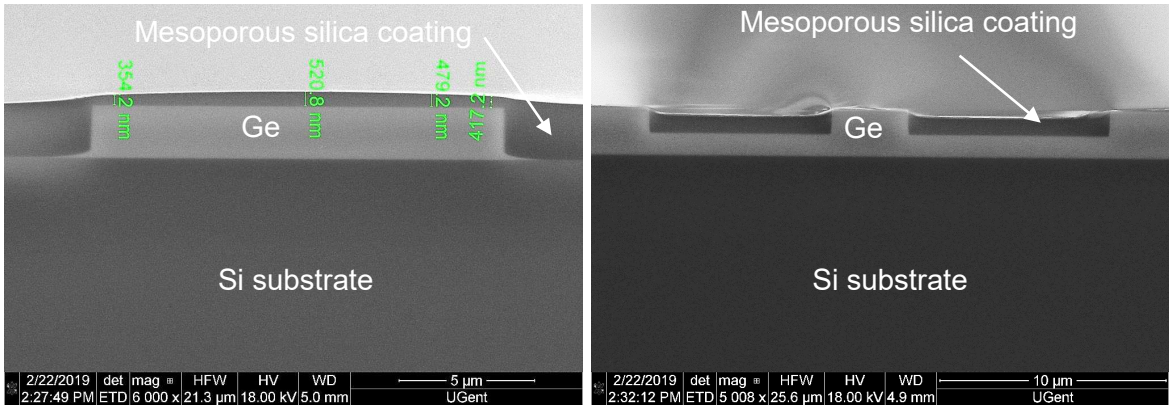

Figure 3.14: SEM cross-section images of coated waveguide structures. (Left) Wide waveguide structures (> 10 µm) were well coated and in the middle of the structures the film thickness complied with the thickness obtained on planar structures. (Right) Coating of trenched structures led to planarization of the gaps between the structures.

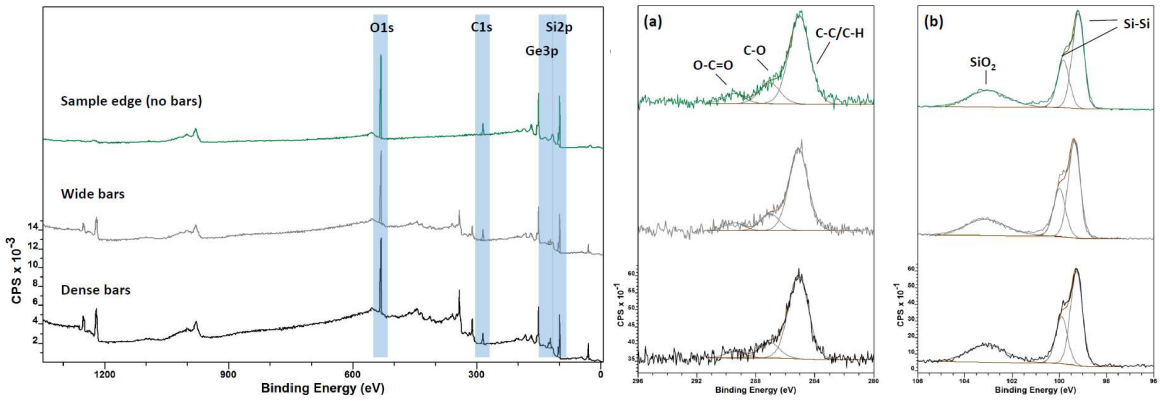

Figure 3.15: XPS survey spectra of the Si/Ge sample for different measurement positions. C1s (a) and Si2p (b) XPS detail spectra at different positions. Experiments performed by Markus Sauer.

As wetting of the SiO_2 film with the Ge and Si substrates seemed to be an issue, the chip surfaces were analyzed for potential contaminations. We hypothesized that residues of perfluorinated polymers formed during the SF_6/CH_4 etching process could cause bad wettability. X-ray photoelectron spectroscopy (XPS, performed by Markus Sauer, AIC, TU Wien) revealed negligible amounts of C-F containing species (0.05 %). Solely 13 - 14 % carbon was detected, which is typically found at surfaces if left at ambient conditions. Therefore, the XPS results contradicted the hypothesis and surfaces can be considered clean. To improve the coating homogeneity, dummy waveguide structures were placed at each side

Die approbierte gedruckte Originalversion dieser Dissertation ist an der TU Wien Bibliothek verfügbar.
The approved original version of this doctoral thesis is available in print at TU Wien Bibliothek.
TU Bibliothek Your knowledge hub WIEN

of the waveguide. As shown in **Figure 3.14**, one layer obtained by spin coating almost planarized 1 µm high waveguide structures. As trenched structures, *i.e.,* waveguide structures with just material etched next to the waveguide in contrast to stand alone waveguides (see **Figure 3.16**), seemed to give the most promising results, new dummy structures were designed and coated with three layers of CTAB 3d hexagonal films and subsequently treated with HMDS in acetone. Thereby, fully covered structures were obtained.

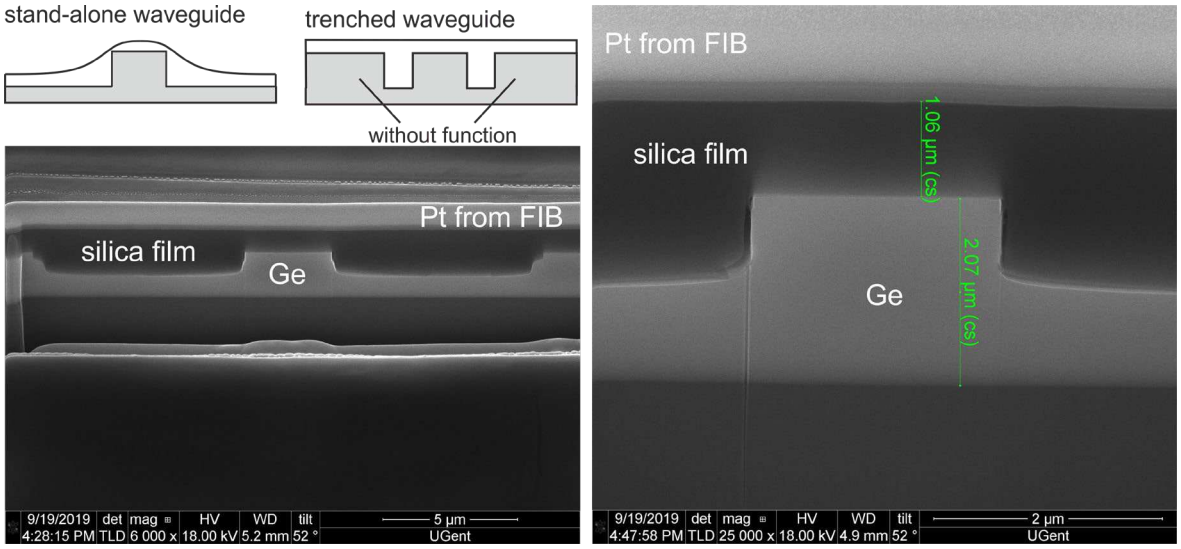

Figure 3.16: Coating of trenched structures: (right, top) schematic representation of stand-alone waveguides as shown in previous figures and trenched structures. (Right) SEM image of FIB cross section of coated trenched structures and corresponding zoom (left).

3.3.2 IOCs for Photothermal Spectroscopy

The following results were obtained in collaboration with Anton Vasiliev, IMEC/Ghent University.

Silicon-on-Insulator IOCs for photothermal spectroscopy in the wavelength range of 3.3 µm,[45] were provided by IMEC and were coated with one layer of CTAB 3d hexagonal film. Transparent films (see microscopy image in **Figure 3.17**) that fully cover the ring resonator structures were obtained (compare FIB cross section).

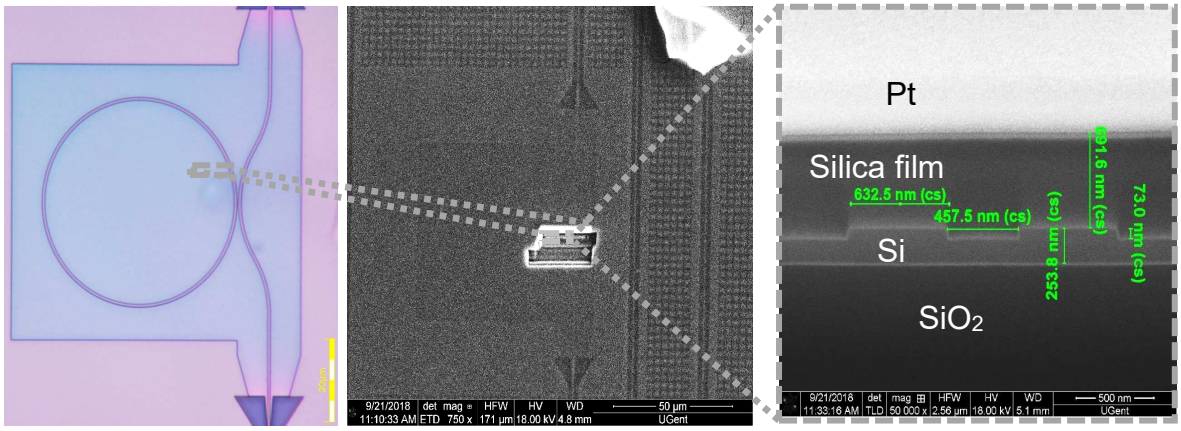

Figure 3.17: Mesoporous silica coating on top of the ring resonator on photothermal chip with SEM zooms and FIB cross section.

Die approbierte gedruckte Originalversion dieser Dissertation ist an der TU Wien Bibliothek verfügbar.
The approved original version of this doctoral thesis is available in print at TU Wien Bibliothek.
TU Bibliothek Your knowledge hub WIEN

First tests were performed with toluene and *n*-hexane vapors showing high enrichment factors. However, the project was not continued as even calcined films show too high background absorption in the used spectral region (due to Si-OH bands at 3200 cm^{-1}).

3.3.3 IOCs for Raman Spectroscopy

The following results were obtained in collaboration with Haolan Zhao, IMEC/Ghent University.

IMEC is developing SiN waveguides for evanescent field Raman spectroscopy,[198] which were also coated with mesoporous silica. As the depth of penetration of the evanescent wave of the NIR laser used for this IOCs (785 nm) is considerably smaller (ca. 100 nm), here, mesoporous silica films with higher ethanol dilution of the used sol for spin coating (volumetric ratio sol:ethanol = 1:2) was used to prepare 200 nm films. As shown in in the FIB-SEM image in **Figure 3.18**, trenches between the SiN waveguides are filled with mesoporous silica.

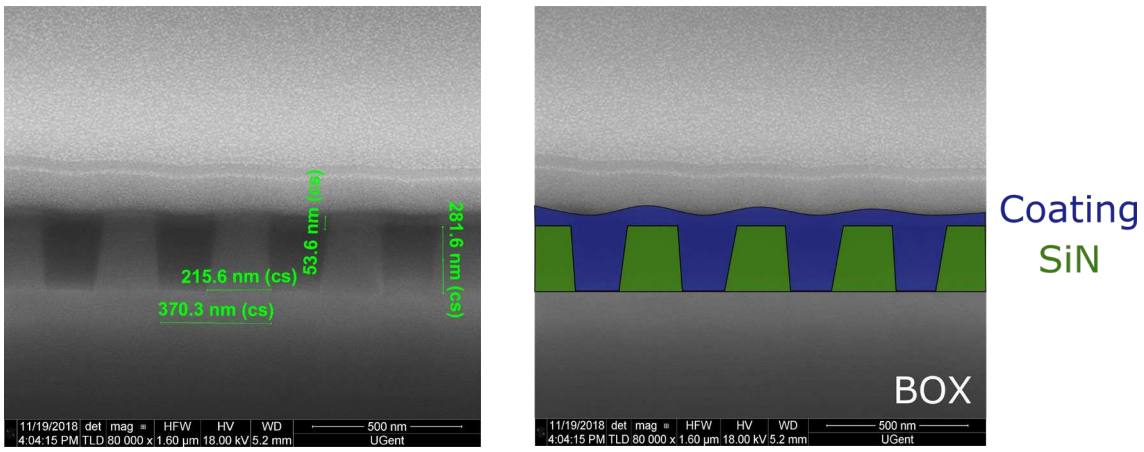

Figure 3.18: Mesoporous silica coating on top of the SiN Raman waveguides investigated by SEM as FIB cross section. BOX… buried oxide.

XRD patterns of coated chips showed the same reflection as obtained on planar surfaces indicating highly ordered films. Note that films were also successfully deposited on gold-coated chips.

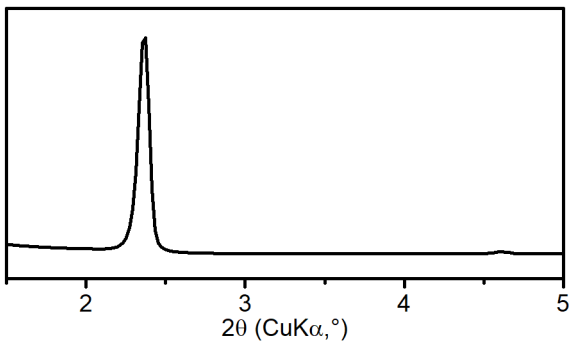

Figure 3.19: XRD pattern of 3d hexagonal CTAB films on Raman IOCs.

The coated IOCs were used for VOC gas-phase sensing and ion-exchange applications. The latter was achieved by introducing a SO_3^--moiety into the silica film.[198]

Die approbierte gedruckte Originalversion dieser Dissertation ist an der TU Wien Bibliothek verfügbar.
The approved original version of this doctoral thesis is available in print at TU Wien Bibliothek.
TU Bibliothek Your knowledge hub WIEN

3.3.4 Coating of Monolithic Laser Chips

The following results were obtained in collaboration with Borislav Hinkov and Florian Pilat, TU Wien.

Recently, QCLs were integrated together with a quantum cascade detectors and plasmonic waveguides on one chip for lab-on-a-chip applications.[37] Some of these chips were provided and coated with mesoporous silica films.

Here, the grooves of the plasmonic waveguides between the laser and detector are ca. 6 µm deep, which complicate full coverage, especially close to the laser and detector ridge. First coating tests were performed on broken chips. It was found that upon surfactant removal, the thick region starts to crack with the standard CTAB 3d hexagonal sol composition. To overcome this, MTES was introduced into the solution (not highly ordered films were thereby obtained, following the composition as given in section 2.3.3.4). Furthermore, experiments employing (3-mercaptopropyl)-trimethoxysilane were performed to enhance compatibility between the gold-coated waveguide and the silica film. The resulting coated chip is shown **Figure 3.20**. Here, also FIB-SEM measurements were performed and revealed good coverage at the waveguide and only minor detachment at the laser and detector ridge.

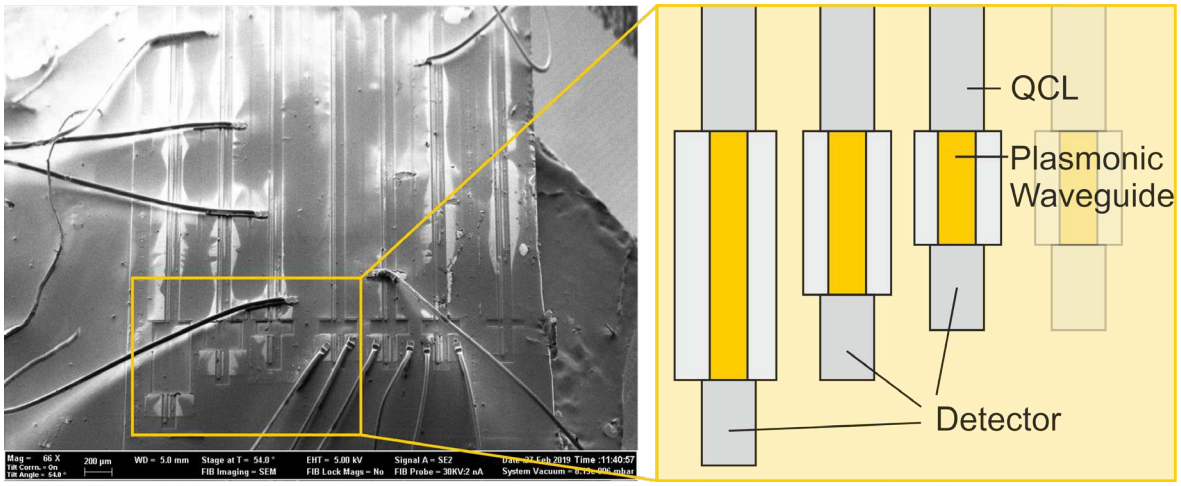

Figure 3.20: SEM image of mesoporous silica coating (TEOS:MTES = 50:50) on top of the monolithic chips shows only minor defects and smoothly covers the surface. (Right) Schematic representation of the chip.

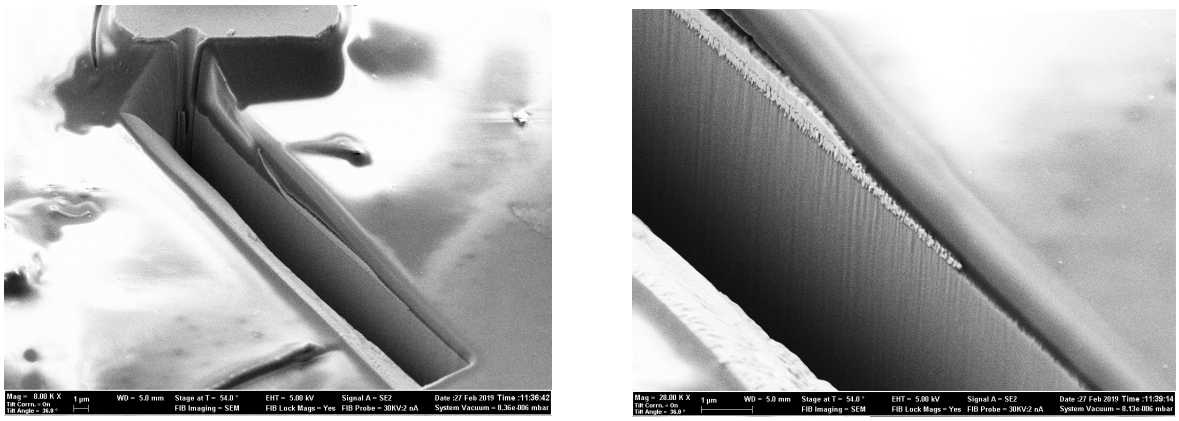

Figure 3.21: FIB-SEM images of mesoporous silica coating on top of the monolithic chip. The FIB cut was done perpendicular to the plasmonic waveguide in the middle between laser and detector.

Die approbierte gedruckte Originalversion dieser Dissertation ist an der TU Wien Bibliothek verfügbar.
The approved original version of this doctoral thesis is available in print at TU Wien Bibliothek.
TU Bibliothek Your knowledge hub WIEN

3.4 Nanoimprinting

The following results were obtained in collaboration with Prof. David Grosso, Aix-Marseille Université; and Nuria Teigell-Beneitez and Jeroen Missinne, IMEC Ghent University

Recently, Prof. Grosso and co-workers reported a Soft-Nano-Imprint-Lithography (soft-NIL) approach to pattern different metal oxide xerogels (hybrid SiO_2, TiO_2, Y-ZrO_2, Al_2O_3).[188] During my research stay in Prof. Grosso's group in January 2019, I tested if it is possible to use soft-NIL to pattern porous waveguide structures.

3.4.1 Considerations for Porous Waveguides

In contrast to the approach in the H2020 Aquarius project, here, the waveguides are porous themselves and no enrichment cladding would be required. To generate the necessary refractive index contrast between bottom cladding and porous waveguide, it was envisioned to use a mesoporous silica film as layer between the waveguide structure and the substrate *e.g.* Si or Ge, compare **Figure 3.22**. Furthermore, refractive index data for several dense oxides were compiled from refractiveindex.info.[10]

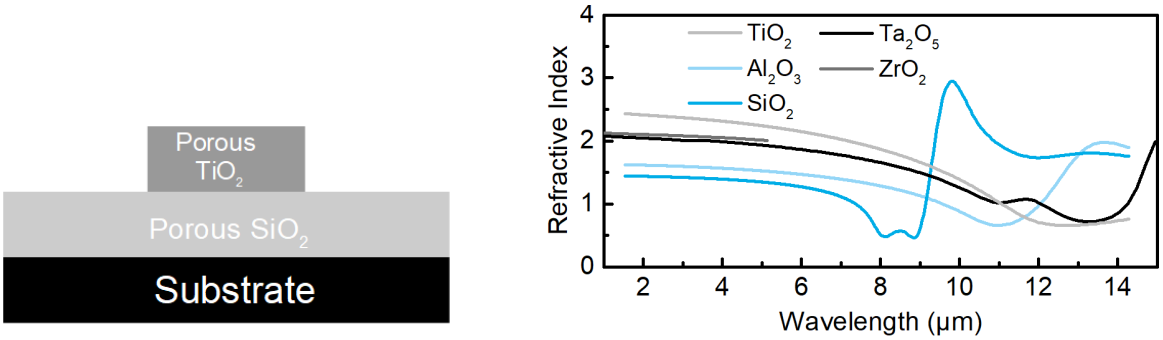

Figure 3.22: (Left) Schematic of soft-Nil printed waveguide structures on porous SiO_2 layer that serves as low RI material for an *e.g.* porous TiO_2 waveguide. (Right) Refractive index spectra of different dense oxides.[10]

The refractive index of porous oxides can be retrieved using the *Bruggeman* effective medium approximation model:[199–201]

$$f_{metaloxide}\frac{n^2_{metaloxide}-n^2_{metaloxide,porous}}{n^2_{metaloxide}+2n^2_{metaloxide,porous}}+f_{air}\frac{n^2_{air}-n^2_{metaloxide,porous}}{n^2_{air}+2n^2_{metaloxide,porous}}=0 \qquad (3.4)$$

where f are the relative volumetric fractions.

Furthermore, the transmission data for some metal oxides for a 100 µm thick sample was retrieved from refractiveindex.info.[10] From these data and using $T = 10^{-A}$, with transmission T and Absorbance A [A.U. = 10 dB], the losses of TiO_2 were calculated for different wavelengths: 36 dB/cm at 1.67 µm, 98 dB/cm at 3 µm and 138 dB/cm at 3.5 µm. These spectral regions were chosen, as *e.g.* BTEX show strong bands in these regions. Due to the high absorbance of TiO_2 for longer wavelengths (> 4 - 5 µm), this region cannot be accessed with TiO_2. Although the losses are high, this needs to be related to dense waveguides as planned in the H2020 Aquarius project, where only ca. 1 % of the intensity of the light can interact with the sample outside the waveguide. If the analyte is adsorbed into the waveguide

Die approbierte gedruckte Originalversion dieser Dissertation ist an der TU Wien Bibliothek verfügbar.
The approved original version of this doctoral thesis is available in print at TU Wien Bibliothek.
TU Bibliothek Your knowledge hub WIEN

and therefore allows for quasi transmission measurements as in the case of porous waveguides, ca. 100 times more interaction is theoretically possible, hence, the waveguides can be 100 times shorter. If the waveguide is shortened by 100 times, we end up with losses of 0.98 dB/100 µm for $\lambda = 3$ µm and 1.38 dB/100 µm for $\lambda = 3.5$ µm for the same effective interaction length as solid waveguides.

3.4.2 Experimental Results

IMEC provided two Si masters, *i.e.,* the stencil for the PDMS molds, with 2 cm long structures with 790 nm and 1550 nm height and different widths ranging from 5 - 100 µm and different distances between these structures. These molds were brought to Prof. Grosso's lab and soft-NIL experiments with methylated SiO_2 and TiO_2 were performed (see section 2.3.6 for experimental details).

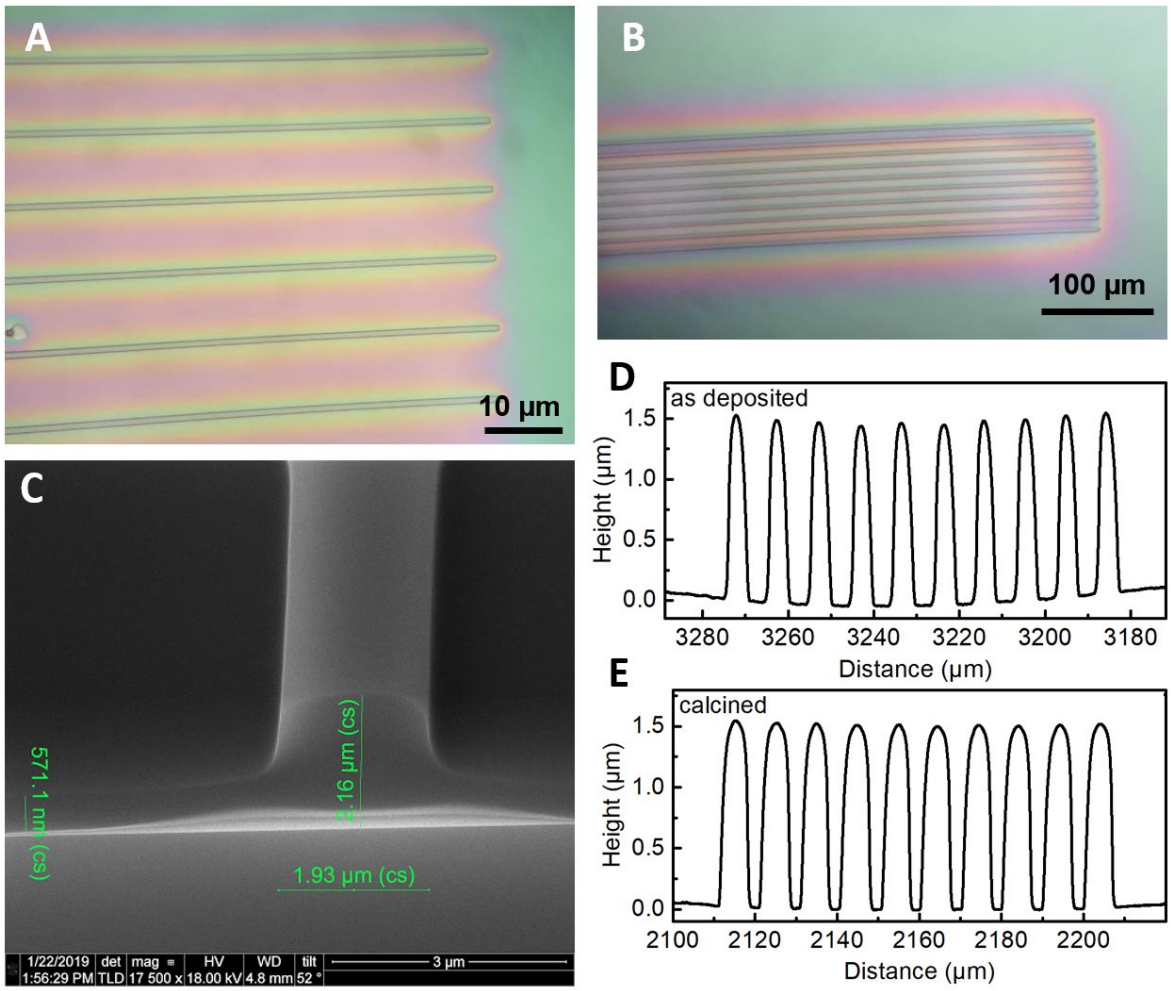

Figure 3.23: Characterization of soft-NIL samples using methylated silica: A and B: microscopy images, C: SEM picture, D and E: profilometer measurements of silica structure as deposited and a calcined methylated silica structure. Note that the difference of structure width results from a different position of the sample on the PDMS stamp.

Light-microscope images of the resulting structures are given in **Figure 3.23 A-B** and show well defined structures as expected from the master. As visible from the greenish background

Die approbierte gedruckte Originalversion dieser Dissertation ist an der TU Wien Bibliothek verfügbar.
The approved original version of this doctoral thesis is available in print at TU Wien Bibliothek.
TU Bibliothek Your knowledge hub WIEN

around the structures and also seen in the SEM image (Figure 3.23 C), a ca. 570 nm thick film is visible below the structures, which stems from excessive pre-deposited film not fully absorbed into the PDMS mold. Furthermore, the obtained structures were characterized using profilometry and showed the expected height of 1500 nm for obtained structures directly after deposition (as deposited) and after calcination (calcined), respectively, (**Figure 3.23 D-E**). The same experiments were performed using TiO_2. Here, obtaining structures with the given high aspect ratio was more difficult, as the shrinkage of TiO_2 upon thermal treatment is more pronounced compared to SiO_2, especially with respect to methylated SiO_2. After calcination at 350 °C, the thickness of the TiO_2 films is reduced to 30 - 40 % of its initial value. This led to cracked and detached structures if Si substrates have been used, but if microscope glass slides had been used, the structures persisted and were also analyzed using profilometry. Profiles are given in **Figure 3.24** and show ca. 500 nm high structures that deform in case of wider structures.

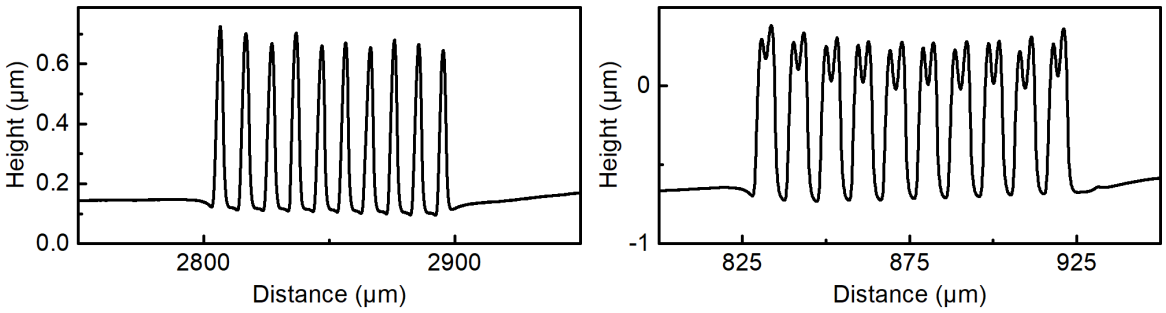

Figure 3.24: Profilometer measurements of calcined TiO_2 structures on Si (left) and glass (right). Note that the difference of structure width results from a different position of the sample on the PDMS stamp.

Finally, micro transfer molding, *i.e.,* filling the cavities of the PDMS stamp using a just deposited film, careful removal of the stamp and placing it on an empty surface, was tested with the same molds. Theoretically, by doing so, the film below the structures should be suppressed. The thereby obtained height profile is given in **Figure 3.25** and shows TiO_2 structures after calcination. The height of 210 nm corresponds to 27 % of the initial height of the used PDMS stamp.

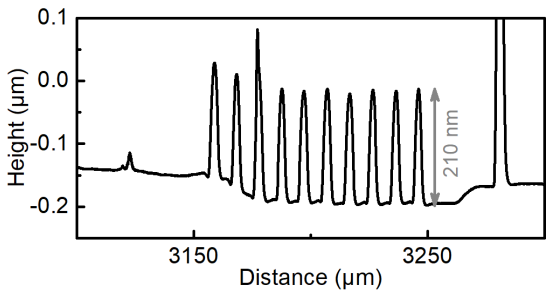

Figure 3.25: Characterization of micro transfer molded TiO_2 on glass.

In conclusion, structures of up to 1.5 µm height were imprinted over long ranges. Therefore, the soft-NIL approach is a promising tool toward porous waveguides.

Die approbierte gedruckte Originalversion dieser Dissertation ist an der TU Wien Bibliothek verfügbar.
The approved original version of this doctoral thesis is available in print at TU Wien Bibliothek.
TU Bibliothek WIEN Your knowledge hub

Die approbierte gedruckte Originalversion dieser Dissertation ist an der TU Wien Bibliothek verfügbar.
The approved original version of this doctoral thesis is available in print at TU Wien Bibliothek.

Die approbierte gedruckte Originalversion dieser Dissertation ist an der TU Wien Bibliothek verfügbar.
The approved original version of this doctoral thesis is available in print at TU Wien Bibliothek.

Chapter 4 Mesoporous Films coated on ATR Crystals for Quantitative Analysis

Mesoporous silica coated ATR crystals were used for different sensing schemes that will be presented in this chapter. Quantification in all of these is based on Lambert-Beer's law and hence the effective path length d_e within the mesoporous film. The retrieval of the latter from theory and its experimental corroboration of the obtained values for d_e will be discussed in **section 4.1**. Then, the application for sensing in aqueous phase on the example of the enrichment of hydrocarbons (**section 4.2**) and ions (**section 4.3**) will be shown. Lastly, the application of mesoporous silica as enrichment layer for volatile organic compounds from gas phase is presented in **section 4.4**.

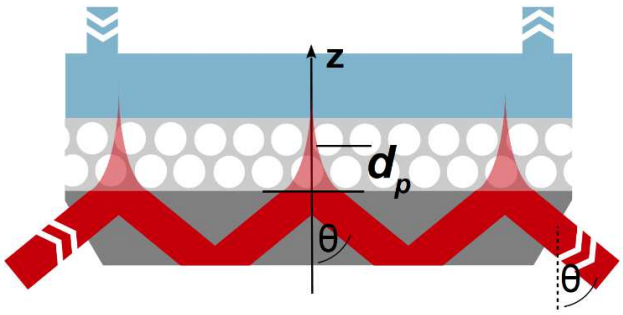

Figure 4.1: Si-ATR crystal (dark gray) coated with mesoporous silica film. IR absorbance takes place within the evanescent field (light red), which extends beyond the crystal into the film and, depending on the film thickness, into the sample solution flushed over the film.

4.1 Determination of the Effective Path Length of the Blank Si ATR Crystal

The data gained from the adsorption experiments via ATR spectroscopy are given in absorption units (A.U.) or band area (A.U. cm^{-1}). For quantitative analysis and for deriving enrichment factors of each film, translation into concentration is necessary. The determination of absolute adsorbed analyte concentrations in, *e.g.*, milligrams of analyte per mass or volume adsorbate in the mesoporous films demands theoretical considerations:

As stated in section 1.1.2 and 1.1.3, the concentration of the analyte is directly proportional to the absorbance A according to Lambert-Beer's law. The path length applies to transmission

measurements and corresponds to the effective path length d_e in ATR spectroscopy, which is defined as "the thickness of a film of the sample material that would give the same absorbance for transmission at normal incidence as that obtained in the ATR experiment"[5,9] (see section **1.1.3** for equations). For multi-reflection ATR crystals, as used in this thesis, the absorbance increases linearly with the number N of active bounces of the ATR element:

$$A = \varepsilon \cdot c \cdot d_e \cdot N \tag{4.1}$$

For a blank Si ATR crystal with $N = 14$, $\theta = 55°$, $n_1 = 3.42$,[10] $n_2 = 1.33$ (water)[11], and $\lambda_0 = 6.1$ µm, equations (1.21)-(1.23) yields $N \cdot d_e$ (1640 cm^{-1}) = 4.23 µm. An experimentally determined value for d_e was obtained by comparing the intensity of the water absorption band at 1640 cm^{-1} measured using a transmission cell with defined path length and the ATR crystal. This led to an experimentally determined d_e of 4.2 µm (0.3 µm for one bounce), which is in good agreement with the theoretically obtained d_e. From these findings, the setup was considered capable of quantitative analysis based on a theoretical understanding of the underlying processes. However, for coated ATR crystals with finite thickness, further considerations are necessary.

4.1.1 Theoretical Evaluation of the Effective Path Length within the Mesoporous Film

For coated ATR crystals, the definition of the effective path length necessary for retrieving adsorbed concentrations and from these also absorbed amounts must take into account that the evanescent field extends beyond the thickness of the film (see **Figure 4.1**). Assuming that the IR absorption of the analyte in the bulk liquid covering the film is negligible, hence the major fraction of the evanescent field is covered by the coating thickness, $d_{e,film}$ defined by **equation (4.2)** which includes the fraction s of the intensity of the evanescent field that is confined within the film. Is is only this fraction of the evanescent field that can be absorbed by adsorbed molecules:

$$d_{e,film} = d_e \, N \, s \tag{4.2}$$

$$s = \frac{\int_0^{th} I(z)dz}{\int_0^{\infty} I(z)dz} = 1 - e^{\frac{-2\,th}{d_p}} \tag{4.3}$$

$$I(z) = I_0 \, e^{\frac{-2\,z}{d_p}} \tag{4.4}$$

where I_0 is the incident power, th is the film thickness, z is the distance from the crystal surface, and d_p is the depth of penetration, which is defined as the distance from the ATR crystal at which the electric field falls to $1/e$ of the electric field at the interface (see section 1.1.3 for further details). Note that even though d_p and d_e are both smaller than the film thickness, a fraction of the evanescent field reaches beyond the film and causes IR absorption of the bulk liquid. As the decay of the evanescent field is also dependent on the refractive indices of both materials, and in the case of a coated ATR crystals it depends on three indices

Die approbierte gedruckte Originalversion dieser Dissertation ist an der TU Wien Bibliothek verfügbar.
The approved original version of this doctoral thesis is available in print at TU Wien Bibliothek.
TU Bibliothek Your knowledge hub WIEN

(ATR crystal, film and layer above the film), the progress of the fall depends also on the water or air layer on top of the film. However, due to the similar refractive indices of water and silica and as the majority of the film covers the evanescent field, no further calculations that take this into account were performed.

When considering a refractive index $n_2 = 1.26–1.37$ for bulk silica[10] (instead of water for the calculations on blank ATR crystals in the previous section), the fractions of the evanescent wave within the film and their corresponding corrected effective path lengths $d_{e,film}$ are given in **Table 4.1**.

Table 4.1: Calculated parameters and effective path lengths within the mesoporous films. [a] depth of penetration, [b] effective path length, [c] fraction of the effective path length within the film, [d] effective path length within the film. $\boldsymbol{\theta} = 55°$, n(Si ATR) = 3.42.

	Wavelength $\boldsymbol{\lambda_0}$ **[µm]**	$\boldsymbol{d_p}$[a] **[µm]**	$\boldsymbol{d_e}$[b] **[µm]**	$\boldsymbol{s}$[c]	$\boldsymbol{d_{e,film}}$[d] **[µm]**
CTAB 3d hexagonal film	6.10	0.388	0.278	0.89	3.45
th = 425 nm	4.45	0.293	0.233	0.95	3.09
CTAB cubic film	6.10	0.388	0.278	0.92	3.59
th = 500 nm	4.45	0.293	0.233	0.97	3.16

Note that for these calculations, the refractive index of bulk silica was used. Later, in section 5.1.2, it will be shown that mesoporous silica has a lower refractive index due to its porosity. The differences between $n_2 = 1.26$ and $n_2 = 1.14$ yield a difference in d_p of 0.009 µm, and a difference for $d_{e,film}$ of 0.52 µm (13 %). This difference was considered in the following section.

4.1.2 Experimental Verification of the Effective Path Length

The theoretically obtained effective path lengths as discussed in the previous section were compared with absorbance measurements of water and nitrile rubber pressed on blank and coated ATR crystals. Values retrieved from water spectra on coated and blank Si ATR crystals (obtained from the spectra in **Figure 3.11**) correspond to 18 % and 10 % of the absorption taking place from the sample located above the film for the CTAB 3d hexagonal film and CTAB cubic film, respectively. Theoretical values were calculated to be 12 % and 8 %, respectively. The higher values were attributed to a small amount of water having penetrated the film (despite being modified with HMDS). In contrast, the rubber will not penetrate the film. Therefore, the nitrile rubber is sensed exclusively in the small fraction of the evanescent field that extends beyond the film. For the C≡N mode at 2230 cm^{-1}, this fraction $(1 - s)$, as obtained using **equation (4.2)**, is 5% and 3%, respectively, for the 3d hexagonal and cubic films. Consequently, the absorbance of the C≡N band on the coated ATR crystals is expected to be reduced to $1 - s$ relative to the absorbance on uncoated crystals. The experimentally obtained absorbance fractions of 5.4 ± 0.8% and 4.3 ± 0.5% for CTAB 3d hexagonal and cubic films, respectively, agree well with the theoretical projections. Therefore, one can reasonably assume that the theoretically obtained effective path lengths $d_{e,film}$ and hence the

Die approbierte gedruckte Originalversion dieser Dissertation ist an der TU Wien Bibliothek verfügbar.
The approved original version of this doctoral thesis is available in print at TU Wien Bibliothek.
TU Bibliothek Your knowledge hub WIEN

retrieved concentrations of adsorbed analytes are in good agreement with the actual values.

4.1.3 Retrieval of Analyte Concentrations inside the Mesoporous Films

A verified $d_{e,film}$ allows for inserting into Lambert-Beer's law if knowing the decadic molar absorption coefficients ε of the respective analyte. For example, ε of benzonitrile and valeronitrile (see section 4.2.2 for further details) were determined by IR transmission measurements to be $\varepsilon = 2350$ A.U. L cm^{-2} mol^{-1} and $\varepsilon = 1388$ A.U. L cm^{-2} mol^{-1} for the C≡N mode of benzonitrile and valeronitrile, respectively.

Concentrations of the analyte within the film were obtained by inserting ε and $d_{e,film}$ into Lambert-Beer's law; the results of concentration series are depicted in **Figure 4.2**.

As for solutions measured on uncoated ATR crystals, the derived theory yields analyte concentrations with respect to the matrix volume. For analytes present within the adsorption layer, this film constitutes the matrix, and hence concentrations are given relative to the volume of the adsorbate *i.e.,* mol per volume silica film. The absolute mass of adsorbed analyte can be retrieved by multiplication of the obtained concentration with the volume of the film, which based on the known film thickness and the probed area is $8.5 \cdot 10^{-5}$ cm^3 and $1 \cdot 10^{-4}$ cm^3 for the CTAB 3d hexagonal and cubic film, respectively. From that, the absolute mass of benzonitrile adsorbed from a 100 mg L^{-1} solution into the film was determined to be 7.4 mg cm^{-3} (0.63 µg per film) and 9.0 mg cm^{-3} (0.88 µg per film) for the 3d hexagonal film and the cubic film, respectively.

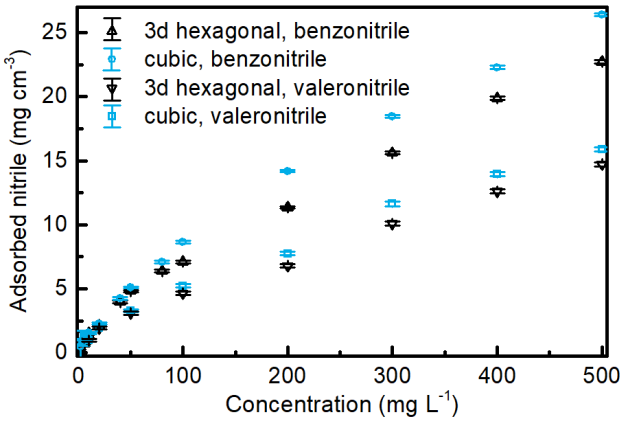

Figure 4.2: Adsorption isotherms of benzonitrile and valeronitrile solutions on 3d hexagonal and cubic mesoporous silica films obtained from Lambert-Beer's law.

These calculations are the basis for all further quantitative considerations in this thesis.

Die approbierte gedruckte Originalversion dieser Dissertation ist an der TU Wien Bibliothek verfügbar.
The approved original version of this doctoral thesis is available in print at TU Wien Bibliothek.
TU Bibliothek Your knowledge hub WIEN

4.2 Enrichment of Hydrocarbons from Aqueous Phase

Within the framework of the H2020 project Aquarius, the enrichment of hydrocarbons from aqueous phase was targeted. This was realized by firstly analyzing the fingerprint region of the IR spectra of aliphatic and aromatic hydrocarbons with special focus on the spectral region 1600 - 1300 cm^{-1} as the used Aquarius EC-QCL emits there. In a next step, model compounds with isolated bands were used for first enrichment experiments using mesoporous silica. After a successful proof-of principle, various analytes were enriched from aqueous phase.

4.2.1 Discrimination of Hydrocarbons in the IR Spectra

Different hydrocarbons have been adsorbed into mesoporous silica within this section. Therefore, it is worth taking a closer look at their spectral features. In the following subsection, spectra of aliphatic and aromatic hydrocarbons in the fingerprint region between 1600 - 1300 cm^{-1} will be discussed.

Different **isomers of octane** were analyzed *via* FTIR ATR spectroscopy. The spectra are depicted in **Figure 4.3**. The straight-chain molecule *n*-tetradecane shows absorptions that correspond to asymmetric and symmetric aliphatic -CH_2- vibration and -CH_3 deformation vibrations (1457 and 1378 cm^{-1}, respectively). All branched molecules (2-methylheptane, 2,2-dimethylhexane and isooctane) show additional absorptions: The isopropyl-moiety of 2-methylheptane has a characteristic "doublet" at 1384 and 1365 cm^{-1} with similar intensity. The *tert*-butyl group of 2,2-dimethylhexane shows an absorption doublet with an intensity ratio of 1:3 at 1393 and 1365 cm^{-1}. Since isooctane consists of an isopropyl- and a *tert*-butyl-group, both previously mentioned vibrations overlap at 1365 cm^{-1}. Since isooctane has no aliphatic methyl-group, no peak at 1379 cm^{-1} is visible.

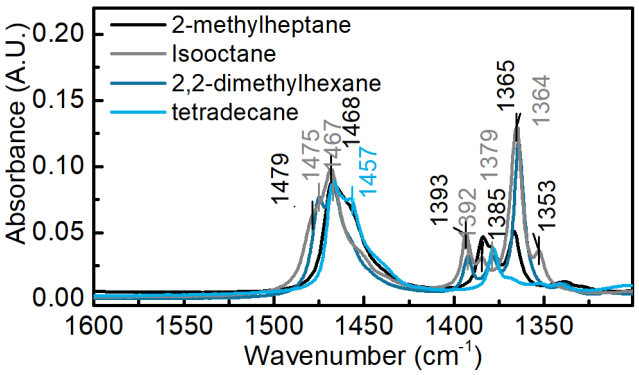

Figure 4.3: FTIR-ATR spectra of octane isomers and *n*-tetradecane recorded on a single bounce ATR unit.

It is well known, that substitution patterns of di-substituted benzenes lead to different absorption patterns in the region below 1000 cm^{-1} with high absorptivity, which has also been intensively exploited for coated ATR crystals in literature (compare section 1.4.1.1). Additionally, the skeletal vibrations involving the C=C stretch vibration modes at ~1500 cm^{-1} are influenced by the substitution patterns and the bonded groups. This spectral region of

Die approbierte gedruckte Originalversion dieser Dissertation ist an der TU Wien Bibliothek verfügbar.
The approved original version of this doctoral thesis is available in print at TU Wien Bibliothek.
TU Bibliothek Your knowledge hub WIEN

xylene isomers and toluene is depicted in **Figure 4.4**. The skeletal ring vibration modes shift to lower wavenumbers for *o*- and *m*-xylene (1492 and 1495 cm^{-1}, respectively), while *p*-xylene has its skeletal ring vibration at 1516 cm^{-1}. Furthermore, shifts in the symmetric methyl deformation mode at ~1380 cm^{-1} are visible.

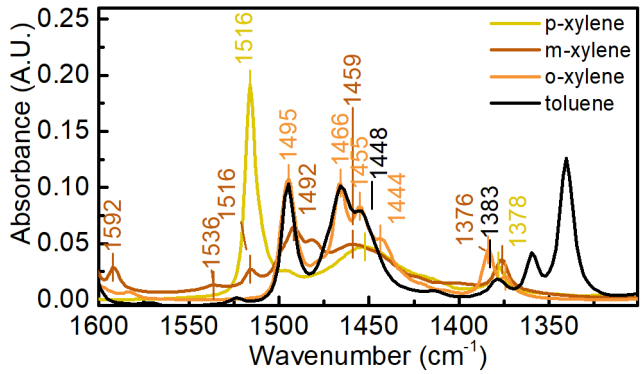

Figure 4.4: FTIR-ATR spectra of xylene isomers and toluene recorded on a single bounce ATR unit.

A similar behavior is observed for the tri-substituted benzenes 1,2,3-, 1,2,4- and 1,3,5-trimethylbenzene (see **Figure 4.5**): The skeletal ring vibrations of 1,2,3- and 1,3,5-trimethylbenzene are shifted to 1474 and 1471 cm^{-1}, respectively while the ring vibration of 1,2,4-trimethylbenzene is observed at 1505 cm^{-1}. It is interesting to note that the strong bands between 1350 - 1530 cm^{-1} corresponding to substitute aromatic hydrocarbons are clearly set apart, hence could serve as a bands for differentiation between aromatic hydrocarbons in complex sample mixtures. This will be employed in section 4.2.5 and 4.4.

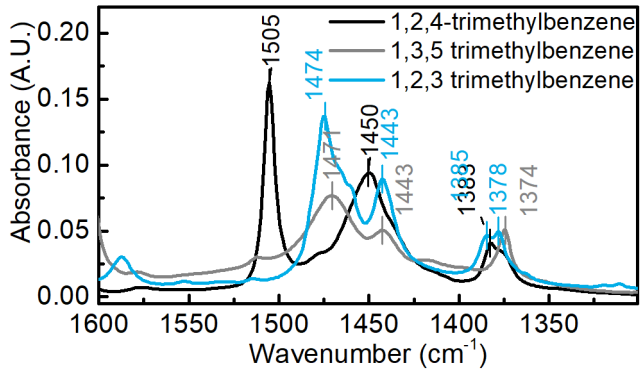

Figure 4.5: FTIR-ATR spectra of different trimethylbenzene isomers recorded on a single bounce ATR unit.

4.2.2 Proof-of-Principle using Benzonitrile and Valeronitrile

For the first enrichment experiments, analytes with isolated spectral features in the region of the highest transmission of the Si ATR crystals were selected. The Si ATR crystal provides maximum transmission in the range of 2000 - 2300 cm^{-1} as illustrated in the single channel spectrum in **Figure 4.6, top.** Within this range, the C≡N vibrational mode of benzonitrile and valeronitrile are found between 2260 and 2220 cm^{-1}, the C≡N vibrational mode of benzonitrile and valeronitrile are found at 2238 cm^{-1} and 2257 cm^{-1}, respectively (compare **Figure 4.6**). Due to these spectral features and because they are still slightly soluble in water,

Die approbierte gedruckte Originalversion dieser Dissertation ist an der TU Wien Bibliothek verfügbar.
The approved original version of this doctoral thesis is available in print at TU Wien Bibliothek.
TU Bibliothek Your knowledge hub WIEN

these substances served as first analytes to prove the principle of using mesoporous silica films for enrichment and sensing.

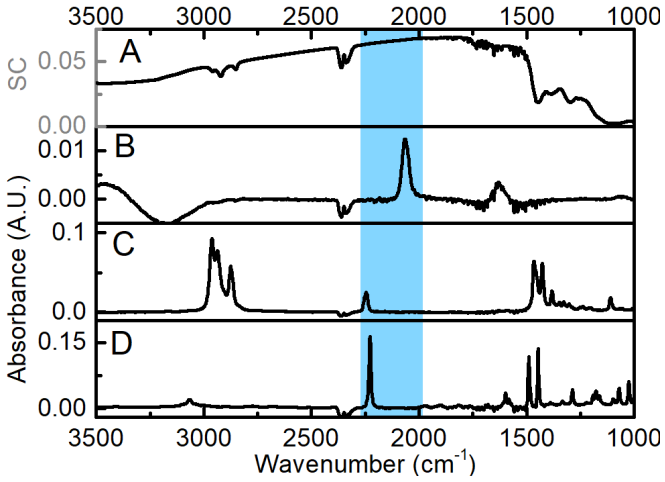

Figure 4.6: (A) Single channel spectrum of uncoated Si ATR crystal and FTIR-ATR spectra of (B) aqueous NaSCN solution (10 g L^{-1}, SCN band at 2010 cm^{-1}), (C) pure valeronitrile (C≡N mode at 2257 cm^{-1}) and (D) pure benzonitrile (C≡N mode at 2238 cm^{-1}).

In addition to organic molecules, aqueous sodium thiocyanate solution (–SCN vibration mode at 2010 cm^{-1}) was applied on uncoated ATR crystals to act as a tracer substance. This tracer aids in determining the time needed to completely exchange the flow cell volume (see subsection 4.2.2.1). This detour was necessary because even the concentrations of saturated benzonitrile and valeronitrile solutions were too low to be detected on uncoated ATR crystals due to the low solubility/absorption coefficients of these compounds.

4.2.2.1 Adsorption/Desorption Studies

The analyte solutions were applied via an automated flow system consisting of a peristaltic pump and a 10-way selection valve (see Figure 2.7 in the section 2.2.1 for further details) that allowed for automated sample selection and reproducible sample injection.

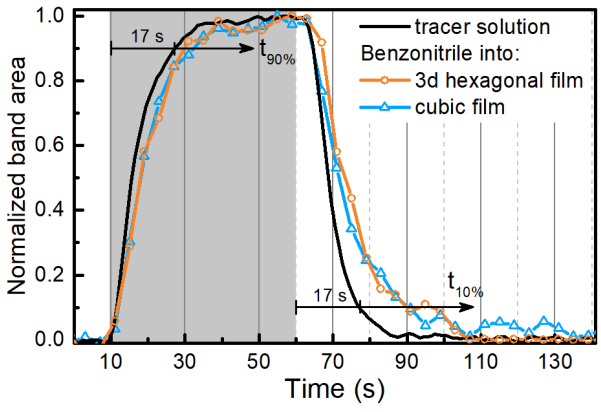

Figure 4.7: Adsorption/desorption profiles of 100 mg L^{-1} benzonitrile onto mesoporous silica films with 3d hexagonal and cubic pores. For comparison, the temporal concentration profile of the NaSCN tracer solution was recorded on uncoated Si ATR crystals and serves as indicator of the actual analyte dispersion in the flow cell. The gray box indicates the time period during which sample was pumped through the sample cell.

To study the speed of adsorption and desorption of benzonitrile on/from the silica film, a defined sequence of water, analyte in water, and water was applied in an automated way while recording one spectrum per second. To this end, a peristaltic pump was placed downstream of the flow cell to draw the sample solutions through the flow cell at 2 mL min^{-1} for 2 min

Die approbierte gedruckte Originalversion dieser Dissertation ist an der TU Wien Bibliothek verfügbar.
The approved original version of this doctoral thesis is available in print at TU Wien Bibliothek.
TU Bibliothek Your knowledge hub WIEN

(placing the pump downstream was necessary to avoid contact of the analyte solution with the polymer tubing of the peristaltic pump which could have caused loss of analyte due to the absorption into the tubing material). Either 100 mg L^{-1} benzonitrile solution or 10 g L^{-1} NaSCN solution were used as analytes. **Figure 4.7** shows the temporal progression of the integrated areas of the C≡N and SCN bands, respectively. An important step in this experimental setup is distinguishing the actual adsorption/desorption process from delays caused by the finite response time of the flow system (flow cell, tubing). To achieve this, a reference solution of NaSCN was applied to an uncoated ATR crystal to give information about the dwell time of the system as well as the time needed to completely exchange pure water with the analyte solution. The sample introduction step of the flow sequence is highlighted in gray in Figure 4.7. The profile depicted in Figure 4.7 shows that 90 % displacement of water by analyte solution requires $t_{90\%}$ = 17 s, and flushing pure water for analyte removal until reaching 10% of IR absorbance requires $t_{10\%}$ = 17 s. The profile of adsorption of benzonitrile into CTAB 3d hexagonal and CTAB cubic mesoporous films closely matches the profile of the NaSCN solution, and only a slight delay of 3 s ($t_{90\%}$ = 20 s) and 5 s ($t_{90\%}$ = 22 s) for $t_{90\%}$, respectively, can be observed. Desorption is significantly slower than adsorption, as indicated by the increase of $t_{10\%}$ for both films by 13 s ($t_{10\%}$ = 30 s) relative to the NaSCN reference measurement, which experienced no retention. For flow rates below 1 mL min^{-1}, slow exchange of the sample volume dominates. However, the flow rate had no effect on the absorption measured after equilibration in the range from 0.5 mL min^{-1} to 2 mL min^{-1}.

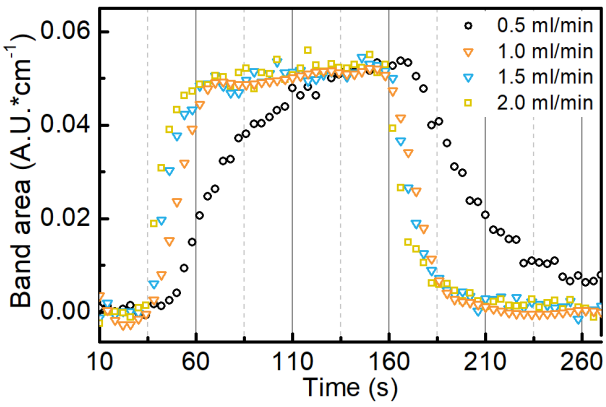

Figure 4.8: Adsorption/desorption profiles of 100 mg L^{-1} benzonitrile solution applied on a 3d hexagonal film with different flow rates.

The time profiles of integrated band areas obtained from different flow rates on the 3d hexagonal film with 100 mg L^{-1} benzonitrile solutions are given in **Figure 4.8**. As shown in this figure, for whatever flow rate between 0.5 mL min^{-1} and 2 mL min^{-1} the same absolute absorbance after 2 min of equilibrium was obtained. However, the enrichment is slower for slower flow rates, as shown in **Figure 4.9**.

All profiles, illustrate the fast adsorption of benzonitrile into mesoporous silica films that has already been concluded from batch experiments,[101] but have never been recorded *in situ*. Furthermore, both structured films are fully recovered after desorption and the IR absorbance

Die approbierte gedruckte Originalversion dieser Dissertation ist an der TU Wien Bibliothek verfügbar.
The approved original version of this doctoral thesis is available in print at TU Wien Bibliothek.
TU Bibliothek Your knowledge hub WIEN

returns to its initial value.

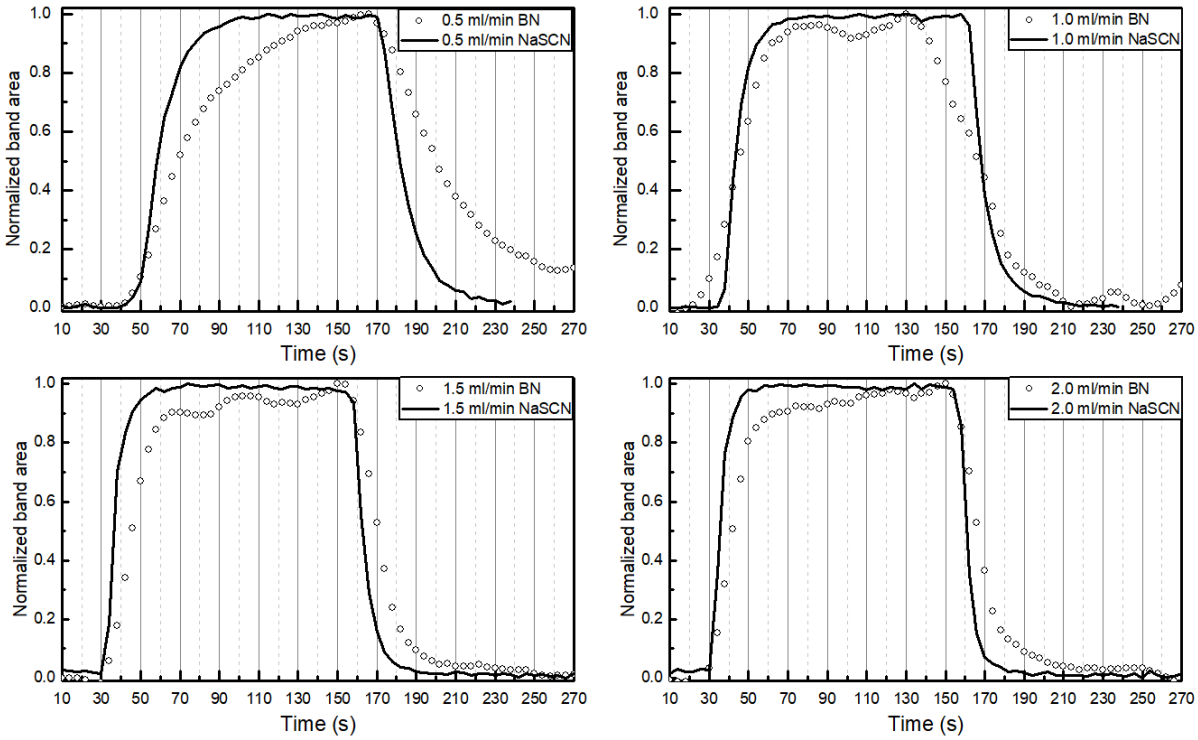

Figure 4.9: Adsorption/desorption profiles of 100 mg L^{-1} benzonitrile solution applied on a 3d hexagonal film with different flow rates. For comparison, the temporal concentration profile of the NaSCN tracer solution was recorded on uncoated Si ATR crystals and serves as indicator of the actual analyte dispersion in the flow cell.

4.2.2.2 Equilibrium Adsorption Experiments

Series of benzonitrile and valeronitrile solutions with concentrations ranging between 1 and 500 mg L^{-1} were applied in triplicate to determine the adsorption capacity of the silica films at equilibrium as well as the calibration function.

The results of three subsequent stepped concentration sequences on a CTAB 3d hexagonal film coated on an ATR crystal are given in **Figure 4.10** and show the high reproducibility of the system.

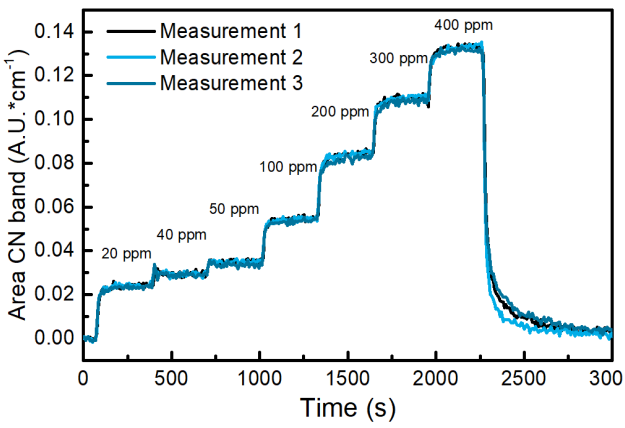

Figure 4.10: Integrated band areas for three subsequent calibration series.

Because the recorded absorbance scales linearly with the concentration of adsorbed nitriles (Lambert-Beer's law, compare 1.1.1), adsorption isotherms can be obtained directly from the

Die approbierte gedruckte Originalversion dieser Dissertation ist an der TU Wien Bibliothek verfügbar.
The approved original version of this doctoral thesis is available in print at TU Wien Bibliothek.

band areas and are depicted in **Figure 4.11**. The CTAB cubic film adsorbed more benzonitrile than the film with CTAB 3d hexagonal structure. The same behavior is observed for valeronitrile, although the band areas are smaller due to the smaller absorption coefficient of the ν–CN vibration of this molecule.

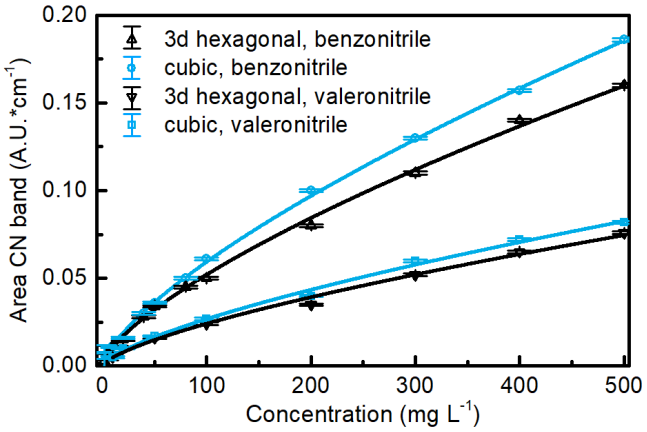

Figure 4.11: Adsorption isotherms of benzonitrile and valeronitrile solutions on 3D hexagonal and cubic mesoporous silica films obtained from CN band areas at different concentrations fitted with the Freundlich equation. The standard deviation was calculated from three consecutive measurements (section Figure 4.10 for data).

For describing adsorption processes the models of *Langmuir* and *Freundlich* are frequently used. Whereas the *Langmuir* model (**equation (4.5)**) assumes monolayer coverage, the *Freundlich* model (**equation (4.6)**) describes multilayer adsorption with decreasing adsorption enthalpy. The models are expressed as

$$q_e = \frac{q_m K_L c}{1 + K_L c} \tag{4.5}$$

$$q_e = K_F c^{\frac{1}{n_F}} \tag{4.6}$$

where q_e (A.U. cm^{-1} for data obtained from IR absorption bands; mg cm^{-3} for absolute concentrations obtained in the following section) is the amount of adsorbed analyte, q_m (A.U. cm^{-1} or mg cm^{-3}) is the maximum adsorption capacity, c is the concentration of applied analyte solutions (mg L^{-1}), K_L (cm^3 mg^{-1}) is the *Langmuir* constant, K_F (A.U. cm^{-1} [mg $L^{-1}]^{-1/n}$; or mg cm^{-3} [mg $L^{-1}]^{-1/n}$) is the *Freundlich* affinity coefficient, and n_F (unitless) is the *Freundlich* linearity index. In the presented experiments, which were performed with sample continuously flushed over the film, c is equal to the applied concentration. This is different from c in batch experiments mainly reported in literature, where adsorption reduces the concentration in the solution.

The experimental adsorption data were fitted with *Langmuir* and *Freundlich* isotherms and the obtained parameters are given in **Table 4.2**. The values of chi square (χ^2, typically used to describe the goodness of fit for non-linear functions) are lower for the Freundlich model, indicating a better fit for this isotherm for both structures.[202]

Die approbierte gedruckte Originalversion dieser Dissertation ist an der TU Wien Bibliothek verfügbar.
The approved original version of this doctoral thesis is available in print at TU Wien Bibliothek.

Table 4.2: Isotherm parameters obtained by fitting the experimental data obtained for benzonitrile and valeronitrile to the Langmuir and Freundlich models.

	Analyte	*Langmuir* fit χ^2	*Freundlich* fit χ^2	K_F [A.U. cm^{-1} (mg L^{-1})$^{-1/n}$]	n_F
CTAB 3d hexagonal film	benzonitrile	$3.5 \cdot 10^{-5}$	$6.3 \cdot 10^{-6}$	0.0021	1.44
	valeronitrile	$1.3 \cdot 10^{-5}$	$3.6 \cdot 10^{-6}$	0.0011	1.42
CTAB cubic film	benzonitrile	$1.8 \cdot 10^{-5}$	$2.4 \cdot 10^{-6}$	0.0023	1.41
	valeronitrile	$9.6 \cdot 10^{-6}$	$2.6 \cdot 10^{-6}$	0.0009	1.39

4.2.3 Different Surface Functionalization

The sensitivity can be further tuned and/or increased by a different functionalizations of the enrichment layer to target the needs of environmental samples. To this end, 3d hexagonally structured films were modified with an octyl- and a phenyl moiety (see experimental section for synthetic details).

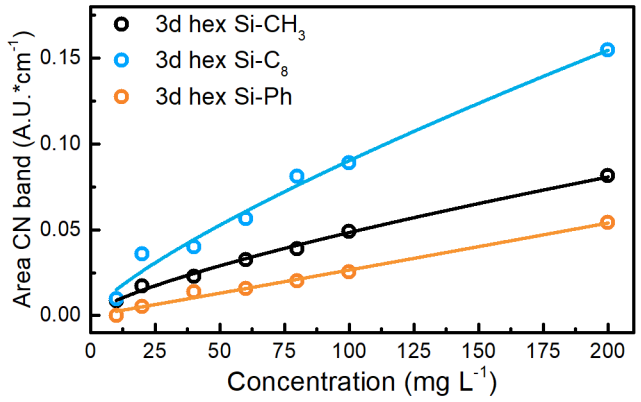

Figure 4.12: Calibration curve for CTAB 3d hexagonal films with different surface functionalization.

The calibration functions are given in **Figure 4.12** and show an increase in adsorption capacity for the octyl-functionalized film and a decrease for the phenyl-silane functionalized film.

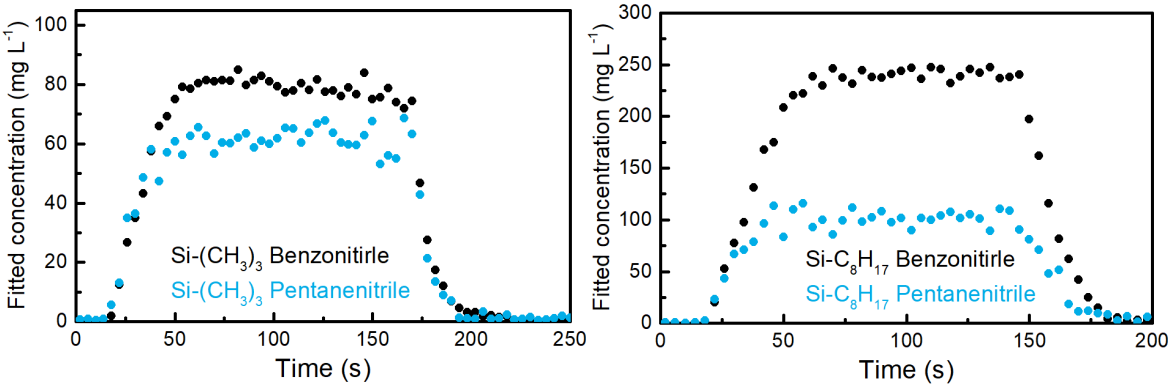

Figure 4.13: Fitted adsorption bands of 100 mg L^{-1} benzonitrile and 100 mg L^{-1} pentanenitrile solution applied to differently modified films.

Die approbierte gedruckte Originalversion dieser Dissertation ist an der TU Wien Bibliothek verfügbar.
The approved original version of this doctoral thesis is available in print at TU Wien Bibliothek.
TU Bibliothek Your knowledge hub WIEN

Furthermore, the selectivity for aliphatic and aromatic nitriles was tested by applying 100 mg L^{-1} benzonitrile and 100 mg L^{-1} pentanenitrile solutions on trimethyl- (HMDS) and octyl-functionalized films. The recorded adsorption bands were fitted with the weighted sum of pure spectra of both substances and normalized to the performance when measuring samples containing only one analyte on trimethyl-functionalized films and are given in **Figure 4.13**. Both films showed for both analytes a fast adsorption and a complete desorption. While the benzonitrile adsorption of binary standards on the trimethyl-functionalized film almost reached the same value as for standards comprising only benzonitrile, the measured absorption is enhanced by a factor of 2.5 for the octyl-functionalized film as opposed to the trimethyl-functionalized film. The adsorption of pentanenitrile in the presence of benzonitrile is lower compared to those obtained analyzing single analyte standards.

4.2.4 Enrichment of Aliphatic Hydrocarbons

The H2020 project Aquarius aimed for sensing "oil-in-water". Therefore, within this thesis, also aliphatic hydrocarbons were tested. Although the norm for determining oil and grease in water is based on tetradecane,[203] here *n*-heptane was used as its solubility in water is slightly higher and in contrast to short aliphatic molecules, the volatility is low and in the range of water (which facilitates working with the solutions).

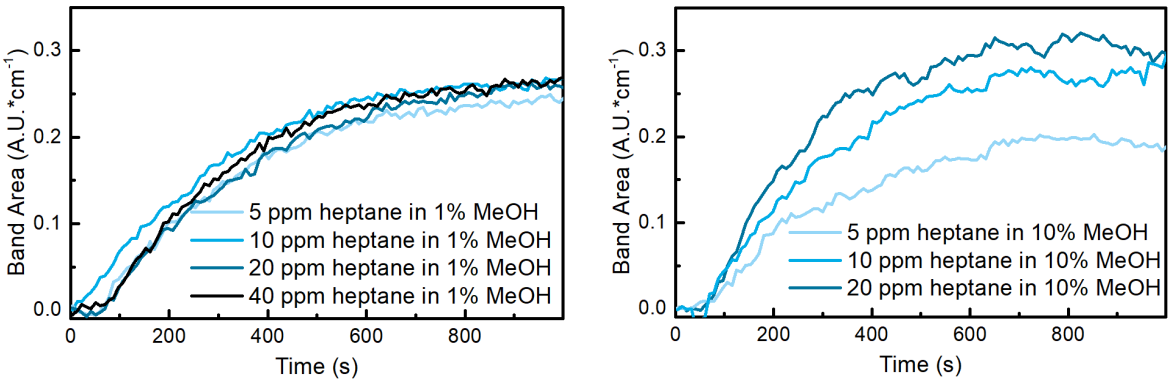

Figure 4.14 Enrichment profiles of *n*-heptane in 1 % methanol in water (left) and 10 % methanol in water with different concentrations.

Here, the major challenge is to obtain well-dissolved standard solutions for reproducible samples that are delivered to the sensor surface. Aliphatic hydrocarbons in contrast to aromatic hydrocarbons have a solubility in water of < 10 mg L^{-1}. An attempt was made to increase the solubility of aliphatic hydrocarbons by the addition of small amounts of methanol and ethanol (this is commonly applied in literature to enhance solubility *e.g.* for chlorinated hydrocarbons, see Ref. 137). Here, *n*-heptane in different methanol/water mixtures was used for first tests. To this end, *n*-heptane in methanol standards were prepared and 1 mL and 10 mL of these methanol standards was added to 99 mL and 90 mL water, respectively. The obtained results from integration of the band at 1470 cm^{-1} are depicted in **Figure 4.14**. The enrichment profile of the 1 % methanol in water concentration series showed long enrichment times of 15 min and a sensor response independent of the analyte concentration. From this

Die approbierte gedruckte Originalversion dieser Dissertation ist an der TU Wien Bibliothek verfügbar.
The approved original version of this doctoral thesis is available in print at TU Wien Bibliothek.
TU Bibliothek Your knowledge hub WIEN

one can conclude that 1 % methanol is not sufficient to dissolve 10 mg L^{-1} heptane in water. If using 10 % methanol in water, it was possible to measure up to 30 mg L^{-1} heptane and it took 5 min to reach an equilibrium in enrichment. Whereas a small concentration dependent sensor response was obtained, the results did not encourage a more in-depth evaluation, mainly because of the most artificial nature of the sample.

The regeneration of the enrichment layer was performed with 50 % ethanol in water, which regenerates the surface within 30 s.

4.2.5 Enrichment of Aromatic Hydrocarbons

In contrast to aliphatic hydrocarbons, aromatic hydrocarbons such as toluene, *p*-xylene, 1,2,4-trimethylbenzene show some solubility with values of 520 mg L^{-1}, 165 mg L^{-1} and 60 mg L^{-1} in water. In addition, the concentrations of these standard solutions can be double checked using UV/Vis spectroscopy as these substances show high absorption between 260 nm - 274 nm. Therefore, all sample solutions of aromatic hydrocarbons were calibrated with UV/Vis spectroscopy (see **Figure 4.15**) and if a linear calibration curve was obtained, a fully dissolved analyte was assumed, which would not have been the case for undissolved hydrocarbons in water. For 1,2,4-trimethylbenzene a linear correlation was only found for < 20 mg L^{-1} and only samples with concentrations below these values were used for enrichment experiments. For the other two analytes, a linear response was obtained for concentrations of up to 100 mg L^{-1}.

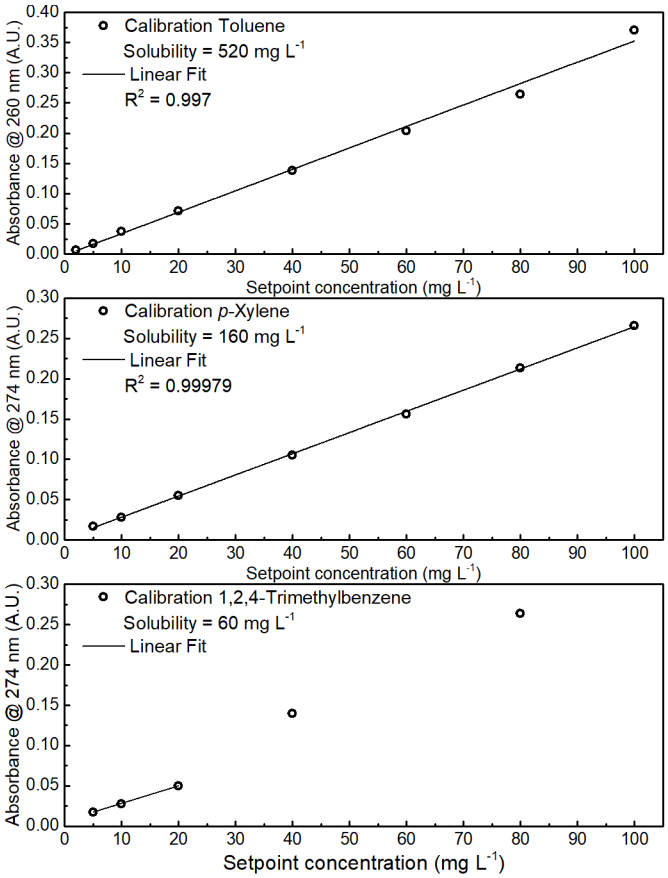

Figure 4.15: Calibration curves of toluene, *p*-xylene and 1,2,4-trimethylbenzene in water obtained from UV/vis spectra.

Die approbierte gedruckte Originalversion dieser Dissertation ist an der TU Wien Bibliothek verfügbar.
The approved original version of this doctoral thesis is available in print at TU Wien Bibliothek.

Absorption coefficients for UV/vis bands from literature were used to calculate the actual concentrations.[204] For all solutions, concentrations were considerably lower as set, which is most likely due to evaporation or incomplete dissolution of the analyte.

The IR absorption coefficients for the band areas were determined using transmission spectra of each analyte in cyclohexane and are given in **Table 4.4**.

The aqueous solutions were applied to the HMDS functionalized CTAB cubic, P123 and F127SS films. In **Figure 4.16, left**, the enrichment of different concentration of *p*-xylene is given and the P123 film shows the highest enrichment.

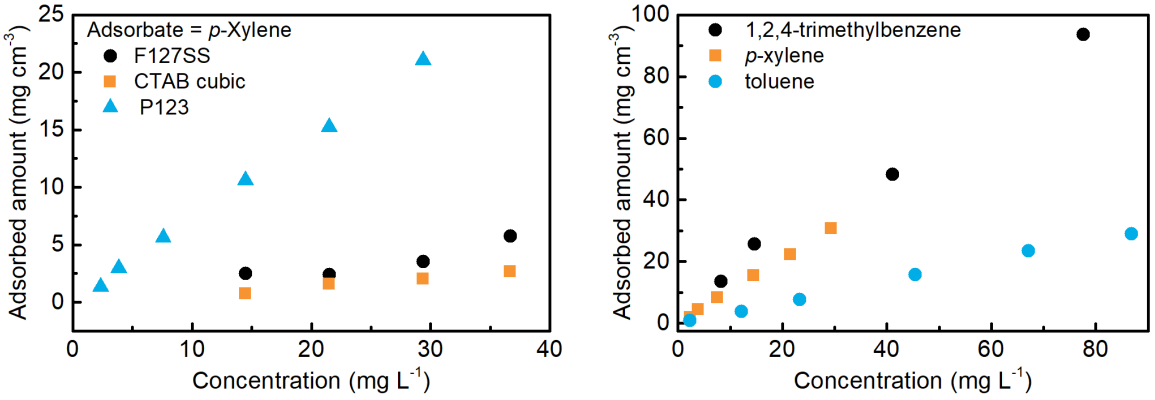

Figure 4.16: (Left) Adsorption isotherms of *p*-xylene into different mesoporous films: F127SS (P = 70 %, D_{pore} = 12.5 nm), CTAB 3d hexagonal (P = 50 %, D_{pore} = 4.8 nm) and P123 (P = 50 %, D_{pore} = 6.8 nm). (Right) Adsorption isotherms for different analytes into the P123 film.

Isotherms were fitted with the *Freundlich* equation and fitting results are given in **Table 4.3**. The fit for the trimethylbenzene isotherm has a considerably higher χ^2as less data points were used for fitting.

Table 4.3: Fitting results for different aromatic hydrocarbons adsorbed into P123 film.

Analyte	*Freundlich* fit χ^2	K_F [mg cm^{-3} (mg L^{-1})$^{-1/nF}$]	n_F
toluene	$2.1 \cdot 10^{-6}$	0.0010	1.01
p-xylene	$3.9 \cdot 10^{-6}$	0.0056	1.01
1,2,4-trimethylbenzene	$2.8 \cdot 10^{-4}$	0.0076	1.15

The adsorption isotherms of different aromatic hydrocarbons into the P123 film are given in **Figure 4.16, right,** and showing higher adsorbed amounts for aromatic hydrocarbons with lower solubility. This difference is quantified using the enrichment factor, which is the ratio of analyte concentration found in the film (as unit mg per volume film) and concentration of the applied solutions retrieved from UV/Vis measurements:

$$Enrichment\ Factor = \frac{c_{analyte\ in\ film}}{c_{analyte\ in\ solution}} \quad (4.7)$$

The thereby obtained enrichment factors for $c_{analyte\ in\ solution}$ = 10 mg L^{-1} are summarized in **Table 4.4**. Note that due to the non-linearity of the isotherms, enrichment factors are

Die approbierte gedruckte Originalversion dieser Dissertation ist an der TU Wien Bibliothek verfügbar.
The approved original version of this doctoral thesis is available in print at TU Wien Bibliothek.
TU Bibliothek WIEN Your knowledge hub

lower for higher concentrations.

Table 4.4: Enrichment factors obtained for different aromatic hydrocarbons for the P123 film.

Analyte	Band position	ε [g/(g · cm)]	Enrichment factor
toluene	1496 cm^{-1}	793	500
p-xylene	1517cm^{-1}	1111	1100
1,2,4-trimethylbenzene	1505 cm^{-1}	715	1800

To relate the results of the different hydrocarbons and to find a link between solubility of each analyte and the enrichment factor, the applied concentrations were normalized to the corresponding saturation solubility, thus $c/c_{saturation}$ was derived (similar to the relative pressure p/p_0 as used in gas sorption and section 5.1). The thereby obtained isotherms are given in **Figure 4.17** and show an interesting behavior: for $c/c_{saturation} < 0.2$, the same linear progression was found for all three analytes. For higher relative concentration, this linear behavior was not observed anymore. As these data points approach saturation, a loss of analyte while sample application or preparation is possible. Despite the two outliers (marked in gray) these findings allow to estimate the expected enrichment factor just from the solubility of the analyte without the need of performing a calibration. Furthermore, they highlight the requirement of low solubility for this sensing scheme to work because for analytes with high water solubility, the $c/c_{saturation}$ is very low, hence also the pore filling and enrichment is low. For future investigation beyond this thesis, it would be worth studying higher $c/c_{saturation}$ values if a similar behavior and hence isotherm shape is also obtained from adsorption from solutions as obtained from gas phase (compare section 1.3.1 and 5.1.1)

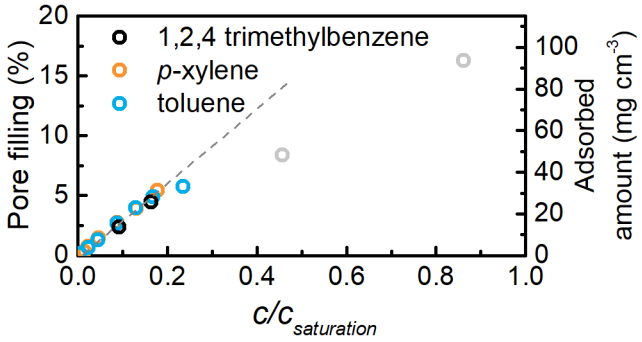

Figure 4.17: Pore filling and adsorbed amount of analyte as function of concentration normalized to the solubility of each analyte.

In addition, the degree of pore filling can be derived from the absorbed amount. To this end, the absorbance expected for a completely filled film is calculated using Lambert-Beer's law, with given film porosity P and density ρ of each analyte. The ratio of the experimentally obtained band area A_{exp} and the theoretically obtained band area for a filled film is defined as pore filling:

$$pore\ filling = \frac{A_{exp}}{d_{e,film} \cdot \varepsilon \cdot \rho \cdot P} \tag{4.8}$$

If inserting into equation (4.8) for all three analytes, pore filling of < 6 % was observed. This

Die approbierte gedruckte Originalversion dieser Dissertation ist an der TU Wien Bibliothek verfügbar.
The approved original version of this doctoral thesis is available in print at TU Wien Bibliothek.
TU Bibliothek WIEN Your knowledge hub

low degree of pore filling should allow for multicomponent analysis, as even if applying all three analytes at once, only a minor fraction of the porous volume is filled, thereby impeding interferences.

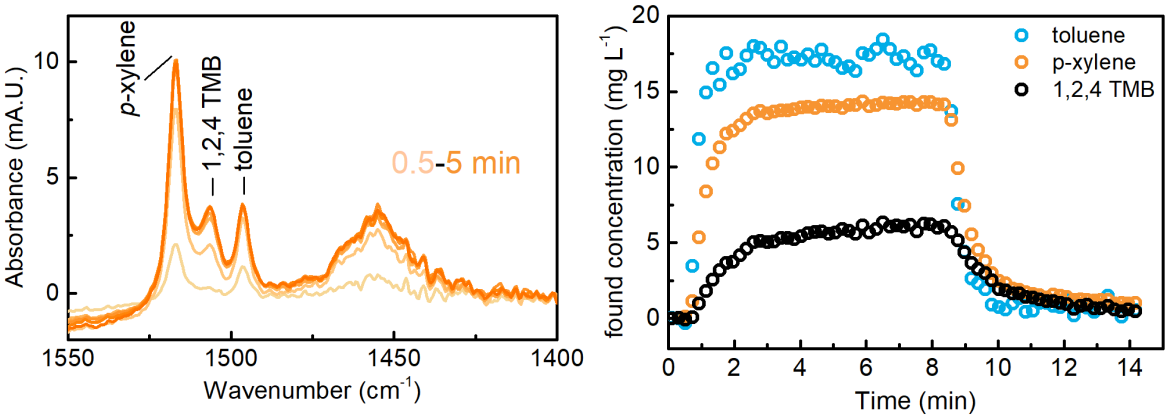

Figure 4.18: (Left) IR spectra of a mix of toluene, *p*-xylene and 1,2,4-trimethylbenzene as a function of time (spectra taken every 30 s). (Right) Found concentrations from fitting three Lorentzian as function of time.

Multiplexing was tested by mixing standard solutions verified by UV/vis spectroscopy with known concentrations. The thereby obtained spectra upon application to the sensor are given in **Figure 4.18**. Already from the spectra it is obvious that adsorption of trimethylbenzene proceeds slower than for the other two analytes as maximum band heights are already achieved after 1 min.

In a very similar fitting routine as will be used in section 4.4, each band was fitted with three Lorentzian curves using a MATLAB script. The thereby obtained band areas were fitted with the *Freundlich* equation that served as calibration function for each analyte. The temporal progression of the found concentrations is given in **Figure 4.18, right**. The applied mixture consisted of 21 mg L^{-1} toluene, 12 mg L^{-1} *p*-xylene and 5 mg L^{-1} 1,2,4-trimethylbenzene. Concentration obtained for the fitting routine were 18 mg L^{-1}, 14 mg L^{-1} and 6 mg L^{-1}, respectively, which corresponds pretty well with the applied concentrations. Lower concentrations for toluene could be found due to evaporation of the analyte while sample handling.

Furthermore, the temporal progression nicely illustrates different speeds of diffusion for different analytes. While toluene reached the plateau within the first 30 s of application, *p*-xylene and 1,2,4-trimethylbenzene reached the maximum value after 1 and 1.5 min, respectively, and vice versa for the desorption.

4.2.6 Conclusion

A new approach for *in situ* monitoring and quantitative analysis of solutes adsorbed on high-surface-area materials is presented. This is demonstrated via the use of different ordered mesoporous silica thin films as enrichment layers in an ATR IR spectroscopic sensing system. Germanium ATR crystals were also employed, allowing to broaden the accessible spectral range. The adsorption/desorption profiles of benzonitrile and valeronitrile (proof-of-principle),

Die approbierte gedruckte Originalversion dieser Dissertation ist an der TU Wien Bibliothek verfügbar.
The approved original version of this doctoral thesis is available in print at TU Wien Bibliothek.
TU Bibliothek Your knowledge hub WIEN

aliphatic and aromatic hydrocarbons and mixture thereof were recorded *in situ* using an automated flow system. Thereby, fast response times were observed for all pore structures and two different classes of analytes, aromatic hydrocarbons and nitriles. In these cases also a complete recovery of the sensor was obtained. After calibration of IR absorption band areas using the *Freundlich* isotherm, limits of detection for nitriles and aromatic hydrocarbons in water were determined to be between 1 and 10 mg L^{-1} for CTAB films with 4 s integration time. Recorded data given in absorption units was translated into mass of adsorbed pollutant in the mesoporous film using theoretical considerations. The calculated spectral signatures of material outside the coated ATR crystal were in good agreement with experimentally observed values. This finding enabled us to quantify the absolute amount of adsorbed analyte by application of Lambert-Beer's law. The adsorbed concentrations within the film obtained in this manner correspond to volumetric enrichment factors of up to 210 for accumulation of nitriles from water and up to 1800 for aromatic hydrocarbons.

In addition, the developed sensor system was also tested with aliphatic hydrocarbons. In this case due to the low solubility of aliphatic hydrocarbons, they required for a mediator solvent (methanol). Because of this mediator the enrichment factors were low, and equilibrium was not even reached after 15 min. Based on the obtained results it was decided to explore other, scientifically more promising research opportunities based on the mesoporous films applied to ATR crystals.

Die approbierte gedruckte Originalversion dieser Dissertation ist an der TU Wien Bibliothek verfügbar.
The approved original version of this doctoral thesis is available in print at TU Wien Bibliothek.
TU Bibliothek Your knowledge hub WIEN

4.3 Enrichment of Anions

Nitrates (mainly KNO_3, $NaNO_3$, NH_4NO_3) are used in thousand-ton scale in agriculture and find their way eventually into ground water and hence into drinking water supplies.[205] Therefore, pollution of nitrates is typically high in rural areas and regularly exceeds the governmentally regulated levels of 50 mg L^{-1}.[206] Up to date, nitrate is sensed either by UV/vis spectroscopy after chemical reaction, direct UV spectroscopy or via ion selective electrodes or ion chromatography.[207]

Ions like NO_3^- shows strong and specific bands in the MIR spectrum at 1395 cm^{-1}. However, to access this absorption band via IR spectroscopy, additional pre-concentration steps are needed as otherwise the sensitivity of IR spectroscopy is limited due to strong background absorption of water that limits the optical path length in this spectral region. It has been shown that the sensitivity can be vastly increased using enrichment layers on ATR crystals (compare section 1.4.1). Until now, they have been employed for enriching apolar substances into apolar coatings. In this context, it has been successfully be shown in this thesis that mesoporous silica films can also be employed. Besides the fast enrichment found for mesoporous silica, their rich surface chemistry allows for tuning the surface chemistry. Therefore, synthetic routes usually found for functionalizing materials used for liquid chromatography can be easily transferred. For ion exchange applications, silica columns with ion exchange groups are commercially available, hence, also the corresponding organosilanes with corresponding functional groups.

In this section, ion exchange groups ($-NH_3^+Cl$ and $-N(CH_3)_3^+Cl$) were covalently introduced into mesoporous silica films coated on ATR crystals to enrich NO_3^-.

4.3.1 Introduction of an Ion Exchange Moiety into Mesoporous Silica

Silanes with ion exchange groups such as amine- or trimethylammonium- moieties are commercially available. First experiments were performed on CTAB 3d hexagonal films functionalized with aminopropyl triethoxysilane (APTES) acting as a weak ion exchange group after acidification with HCl yielding a $-NH_3^+Cl$ group. This film was applied on a Si ATR crystal and placed in the liquid flow cell placed in the sample compartment of a Vertex 80v spectrometer. Right from the beginning of the water application negative bands at 1600 cm^{-1} corresponding to the N-H vibrations in the NH_3^+ moiety appeared. It turned out that pristine mesoporous silica and silica functionalized with APTES is not stable under aqueous conditions, as reported in literature for powders.[208,209] In a second step, an APTES functionalized film was post-functionalized with HMDS (known as *end-capping* for chromatography columns) to prevent self-cleavage of the aminopropyl group. However, this film was also not stable and the aminopropyl moiety leached out of the film. Although APTES functionalized mesoporous silica particles had been used for nitrate removal in batch experiments, it was not reported if the particles could be recovered and how the material was effected by the nitrate solutions.[210,211] To overcome the self-destruction of APTES, a

Die approbierte gedruckte Originalversion dieser Dissertation ist an der TU Wien Bibliothek verfügbar.
The approved original version of this doctoral thesis is available in print at TU Wien Bibliothek.
TU Bibliothek Your knowledge hub WIEN

trimethylammonium group (TMAC) was introduced that might decrease bleaching due to steric hindrance. Furthermore, remaining free Si-OH groups were saturated with methyltrichlorosilane (MTCS). In addition, films were calcined prior functionalization, to further increase the stability of the silica network.

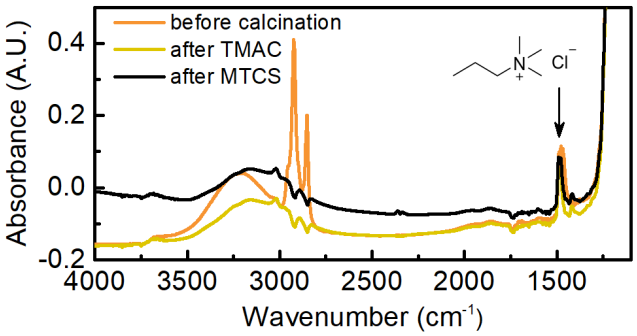

Figure 4.19: ATR IR spectra of CTAB 3d hexagonal film before calcination, after functionalization with TMAC and MTCS.

The spectra obtained between each step of the synthesis are given in **Figure 4.19**. Before calcination strong C-H vibrations around 2900 cm^{-1}, -CH_2 deformation band at 1470 cm^{-1} and C-N vibration of the trimethylammonium group at 1480 cm^{-1} were visible and corresponded to the template CTAB. After calcination and functionalization, the band corresponding to the trimethylammonium group at 1480 cm^{-1} of TMAC was present. From this spectrum, the number of trimethylammonium moieties present in the film were derived by inserting into Lambert-Beer's law with $d_{e,film}$ = 6.82 µm (at 1480 cm^{-1}, th = 400 nm, compare section 4.1) and ε = 4792 L cm^{-2} mol^{-1} of the corresponding C-N^+ vibration obtained from IR transmission measurements (band area integrated between 1532 - 1432 cm^{-1}). Thereby, a trimethylammonium concentration of 1.32 mol L^{-1}_{film} was obtained, which is equivalent to $1.06 \cdot 10^{-6}$ mol_{NH3+} per film volume.

4.3.2 Proof-of-Principle using a P123 Film

A P123 film functionalized with TMAC and MTCS, coated on a Si ATR crystal, was inserted into the liquid flow cell and measurements were performed with a Vertex 80v spectrometer.

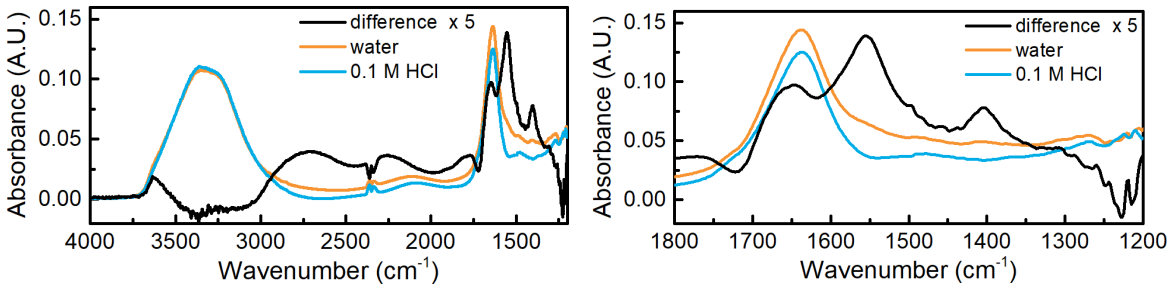

Figure 4.20: ATR IR spectra recorded after flushing water and 0.1 M HCl for 5 min over a functionalized with TMAC P123 film.

As the TMAC group is considered a strong anion exchange moiety, it is not regenerated by flushing pure water, but it demands for a regeneration step. Here, diluted HCl was used. Spectra of water and 0.1 M HCl applied to the functionalized film were recorded and strong

Die approbierte gedruckte Originalversion dieser Dissertation ist an der TU Wien Bibliothek verfügbar.
The approved original version of this doctoral thesis is available in print at TU Wien Bibliothek.
TU Bibliothek Your knowledge hub WIEN

changes in the spectra due to changing pH value and hence changes in the water H-O-H bending vibration at 1640 cm^{-1} were observed (see **Figure 4.20**). A difference spectra was derived using the diluted HCl spectrum as background to highlight the differences. In addition to the shift in the bending vibration of water, a band at 1403 cm^{-1} arises upon changing from the regeneration solution to water. As this band overlaps with the to-be analyzed nitrate band at 1395 cm^{-1}, spectra for nitrate quantification were calculated with the background spectrum of water, not HCl that is recorded at the beginning of each enrichment step, and thus after regeneration. The resulting differences in the $NaNO_3$ bands in the spectra are shown in **Figure 4.21** for the enrichment of a 40 mg L^{-1} $NaNO_3$ solution using a TMAC functionalized P123 film. The spectra obtained from the background spectra of pure water is in accordance with the spectra obtained on a single bounce ATR unit of a 10 g L^{-1} $NaNO_3$ solution.

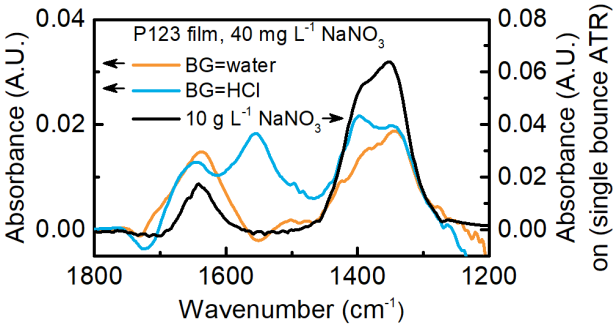

Figure 4.21: ATR IR spectra of water and 0.1 M HCl applied to a P123 film functionalized with TMAC.

All nitrate enrichment experiments were performed by flushing 5 mL of 0.1 M HCl for conditioning followed by 5 mL of the respective $NaNO_3$ solution with 1 mL min^{-1} flow velocity using a peristaltic pump. The nitrate band was integrated between 1465 cm^{-1} and 1290 cm^{-1} and the band area during application for different nitrate concentrations is given in **Figure 4.22**. These profiles show a fast enrichment that stabilizes within the first 2 min.

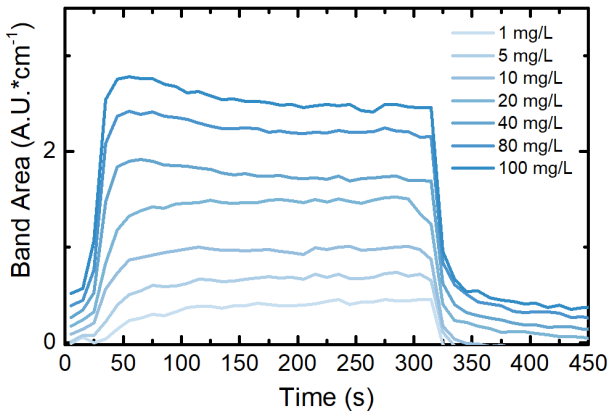

Figure 4.22: Nitrate band area as function of time for different $NaNO_3$ concentrations obtained on a TMAC functionalized P123 film.

The obtained band areas for three consecutive adsorption experiments per concentration after 2 min were plotted as function of applied $NaNO_3$ concentration yielding an isotherm that was fitted with the *Langmuir* and *Freundlich* function (see section 4.2.2.2 for equations, **Figure 4.23**). In contrast to the adsorption isotherms obtained in the previous sections, here, the *Langmuir* function fits better ($\chi^2 = 0.009$ for the *Langmuir* fit compared to $\chi^2 = 0.049$ for

Die approbierte gedruckte Originalversion dieser Dissertation ist an der TU Wien Bibliothek verfügbar.
The approved original version of this doctoral thesis is available in print at TU Wien Bibliothek.
TU Bibliothek WIEN Your knowledge hub

the *Freundlich* fit). This result was expected, as compared to the rather unspecific adsorption of hydrocarbons into hydrophobic mesoporous silica films that allows for multilayer adsorption (according to the *Freundlich* function), the trimethylammonium moiety in the TMAC functionalized films offers just one binding site per nitrate ion. This is in accordance with the definition of Langmuir adsorption.

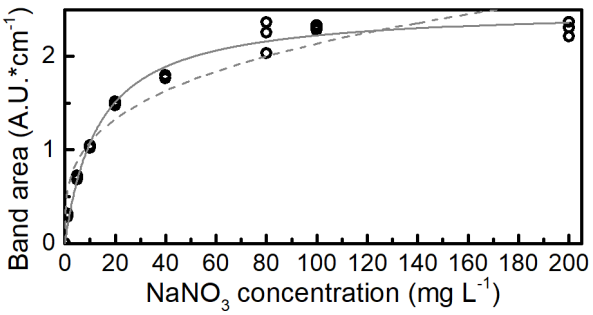

Figure 4.23: Isotherms obtained from three consecutive sample applications fitted with the Langmuir function (solid line) and Freundlich equation (dashed line).

4.3.3 TMAC Functionalized CTAB Film

A TMAC functionalized CTAB 3d hexagonal film coated on a Ge ATR crystal was used for further investigations (compare spectra of film in Figure 4.19). This film was also inserted in the liquid flow cell in the sample compartment of the Vertex 80v and sample application was carried out as explained in the previous section. Using this film, again $NaNO_3$ concentrations as low as 1 mg L^{-1} could be analyzed. Furthermore, the fraction of interacting trimethylammonium groups was derived: As calculated in section 4.3.1, $1.26 \cdot 10^{-7}$ mol of trimethylammonium moiety are present in the film (1.56 mol L^{-1}). If assuming that every chloride ion from the regeneration step is replaced with a nitrate ion this would correspond to a NO_3^- concentration in the film of 98 g L^{-1}_{film}. The absorption coefficient of the nitrate band between 1250 cm^{-1} and 1500 cm^{-1} was derived from a transmission measurement of a 10 g L^{-1} solution to be $\varepsilon = 697$ L g^{-1} cm^{-2}. The nitrate concentration in the film obtained from the enrichment of a 5 mg L^{-1} $NaNO_3$ solution equaled 18.7 g L^{-1}. This corresponded to trimethylammonium moiety consumption of 19 % and an enrichment factor of 3740.

Until now, standard solutions were obtained from $NaNO_3$ distilled water and thereby preventing any interferences with other anions. To account for them, standard solutions were prepared using tap water. However, even for concentrations as high as 100 mg L^{-1} $NaNO_3$ in tap water, no band corresponding to nitrate was visible in the spectrum. Thus no enrichment was achieved. Furthermore, enrichment was tested with 5 mg L^{-1} $NaNO_3$ and 5 mg L^{-1} Na_2SO_4 without success.

Apparently, the affinity of the trimethylammonium group is higher toward multiply charged anions such as sulfate and phosphate. In order to decrease the affinity toward these anions, an ammonium moiety with *n*-butyl groups instead of methyl groups could decrease the affinity to multiple charged, bigger anions as the ammonium cation would be less accessible to large ions due to steric hindrance of the butyl groups.

Die approbierte gedruckte Originalversion dieser Dissertation ist an der TU Wien Bibliothek verfügbar.
The approved original version of this doctoral thesis is available in print at TU Wien Bibliothek.

4.4 Enrichment from Gas Phase

Volatile organic carbons (VOCs) typically originate from combustion processes, paints and inks, fuel products, or farming. Their harmful effects on human health and the environment demand for their continuous monitoring, especially in indoor environments, where up to ppm-concentration were reported.[212–215] An increasing awareness for environmental protection and personal safety has fueled the development of a broad variety of VOC sensors based on i) photo-ionization detectors (PID)s, (ii) electrochemical sensors, (iii) metal oxide sensors, (iv) UV spectrometers, or (v) micro-gas chromatographs.[216] However, these sensors are either not selective, interfere with other compounds found in air (*e.g.* NO, NO_2 or CO interfere with metal oxide sensors) or are bulky and expensive, as it is the case of chromatographs. Therefore, it is still challenging to detect VOCs at low concentrations in a complex atmosphere.

With respect to selectivity, FTIR spectroscopy has proven a great candidate as it probes the molecule's characteristic vibrations in the fingerprint region of the spectrum.[217] However, high sensitivity in IR spectroscopy demands for long interaction path lengths, which are typically realized using multi-pass cells.[218] In this section, the high enrichment factors and the versatility of mesoporous silica films as enrichment materials for sensing VOCs in gas phase is presented. The enrichment of three VOCs into mesoporous films with three different pore sizes coated on Si ATR crystals was investigated for single components (section 4.4.1) and gas mixtures under dry and humidified conditions (section 4.4.2).

4.4.1 Adsorption of Single BTEX Molecules

To showcase the capability of mesoporous silica coated ATR crystals to sense VOC, three aromatic hydrocarbons with different saturation pressures were selected: Toluene (p_{sat} = 2.66 kPa), *p*-xylene (p_{sat} = 1.18 kPa) and 1,2,4-trimethylbenzene (p_{sat} = 0.28 kPa) (all values given for 298 K). For experimental setup and sample preparation see section 2.2.3. FTIR-ATR spectra of all three VOCs in liquid phase are given in **Figure 4.24**, orange curves. The bands at 1496 cm^{-1}, 1517 cm^{-1} and 1506 cm^{-1} stem from the skeletal ring vibrations of toluene, *p*-xylene and 1,2,4-trimethylbenzene, respectively. Concentration series between 5 - 800 ppmv were applied to the three different mesoporous films. Figure 4.24, black curves, show exemplarily spectra of toluene, *p*-xylene and trimethylbenzene with 786 ppmv, 787 ppmv and 80 ppmv, respectively, adsorbed into the mesoporous silica film produced using CTAB. Note, due to the adsorption into the film, the skeletal ring vibrations have the same band positions as found in neat spectra (compare black and orange curves). The additional band at 1620 cm^{-1} is associated with the bending vibration of water that is also present in the gas streams as *e.g.* the respective liquids were not anhydrous and this residual water also adsorbs into the films. The redshift of the bending vibration is a result of the hydrophobic functionalization that largely impede the water molecule's interactions with the surface, which influences the local order of water and hence the water vibrations.[219,220] Due to the hydrophobic surface functionalization of the film with HMDS, this adsorption could be decreased to less

Die approbierte gedruckte Originalversion dieser Dissertation ist an der TU Wien Bibliothek verfügbar.
The approved original version of this doctoral thesis is available in print at TU Wien Bibliothek.
TU Bibliothek Your knowledge hub WIEN

than 1 % compared the absorbance of water vapor on pristine mesoporous silica for the same humidity (compare with spectra from section 5.1).

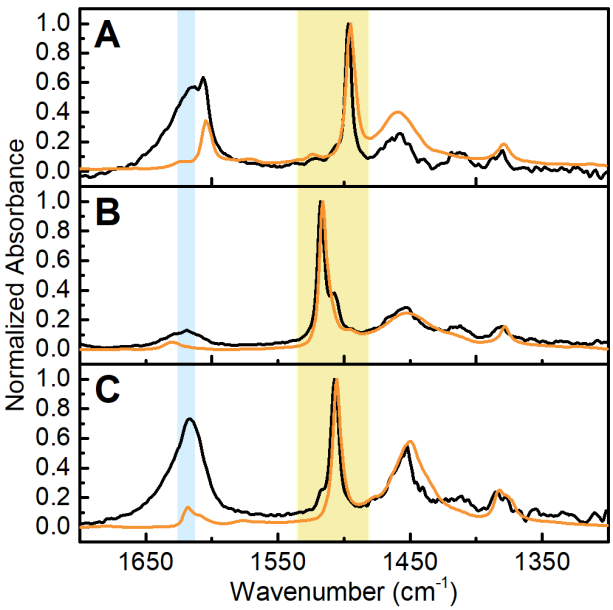

Figure 4.24: FTIR spectra(normalized to a peak absorbance of 1) of toluene (A), *p*-xylene (B) and 1,2,4-trimethylbenzene (C) obtained after enrichment into the mesoporous silica film synthesized using CTAB (black curves) and for the pure substance on a commercial ATR unit (orange spectra). Bands of adsorbed water are highlighted in blue and the spectral region of interest with skeletal ring vibrations of toluene at 1496 cm^{-1}, *p*-xylene at 1517 cm^{-1} (residuals of trimethylbenzene are visible in the spectrum) and 1,2,4-trimethylbenzene at 1506 cm^{-1} is highlighted in yellow.

The area of Lorentzian profiles fitted to the absorption bands shown in **Figure 4.24** were used for quantitative analysis. The band areas obtained for a concentration series of toluene adsorbed into the mesoporous silica film prepared using CTAB are depicted in **Figure 4.25A**. Here, the concentration was increased every minute and spectra were recorded every 10 s. The fast adsorption, hence short response time, was similar for all three VOCs and all three films (compare **Figure 4.26** and **Figure 4.27**).

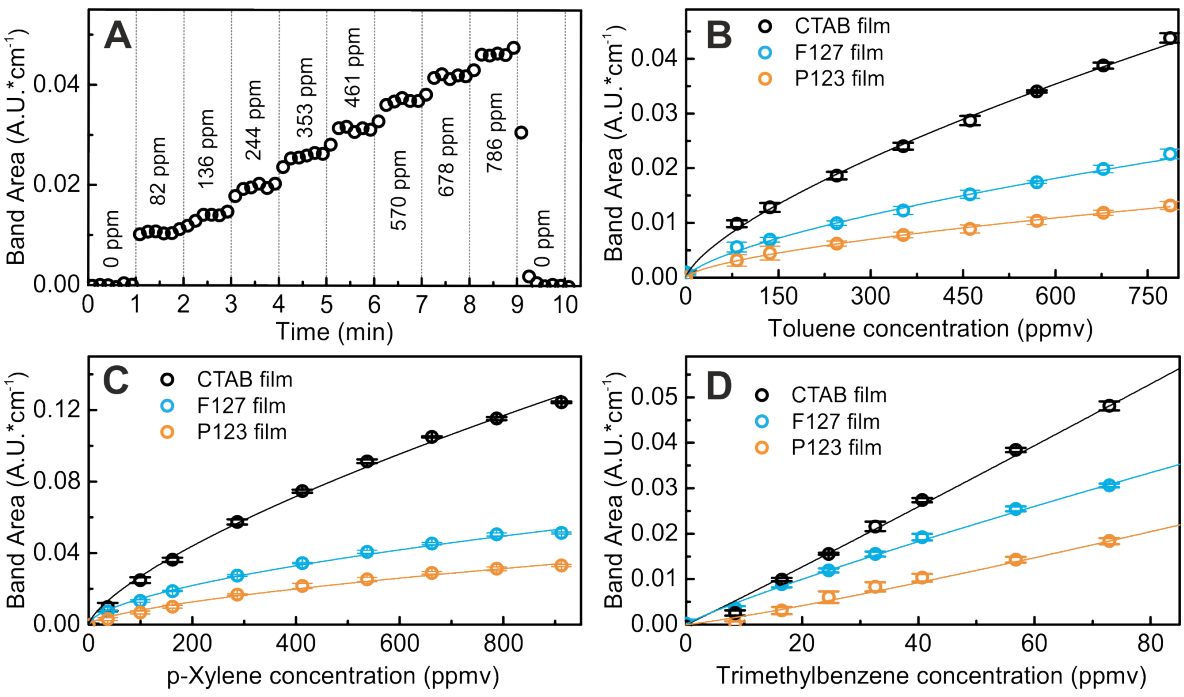

Figure 4.25: (A) Calibration of the mesoporous silica film prepared using CTAB for toluene. (B-D): Adsorption isotherms of different mesoporous films for (B) toluene, (C) *p*-xylene and (D) 1,2,4-trimethylbenzene.

Die approbierte gedruckte Originalversion dieser Dissertation ist an der TU Wien Bibliothek verfügbar.
The approved original version of this doctoral thesis is available in print at TU Wien Bibliothek.
TU Bibliothek Your knowledge hub WIEN

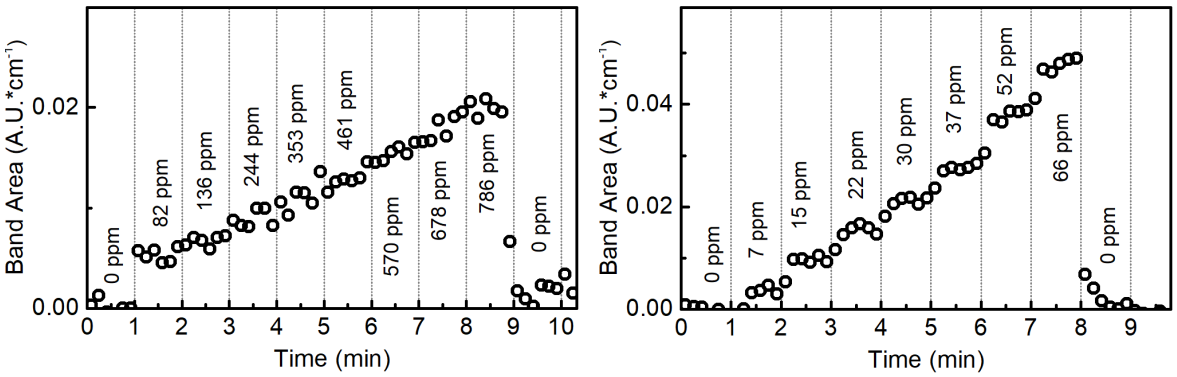

Figure 4.26: Calibration of the mesoporous silica film prepared using CTAB for *p*-xylene (left) and trimethylbenzene (right).

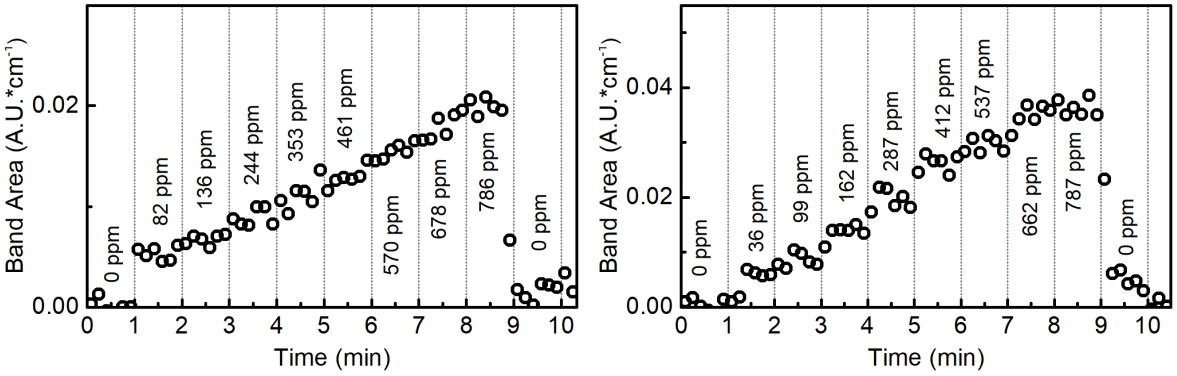

Figure 4.27: Calibration of the mesoporous silica film prepared using F127SS for toluene (left) and P123 for *p*-xylene (right).

The complete regeneration of all films was simply achieved by flushing the flow cell with pure N_2 with the signal returning back to its initial absorbance within seconds.

The band areas for concentration series of all VOCs adsorbed into all three films are given in **Figure 4.25**. For all VOCs, the mesoporous silica film prepared using CTAB with smallest pore size shows superior adsorption behavior, followed by the film prepared using F127 and the film synthesized with P123.

Table 4.5: Calibration function parameters obtained from a fit with the Freundlich equation.

	Analyte	K_F [A.U. cm^{-1} (ppmv)$^{-1/n}$]	n_F
CTAB 3d hex film	toluene	$3.9 \cdot 10^{-4}$	1.42
	p-xylene	$1.0 \cdot 10^{-3}$	1.54
	1,2,4-trimethylbenzene	$7.3 \cdot 10^{-4}$	1.01
F127SS film	toluene	$2.47 \cdot 10^{-5}$	1.48
	p-xylene	$4.65 \cdot 10^{-4}$	1.45
	1,2,4-trimethylbenzene	$9.11 \cdot 10^{-4}$	1.19
P123 film	toluene	$1.91 \cdot 10^{-5}$	1.58
	p-xylene	$3.75 \cdot 10^{-4}$	1.51
	1,2,4-trimethylbenzene	$2.27 \cdot 10^{-4}$	1.01

The calibration functions were described by the *Freundlich* equation, which describes multilayer adsorption of adsorbates typically found in mesoporous materials (see section

Die approbierte gedruckte Originalversion dieser Dissertation ist an der TU Wien Bibliothek verfügbar.
The approved original version of this doctoral thesis is available in print at TU Wien Bibliothek.
TU Bibliothek Your knowledge hub WIEN

4.2.2.2 for the equations).[84] With, q_e is the amount of adsorbed analyte (corresponding to the obtained band areas in A.U. cm^{-1}), c is the concentration in the gas (ppmv), K_F (A.U. cm^{-1} $[ppmv]^{-1/n}$) is the Freundlich affinity coefficient, and n_F (unitless) is the Freundlich linearity index. **Table 4.5** summarizes the fitted parameters.

Due to the low concentrations applied for trimethylbenzene chosen due to its low saturation vapor pressure, an almost linear calibration function was obtained, while for toluene and *p*-xylene the calibrations curve flattens out for higher concentrations, which is reflected in higher n values. This is due to a lower affinity of the analyte to the adsorbate for an increasing number of adsorbed monolayers. For all analytes, relative vapor pressures of $p/p_0 < 0.1$ were applied, which is the region of monolayer formation typically found in gas sorption experiments for mesopores. Within this region, no capillary condensation and, hence, no hysteresis between adsorption and desorption occurs,[84] ensuring reversible sensing.

The obtained calibration functions allow for retrieving the LOD defined as $q_e(\mathrm{LOD}) = 3\,\sigma,\cdot$ with σ being the standard deviation derived from consecutive 100 % lines. The LODs for the best performing film are 7 ppm, 6 ppm and 3 ppm for toluene, *p*-xylene and 1,2,4-trimethylbenzene, respectively. To put these LODs into perspective and compare them to transmission measurements, it is interesting to consider the effective optical path length for which these numbers were obtained. $d_{e,eff}$ within the film on an ATR crystal was derived as discussed in section 4.1. For the mesoporous silica film prepared with CTAB with a film thickness $th = 400$ nm, $n_{SiO2\text{-}film} = 1.13$ (compare section 5.1.2 for value), $n_{Si\text{-}ATR} = 3.42$, a $d_{e,eff} = 6.3$ µm at $\tilde{\nu} = 1500$ cm^{-1} was found. This allows for retrieving an enrichment factor defined as the ratio between the band area A_{ATR} obtained from ATR spectra and simulated band areas $A_{transmission}$ one would obtain for the same path length $d_{e,eff}$ based on reference spectra from the PNNL database:

$$Enrichment\ Factor = \frac{A_{ATR}}{A_{transmission}} = \frac{\varepsilon \cdot c_{film} \cdot d_{e,eff}}{\varepsilon \cdot c_{gas} \cdot d_{e,eff}} \qquad (4.9)$$

Assuming the same absorption coefficient ε for the area of a given band in condensed and gas phase, the enrichment factor also corresponds to the ratio of the volumetric concentrations c_{film} *and* c_{gas} (mol L^{-1}) in the mesoporous film and in the gas. The enrichment factors obtained for 10 ppmv are 9600, 20480 and 32770 for toluene, *p*-xylene and 1,2,4-trimethylbenzene, respectively. Note that for higher concentrations the enrichment factor is lower due to the non-linearity of the calibration functions. The highest enrichment factor was found for 1,2,4-trimethylbenzene, the VOC with the lowest saturation vapor pressure and hence highest affinity to condense at surfaces, while toluene, having the highest saturation vapor pressure, yielded the lowest enrichment factor.

4.4.2 Adsorption of BTEX Gas Mixtures

A VOC mixture was prepared by inserting the premixed VOC solution into the gas container. With the same fitting routine as for the single component calibrations, three Lorentzian

Die approbierte gedruckte Originalversion dieser Dissertation ist an der TU Wien Bibliothek verfügbar.
The approved original version of this doctoral thesis is available in print at TU Wien Bibliothek.
TU Bibliothek Your knowledge hub WIEN

profiles were fitted to the obtained spectra.

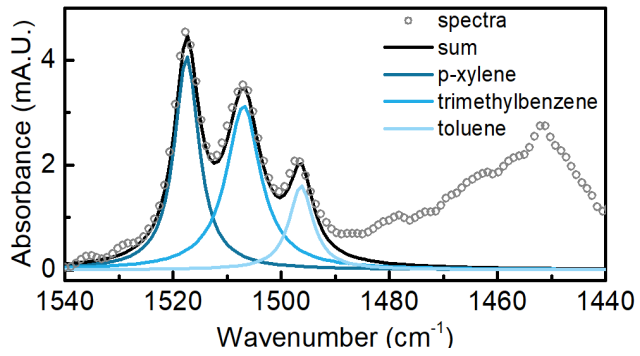

Figure 4.28: FTIR spectra of a mixture of VOC enriched on the mesoporous silica film prepared using CTAB with deconvolution using Lorentzian curves.

The spectrum of a VOC mixture with 146 ± 10 ppmv toluene, 151 ± 10 ppmv *p*-xylene and 58 ± 10 ppmv 1,2,4-trimethylbenzene adsorbed into the mesoporous silica film prepared using CTAB and the corresponding Lorentzian profiles are depicted in **Figure 4.28**. The obtained profile areas were inserted into the calibration function with parameters given in Table 1. The so found concentrations of 153 ± 15 ppmv toluene, 143 ± 12 ppmv *p*-xylene and 52 ± 8 ppmv 1,2,4-trimethylbenzene are in very good agreement with the applied concentrations.

In a next step, this gas mixture was humidified by bubbling the stream of N_2 through water at 25 °C prior to mixing with the stream of diluted VOC from the pressure vessel. The thereby obtained gas transmission spectrum for 15 % humidity and 277 ± 10 ppmv toluene, 232 ± 10 ppmv *p*-xylene and 82 ± 10 ppmv trimethylbenzene given in **Figure 4.29, left,** shows the broad P and R branches of the water vapor deformation band. The VOCs' absorption bands present in the mixture are practically indistinguishable from the large water background. The humidified gas mixtures were then applied to the mesoporous silica film prepared using CTAB and the thus obtained spectrum is depicted in Figure 4.29, right.

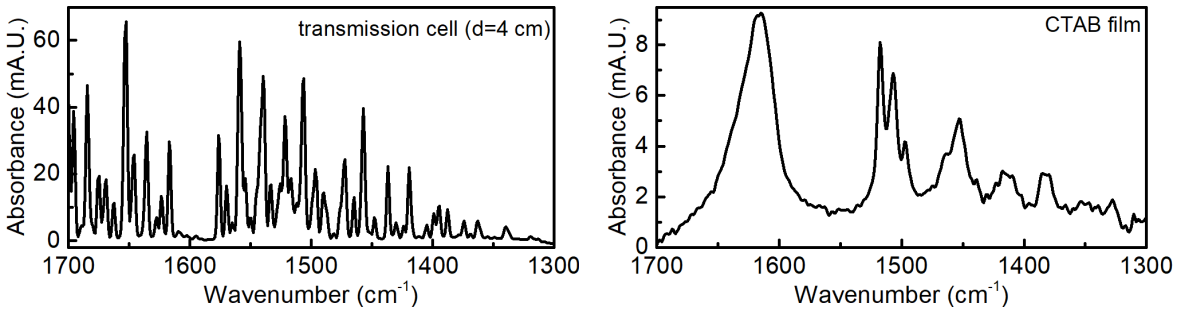

Figure 4.29: FTIR spectra of a mixture of VOC in humidified air obtained from a transmission measurement (left) and adsorbed to the mesoporous silica film produced using CTAB 3d hexagonal (right).

In addition to the well resolved VOC bands around 1500 cm^{-1}, a band of condensed water at 1620 cm^{-1} is visible. Since the film thickness of 400 nm largely covers the evanescent field, no bands associated with water vapor are present allowing for quantitative analysis of the adsorbed VOCs.

Die approbierte gedruckte Originalversion dieser Dissertation ist an der TU Wien Bibliothek verfügbar.
The approved original version of this doctoral thesis is available in print at TU Wien Bibliothek.
TU Bibliothek Your knowledge hub WIEN

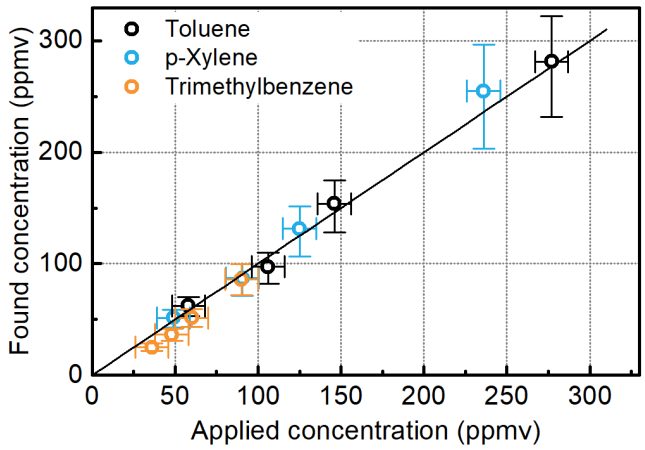

Figure 4.30: Found and applied concentrations for VOC mixtures on mesoporous silica film produced using CTAB from calibration.

The gas mixture was further mixed with humidified N_2 to yield a relative humidity up to 60 % and the findings for a concentration range between 25 - 300 ppmv VOC with varying relative humidity between 60 % and 15 % is given in **Figure 4.30** (see **Table 4.6** for values). Here, the high humidity does not interfere with the measurement and the applied concentrations are in excellent agreement with the found VOC concentrations.

Table 4.6: Found and applied concentrations for VOC mixtures on mesoporous silica film produced using CTAB from calibration. TMB.. trimethylbenzene

RH (%)	toluene applied	toluene found	*p*-xylene applied	*p*-xylene found	TMB applied	TMB found
15	58 ± 10	62 ± 8	49 ± 10	52 ± 7	36 ± 10	25 ± 1
25	106 ± 10	97 ± 13	91 ± 10	87 ± 12	48 ± 10	36 ± 5
35	146 ± 10	154 ± 21	125 ± 10	131 ± 20	60 ± 10	52 ± 8
60	277 ± 10	281 ± 39	236 ± 10	255 ± 40	90 ± 10	86 ± 14

4.4.3 Conclusion

Mesoporous silica films with three different pore sizes between 5 - 12.5 nm coated on Si ATR crystals were used as enrichment material for VOC gas sensing and their sensing performance was evaluated using FTIR spectroscopy. The film with the smallest pore size clearly stood out and reached enrichment factors from 9000 up to 32000, depending on the VOC studied. Moreover, limits of detection as low as 3 - 7 ppmv with solely 6.3 µm effective path length were achieved. The remarkable increase in sensitivity was also reached in high-humidity atmosphere, which was enabled by organic functionalization of the mesoporous silica to largely exclude water interferences.

Die approbierte gedruckte Originalversion dieser Dissertation ist an der TU Wien Bibliothek verfügbar.
The approved original version of this doctoral thesis is available in print at TU Wien Bibliothek.
TU Bibliothek Your knowledge hub WIEN

Die approbierte gedruckte Originalversion dieser Dissertation ist an der TU Wien Bibliothek verfügbar.
The approved original version of this doctoral thesis is available in print at TU Wien Bibliothek.
TU Bibliothek Your knowledge hub WIEN

Die approbierte gedruckte Originalversion dieser Dissertation ist an der TU Wien Bibliothek verfügbar.
The approved original version of this doctoral thesis is available in print at TU Wien Bibliothek.

Chapter 5 *In Situ* Monitoring of Process at Interfaces

In addition to quantitative analysis ATR-FTIR spectroscopy also allows to monitor qualitatively chemical and physical processes at interfaces. All applications of mesoporous materials in industry and research, such as (photo)catalysis,[60–62] separation,[63] electrochemistry,[64] or (bio-)sensing[65,175] benefit from the materials high-surface area and defined porosity. Their functionality and applicability in these various disciplines depends, however, not only on their large specific surface area, but fundamentally also on the adsorbate-surface interactions. The latter play a pivotal role and drive researchers to investigate the bonding mechanisms *e.g.* H-bonding or $\pi - \pi$ interactions. Such information is of particular interest for water at surfaces,[221,222] as it will be discussed in **section 5.1**. In addition to information on water interacting with itself and the surface of the mesopore, water adsorption into mesoporous materials also allows to derive porosity and pore size distribution (PSD) of the investigated film.

In **section 5.2** the theoretical calculations and the experimental corroboration for desorption under cavitation for different solvents will be presented.

Heterogenous photocatalytic reactions take place at the interface between liquid and solid catalyst. In cooperation with the group of Prof. Eder, Institute for Materials Chemistry, TU Wien, the photodeposition of platinum on titanium nanoparticles and simultaneous photooxidation of methanol was monitored *in situ*. A dedicated flow cell setup was designed (see section 2.1.3 for details of the setup) and the thus obtained results are given in **section 5.3**.

5.1 Porosity, Pore Size Distribution and Investigations of Structure of Water in the Pore

The understanding of the local structure of water, especially in confined spaces like mesopores, is still object of intensive studies.[223,224] Because of its high polarity, water and its manner of

adsorption are strongly influenced by the surface's hydrophobicity and the H-bonding formed with the surface.[221–224] Infrared (IR) spectroscopy has proven an ideal method for studying adsorbed water, both qualitatively and quantitatively, as it is very sensitive to water and its states of hydrogen bonding.[88,222,225–227] The ν(O-H) stretching bands located between 3000 cm^{-1} and 3800 cm^{-1} give rich qualitative information as they are strongly affected by the molecule's environment and the structure of water. Several water complexes have been reported that can be distinguished within this region based on IR spectroscopy.[89,228] The second intense band of water, located at 1640 cm^{-1}, is attributed to the H-O-H bending and is widely insensitive to the molecular surrounding. Therefore, it can be used as a robust measure for the quantity of adsorbed water.

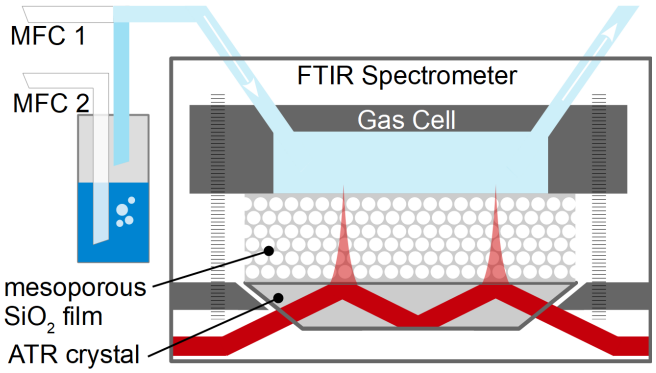

Figure 5.1: Mesoporous silica film coated on ATR crystal (Germanium, 20 active bounces) placed in a flow cell that is inserted into the beam path of an FTIR spectrometer and purged with humidified air.

Although the plentiful information obtained from IR spectroscopy of water in mesoporous silica has been studied, *e.g.* for low temperatures and/or under static conditions, the progression of water's local structure during adsorption/desorption has not been investigated yet. Measurements during adsorption/desorption from the gas phase at controlled humidity are needed to study the degree of pore filling as a function of the local structure of water. While such measurements have been reported for planar, dense SiO_2 films, the strong effects of confined spaces on the structure of adsorbed water sparked interest in a corresponding study on mesoporous materials.[227,229–231] In order to discuss the water adsorption/desorption process quantitatively and qualitatively, geometric parameters such as porosity and pore size distribution (PSD) are needed. The well-characterized optical setup developed in this thesis allows, for the first time, to use ATR spectroscopy for porosimetry. PSD and porosity can be calculated using a modified Kelvin equation based on absolute water contents derived from IR spectra.

5.1.1 Monitoring Water Adsorption and Desorption in Mesoporous Silica

The relative humidity was controlled using two MFC to mix a dry and a moistened flow of N_2 with a constant total flux of 2 L min^{-1} (see section 2.2.3.1 for experimental details). This flow was applied to Germanium ATR crystals coated with mesoporous silica films that were inserted into the beam path of a commercial FTIR spectrometer using a home-built flow cell. Before every adsorption/desorption experiment, the silica films were exposed to a dry airflow

Die approbierte gedruckte Originalversion dieser Dissertation ist an der TU Wien Bibliothek verfügbar.
The approved original version of this doctoral thesis is available in print at TU Wien Bibliothek.
TU Bibliothek Your knowledge hub WIEN

to remove water adsorbed from ambient conditions until the spectra were stable, which was typically achieved after 5 min. Afterwards, relative vapor pressures between $p/p_0 = 0 - 0.95$. The experiments started at $p/p_0 = 0$ with stepwise increasing relative vapor pressure with 2 min holding time at each step, while recording FTIR spectra every 20 s. After having reached $p/p_0 = 0.95$ the water content was stepwise reduced back to 0. The thereby obtained spectra of adsorbed water into the mesoporous silica films as function of relative vapor pressure are given in **Figure 5.2A**.

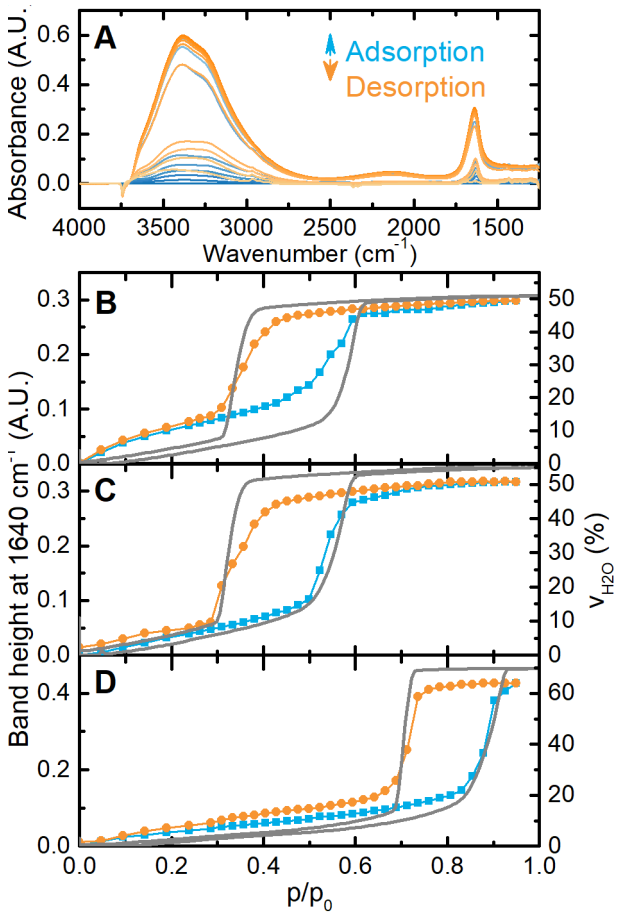

Figure 5.2: (A) Evolution of water spectra with adsorption (blue) and desorption (orange) of water vapor. Relative humidity is stepped by $p/p_0 = 0.1$ between consecutive spectra. Background taken at $p/p_0 = 0$. (B-D) Isotherms of CTAB 3D hexagonal film (B), CTAB cubic film (C), and F127SS film obtained from IR experiments compared with ellipsometric porosimetry (gray).

While the OH stretching vibrations are greatly affected by water local structure and hydrogen bonding to itself and the surface (compare section 5.1.4), the bending vibration does not vary significantly. Therefore, its band height is used in this study as a robust quantitative measure for the amount of water adsorbed in the film.

For all films a reversible isotherms type IV, according to IUPAC classification,[84] with the characteristic steep increase of water content upon capillary condensation and desorption of water at lower relative humidity as characteristic for mesoporous materials was found.[84] The hysteresis between the adsorption and desorption can have different origins: (i) microporosity, which causes desorption by cavitation at p/p_0 =0.3 - 0.4 (compare section 1.3.1.3 and section 5.2), (ii) smaller interconnections that are too low in volume and do not affect the adsorption branch, or (iii) change of meniscus between adsorption and desorption from cylindrical to spherical.[232]

Die approbierte gedruckte Originalversion dieser Dissertation ist an der TU Wien Bibliothek verfügbar.
The approved original version of this doctoral thesis is available in print at TU Wien Bibliothek.

The films were furthermore characterized by EP and the hereby-obtained values for the porosity are given in **Table 5.1** as well. The corresponding isotherms are given in Figure 5.2B-D, showing good agreement with the values obtained by ATR spectroscopy. We attribute the small differences between calculated porosities (*i.e.,* the height of the isotherms) to the wrong assumption for the density of water. In contrast to the density of 1 g cm^{-3} used herein, values of ca. 0.9 g cm^{-3} were reported and explained with either incomplete pore filling[233] or, as discussed later, the different nature of water in confined pores. Remaining differences between results obtained via ATR spectroscopy and EP may originate from small differences in the measurement setups as for EP the p/p_0 was ramped, while IR measurements were performed with a stepwise increase. Further discussion of the differences would require side-by-side measurements in the same laboratory under the same conditions.

5.1.2 Retrieval of Adsorbed Water Concentration and Porosity

Calculating the porosity and PSD of the film required calculating the amount of adsorbed water per film unit volume, $v_{H2O} := V_{H2O}/V_{film}$, from the recorded absorbance. To this end, $d_{e,film}$ was derived (compare Figure 5.1 and according to section 4.1) for all films and are given in **Table 5.1**. v_{H2O} can be calculated as the ratio of measured water absorbance in the silica film, $A_{H2O\ in\ film,}$ and the absorbance one would measure if no water was displaced by the silica network, *i.e.,* if no silica film was on the ATR crystal but a water film with the same thickness (see equation (5.1)). $\varepsilon_{1640cm^{-1}}$ = 21.4 L mol^{-1} cm^{-1} is the specific absorption coefficient of water and c is water's concentration in the film.

$$v_{H2O} = \frac{A_{H_2O\ in\ film}}{A_{pure\ H_2O\ film}} = \frac{A_{H_2O\ in\ film}}{\varepsilon_{H_2O} \cdot c_{pure\ H_2O} \cdot d_{e,film,i}} \qquad \textbf{(5.1)}$$

Herein, $c_{pure\ H_2O}$ = 55.6 mol L^{-1}. Equation (5.1) is valid if the absorption coefficient of adsorbed water is the same as for liquid water, which implies that the density of water ρ = 1 g cm^{-3} does not change.

Table 5.1: Summary of calculated parameters. [a]obtained from the ratio of water concentration in film to complete water film with same thickness.

	$d_{e,film,0}$ initial guess	Corrected $d_{e,film}$ [µm] $p/p_0 = 0$	Corrected $d_{e,film}$ [µm] p/p_0=0.95	c_{H2O} [mol_{H2O}/dm^3_{film}] *at* p/p_0=0.95	Corrected Porosity (%)	Porosity from EP	$n_{porous\ SiO2}$ at p/p_0=0; λ=6.1 µm
CTAB 3d hex	4.99	4.31	5.31	27.2	49	51	1.13
CTAB cubic	5.07	4.42	5.07	28.1	51	55	1.13
F127SS	5.44	4.51	5.68	35.4	63	68	1.09

Porosity P of the film is defined as water fraction at fully filled pores at highest humidity, P:= $v_{H2O}(p/p_0 = 0.95)$. As $d_{e,film}$ and hence v_{H2O} depends, amongst others, on the refractive

Die approbierte gedruckte Originalversion dieser Dissertation ist an der TU Wien Bibliothek verfügbar.
The approved original version of this doctoral thesis is available in print at TU Wien Bibliothek.
TU Bibliothek Your knowledge hub WIEN

index of the film, it changes significantly during adsorption experiments due to the displacement of air ($n_{air} = 1$) by water ($n_{H2O} = 1.33$). To take this into account in the calculation of P, an iterative calculation was employed: The initial porosity P_0 is calculated using equation (5.1) and initial $d_{e,0}$ calculated assuming $n_{film} = n_{SiO2} = 1.26$ at 1640 cm^{-1}.[10] Next, the refractive index $n_{film,1}$ of the film of porosity P_0, filled with water, is calculated using the *Bruggeman* effective medium approximation[199–201] (BEMA) yielding a new estimate of n_{film} and hence $d_{e,1}$ and starting the next iterative cycle.

$$(1 - P_{i-1})\frac{n_{SiO2}^2 - n_{film,i}^2}{n_{SiO2}^2 + 2n_{film,i}^2} + P_{i-1}\frac{n_{H2O}^2 - n_{film,i}^2}{n_{H2O}^2 + 2n_{film,i}^2} = 0 \qquad (5.2)$$

The found porosity converged after three iterations and is given in **Table 5.1**.

Once the porosity was determined, v_{H2O} (p/p_0) of all other measurement points upon pore filling could be calculated. Here, since the pores are only partially filled, three components, SiO_2, N_2 and H_2O, must be considered for calculating the correct $d_{e,film,corr}(p/p_0)$. First, the refractive index of the film of porosity P and empty pores (as obtained using **equation (5.3)**) is used to calculate $d_{e,film}$ (values given in **Table 5.1**). While the refractive index of SiO_2 and its fraction, *i.e.,* 1-P, remain constant, the pore volume fraction P is filled with water while air is replaced. This replacement is assumed to scale with the measured absorption at 1640 cm^{-1} from zero at $A(p/p_0 = 0)$ to one at $A(p/p_0 = 0.95)$. An effective refractive index of the partially filled pore volume, $n_{pore}(p/p_0)$ was defined using the BEMA and the volume fraction $f_{H2O,fill}$ occupied by water:

$$(1 - f_{H2O,fill})\frac{n_{air}^2 - n_{pore}^2(p/p_0)}{n_{air}^2 + 2n_{pore}^2(p/p_0)} + f_{H2O,fill}\frac{n_{H2O}^2 - n_{pore}^2(p/p_0)}{n_{H2O}^2 + 2n_{pore}^2(p/p_0)} = 0 \qquad (5.3)$$

Next, $n_{film}(p/p_0)$ was calculated (compare **Figure 5.3-5.5, left)** using n_{pore} and n_{SiO2} by inserting into a second BEMA (equation (5.4)), which allows to calculate a corrected $d_{e,film,corr}(p/p_0)$ (see **Figure 5.3-5.5, right**), which is then inserted into Lambert-Beer's law to retrieve the volumetric concentration of water in the film, v_{H2O}, plotted in **Figure 5.2**.

$$(1 - P)\frac{n_{SiO2}^2 - n_{film}^2(p/p_0)}{n_{SiO2}^2 + 2n_{film}^2(p/p_0)} + P\frac{n_{pore}^2 - n_{film}^2(p/p_0)}{n_{pore}^2 + 2n_{film}^2(p/p_0)} = 0 \qquad (5.4)$$

Die approbierte gedruckte Originalversion dieser Dissertation ist an der TU Wien Bibliothek verfügbar.
The approved original version of this doctoral thesis is available in print at TU Wien Bibliothek.
TU Bibliothek Your knowledge hub WIEN

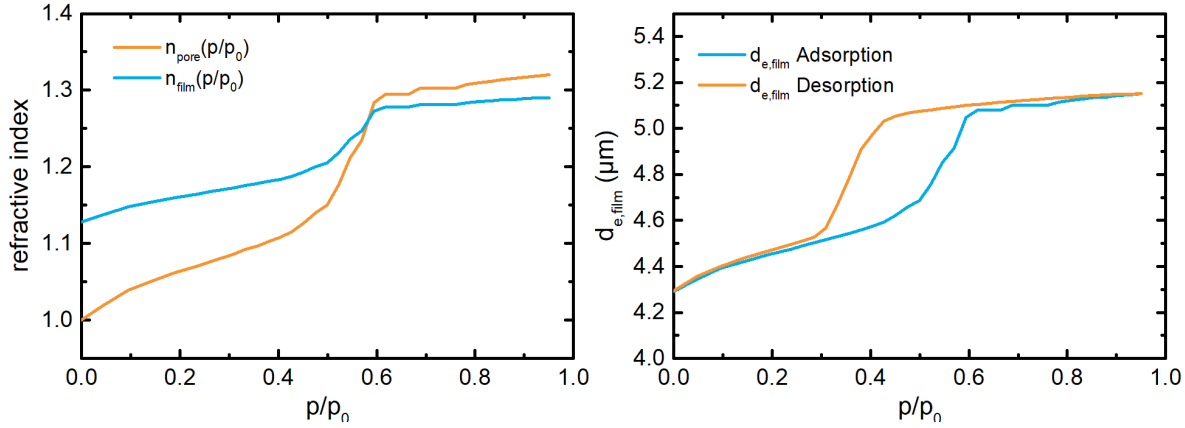

Figure 5.3: Relative vapor pressure dependence of refractive index (left, λ = 6.1 µm) of an increasingly filled mesoporous film and corresponding $d_{e,film}$ (right) for a CTAB 3d hexagonal film.

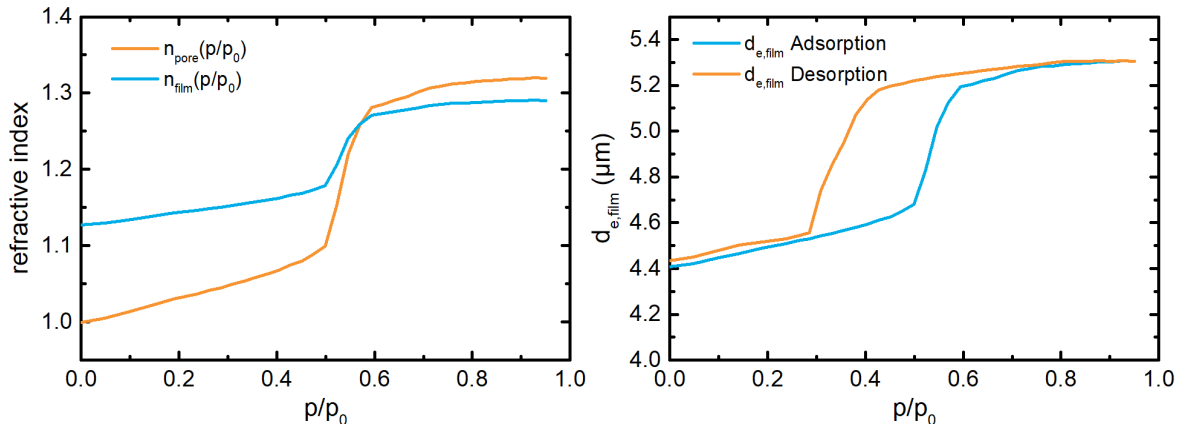

Figure 5.4: Relative vapor pressure dependence of refractive index (left, λ = 6.1 µm) of an increasingly filled mesoporous film and corresponding $d_{e,film}$ (right) for a CTAB cubic film.

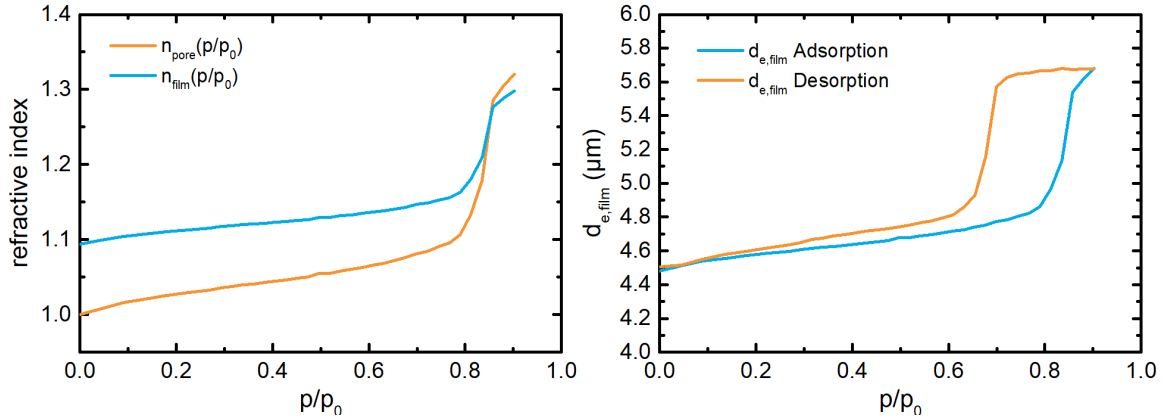

Figure 5.5: Relative vapor pressure dependence of refractive index (left, λ = 6.1 µm) for an increasingly filled mesoporous film and corresponding $d_{e,film}$ (right) for a F127SS film.

5.1.3 Pore Size Distribution

Similar to other porosimetry techniques, the isotherms obtained in the previous section were analyzed by the Kelvin equation to derive the pore size distribution (see section 1.1.3.1 for further fundamental details).[91–94]

Die approbierte gedruckte Originalversion dieser Dissertation ist an der TU Wien Bibliothek verfügbar.
The approved original version of this doctoral thesis is available in print at TU Wien Bibliothek.
TU Bibliothek Your knowledge hub WIEN

The surface tension γ is a function of curvature and was modified by the *Tolman* model with a fixed *Tolman* length δ, with δ=0.096 nm being the O-H bond length.[98,99] For the adsorbate water, $\gamma_{lv} = 7.28 \cdot 10^{-2}$ J m^{-2}, $V_m = 18.04 \cdot 10^{-6}$ m^3 mol^{-1}, $\theta_{CA} = 27°$, $T = 298$ K, $R = 8.314$ kg m^2 s^{-2} mol^{-1} K^{-1}, $\delta = 9.6\ 10^{-11}$ m were inserted. The geometric factor G was calculated according to the Isotropic Inorganic Pore Contraction model,[91] which describes the pore anisotropy resulting from the shrinkage of the film upon calcination (see section 3.2). r_K solely describes the radius of the meniscus and for determining the actual pore diameter the thickness t of the adsorbate layer on the pore wall has to be added: $D_{pore} = 2 \cdot (r_k + t)$.[234] Here, the film thickness t of water adsorbed on planer SiO_2 as a function of relative humidity as obtained from literature was used and fitted with a third order polynomial function (see Figure 5.6):[225,229]

$$t = 6.10 \cdot \left(\frac{p}{p_0}\right)^3 - 9.05 \cdot \left(\frac{p}{p_0}\right)^2 + 5.42 \cdot (p/p_0) - 0.16 \qquad (5.5)$$

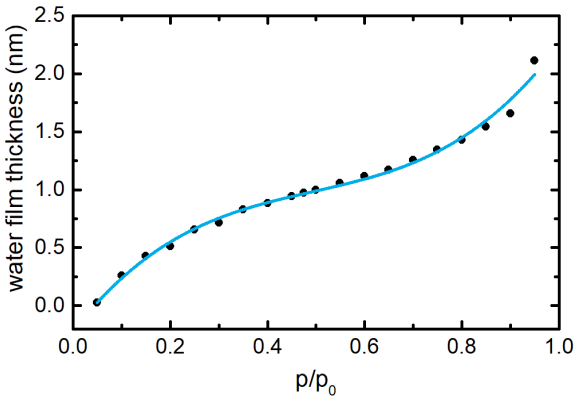

Figure 5.6: Water adsorption on planar SiO_2 obtained from literature.[225,229]

Finally, the pore size distribution is obtained by taking the derivative of the adsorbed volume v_{H2O} with respect to D_{pore} and plotting the result versus D_{pore} on the x-axis (see **Figure 5.7**).

As discussed in the previous section, the hysteresis present in the isotherms is due to pore blocking of smaller interconnections. In this case, the adsorption branch can be used to estimate the pore size whereas the desorption branch is associated to the interconnection size and not the pore size itself.[97,234] For both CTAB films desorption occurs at $p/p_0 \approx 0.4$, the typical experimentally obtained cavitation pressure for water in mesopores (see section 5.2 for calculations). This suggests that water desorbs from these films under cavitation conditions rather than equilibrium conditions. Thus, the interconnection size distributions may be overestimated. In contrast, the desorption branch obtained from the F127SS film occurs at $p/p_0 > 0.3$ ($p/p_0 \approx 0.7$), therefore equilibrium desorption can be concluded and the found PSD reflects the real size distribution of interconnections.

The obtained PSDs for all films were compared with the established EP. The results are included in **Figure 5.7** and show excellent agreement with the PSDs obtained from ATR spectroscopy.

Die approbierte gedruckte Originalversion dieser Dissertation ist an der TU Wien Bibliothek verfügbar.
The approved original version of this doctoral thesis is available in print at TU Wien Bibliothek.
TU Bibliothek Your knowledge hub WIEN

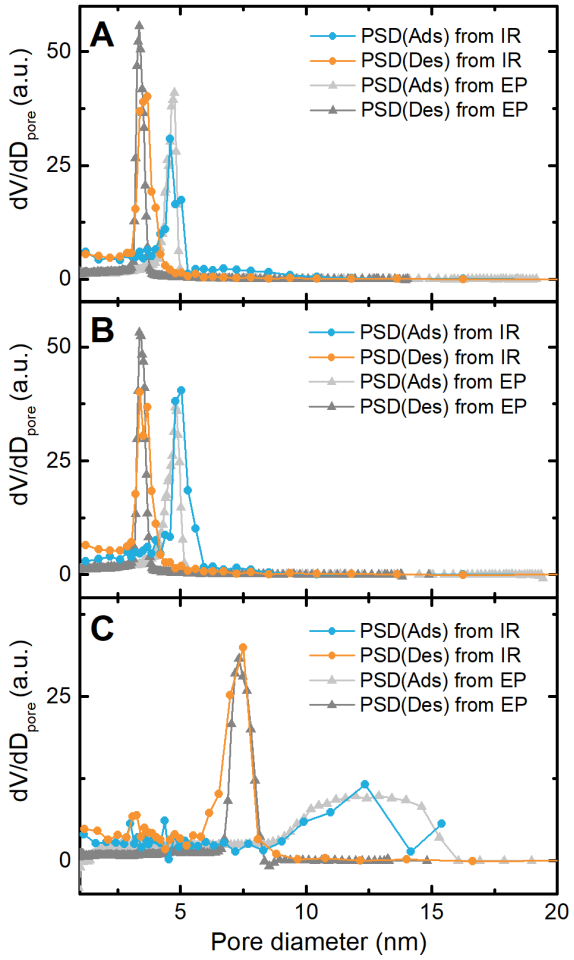

Figure 5.7: Pore Size Distribution of CTAB 3d hexagonal film (A), CTAB cubic film (B) and F127SS film (C) obtained from ATR spectroscopy compared with the results of EP (gray).

5.1.4 Structure of Confined Water during Adsorption

O-H stretching vibrations and the less intense overtone of water's bending vibration between 3000 and 3800 cm^{-1} provide rich information about the structure of silica as well as the adsorbed water[235,236] **Figure 5.8** shows a close-up of the normalized bands in this spectral region corresponding to the adsorption branch in Figure 5.6B.

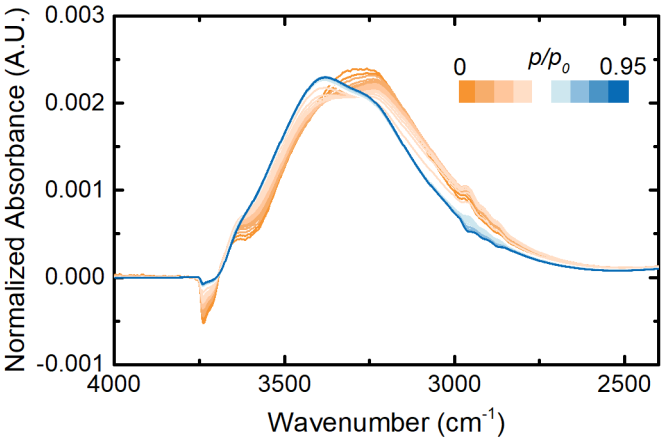

Figure 5.8: FTIR spectra of water adsorption into the 3d hexagonal film in the ν(O-H) region normalized to the entire band area between 2400 and 3800 cm^{-1}. Background spectrum was taken under dry (p/p_0=0) conditions. Bands between 3000 – 2800 cm^{-1} are attributed to hydrocarbons accumulated from the gas phase.

With increased filling of the pores, a clear shift in the maximum of the spectra from 3230 cm^{-1}

Die approbierte gedruckte Originalversion dieser Dissertation ist an der TU Wien Bibliothek verfügbar.
The approved original version of this doctoral thesis is available in print at TU Wien Bibliothek.

to 3400 cm^{-1} is visible. This shift has been previously observed for planar silica surfaces and was attributed to different ratios of "ice-like" water (3230 cm^{-1}) and "liquid-like" water (3400 cm^{-1}) on SiO_2 films upon increasing relative humidity.[229] *Asay et al.* ascribe the "ice-like" character of the first monolayers of the adsorbed water to surface-induced ordering due to strong hydrogen bonding with the silica surface. After the third monolayer of water, this structuring effect decreases and the water band shifts to higher wavenumbers. Furthermore, *Mallamace et al.* studied water confined in mesoporous silica at low temperature using FTIR spectroscopy. They distinguished five bands within the ν(O-H) region: I) 3220 cm^{-1} attributed to fully bonded water of low density having a coordination number close to four, as observed in ice; II) 3400 cm^{-1} for water having an average degree of connection greater than for dimers and trimers but lower than for I), III) 3540 cm^{-1} corresponding to water molecules that are poorly connected to their environment, IV) 3620 cm^{-1} for water in trimers and tetramers, and V) 3140 cm^{-1} for a second local structure of low-density water.[89] The bands observed at higher frequencies (II-IV) were attributed to high-density (HD) water, whose local tetrahedrally coordinated H-bonding structures is not fully developed.[89] Here, water molecules exist in small clusters of up to four molecules. Bands I+V were attributed to low density water (LD water, with a density close to the one of ice).[88,89,237]

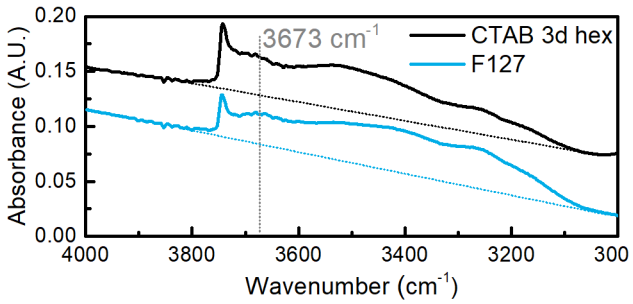

Figure 5.9: IR spectra of dry films. Background spectra is an uncoated Ge ATR crystal.

In the present study, an additional band at 3745 cm^{-1} was observed that corresponds to isolated silanol groups ν(Si-O-H) that exist only in anhydrous conditions. Due to their hydrophilic nature, these silanol groups are hydrated immediately if water vapor is present and since the background spectra are recorded on dry films this leads to the negative peak observed in Figure 5.8.[235] Since the silanol groups influence the hydrophilicity and hence the hydration mechanism of silica, the silanol content was calculated for the CTAB 3d hexagonal and the F127SS film: This content can be determined with the means of IR spectroscopy. Here, typically the band height at 4500 cm^{-1} or 3673 cm^{-1} and the absorption coefficient of the latter of $\varepsilon = 78$ L mol^{-1} cm^{-1} is used.[238,239] Due to the lack of spectral information above 4000 cm^{-1},[g] the band at 3673 cm^{-1} was used for silanol content determinations (see **Figure 5.9** for spectra). The results on Si-OH groups per nm^2 are given in **Table 5.2**. The obtained values of 13 and 12 OH-groups nm^{-2} are on the upper end of the range of theoretical

[g] For spectra recorded after this study of the same calcined films, no bands > 4000 cm^{-1} could be observed.

Die approbierte gedruckte Originalversion dieser Dissertation ist an der TU Wien Bibliothek verfügbar.
The approved original version of this doctoral thesis is available in print at TU Wien Bibliothek.
TU Bibliothek Your knowledge hub WIEN

considerations and typically obtained values.[240]

Table 5.2: Calculations of the silanol content. Surface area for calculation on OH/nm² were obtained from the number of pores and the corresponding geometry (compare Table 5.7).

	$d_{e,corr}$ (3673 cm^{-1}) for p/p_0= 0	c_{OH} (mol/L)	mol$_{OH}$/film	OH/nm²
CTAB 3d hex	2.16	2.09	$1.7 \cdot 10^{-6}$	13
F127SS	2.07	1.67	$2.0 \cdot 10^{-6}$	12

No bands were observed > 4000 cm^{-1}, which would allow for more accurate silanol content quantification according to literature, the OH stretching region between 3800 - 3000 cm^{-1} for both films was integrated yielding 16.7 and 17 A.U. cm^{-1}. Note that calculating the silanol content is difficult because only values for the band at 3673 cm^{-1} are well documented in literature and many reports state that using the range between 3800 - 3000 cm^{-1} for silanol content determination is highly influenced by the silanol content itself and by remaining water.[240] It is therefore stressed that the absolute number for OH groups/nm² are somewhat uncertain. However, given the very similar band areas and silanol contents obtained in Table 5.2, the surface hydrophilicity and hence the wetting mechanism for both films was assumed to be similar and comparable.

The ν(O-H) region of the spectra obtained for the smallest (CTAB 3d hexagonal) and the biggest (F127) pore system were deconvolved, in accordance with Refs. [88,89], by fitting the spectra using six Gaussian profiles with fixed peak positions (3140, 3220, 3400, 3540, 3620 and 3745 cm^{-1}) and widths.[88,89] Here, the band fitting was adopted where different spectral bands were curve assigned to single absorption bands, where contributions of the asymmetric and symmetric stretch were combined into a single band. The results are given in **Figure 5.10** and **Figure 5.11**, respectively.

All band areas except for the isolated silanol groups at 3745 cm^{-1} increase with p/p_0 (compare Figure 5.10A and Figure 5.11A). As can be seen from Figure 5.10B and Figure 5.11B, the relative amount of LD water changes significantly during pore condensation. Before pore condensation at p/p_0 = 0.5 or p/p_0 = 0.8, respectively, (see Figure 5.2B and C) the major fraction of water species corresponds to LD water. After pore condensation, the main fraction is the sum of peak III and IV that corresponds to HD, liquid-like water with low order. If considering the simplest picture of pore filling, a complete layer of water on the materials surface is assumed before a subsequent layer is formed (compare **Figure 5.12A**). Based on this hypothesis, several monolayers of water, most of which are strongly associated with the surface and hence contributing to the fraction of LD water, are forming before capillary condensation occurs. At this point, the remaining center part of the pores is filled predominately with bulk-like, less structured HD water. A stable concentration of the LD water after pore condensation would verify this hypothesis. However, the presented results do not fully agree with this simple picture but show an increase of the LD water at and after capillary condensation at p/p_0 = 0.5 and p/p_0 = 0.8 as visible in Figure 5.10A and Figure

Die approbierte gedruckte Originalversion dieser Dissertation ist an der TU Wien Bibliothek verfügbar.
The approved original version of this doctoral thesis is available in print at TU Wien Bibliothek.
TU Bibliothek WIEN Your knowledge hub

5.11A, respectively. From the abrupt increase of the LD fraction at capillary condensation one can assume that the center of the pore is not exclusively filled with HD water but also with LD water. In return, the HD fraction is also growing less strongly from $p/p_0 = 0$ on.

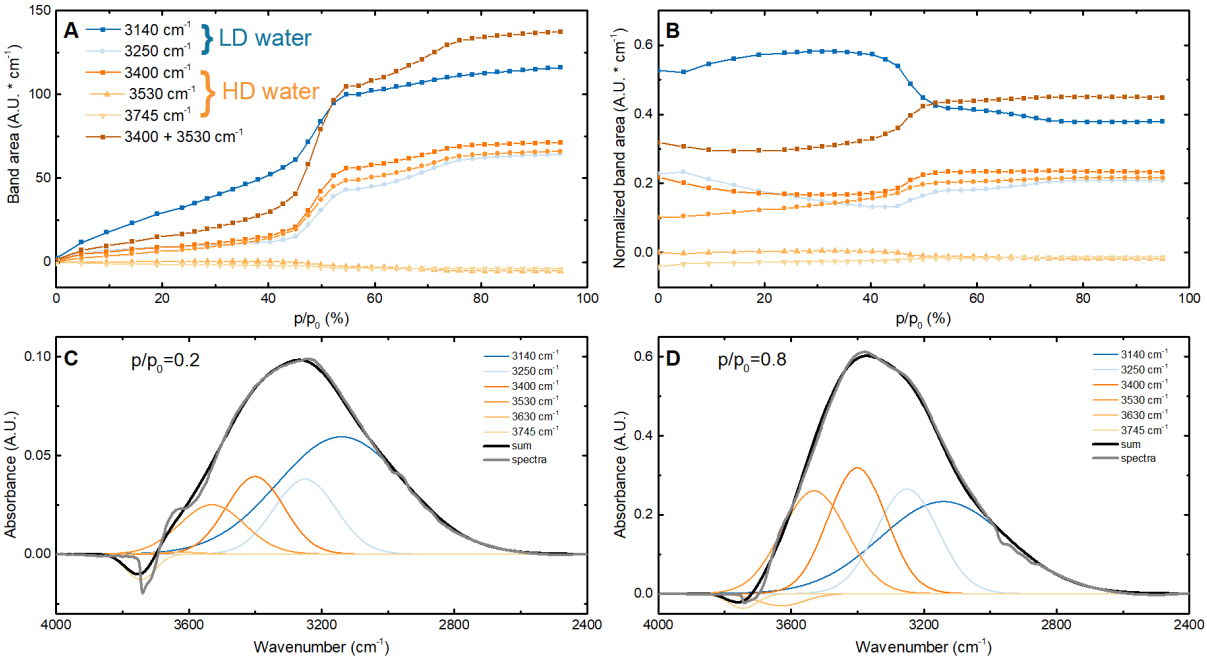

Figure 5.10: Deconvolution of ν(O-H) region obtained for CTAB 3d hexagonal film during increasing p/p_0: peak area for different bands (A), band area normalized to the total band areas (B), multi-Gaussian fit of spectra before (C) and after (D) pore condensation.

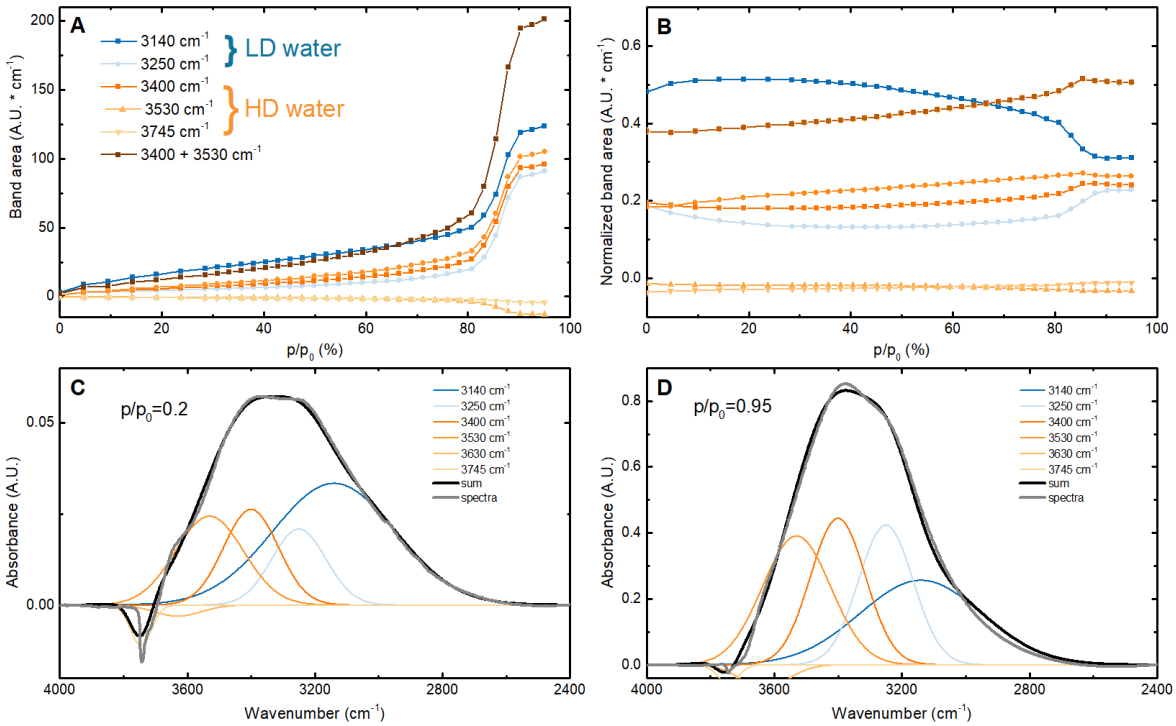

Figure 5.11: Deconvolution of ν(O-H) region obtained for F127SS film during increasing p/p_0: peak area for different bands (A), band area normalized to the total band areas (B), multi-Gaussian fit of spectra before (C) and after (D) pore condensation.

Die approbierte gedruckte Originalversion dieser Dissertation ist an der TU Wien Bibliothek verfügbar.
The approved original version of this doctoral thesis is available in print at TU Wien Bibliothek.
TU Bibliothek Your knowledge hub WIEN

Kocherbitov et al. found a similar adsorption behavior and concluded that in contrast to the simple hypothesis, the pore surface is only partially covered with water and hydrophobic patches at the pore walls, *i.e.,* spots with low silanol density, are wetted at higher relative vapor pressures after capillary condensation (compare **Figure 5.12B**).[233] This conclusion is in accordance with the presented findings: The concentration of surface-associated water species, *i.e.,* water, still increases after capillary condensation (Figure 5.10A and Figure 5.11A).

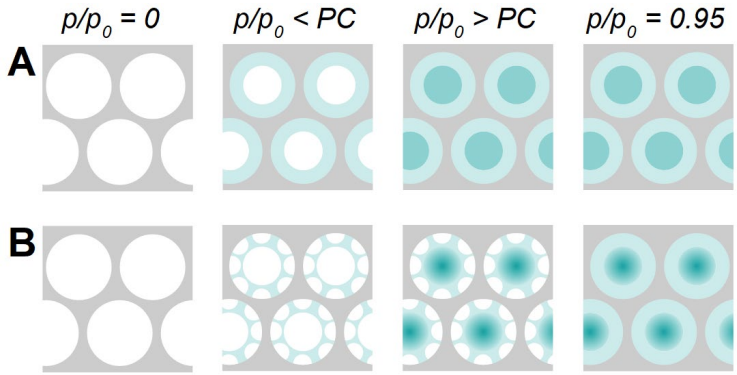

Figure 5.12: Schematic representation of different hypothesis of water adsorption in mesopores for LD water (light blue) and HD water (dark blue) adsorption at different p/p_0. (A) Before pore condensation (PC) LD water fully convers the pore surface. (B) Pore surface is fully covered after pore condensation.

5.1.5 Calculation of Surface-Induced Ordered Water Monolayers

The obtained water concentrations can be used to estimate the thickness of the LD water film with a monolayer thickness of 0.28 nm.[241] Only at high humidity ($p/p_0 = 0.95$) the pores are fully filled, and monolayers of water are not disrupted by hydrophobic patches (compare Figure 5.12B). Therefore, this analysis was only performed for the fully filled pores. For the calculations, a porous volume comprised of spheroids (according to IIC model[91]) was assumed with pore diameter of $b = 4.7$ nm and $a = 6.3$ nm for the 3d hexagonal film, and $b = 12.5$ nm and $a = 19.5$ nm for the F127SS film, respectively, with a retrieved from the anisotropy factor $A_{pore} = a/b$ (see Table 3.4).

From ATR crystal dimensions ($l \times w = 2 \times 1$ cm^2) and measured film thickness th, the film volume as well as the pore volume were calculated using $V_{film} = l \cdot w \cdot th$ and $V_{pore,tot} = P \cdot V_{film}$.

Table 5.3: Calculated film parameters.

	l nm	w nm	th nm	V_{film} nm^3	porosity	$V_{pore,tot}$ nm^3
CTAB 3d hex	$2 \cdot 10^7$	$1 \cdot 10^7$	400	$8 \cdot 10^{16}$	0.5	$4 \cdot 10^{16}$
F127SS	$2 \cdot 10^7$	$1 \cdot 10^7$	600	$1.2 \cdot 10^{17}$	0.64	$7.68 \cdot 10^{16}$

The pore volume V_{pore} and the number of pores within the entire film N_{pore} were calculated using equation (5.6) and (5.7):

$$V_{pore} = \frac{4}{3} \cdot \pi \cdot b \cdot a^2 \qquad (5.6)$$

Die approbierte gedruckte Originalversion dieser Dissertation ist an der TU Wien Bibliothek verfügbar.
The approved original version of this doctoral thesis is available in print at TU Wien Bibliothek.
TU Bibliothek Your knowledge hub WIEN

$$N_{pore} = \frac{V_{pore,tot}}{V_{pore}} \quad (5.7)$$

Table 5.4: Calculated pore parameters.

	pore diameter d_a nm	pore diameter d_b nm	pore radius a nm	pore radius b nm	V_{pore} nm³	N_{pore}
CTAB 3d hex	6.25	4.7	3.1255	2.35	96.16	$4.16 \cdot 10^{14}$
F127SS	19.5	12.5	9.75	6.25	2488.73	$3.09 \cdot 10^{15}$

For calculating the volume of LD water for one pore for each subsequent monolayer, $V_{LDwater,ML,i}$ with a monolayer number i, a molar volume of ice $V_{m,ice} = 19.6$ cm³ mol^{-1}, was retrieved from the molar mass of water $M_W(H_2O) = 18.02$ g mol^{-1} and density of ice ρ(ice) $= 0.92$ g cm^3.[242]

$$V_{LDwater,MLi} = V_{pore} - \frac{4}{3} \cdot \pi \cdot (b - i \cdot d_{ML}) \cdot (a - i \cdot d_{ML})^2 \quad (5.8)$$

$$V_{LDwater,MLi,tot} = V_{LDwater,MLi} \cdot N_{pore} \quad (5.9)$$

Table 5.5: Calculated volume of LD water monolayers.

ML	thickness L nm	CTAB nm³	F127 nm³
1	0.28	$1.08 \cdot 10^{16}$	$7.60 \cdot 10^{15}$
2	0.56	$1.95 \cdot 10^{16}$	$1.47 \cdot 10^{16}$
3	0.84	$\mathbf{2.63 \cdot 10^{16}}$	$2.13 \cdot 10^{16}$
4	1.12	$3.14 \cdot 10^{16}$	$2.74 \cdot 10^{16}$
5	1.4	$3.51 \cdot 10^{16}$	$3.31 \cdot 10^{16}$
6	1.68	$3.76 \cdot 10^{16}$	$3.83 \cdot 10^{16}$
7	1.96		$\mathbf{4.31 \cdot 10^{16}}$
8	2.24		$4.76 \cdot 10^{16}$

The water concentration c_{H_2O} within the film at $p/p_0 = 0.95$ is given in Table 5.1 and was calculated using Lambert-Beer's law. This concentration was used to calculate the amount of water within the film $n_{LDwater,film}$ in mol$_{H2O}$. The molar fraction of LD water $f_{LDwater}$ is the sum of band areas corresponding to LD water (3140 cm^{-1} and 3250 cm^{-1}) normalized by the overall band area (3000– 3800 cm-1) as given in Figure 5.10B and Figure 5.11B.

$$n_{LDwater,film} = \frac{c_{H2O}}{V_{film}} \cdot f_{LDwater} \quad (5.10)$$

$$V_{LDwater} = n_{LDwater,film} \cdot V_{m,ice} \quad (5.11)$$

Die approbierte gedruckte Originalversion dieser Dissertation ist an der TU Wien Bibliothek verfügbar.
The approved original version of this doctoral thesis is available in print at TU Wien Bibliothek.
TU Bibliothek Your knowledge hub WIEN

Table 5.6: Volume of LD water calculated from IR absorbance.

	$n_{water\ in\ film}$ mol	*LD fraction*	$n_{LDwater,film}$ mol/film	$volume_{LD\ water}$ nm³
CTAB 3d hex	$2.18 \cdot 10^{-6}$	0.59	$1.28 \cdot 10^{-6}$	$\mathbf{2.52 \cdot 10^{16}}$
F127SS	$4.25 \cdot 10^{-6}$	0.54	$2.29 \cdot 10^{-6}$	$\mathbf{4.49 \cdot 10^{16}}$

By comparing the calculated volume of LD water in each film (Table 5.6) with the values in Table 5.5, the number of monolayers can be estimated. If assuming a monodisperse system, the calculations yield 3 and 7 monolayers for the CTAB and F127SS film, respectively. These values represent an upper limit for the numbers of LD monolayers because pore interconnections and microporosity were excluded which lead to an underestimation of the pore surface. Even for this upper limit assumption, the number of monolayers for the CTAB film was smaller than the number of 4 monolayers reported for planar SiO_2.[229]

However, PSD confirmed pore interconnections > 2 nm for the F127SS film and the microporosity of both films could be assessed from isotherms using the *t*-plot method (see **Figure 5.13**) by drawing a tangent along the adsorption branch before pore condensation. The intercept of the y-axis corresponds to the microporosity and was found to be 8 % and 4 % of the total porosity for the CTAB and the F127SS film, respectively.

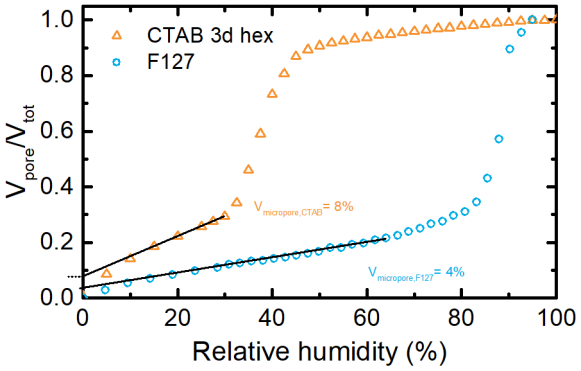

Figure 5.13: Water adsorption isotherms normalized to the total pore volume V_{tot}. Tangents are set to derive the microporous fraction of the porosity of the film.

Microporosity was simulated by a bidisperse system with pore diameters as given above and 1 nm micropores constituting 8 % and 4 %, respectively, of the total pore volume was assumed. This assumption may be not correct but is given as an example (compare Table 5.7 - 5.9 for calculations according to the monodisperse system).

Table 5.7: Calculated film parameters including microporosity.

	l nm	*w* nm	*th* nm	V_{film} nm^3	porosity	$V_{pore,tot}$ nm^3
CTAB 3d hex mesopores	$2 \cdot 10^7$	$1 \cdot 10^7$	400	$8 \cdot 10^{16}$	0.42	$3.4 \cdot 10^{16}$
CTAB 3d hex micropores					0.08	$6.4 \cdot 10^{15}$
F127SS mesopores	$2 \cdot 10^7$	$1 \cdot 10^7$	600	$1.2 \cdot 10^{17}$	0.60	$7.2 \cdot 10^{16}$
F127SS micropores					0.04	$4.8 \cdot 10^{15}$

Die approbierte gedruckte Originalversion dieser Dissertation ist an der TU Wien Bibliothek verfügbar.
The approved original version of this doctoral thesis is available in print at TU Wien Bibliothek.
TU Bibliothek Your knowledge hub WIEN

Table 5.8: Calculated pore parameters including microporosity.

	pore diameter d_a	pore diameter d_b	pore radius a	pore radius b	V_{pore}	N_{pore}
	nm	nm	nm	nm	nm^3	
CTAB 3d hex meso	6.25	4.7	3.13	2.35	96.2	$3.49 \cdot 10^{14}$
CTAB 3d hex micro	1	1	0.5	0.5	0.5	$1.22 \cdot 10^{16}$
F127SS meso	19.5	12.5	9.75	6.25	2488.7	$2.89 \cdot 10^{13}$
F127SS micro	1	1	0.5	0.5	0.5	$9.17 \cdot 10^{15}$

Table 5.9: Calculated volume of LD water monolayers (MLs) including micropores.

ML	thickness L	CTAB mesoporous	CTAB microporous	CTAB sum	F127 mesoporous	F127 microporous	F127 sum
	nm	nm^3					
1	0.28	$9.07 \cdot 10^{15}$	$5.9 \cdot 10^{15}$	$1.5 \cdot 10^{16}$	$7.1 \cdot 10^{15}$	$4.4 \cdot 10^{15}$	$1.2 \cdot 10^{16}$
2	0.56	$1.64 \cdot 10^{16}$	$6.4 \cdot 10^{15}$	$\mathbf{2.3 \cdot 10^{16}}$	$1.4 \cdot 10^{16}$	$4.8 \cdot 10^{15}$	$1.9 \cdot 10^{16}$
3	0.84	$2.21 \cdot 10^{16}$	$8.4 \cdot 10^{15}$	$3.0 \cdot 10^{16}$	$2.0 \cdot 10^{16}$	$6.3 \cdot 10^{15}$	$2.6 \cdot 10^{16}$
4	1.12	$2.64 \cdot 10^{16}$	$1.9 \cdot 10^{16}$	$4.5 \cdot 10^{16}$	$2.6 \cdot 10^{16}$	$1.4 \cdot 10^{16}$	$\mathbf{4.0 \cdot 10^{16}}$
5	1.4				$3.1 \cdot 10^{16}$	$3.3 \cdot 10^{16}$	$6.4 \cdot 10^{16}$
6	1.68				$3.6 \cdot 10^{16}$	$6.8 \cdot 10^{16}$	$1.0 \cdot 10^{17}$
7	1.96				$4.0 \cdot 10^{16}$	$1.2 \cdot 10^{17}$	$1.6 \cdot 10^{17}$

Again, the volume of LD monolayers for different numbers of layers were compared with the experimentally obtained volume of water (Table 5.6). This yielded 2 and 4 monolayers for the CTAB and F127SS film, respectively. The result for the large pore system (F127SS film) is in agreement with the previously reported number of 4 surface-induced ordered monolayers found on planer SiO_2.[229] However, the number of LD water monolayers found in the small pore film is considerably smaller. For the CTAB 3d hexagonal film 3 and 2 monolayers of LD water with and without microporosity, respectively, were observed. These values agree well with the generally observed number of two surface-affected monolayers in confined fluids at pore surfaces.[243]

Note that the thickness of surface-induced structured water do not allow for conclusions about the overall water thickness t as needed for PSD calculations in the previous section.

5.1.6 Conclusion

In conclusion, a changing of structure of water in mesoporous silica films as function of relative water vapor pressure *in situ* during adsorption and desorption was observed. In addition to the structural study of adsorbed water, ATR-FTIR spectroscopy was also used for determining the porosity and pore size distribution of the mesoporous silica films under study. The porosity and pore size distribution retrieved using the Kelvin equation were in excellent agreement

Die approbierte gedruckte Originalversion dieser Dissertation ist an der TU Wien Bibliothek verfügbar.
The approved original version of this doctoral thesis is available in print at TU Wien Bibliothek.
TU Bibliothek Your knowledge hub WIEN

with values obtained from established ellipsometric porosimetry. The high sensitivity of the stretching vibrations to the water molecule's states of hydrogen bonding enabled distinguishing bulk liquid and surface-induced ordered water, depending on its proximity to the surface. The IR spectra between 3000 cm^{-1} and 3800 cm^{-1} were deconvolved giving the humidity-dependent development of different water species in SiO_2 mesopores. Based on this, the number of surface-induced ordered water monolayers was estimated and pores with a diameter of ca. 13 nm yielded values that coincide with reported values for water on planar SiO_2 surfaces, while smaller pores showed a significantly lower number of ordered water layers. Given these results, a drastic change in the water structure in confined spaces between a 5 and 13 nm pore diameter was observed.

This work was later expanded for the study of other molecules as shown in the next chapter.

Die approbierte gedruckte Originalversion dieser Dissertation ist an der TU Wien Bibliothek verfügbar.
The approved original version of this doctoral thesis is available in print at TU Wien Bibliothek.
TU Bibliothek Your knowledge hub WIEN

5.2 Desorption under Cavitation for Different Solvents

Cavitation is defined as the spontaneous change of a metastable liquid to a small vapor-filled cavity. The cavitation pressure p_l^{cav} is a mechanical tension (= negative pressure) that a liquid can sustain before cavitation occurs. The phenomenon of cavitation can be observed in desorption isotherms for pore radii or pore interconnection radii below a critical liquid droplet radius, hence pore radius, r_c, that only depends on the surface tension of the adsorbate and pressure difference (*Laplace* equation):[99,244]

$$r_c = \frac{2 \cdot \gamma_{lv}(r_c)}{(p_l - p_v)} \tag{5.12}$$

where γ_{lv} corresponds to the surface energy per unit surface area at the liquid-vapor interface of a droplet, p_v is the partial pressure in the gas above the liquid droplet and p_l is the pressure in the liquid droplet, when the gas and liquid are at the same chemical potential. For N_2 sorption at 77 K, the critical pore diameter was found to be 4 - 5 nm and cavitation occurs at the relative partial pressure $p/p_0 = 0.4$ - 0.5.[245]

For pressures far from the critical point $p_v - p_l \sim p_0(T) - p_l$, with the saturation vapor pressure p_0. The free energy of a bubble can be written as

$$E = 4 \cdot \pi \cdot R^2 \cdot \gamma_{lv} - \frac{4 \cdot \pi}{3} R^3 \cdot |p_0 - p_l| \tag{5.13}$$

where R is the radius of the bubble. The first term represents the energy cost of introducing the interface between liquid and vapor, while the second term corresponds to the free energy gain from converting liquid to gas. E has its maximum value E_b at the critical radius r_c (equation (5.12)):[246]

$$E_b = \frac{16 \cdot \pi \cdot \gamma_{lv}^3}{3 \cdot (p_0 - p_l)^2} \tag{5.14}$$

E_b represents an energy barrier to nucleate a microscopic seed from which a phase transition (liquid → gas) can grow and eventually yielding the macroscopic event of cavitation. For bubbles smaller than r_c, the bubble will be driven by thermodynamic forces to shrink rather than to grow and no macroscopic event (=cavitation) can take place.[246] The rate of nucleation Γ per unit volume and time can be derived from classical nucleation theory:[246–248]

$$\Gamma \cdot V_{pore,total} \cdot t = \Gamma_0 \cdot V_{pore,total} \cdot t \cdot e^{-\frac{E_b}{k_b T}} \tag{5.15}$$

Herein, Γ_0 is a kinetic prefactor and can be understood as the attempt frequency for bubble formation per unit time. Γ_0 can be estimated to be $\frac{k_b T}{h \cdot v_N} = 2.08 \cdot 10^{41}$ m^{-3} s^{-1} (for water), with the *Planck's* constant h and the density of independent nucleation sites $\frac{1}{v_N} = \frac{\rho \cdot N_A}{M_w}$ and the liquid density ρ, *Avogadro's* number N_A and molecular weight M_w. Cavitation becomes probable when in a porous volume $V_{pore,total}$ in a given time t, $\Gamma \cdot V_{pore,total} \cdot t > 1$. By inserting $\Gamma \cdot V_{pore,total} \cdot t = 1$ into equation (5.13) and solving for E_b this yields:

Die approbierte gedruckte Originalversion dieser Dissertation ist an der TU Wien Bibliothek verfügbar.
The approved original version of this doctoral thesis is available in print at TU Wien Bibliothek.
TU Bibliothek Your knowledge hub WIEN

$$E_b = k_b \cdot T \cdot \ln(\Gamma_0 \cdot V_{pore,total} \cdot t) \tag{5.16}$$

Inserting equation (5.16) into (5.14) and solving for $p_0(T) - p_l$ yields equation (5.17) with $p_l = p_l^{cav}$, the cavitation pressure:

$$p_l^{cav} - p_0 = \sqrt{\frac{16 \cdot \pi \cdot \gamma_{lv}^3}{3 \cdot k_b \cdot T \cdot \ln(\Gamma_0 \cdot V_{pore,total} \cdot t)}} \approx p_l^{cav} \tag{5.17}$$

As p_0 is negligible as $p_l \gg p_0$.The logarithmic dependence of E_b allows retrieving p_l^{cav} without knowing $V_{pore,total}$ or Γ_0 precisely, as very different $\Gamma_0 \cdot V_{pore,total} \cdot t$ yield nearly the same theoretical cavitation pressure. p_l^{cav} was calculated for water, methanol, isopropanol and toluene adsorbed into mesoporous silica with $T = 293.15$ K, $V_{pore,total} = 4 \cdot 10^{-11}$ m^3 (for CTAB 3d hexagonal film, see section 5.1.4), and $t = 1$ s and is given in Table 5.10.

Table 5.10: Parameters of different solvents used for calculating the cavitation pressure. * $\boldsymbol{\delta} = 0.2 \cdot \boldsymbol{\sigma}$, for nonpolar molecules;[249]. $^+$ $\boldsymbol{\delta} = 0.36 \cdot \boldsymbol{\sigma}$ for polar molecules. $\boldsymbol{\sigma}$... kinetic molecular diameter, for values of all molecules see Ref. [250] and [251]

	$\gamma_{lv,0}$ (J m^{-2})	p_0 (Pa)	Mw (g mol^{-1})	ρ (g cm^{-3})	δ (nm)	θ_{CA}	p_l^{cav} (Pa)	r_c (nm)
water	$72.80 \cdot 10^{-3}$	206.5	18	1	0.096$^+$	27	**$-1.53 \cdot 10^8$**	**0.95**
methanol	$22.70 \cdot 10^{-3}$	$13.02 \cdot 10^3$	32.04	0.79	0.137$^+$	0	**$-2.68 \cdot 10^7$**	**1.69**
isopropanol	$21.70 \cdot 10^{-3}$	$4.21 \cdot 10^3$	60.10	0.79	0.169$^+$	0	**$-2.74 \cdot 10^7$**	**1.68**
toluene	$28.52 \cdot 10^{-3}$	$2.89 \cdot 10^3$	92.14	0.87	0.118*	0	**$-3.80 \cdot 10^7$**	**1.50**
liquid N_2 (at 77 K)	$8.94 \cdot 10^{-3}$	$101.33 \cdot 10^3$	28	0.81	0.073*	0	**$-1.32 \cdot 10^7$**	**1.35**

By inserting p_l^{cav} in the *Laplace* equation (5.12), the critical bubble radius r_c can be retrieved. Furthermore, the obtained p_l^{cav} can be inserted for p_l into the *Kelvin-Laplace* equation to retrieve the relative partial pressure p/p_0 at which cavitation can be expected:

$$p_l - p = \frac{R_g\, T}{V_m \cdot \cos(\theta_{CA})} \ln\left(\frac{p}{p_0}\right) \approx p_l^{cav} \tag{5.18}$$

The approximate equal sign holds for $p_l \gg p$, which is the case for $p_l = p_l^{cav}$. With the saturation pressure p_0 at 293 K given in Table 5.10, p/p_0 at which cavitation occurs was calculated for all four solvents and the results are given in **Table 5.12**.

To verify these calculations, desorption isotherms for four different solvents (methanol, isopropanol, toluene and water) were recorded according to section 5.1. The isotherms obtained for the CTAB 3d hexagonal film are given in **Figure 5.14**. The points from where on desorption (defined as first p/p_0 data point from which the curves starts decreasing) via cavitation occurs are marked with arrows and the corresponding p/p_0 are summarized in Table 5.12.

Die approbierte gedruckte Originalversion dieser Dissertation ist an der TU Wien Bibliothek verfügbar.
The approved original version of this doctoral thesis is available in print at TU Wien Bibliothek.
TU Bibliothek Your knowledge hub WIEN

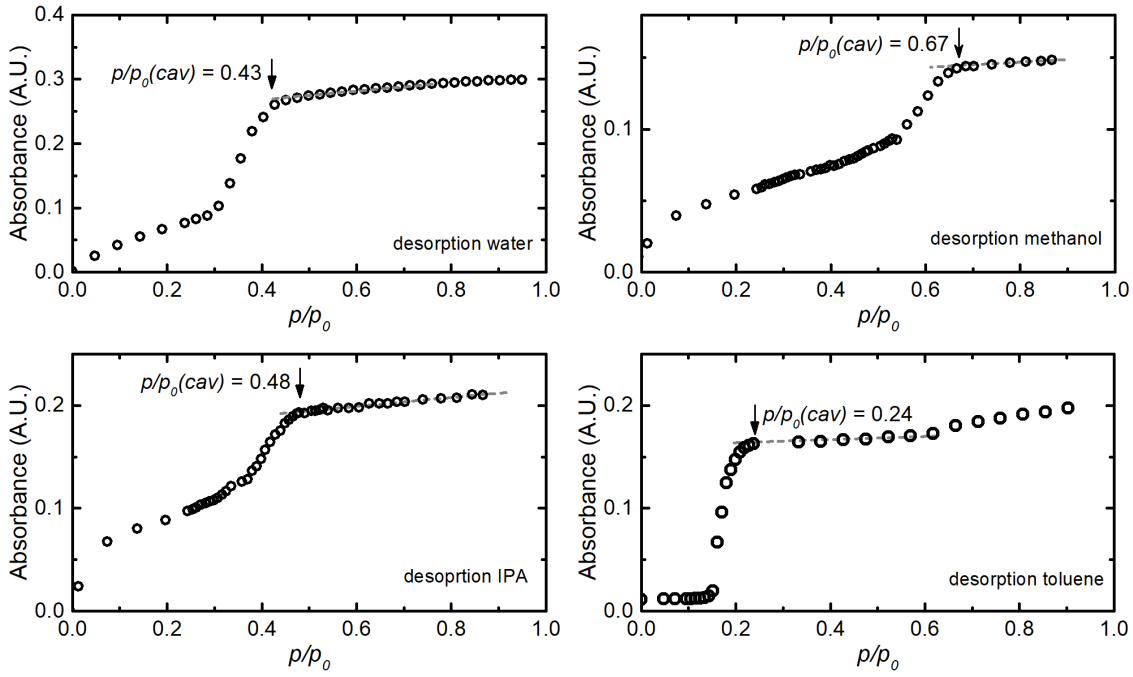

Figure 5.14: Desorption branch of isotherms obtained with water, methanol, isopropanol and toluene as adsorbate. Onsets of pore emptying under cavitation are indicated by arrows.

The calculated and found values for $p/p_0(cav)$ for methanol, isopropanol and toluene are in rough agreement. The obtained $p/p_0(cav)$ for water is considerably higher. As discussed in section 1.3.1.3 and section 5.1, the surface tension, with which the cavitation pressure scales to the power of 3/2, is a function of the size of the liquid bubble and hence the filled pore radius. For the calculations above, the bulk surface tensions $\gamma_{lv.0}$ were inserted, which yields the lower limits of p/p_0(cavitation) if assuming that the surface tension decreases with decreasing droplet size. The relative vapor pressures p/p_0(cav) were calculated for corrected surface tensions using equation (1.34) based on the *Tolman* length δ (see section 1.3.1.3 and section 5.1.3 for further details, for the CTAB 3d hexagonal film: $G = 1.33$ and $r_k = r_c$). The Tolman length for the four solvents are given in Table 5.10 and the corrected $p/p_0(cav)$ are given in Table 5.11. The correction yielded values that are in very good agreement with the experimentally obtained values.

Table 5.11: Calculated and found p/p_0 at which cavitation occurs in a 3d hexagonal CTAB film. T = 293.15 K.

	calculated $p/p_0(cav)$	**calculated $p/p_0(cav)$ with γ_{lv} correction**	**found $p/p_0(cav)$**
water	0.32	0.44	0.43
methanol	0.64	0.68	0.67
isopropanol	0.45	0.52	0.48
toluene	0.19	0.25	0.24
liquid N_2 (at 77 K)	0.49	0.52	typically found in literature: 0.5[84,245]

Die approbierte gedruckte Originalversion dieser Dissertation ist an der TU Wien Bibliothek verfügbar.
The approved original version of this doctoral thesis is available in print at TU Wien Bibliothek.

Note that the *Tolman* length is still a highly debated constant and values, especially for solvents other than water, are rare to non-existent in literature.[252,253] However, for water, the community seems to have agreed on $\delta = 0.1$ nm and this value is often referred to as *molecular diameter*. In fact, the kinetic molecular diameter of water is $\sigma(H_2O) = 0.265$ nm and referring the *Tolman* length to the molecular diameter appears somewhat misleading. Actually, a length scale of 0.1 nm resembles the O-H bond length being 0.096 nm,[254] which corresponds to $0.36 \cdot \sigma(H_2O)$. *Pratasova et. al* reported that δ(ethanol) $= 0.2$ $(0.47 \cdot \sigma)$ nm best describes their ethanol adsorption isotherms but δ was fitted only to the physisorption data.[253] Furthermore, theoretical considerations predicted and molecular dynamics simulations confirmed that $\delta = 0.2 \cdot \sigma$ for nonpolar molecules.[249]
In the absence of exact values in literature and by attempting to relate δ to molecular properties, here, δ(polar molecules) $= 0.36 \cdot \sigma$ and δ(nonpolar molecules) $= 0.2 \cdot \sigma$ was defined for correcting the surface tension, with water, methanol and isopropanol considered polar and toluene and liquid N_2 being nonpolar. This definition yielded corrected $p/p_0(cav)$ that corresponded very well with the experimentally obtained data, except for isopropanol. If considering isopropanol nonplar too, $p/p_0(cav) = 0.50$.

Given these results, the relative vapor pressure at which cavitation should occur could be predicted accurately for four solvents. However, further investigations *e.g.* via molecular dynamic simulations or further experiments with other solvents, are still pending to refine the definition of the used *Tolman* length.

Die approbierte gedruckte Originalversion dieser Dissertation ist an der TU Wien Bibliothek verfügbar.
The approved original version of this doctoral thesis is available in print at TU Wien Bibliothek.
TU Bibliothek Your knowledge hub WIEN

5.3 Photocatalytic Reactions Monitored by ATR-FTIR Spectroscopy

The following results were obtained in collaboration with Greta Haselmann, TU Wien/RTWH Aachen, Jia Wang TU Wien, and Karin Wieland TU Wien/TU München.

Hydrogen as a solar fuel is a promising sustainable alternative to conventional fossil fuels due the high abundance of hydrogen in the biosphere. In its molecular form, H_2, it has the highest specific energy density, 120 MJ kg^{-1}, of all known substances, while the only by-product upon burning with O_2 is water.[255–257] To date, H_2 has been obtained primarily from unsustainable steam reforming processes.[258] Photocatalytic water splitting, which has evolved as a promising source of H_2, offers an environmentally friendly alternative that mimics photosynthetic processes.[259] In this context, photocatalytic powder suspensions of Pt-loaded TiO_2 in aqueous methanol solutions have developed as the benchmark photocatalytic reference system for various applications including the H_2 evolution reaction (HER).[260–264] Although it is the benchmark, the reaction mechanisms are still under investigation.[265–268] Methanol serves as a so-called sacrificial agent to eliminate kinetic limitations from the O_2 evolution reaction.[269] However, the term sacrificial agent can be misleading as it implies an innocent role of methanol in the HER; in actuality, H_2 generated from aqueous methanol solutions mainly originates from the photooxidation of methanol (equation (5.19)).[269,270]

$$CH_3OH + H_2O \xrightarrow[Pt/TiO_2]{h\nu} CO_2 + 3H_2 \qquad \textbf{(5.19)}$$

Haselmann et al. recently showed an unprecedented early-stage decrease in the H_2 evolution rate on Pt-loaded TiO_2 during the HER and photooxidation of methanol using a combination of *in situ* Pt photodeposition and an online gas analyzing unit that enables monitoring of the reaction at the moment all active components (metal oxide and co-catalyst) are combined.[271] This decrease strongly depended on several parameters: *i.e.*, it was observed primarily at low Pt loadings (*e.g.*, 0.25 wt %–0.4 wt % Pt) with methanol concentrations above 25 vol % and was amplified at high UV intensities and after ultrasonication pretreatment of TiO_2 suspensions. This indicated a critical role of the defect concentration in relation to the number of Pt particles in the system.[271] The drop in H_2 evolution rate was accompanied by an increase in CO concentration. Prior studies have found that some parameters, such as a high methanol concentration, can lead to bimolecular side reactions, favoring a methyl formate pathway.[267,268] This is generally in line with previous findings of *Haselmann et al.*,[271] and it was assumed that a shift in the oxidation mechanism of methanol from the direct pathway via a formaldehyde intermediate toward a side reaction via a methyl formate intermediate could cause the decrease in the H_2 evolution rate. However, a more intricate influence of Pt loading and defect concentration in a material on the actual reaction mechanism could be expected. Therefore, this work was dedicated to the development of an experimental platform for real-time, *in situ* studies of the chemical processes taking place in heterogeneous photocatalysis. Furthermore, the developed system was applied to illuminate the reaction pathways leading to the

Die approbierte gedruckte Originalversion dieser Dissertation ist an der TU Wien Bibliothek verfügbar.
The approved original version of this doctoral thesis is available in print at TU Wien Bibliothek.
TU Bibliothek Your knowledge hub WIEN

aforementioned Pt loading-dependent deactivation phenomenon that was previously observed in a liquid-phase photocatalysis setup.[271] Here, FTIR spectroscopy was employed as a powerful tool for mechanistic studies. FTIR spectroscopy enables the detection of surface radicals and reaction intermediates and provides information about characteristic vibrations of molecules on surfaces during a reaction.[272–274] In the context of photocatalysis, such IR spectroscopic studies have typically been carried out in the gas phase with pre-deposited noble metal co-catalysts.[267,275–280] For example, *Chiarello et al.* investigated different types of noble metals (Ag, Au, Au-Ag alloy, and Pt) with respect to their performance during the photoreforming of methanol upon mild heating (55 ± 5 °C) using an ATR cell.[267] While keeping the co-catalyst loading at either 0.5 or 1.0 wt %, they observed different reaction selectivities and rates for different methanol concentrations (1 – 100 vol %), in agreement with previous findings of *Haselmann et al.*[271] Interestingly, they additionally observed a nonlinear correlation between the H_2 generation rate and an increase in metal loading from 0.5 wt % to 1.0 wt % Pt on P25. A further systematic investigation of the noble metal loading, however, exceeded the scope of their work. Similar to the discussed approach, *Highfield et al.* studied the platinization of pre-sorbed H_2PtCl_6 on TiO_2 in combination with the gas-phase photoreforming of methanol using a diffuse reflectance infrared Fourier transform spectroscopy (DRIFTS) cell coupled to a mass spectrometer.[266] Interestingly, they observed increasing coverage of Pt with CO during the photoreforming of methanol, which they attributed to the dissociation of the formaldehyde intermediate on Pt. However, in contrast to this study, their experiments were focused on investigating the effects of elevated temperatures (<70 °C) on the gas-phase photoreforming process of methanol, while keeping the loading constant at 1 wt % Pt.

To replicate previous reaction conditions of *Haselmann et al.* as closely as possible, it was chosen to conduct the experiments in the liquid phase. For liquid-phase measurements, ATR spectroscopy of thin films is the preferred method: because the evanescent wave only shallowly penetrates the liquid film, penetrating mainly the catalyst deposited on the ATR crystal, spectral interference from the liquid is largely decreased compared to IR transmission measurments.[272] This surface sensitivity of ATR spectroscopy has been successfully exploited for monitoring catalytic reactions.[273,281]

5.3.1 Experimental Procedures

This experimental section is not given in chapter 2 as characterization of the photocatalyst and P25 spin coating was performed by Greta Haselmann and Jia Wang. However, this information is added here as it constitutes and essential part of this work on photocatalysis.

5.3.1.1 Characterization of the Photocatalyst

Transmission electron microscopy (TEM) images were obtained on a FEI Tecnai F20 operated at an acceleration voltage of 200 kV. For sample preparation, the spin-coated TiO_2 film was carefully scraped off the Si ATR crystal with a spatula and placed onto copper grids coated with a holey carbon film (200 mesh, *Science Services GmbH*, Germany).

Die approbierte gedruckte Originalversion dieser Dissertation ist an der TU Wien Bibliothek verfügbar.
The approved original version of this doctoral thesis is available in print at TU Wien Bibliothek.
TU Bibliothek WIEN Your knowledge hub

EDX spectra were collected with an EDAX Apollo XLTW SDD detector (<129 eV resolution). Pt particle size distributions were established using ImageJ software and statistically analyzed using OriginPro 2016.

Raman spectra were measured on a Horiba Jobin-Yvon LabRAM 800HR spectrometer equipped with an edge filter (1800 1/mm grating), an external frequency-doubled Nd:YAG laser (Oxxius LMX 532 nm, maximum power output < 55 mW) as monochromatic light source, a Synapse Open-Electrode-CCD detector, and an optical microscope (Olympus BX40) with a motorized xyz-stage.

Powder X-ray diffraction (XRD) patterns were recorded using a PANalytical X'Pert Pro multipurpose diffractometer (MPD) in Bragg Brentano geometry (Cu K_α λ = 1.5406 Å, 45 kV, 40 mA), equipped with a BBHD mirror and an X-Celerator multichannel detector. Samples were scanned at a 2θ angle of 20° to 80°.

X-ray photoelectron spectroscopy (XPS) was carried out on a custom-built SPECS XP spectrometer equipped with a monochromatic Al-K_α X-ray source (µFocus 350) and a hemispherical WAL-150 analyzer (acceptance angle: 60°). All samples were mounted onto the sample holder using double-sided carbon tape. Pass energies of 100 eV and 30 eV and energy resolutions of 1 eV and 100 meV were used for survey and detail spectra, respectively (beam energy and spot size: 70 W onto 400 µm, angle: 51° to sample surface normal, base pressure: $5 \cdot 10^{-10}$ mbar). Data analysis was performed using CASA XPS software, employing transmission corrections, Shirley backgrounds,[282,283] and Scofield sensitivity factors.[284] Charge correction is applied so that the signal of adventitious carbon is shifted to a binding energy (BE) of 284.8 eV.

5.3.1.2 Dedicated Setup for *in situ* ATR-FTIR Spectroscopy of Heterogeneous Photocatalytic Reactions

For details on the flow cell setup, see section 2.1.3. During the photooxidation experiments on TiO_2 thin films, FTIR measurements were performed using *Clipsi* placed into the sample compartment of a Bruker Vertex 80v FTIR spectrometer. For UV top-irradiation a 200 W super-pressure Hg lamp (Lumatec SUV-DC, λ = 240 to 500 nm, 1.2 W) was used.

FTIR spectra were acquired with a spectral resolution of 4 cm^{-1}, and a total of 32 scans (4 s, double-sided, backward forward acquisition mode) were averaged per spectrum.

The reaction solution was pumped into the ATR flow cell at a flow rate of 1 mL min^{-1} under inert atmosphere using a peristaltic pump, 1/16" PTFE tubing (0.5 mm I.D.) and 1/16" stainless steel tubing, and a balloon filled with N_2. After flushing 5 mL of solution through the system, the flow was stopped, and a dark background spectrum was collected. As the flow cell tubing typically exhibits very low diffusion due to the small diameter of both the inlet and outlet (0.5 mm), a pseudo-closed system was assumed. Data recording was started concurrent with UV illumination. During the first 5 min of reaction, a spectrum was recorded every 10 s, and then every 30 s. Illumination was stopped after 70 min and the coated ATR crystal was recovered from the cell and rinsed with ethanol to remove residual reaction solution. High

Die approbierte gedruckte Originalversion dieser Dissertation ist an der TU Wien Bibliothek verfügbar.
The approved original version of this doctoral thesis is available in print at TU Wien Bibliothek.
TU Bibliothek Your knowledge hub WIEN

reproducibility of the experiments was verified by comparing the band heights of the most relevant bands of each Pt loading for repeated measurements, which showed deviations of < 10 %.

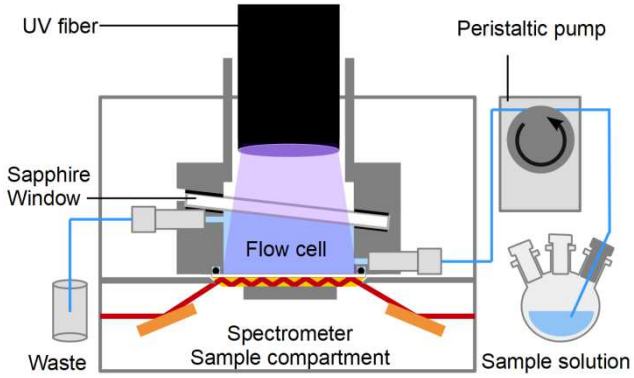

Figure 5.15: Optical setup consisting of a flow cell placed on a Si ATR crystal within the sample compartment of a commercial FTIR spectrometer. The cell is top-irradiated with a UV light via a fixed light guide placed on top of a sapphire window.

5.3.1.3 Preparation of TiO_2 Thin Films on ATR Crystal via Spin-coating

The Si ATR crystals used for the FTIR-ATR experiments were spin-coated with a viscous TiO_2 (P25) paste, resulting in a thin film of 500 – 1000 nm (Figure 5.16). The thickness of the P25 coating was designed to match the effective path length of $d_p = 0.36$ – 0.66 µm (2200 - 1200 cm^{-1}) of the evanescent wave of the ATR crystal to allow for probing of the reactions exclusively at the TiO_2 surface. For the P25 paste, a 10 wt % ethyl cellulose (EC, 48.0 – 49.5 % (w/w) ethoxyl basis, *Sigma Aldrich*) ethanolic solution was first prepared. Then, 2.0 g of P25 (Aeroxide® P-25, *Acros Organics*) and 8.1 g terpineol (anhydrous, mixture of isomers, *Sigma Aldrich*) were added to 10 g of the EC-ethanolic solution. After 10 min of stirring, 35 mL of ethanol was added. The mixture was sonicated three times for 5 min each with a sonication finger (20 kHz, 10 % amplitude, SONOPLUS HD3200, *Bandelin*) and stored in the fridge for later use. Before spin-coating, the viscous paste was stirred overnight at room temperature and the Si ATR crystals were rinsed with ethanol and isopropanol. The P25 paste was spread over the Si ATR crystal before starting rotation. Each Si ATR crystal was covered with 100 µL P25 paste and spin-coated at 6000 rpm for 45 s (ramp time: 2.5 s). After spin-coating, the film was pre-heated at 100 °C for 20 min and then annealed at 500 °C for 30 min.

5.3.1.4 Preparation of the Reaction Solutions

An aqueous methanol solution (100 mL, 50 vol %, HPLC-grade methanol, *VWR*) containing H_2PtCl_6 as precursor for the photodeposition of Pt nanoparticles was bubbled with inert gas in a three-neck round bottom flask for 10 min and then sealed until used for the ATR-FTIR experiments. Calculations of H_2PtCl_6 concentrations for different Pt loadings were thus based on the volume of the flow cell (700 µL) and mass of TiO_2 (0.28 mg). H_2PtCl_6 concentrations of $7.18 \cdot 10^{-6}$ M, $1.45 \cdot 10^{-5}$ M, $2.90 \cdot 10^{-5}$ M, and $5.74 \cdot 10^{-5}$ M were used, corresponding to nominal Pt loadings of 0.35 wt %, 0.7 wt %, 1.4 wt %, and 2.7 wt % Pt.

Die approbierte gedruckte Originalversion dieser Dissertation ist an der TU Wien Bibliothek verfügbar.
The approved original version of this doctoral thesis is available in print at TU Wien Bibliothek.
TU Bibliothek Your knowledge hub WIEN

5.3.1.5 Multivariate Analysis using MCR-ALS

MCR-ALS analysis was performed using a freely available MATLAB GUI.[285] The accessible spectral range between 2200 – 1180 cm^{-1}, which covers the main part of the spectral fingerprint region, was selected for detailed analysis. To correct for baseline drifts, the absorbance at 2200 cm^{-1} was fixed to zero by subtracting the absorbance at this wavenumber from each spectrum. Prior to MCR-ALS, an evolving factor analysis (EFA) was performed to determine initial estimates in an exploratory analysis. Spectra were normalized by height. MCR-ALS analysis was performed with a non-negativity concentration constraint (fnnls, for all species). The MCR-ALS iteration process was stopped when the data set converged. Convergence was considered achieved as soon as the difference in the standard deviation of the residuals between experimental and calculated data was less than 0.1% between two consecutive iterations.

5.3.2 Characterization of Pt-loaded TiO_2 Thin Films

Figure 5.16 shows typical TEM images of P25 films after photodeposition of 0.35 wt %, 0.7 wt %, 1.4 wt %, and 2.7 wt % Pt, which reveal a clear increase in the number of Pt particles with increasing nominal Pt loading.

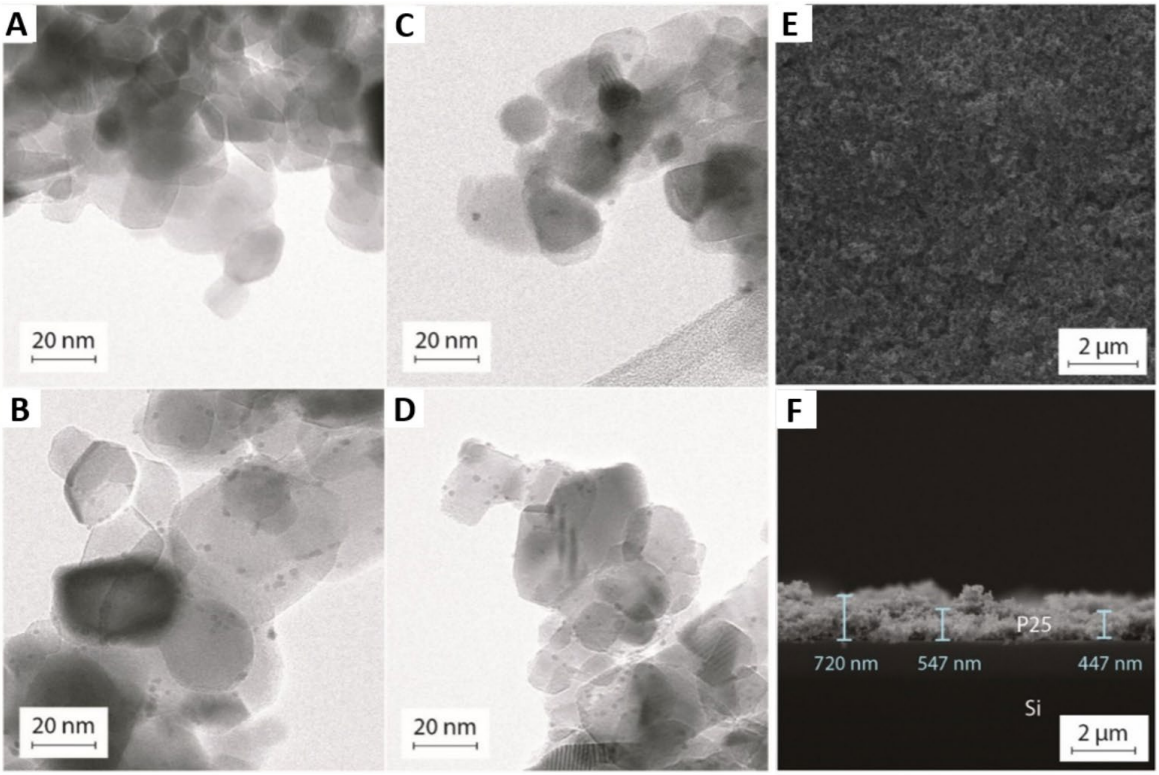

Figure 5.16: (A-D) TEM images of P25 with nominal loadings of (A) 0.35 wt.%, (B) 0.7 wt.%, (C) 1.4 wt.%, and (D) 2.7 wt.% Pt. (E-F) SEM images of P25 film spin-coated onto a Si single crystal: (E) top view (F) profile view.

Particle size distributions showed a similar median particle sizes of 2 – 2.4 nm for all loadings (**Table 5.12**). This was in agreement with previous findings that showed that the number of Pt particles rather than particle size increases with increasing Pt loading.[286] The lowest Pt

Die approbierte gedruckte Originalversion dieser Dissertation ist an der TU Wien Bibliothek verfügbar.
The approved original version of this doctoral thesis is available in print at TU Wien Bibliothek.

loading (0.35 wt %) also exhibited the smallest Pt particle size with a median of 2.0 nm. However, it was also noticed that Pt particles smaller than 1.5 nm were almost indistinguishable from TiO_2, hence it was assumed that the median values are overestimated in some cases.

For both, XPS and ICP-MS, the general trend of an increasing Pt loading agreed with an increasing applied H_2PtCl_6 concentration (Table 5.12). However, as a surface-sensitive technique, XPS overestimates the actual Pt loading as it does not account for the bulk TiO_2. For ICP-MS, agglomeration of TiO_2 nanoparticles contributes to a rather large measurement error. In particular, low loadings were indistinguishable and the obtained values most likely did not reflect the actual Pt loading.

Table 5.12: Quantification of Pt for Pt-loaded P25 thin films on Si ATR crystals.

Nominal Pt loading wt %	ICP-MS	XPS	TEM-EDX
0.35	0.50 ± 0.04	1.26 ± 0.59	0.23 ± 0.12
0.70	0.37 ± 0.02	4.85 ± 0.97	Not measured
1.38	1.19 ± 0.52	5.73 ± 0.54	Not measured
2.72	5.14 ± 0.31	21.44 ± 01.56	1.73 ± 0.91

TEM-EDX seemed to be the most useful technique in the quantification of actual Pt loadings. The average values based on statistical evaluation agreed best with the nominal Pt loadings. No structural changes of the TiO_2, *i.e.,* in phase composition or defects/lattice strain from UV irradiation or Pt deposition were observed after ATR-FTIR experiments as confirmed by Raman spectroscopy, XRD and XPS data (**Figure 5.17** and **Figure 5.18**).

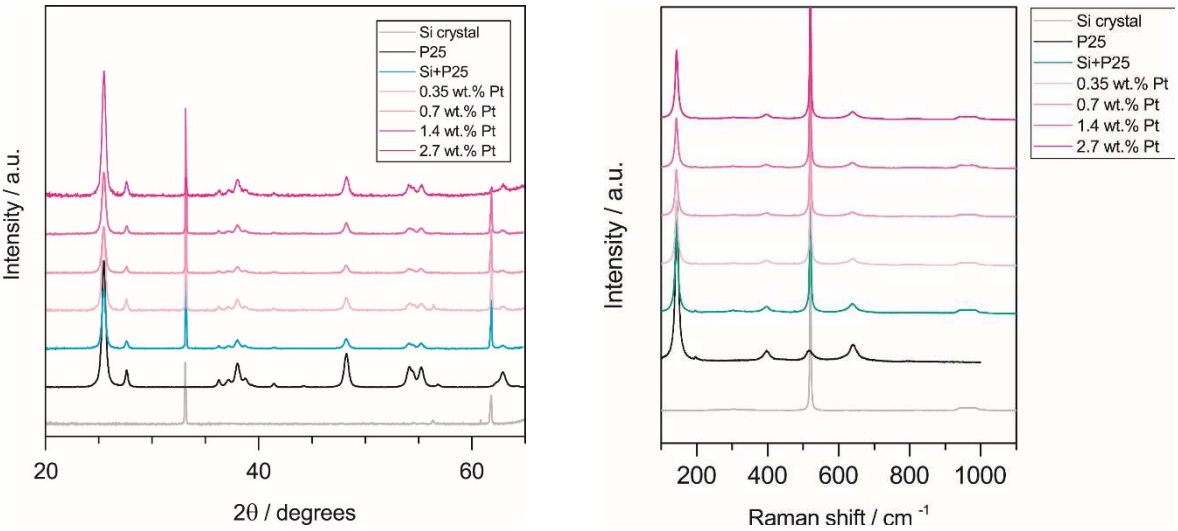

Figure 5.17: (Left) XRD of P25 spin-coated onto Si ATR crystals loaded with 0.35 wt.%, 0.7 wt.%, 1.4 wt.% and 2.7 wt.% Pt, including reference spectra of the pristine Si crystal, P25, and P25 on Si without Pt. (Right) Raman spectra of P25 spin coated onto Si ATR crystals loaded with 0.35 wt.%, 0.7 wt.%, 1.4 wt.% and 2.7 wt.% Pt, including reference spectra of the pristine Si crystal, P25, and P25 on Si without Pt.

In particular, Raman spectra of the thin films (Figure 5.17, right) showed no shift or peak

Die approbierte gedruckte Originalversion dieser Dissertation ist an der TU Wien Bibliothek verfügbar.
The approved original version of this doctoral thesis is available in print at TU Wien Bibliothek.
TU Bibliothek Your knowledge hub WIEN

broadening with increasing Pt loading often associated with defect formation or lattice strain, in contrast to the previous report of *Haselmann et al.* on powder suspensions.[271] This might have been due to the different sample preparation, which included a short oxidation step. XPS detail spectra of the Pt 4f signal confirmed the presence of metallic Pt^0 (**Figure 5.18**). After subtracting the background signal found in the TiO_2 reference, the Pt 4f spectrum could be sufficiently deconvolved using Pt^0 as the sole component. This confirmed the complete reduction of the acid precursor and deposition of metallic Pt^0 nanoparticles (Pt $4f_{7/2}$ = 70.2-70.6 eV).[287,288]

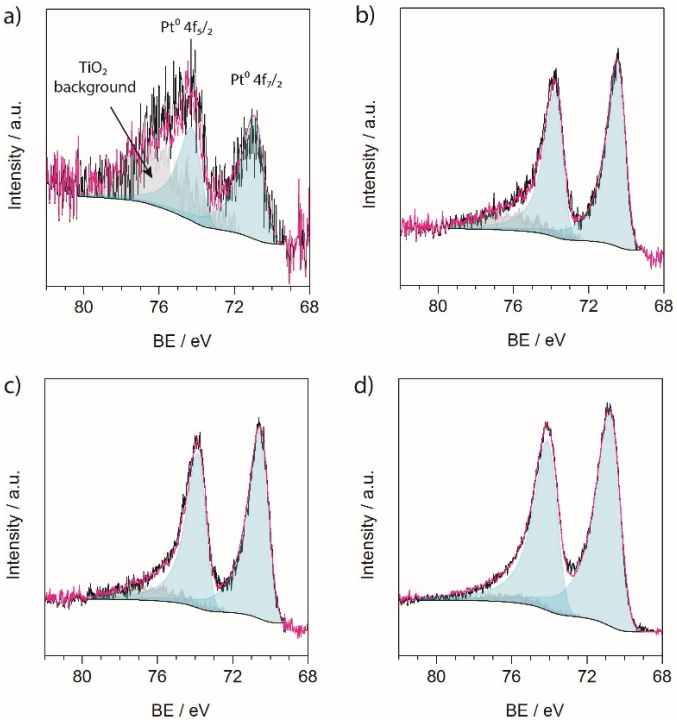

Figure 5.18: XPS Pt 4f detail spectra of P25 spin-coated onto Si ATR crystals loaded with a) 0.35 wt %, b) 0.7 wt. %, c) 1.4 wt % and d) 2.7 wt % Pt by photodeposition. Line shape LA (1.2,85,70), Δ_{metal} = 3.33 eV

5.3.3 Reaction Monitoring under UV Irradiation with ATR-FTIR Spectroscopy

Several processes occurred upon illumination of the TiO_2 thin films on the Si ATR crystals immersed in aqueous solutions of methanol. These processes were reflected in changes in the recorded FTIR spectra. UV illumination-induced spectral changes of the Si crystal and TiO_2 partially overlapped with the photoreactions to be studied: UV illumination of Si ATR crystals induced a continuous increase of the baseline of the blank Si ATR spectra (**Figure 5.19**).

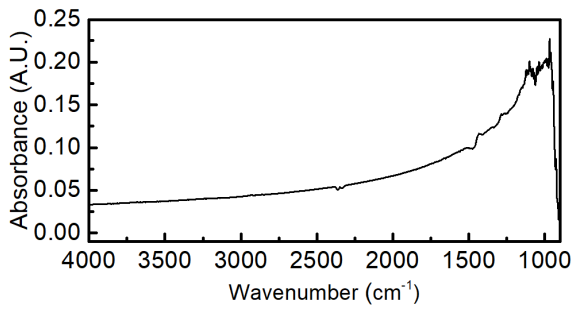

Figure 5.19: IR spectra of blank Si ATR crystal under UV irradiation. The background spectrum is the blank Si ATR crystal with UV off.

Die approbierte gedruckte Originalversion dieser Dissertation ist an der TU Wien Bibliothek verfügbar.
The approved original version of this doctoral thesis is available in print at TU Wien Bibliothek.
TU Bibliothek Your knowledge hub WIEN

In addition, it is known that UV irradiated TiO_2 shows a raised baseline toward the red end of the spectrum,[289,290] similar to the effect found for UV irradiated Si in this study. Therefore, the rise in the baseline was attributed to these two effects (**Figure 5.20**).

FTIR difference spectra were derived to monitor the photoreactions *in situ* for four Pt loadings (0.35 wt %, 0.7 wt %, 1.4 wt %, and 2.7 wt % Pt; Figure 5.20B shows the spectra for nominal loading of 0.7 wt % Pt; see Figure 5.20C-E for other loadings). This allowed to differentiate the comparable small bands originating from the photodeposition of Pt particles as well as the photooxidation of methanol (compare Figure 5.20A) from the observed changes that accompanied the photoreactions. The difference spectra were obtained by using the spectrum of the flow cell filled with reaction solutions but without UV illumination as the background spectrum.

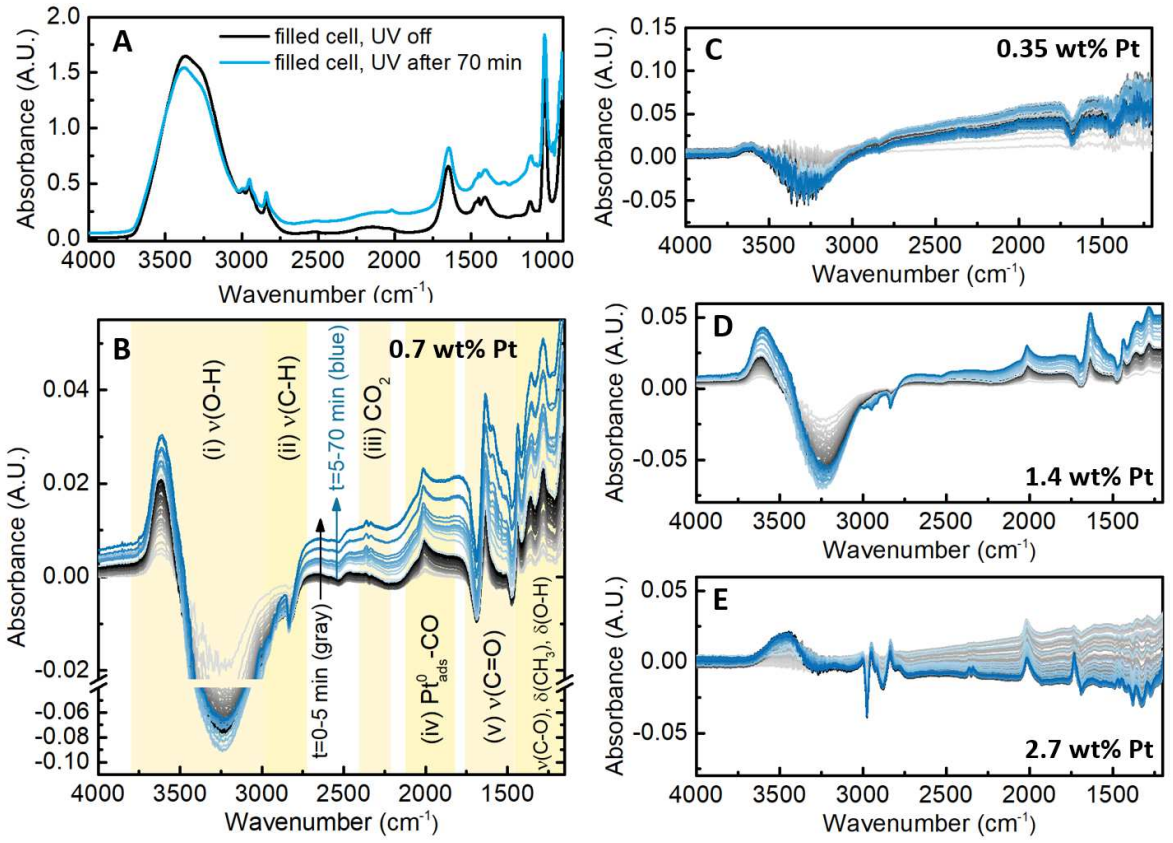

Figure 5.20: IR spectra recorded during UV illumination with 0.7 wt % Pt: (A) IR spectra obtained with the blank Si ATR as background spectrum (B) Difference spectra where gray to black spectra correspond to the first 5 min of the reaction with a measurement interval of 10 s. Blue spectra correspond to the time frame of t = 5 - 70 min (from light to dark blue, respectively) with a measurement interval of 5 min between single spectra. The background spectrum was recorded of the filled flow cell without UV illumination. Areas of interest for the analysis of platinization and photooxidation processes are highlighted for better reference. (C) 0.35 wt % Pt, (D) 1.4 wt % Pt; (E) 2.7 wt % Pt.

The FTIR difference spectra depicted distinct changes over the course of the photoreaction that could be divided into five main spectral contributions consisting of the following vibrations (compare Figure 5.20B): (i) The ν(O–H) bands of H_2O, methanol, and Ti–OH in TiO_2 showed strong bands in this region. Here, small absolute changes in the spectrum at the

Die approbierte gedruckte Originalversion dieser Dissertation ist an der TU Wien Bibliothek verfügbar.
The approved original version of this doctoral thesis is available in print at TU Wien Bibliothek.
TU Bibliothek Your knowledge hub WIEN

strong absorbance of the ν(O–H) band of H_2O/methanol at 3300 cm^{-1} of a few percent of the initial band (Figure 5.20A), which could stem from a change in refractive index of Si or TiO_2 upon UV irradiation, changes in pH value, or small changes in temperature, result in strong changes in the band in the difference spectra (Figure 5.20B). In addition, upon UV irradiation of TiO_2, Ti–OH hydroxyl groups were formed with the corresponding ν(O–H) band, which is affected by photogenerated electrons.[291,292] Due to these overlapping shifts induced by different physical processes, qualitative statements regarding changes in this region or association of these changes to the actual photoreaction remain challenging and are subject to further investigations. This study focused on the fingerprint region (regions iv and v) of the IR spectra of the different intermediates of the photooxidation of MeOH. (ii) Bands corresponding to the ν(C–H) vibrations of all organic species were located between 3050 and 2700 cm^{-1}. The negative bands observed in this range can were attributed primarily to the decomposition of organic contaminants typically found on P25 stored at ambient conditions.[293] These bands formed immediately upon UV illumination and stabilized within the first 10 min, indicating that all contaminants were completely degraded. Furthermore, the differential spectra did not show any significant changes in the intensities of vibrations associated with methanol or methoxy. Due to the excess of methanol above the P25 film, its concentration thus appeared stable during the photoreaction. In addition, a negative band at 2830 cm^{-1} was observed. (iii) The ν_{asym}(C=O) vibrations of gaseous and dissolved CO_2 were visible as P- and R-branches between 2380 and 2320 cm^{-1} and as a single band at 2345 cm^{-1},[294] respectively. The visible bands of gaseous CO_2 were due to residual CO_2 from the atmosphere in the dry air flushed interferometer compartment and were not considered to originate from the photoreaction. On the other hand, dissolved CO_2 stemmed from the photocatalytic reaction. (iv) Bands associated with CO and CO coordinated to Pt were located between 2200 and 1950 cm^{-1}. The band of CO adsorbed to ionic Pt sites (Pt^{x+}–CO_{ads}) and on metallic Pt sites (linear Pt^0–CO_{ads}) were found at >2100 cm^{-1} and <2100 cm^{-1}, respectively (see section 5.3.4 for a detailed discussion).[266,295–297] (v) Bands between 1750 and 1450 cm^{-1} stemmed from the $\nu_{asym/sym}$(C=O) vibration of carbonyl functionalities.[276,298–300] The negative band at 1690 cm^{-1} was assigned to the same contaminants as those found in region (ii).[293] Bands below 1400 cm^{-1} were associated with deformation vibrations of $–CH_3$ and O–H as well as vibrations of C–O.

The latter two regions were key regions in determining the various decomposition products upon photooxidation of methanol and will be discussed in more detail in the next section.

5.3.4 Spectroscopic Investigations of CO Adsorbed on Pt

A very prominent feature of the IR spectra in these systems (aside from the organic intermediate species) was comprised of the Pt^0–$CO_{(ads)}$ bands that form during the photoreaction. Although CO is a common catalyst poison and possible byproduct during the photooxidation of methanol, the exact role of CO remains uncertain. *Highfield et al.* observed increasing coverage of Pt with CO, which they attributed to the dissociation of the formaldehyde intermediate on Pt; however, they remained inconclusive about the role of

Die approbierte gedruckte Originalversion dieser Dissertation ist an der TU Wien Bibliothek verfügbar.
The approved original version of this doctoral thesis is available in print at TU Wien Bibliothek.
TU Bibliothek Your knowledge hub WIEN

CO.[266] In a more recent study, *Chiarello et al.* further investigated the CO adsorption on differently sized Pt particles and found that CO irreversibly adsorbed on Pt nanoparticles during the photoreaction; they assigned this to a lower photoactivity of nanoparticles than of nanoclusters, for which CO adsorption was reversible.[265] Regardless, the temporal progression of the intensity of the Pt^0–$CO_{(ads)}$ band could serve as a measure of Pt nanoparticle coordination and CO coverage,[301–304] thus allowing for *in situ* monitoring of the photodeposition process.

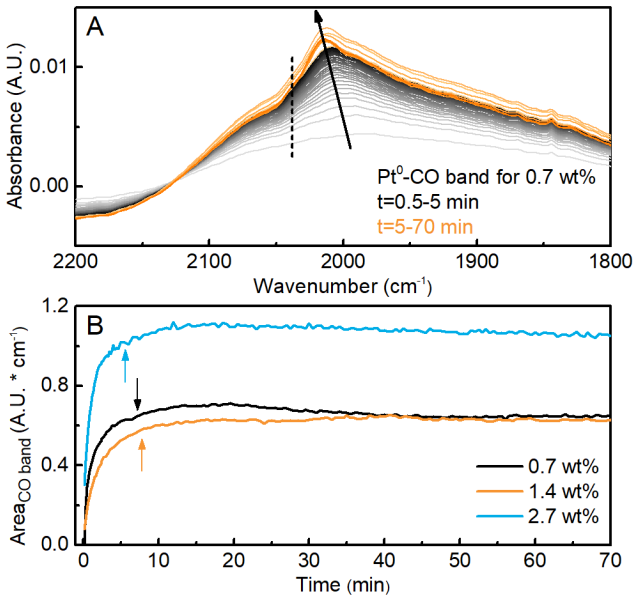

Figure 5.21: (A) FTIR spectra showing the temporal progression of Pt^0–$CO_{(ads)}$ for 0.7 wt % Pt loading. The clear peak shift and development of a shoulder at higher wavenumbers indicates a change of Pt particle geometry and CO coverage. (B) Area of the Pt^0–CO band as a function of time. Arrows indicate when 90% of the maximum band area is achieved ($t_{90\%}$).

Figure 5.21 provides as an example a time-resolved close-up of the spectral region containing the Pt^0–CO_{ads} band (shifting from ≈2000 cm^{-1} to 2018 cm^{-1}) under UV illumination for the sample with 0.7 wt % Pt (see **Figure 5.22** for all loadings) and the corresponding development of the band area for all Pt loadings.

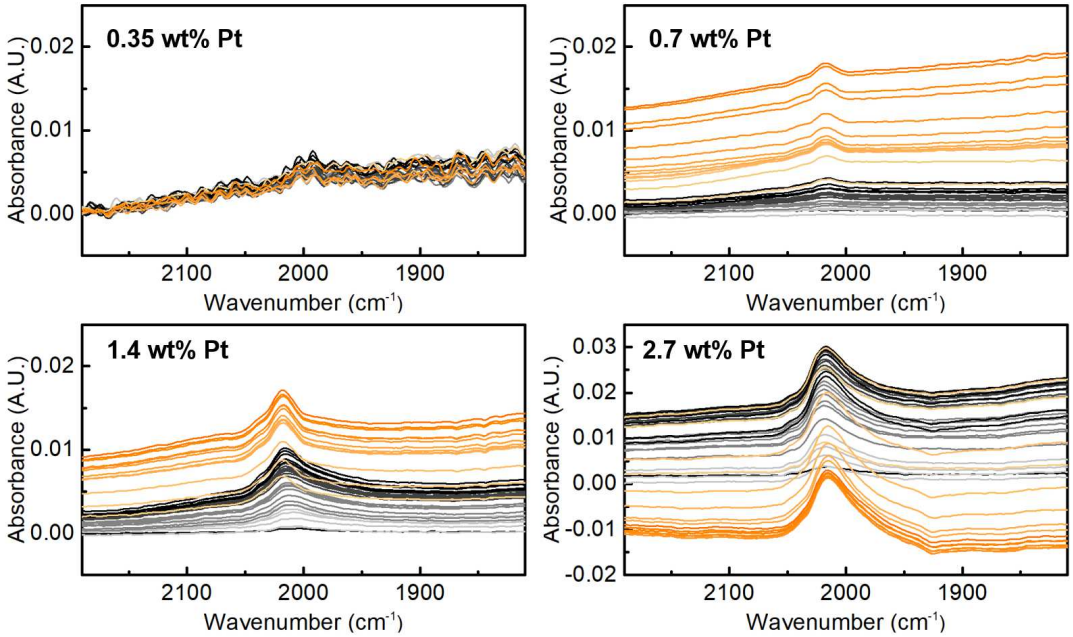

Figure 5.22: Close up of IR spectra of different Pt loadings.

Die approbierte gedruckte Originalversion dieser Dissertation ist an der TU Wien Bibliothek verfügbar.
The approved original version of this doctoral thesis is available in print at TU Wien Bibliothek.
TU Bibliothek WIEN Your knowledge hub

The formation of a Pt^0–$CO_{(ads)}$ band was immediately visible during the first minutes of irradiation, likely arising from the immediate dissociation of methanol or an intermediate as previously reported by *Highfield et al.* (Figure 5.21A).[266]

The lowest Pt concentration of 0.35 wt % showed only a very small Pt^0–$CO_{(ads)}$ band at 1999 cm^{-1} during UV illumination for 70 min (Figure 5.22). The band position at lower wavenumbers compared to the higher loadings could stem from either lower CO coverage or small Pt particle size (see below for further explanation). Although the presence of Pt particles was confirmed by TEM and XPS (Figure 5.16 and Figure 5.18), particles smaller than 1.5 nm were hard to distinguish from TiO_2 in TEM due to low contrast; other spectral features assigned to the photoreaction could not be distinguished, indicating the limitations in sensitivity of the ATR-FTIR setup.

Integration of the Pt^0–$CO_{(ads)}$ band showed that 90% of the maximum area of the Pt^0–$CO_{(ads)}$ band was reached within 7 min, 8 min, and 6 min, respectively, for 0.7 wt %, 1.4 wt %, and 2.7 wt % Pt ($t_{90\%}$, indicated by arrows in Figure 5.21B). Subsequently, the area increased more slowly until the maximum value was reached at ≈15 min for all loadings ($t_{100\%}$). The absorption coefficient of the Pt^0–$CO_{(ads)}$ band is not identical for every site on a Pt particle, impeding quantitative statements regarding the different Pt sites.[301,305,306] In addition to the increase in absorbance during the first 15 min of each experiment, a continuously increasing peak shift toward higher wavenumbers as the reaction proceeded was observed, starting almost from the beginning of illumination. This significant peak shift from 2000 to 2018 cm^{-1} indicated a strong dipole-dipole coupling induced by the increasing surface coverage of Pt with CO.[281,303,304,307–309] At the same time, a shoulder evolved at 2038 cm^{-1} after about 5 min that was assigned to CO situated on higher coordinated Pt.[301,302]

The Pt^0–$CO_{(ads)}$ band is strongly influenced by the adsorption site of the CO molecule on the Pt nanoparticle, *i.e.*, its binding energy, and hence the band position and absorption coefficient on corners, edges, and facets depends on the coordination numbers of the bonded Pt atom.[301–304] *Christopher and coworkers* recently identified the linear Pt^0–$CO_{(ads)}$ band positions related to well-coordinated Pt atoms (Pt_{WC}, 8- and 9-fold Pt coordination, as for terraces), undercoordinated Pt (Pt_{UC}, 6- and 7-fold Pt coordination, as found on steps, corners, and edges), and highly undercoordinated Pt sites (Pt_{HUC}, below 6-fold Pt coordination), respectively, as 2098 – 2080 cm^{-1}, 2075 – 2060 cm^{-1}, and 2055 – 2000 cm^{-1} via gas-phase DRIFTS measurements.[303,304] As the coordination number increases with Pt particle size, these bands were used to monitor the growth in coordination and thus Pt particle size. Apart from a water-induced red shift of ~50 cm^{-1} in the studied liquid system due to H-bonding of water with CO,[310] compared to the gas-phase measurements performed in Refs. [303] and [304], the shapes of the observed bands (**Figure 5.23**) agreed very well with *Christopher et al.'s* spectra of CO adsorbed on 1.4 – 3 nm Pt nanoparticles.[304]

Die approbierte gedruckte Originalversion dieser Dissertation ist an der TU Wien Bibliothek verfügbar.
The approved original version of this doctoral thesis is available in print at TU Wien Bibliothek.
TU Bibliothek Your knowledge hub WIEN

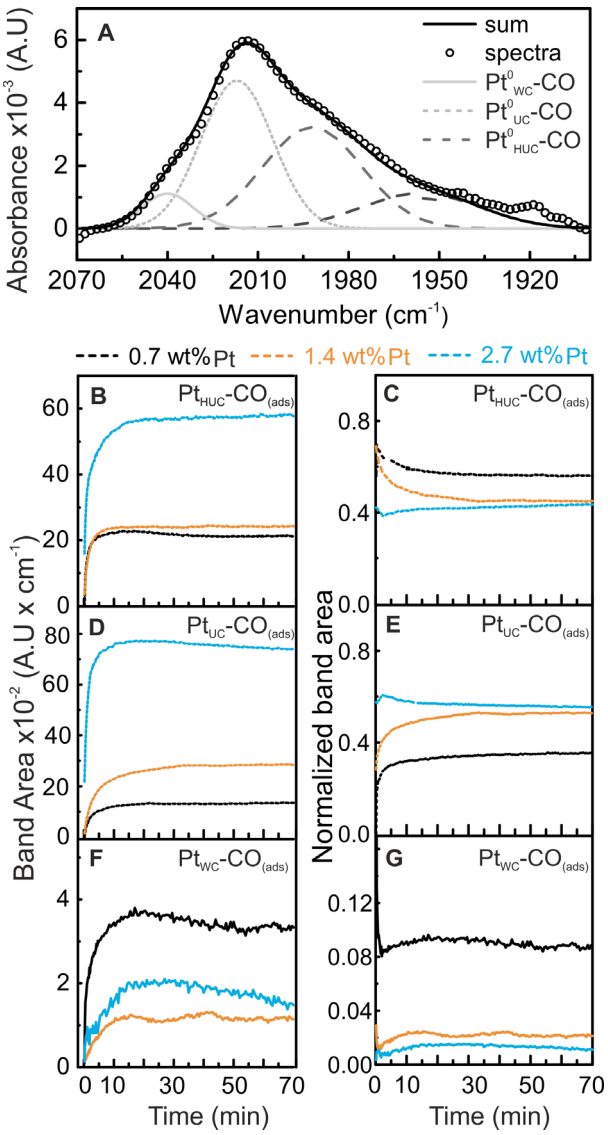

Figure 5.23: (A) Area of Gaussian profiles fitted to the Pt^0–$CO_{(ads)}$ band after 65 min of photoreaction for 0.7 wt % Pt. Fitted absolute areas of the bands attributed to (B) highly undercoordinated Pt_{HUC}, (D) undercoordinated Pt_{UC}, and (F) well-coordinated Pt_{WC}. Band areas of (C) Pt_{HUC}, (E) Pt_{UC}, and (G) Pt_{WC}, normalized to the sum of the band areas. The highest coordination of CO on Pt_{WC} is shown for 0.7 wt % Pt, whereas 1.4 and 2.7 wt % Pt behave similarly for all Pt types.

To monitor the evolution of the Pt^0–$CO_{(ads)}$ and hence the Pt particle growth, the entire Pt^0-$CO_{(ads)}$ band for all samples (except for 0.35 wt % Pt) was deconvolved to determine the theoretical positions of CO adsorbed on differently coordinated Pt. **Figure 5.23A** shows an example for 0.7 wt % Pt at 65 min, focusing on the bands at 2038 cm^{-1} (Pt_{WC}) and 2016 - 2018 cm^{-1} (Pt_{UC}) as well as the two bands at 1956 and 1991 cm^{-1} (Pt_{HUC}). The progression of the band area of each component as a function of time for all Pt loading samples is illustrated in Figure 5.23B, D, and F and is analogous to the progression of the total Pt^0-$CO_{(ads)}$ band in Figure 5.21B. The panels on the right (Figure 5.23C, E, and G) correspond to the normalized band areas. The time needed to reach 90 % of the maximum band area for each Pt species ($t_{90\%}$) is given in **Table 5.13**. For all three Pt loadings, the band area attributed to Pt_{HUC} reaches $t_{90\%}$ within the first 4 min, followed by Pt_{UC} ($t_{90\%}$ = 9 min) and Pt_{WC} ($t_{90\%}$ = 9-13.5 min). The ordered values of $t_{90\%}$ from low to high coordination number matched a growth mechanism of Pt from smaller to larger particles. The population of Pt_{HUC} reaches $t_{90\%}$ first due to the multiple corners of which small nanoparticles are solely composed.[301,302] For all three analyzed loadings, the number of corners reaches stability after

Die approbierte gedruckte Originalversion dieser Dissertation ist an der TU Wien Bibliothek verfügbar.
The approved original version of this doctoral thesis is available in print at TU Wien Bibliothek.
TU Bibliothek Your knowledge hub WIEN

10 min, which matched the obtained values of $t_{90\%}$ for the whole band (Figure 5.21). Due to the high population of Pt_{HUC} in small nanoparticles (< 1.5 nm) and the larger absorption coefficient of this species,[301,305,306] they made up the main contribution to the area of the Pt^0-$CO_{(ads)}$ band (compare normalized band areas) at the beginning of the reaction. As the nanoparticles grow, the contribution of Pt particles with higher coordination number increased and CO adsorbed to Pt_{UC}. Lastly, the population of well-coordinated Pt_{WC} stabilized after 20 min and nanoparticle growth was considered complete. The achievement of a stable Pt concentration of all populations suggested a full consumption of the H_2PtCl_6 precursor in the irradiated flow cell volume. This further supported the assumption of a pseudo-closed flow cell with negligible diffusion of the excess H_2PtCl_6 precursor remaining in the tubing in- and outlets.

Table 5.13: Values of $t_{90\%}$ and $t_{100\%}$ obtained from deconvolution of the Pt^0–$CO_{(ads)}$ band. Similar values are obtained for all loadings, indicating similar coverage or Pt growth behavior for all Pt loadings.

	$t_{90\%}$ ($t_{100\%}$) in [min]		
	Pt^0_{HUC}	**Pt^0_{UC}**	**Pt^0_{WC}**
0.7 wt % Pt	4 (14)	9 (22)	9.5 (20)
1.4 wt.% Pt	4 (15)	8.5 (19)	13 (21)
2.7 wt.% Pt	4 (15)	9 (15)	13.5 (21)

Another possible explanation of the development of the Pt^0–$CO_{(ads)}$ bands is that a step-wise adsorption of CO onto Pt sites of different reactivity was actually observed: first, CO may adsorb at the more reactive highly undercoordinated sites, then at undercoordinated sites, and finally at well-coordinated Pt sites. However, since the amount of Pt and thus the number of Pt sites differed between samples, one would also expect to see differences in the time scale of such a step-wise adsorption of CO on different Pt sites. However, the theoretically possible amount of CO in the system was derived from the formate concentration calculated from the band intensities compared with pure spectra obtained from known concentrations. If all formate species are converted to CO, it would be present in greater than 500-fold excess after 10 min of reaction time. Thus, conversion of even a small fraction of the formate would have resulted in saturation of Pt with CO after the first minutes of the reaction. Therefore, it was concluded that the increasing band intensity of the Pt^0–$CO_{(ads)}$ band could indeed be attributed to and useded to follow the Pt particle growth and was not solely due to increasing CO coverage.

5.3.5 Photocatalytic Decomposition of Methanol

The time-resolved evolution of IR spectra with respect to the possible intermediates during the photocatalytic decomposition of methanol for each Pt loading was investigated further.
The pathway for the direct oxidation of methanol proceeds via step-wise consumption of photogenerated holes (direct pathway, equation (5.20)). First, methanol deprotonates and the

Die approbierte gedruckte Originalversion dieser Dissertation ist an der TU Wien Bibliothek verfügbar.
The approved original version of this doctoral thesis is available in print at TU Wien Bibliothek.
TU Bibliothek Your knowledge hub WIEN

resulting methoxy groups adsorb preferably at oxygen vacancy sites on the TiO_2 surface.[311–315] The adsorbed methoxy group consumes a hole and forms a methoxy radical that can further deprotonate upon consumption of another hole to form formaldehyde, CH_2O.

CH_2O further oxidizes to CH_2O_2. This intermediate has been identified as both formic acid and dioxomethylene (DOM).[266,267,275,316] The oxidation step can proceed either (i) through direct consumption of a lattice oxygen by CH_2O and consequent filling of the resulting vacancy by dissociative adsorption of a water molecule or (ii) via direct hydration of CH_2O to methanediol and finally partial dehydration to DOM. DOM can further decompose into adsorbed methoxy and formate species via a Cannizzaro disproportionation. In a final step, CH_2O_2 decomposes to CO_2 and H_2:[266,267,275,316]

$$CH_3OH \xrightarrow{-H^+} CH_3O_{(a)}^- \xrightarrow[+h^+]{} CH_3O_{(a)}\cdot \xrightarrow[+h^+]{-H^+} CH_2O_{(a)} \xrightarrow[H_2O \quad 2H^+]{} CH_2O_{2(a)} \xrightarrow[+2h^+]{-2H^+} CO_2 \qquad \textbf{(5.20)}$$

Haselmann et al. previously suggested a shift from the direct pathway toward a side reaction via a methyl formate intermediate.[271] The photocatalytic decomposition of methyl formate, which can be formed by a bimolecular side reaction of methanol (equation (5.21)), has previously shown slower reaction kinetics than decomposition of formic acid and increased CO generation.[267,317] Methyl formate can form through cross-coupling of formaldehyde with methoxy adsorbed on TiO_2 or through the reaction of two neighboring methoxy groups under abstraction of H_2.[265,268,315,318] It can then further disproportionate to formate, finally resulting in CO formation by a reverse water-gas shift reaction (equation (5.22)):[266]

$$2CH_3OH \xrightarrow{-4H^+} HCOOCH_3 \xrightarrow[+OH(a)]{-H^+} CH_3O_{(a)} + HCOO_{(a)} \qquad \textbf{(5.21)}$$

$$HCOO_{(a)} \longrightarrow CO + OH_{(a)} \qquad \textbf{(5.22}$$

The reference spectra of the possible key intermediates formaldehyde, formic acid, formate, and methyl formate, each added to a slurry with anatase, rutile, or P25, are summarized in **Figure 5.24** and **Figure 5.25**. In agreement with literature, the symmetric and asymmetric C=O stretch vibrations between 1735 - 1450 cm^{-1} of carbonyl moieties were found to drastically differ between the adsorbed state on TiO_2[299,300,319] and the dissolved state in aqueous (methanolic) solutions.[320] For example, the band of formaldehyde is shifted from 1730 cm^{-1} to 1465 cm^{-1} if the species is adsorbed to TiO_2. In addition, if formaldehyde is dissolved in water, it forms its hydrate, methanediol, or methoxy methanol if dissolved in aqueous methanol solution with characteristic bands at 1300 cm^{-1} and 1196 cm^{-1}.[320,321] Formaldehyde can bind to the TiO_2 surface via its oxygen in an $\eta 1(O)$ configuration as intact formaldehyde molecule or yielding a new species, namely dioxymethylene (DOM) and polyoxmethylene.[319] DOM has distinct spectral features at 1485 - 1460 cm^{-1} and 1420 - 1410 cm^{-1} attributed to $\delta(CH_2)$ and $\omega(CH_2)$, respectively.[322]

Die approbierte gedruckte Originalversion dieser Dissertation ist an der TU Wien Bibliothek verfügbar.
The approved original version of this doctoral thesis is available in print at TU Wien Bibliothek.
TU Bibliothek Your knowledge hub WIEN

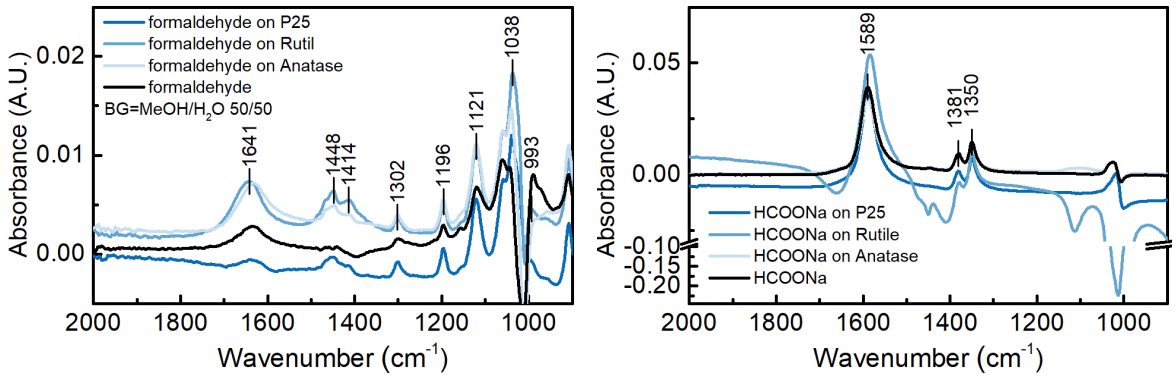

Figure 5.24: IR spectra of formaldehyde (left) and sodium formate (right) on different TiO_2.

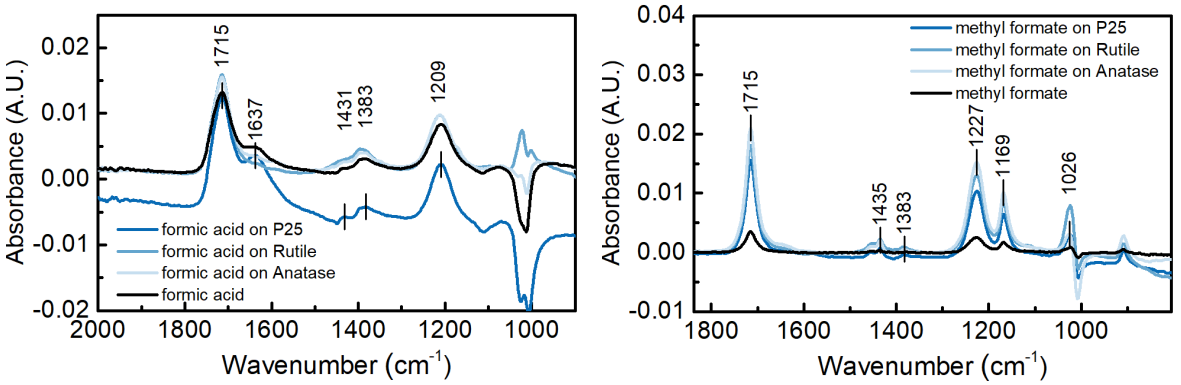

Figure 5.25: IR spectra of formic acid (left) and methyl formate (right) on different TiO_2.

Table 5.14: Bands of possible intermediates for the photooxidation of methanol as identified during *in situ* ATR-FTIR experiments of different Pt loadings on TiO_2 thin films. * found in the pure substance spectra recorded for this study. LAS = Lewis acid sites.

Species	vibration	0.7 wt.%	1.4 wt.%	2.7 wt.%
CO_2	ν_{as}(C=O)[294], dissolved	-	-	2345
CH_2O	ν_{as}(C=O)[319,299]	1732	1728	1728
	ν_{as}(C=O)[319,299] chemisorbed	1703	1703	1703
	ν_{as}(C=O) coordinated to Ti^{4+} [299,*]	-	-	1465
	methoxy methanol[320,321,*]	-	-	1297
	methoxy methanol[320,321,*]	-	-	1196
DOM	δ(C-H_2) [299,322,323]	-	-	1475
	ω(CH2) [299,322,323]	-	-	1410
$HCOO^-_{ads}$	ν_{asym}(C=O)[276,298,324,325,*]	1587	1587	-
	ν_{sym}(C=O) + δ(C-H,*)	1340-1380	1340-1380	-
HCOOH/ $HCOOCH_3$	ν(C=O) adsorbed on TiO_2*	1635	1635	-
	δ_{as}(C-H) LAS[299,300]	1452	1452	-
	δ_s(C-H) LAS[299,300,*]	1437	1437	-
	ν(C-O)	1280	1280	-

The ν_{as}(C=O) of formic acid and methyl formate shifts from 1715 cm^{-1} to 1635 cm^{-1} when bound to TiO_2. Bands associated with formic acid and methyl formate bonded to Lewis acid

Die approbierte gedruckte Originalversion dieser Dissertation ist an der TU Wien Bibliothek verfügbar.
The approved original version of this doctoral thesis is available in print at TU Wien Bibliothek.
TU Bibliothek Your knowledge hub WIEN

sites (LAS) of TiO_2 appeared in addition to bands of the dissolved species at 1450 cm^{-1} and 1435 cm^{-1}. Note that the obtained results suggest that a differentiation between formic acid and methyl formate is not possible, which was also previously stated.[326] In contrast, the ν(C=O) bands assigned to $HCOO^-_{ads}$ (1587 and 1380 cm^{-1}) did not change upon adsorption and the difference between ν_{sym}(C=O) and ν_{asym}(C=O) of 200 cm^{-1} allows for assuming a bridging bidentate structure of the formate ion on TiO_2.[298] The corresponding changes in the IR spectra in the range of interest are depicted in Figure 5.26 for all Pt loadings. The gray and black traces correspond to spectra obtained during the first 5 min of UV irradiation (one spectrum every 10 s), while spectra shown in orange were recorded from 5 to 70 min at 5 min intervals. Note the strong baseline shift induced upon excitation of TiO_2[290,293] and the Si ATR crystal (Figure 5.19).

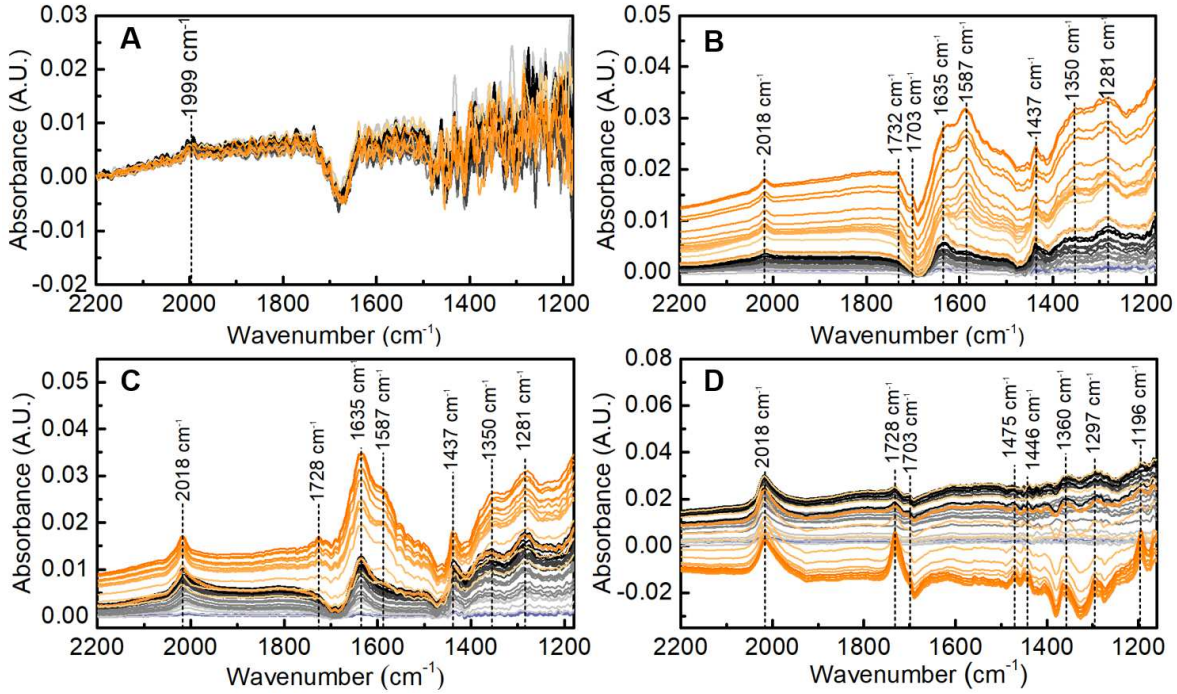

Figure 5.26: IR spectra of (A) 0.35 wt.% Pt, (B) 0.7 wt.% Pt, (C) 1.4 wt.% Pt, and (D) 2.7 wt.% Pt. Main bands of intermediates and Pt^0-CO are marked by dotted black lines. Gray to black curves correspond to spectra taken within the first 5 min of reaction with 10 s interval, followed by the light orange to orange spectra taken between 5 - 70 min every 5 min. The according band assignments are listed in Table 2. Only faint signals can be observed for the 0.35 wt % Pt sample, indicating the lower limit of sensitivity of this technique. While the intermediate loadings of 0.7 wt % and 1.4 wt % Pt show very similar spectral progression, clear differences can be found for the 2.7 wt % Pt loading.

The main bands of interest are highlighted in **Figure 5.26** and summarized in **Table 5.14**, together with respective literature references. The 0.35 wt % Pt loading resulted in only faint and unresolved signals. For the experiments with medium Pt loadings (0.7 and 1.4 wt % Pt), bands arise at 1635, 1452, 1437, and 1280 cm^{-1} that were mainly associated with adsorbed formate and with formic acid/methyl formate (Table 5.14).[299,300] After 10 min of illumination, small features appeared at 1587 and 1340 – 1380 cm^{-1} that were assigned to formaldehyde.[276,298,324,325] Interestingly, the ratio of the adsorbed formate to formic acid/methyl

Die approbierte gedruckte Originalversion dieser Dissertation ist an der TU Wien Bibliothek verfügbar.
The approved original version of this doctoral thesis is available in print at TU Wien Bibliothek.
TU Bibliothek WIEN Your knowledge hub

formate bands at 1635 cm^{-1} and 1587 cm^{-1} is reversed for 0.7 wt % and 1.4 wt % Pt (Figure 5.26B and C). In strong contrast, the experiment with 2.7 wt % Pt showed bands that were assigned solely to formaldehyde, DOM/methoxy methanol, and dissolved CO_2.

These results suggested that different Pt loadings have different methanol oxidation mechanisms under otherwise fixed conditions: for 0.7 and 1.4 wt % Pt, methanol oxidation seemed to proceed via a methyl formate intermediate followed by disproportionation to adsorbed formate (equations (5.21) and (5.22)), whereas for 2.7 wt % Pt, the reaction followed the direct pathway via formaldehyde formation (equation (5.20)). This drastic Pt loading-dependent change of the reaction mechanism was presumed in the previous work of *Haselmann et al.*,[271] but to the best of our knowledge, it has not been previously observed for the photocatalytic decomposition of methanol. The Pt^0–$CO_{(ads)}$ bands develop similarly for all Pt loadings (Figure 5.21B and Table 5.13); however, in particular for 0.7 and 2.7 wt % Pt loading, drastic differences in the decomposition spectra (Figure 5.23C, E, and G) are seen. Hence, the observed changes in the intermediate formation were directly attributed to the higher Pt loading, independent of amount of CO present in the system or Pt particle growth dynamics.

5.3.6 Temporal Correlation between Pt^0-$CO_{(ads)}$ Bands and Photooxidation Products using MCR-ALS Analysis

To further investigate these pathways, the temporal progression of the Pt^0–$CO_{(ads)}$ bands were correlated with the evolution of methanol degradation products via multivariate data analysis. Multivariate curve resolution (MCR) is used to mathematically decompose the instrument response matrix, $\boldsymbol{D}$ (here, the IR spectra recorded over time), consisting of a mixture of multiple components into the pure counterparts, $\boldsymbol{S}$ (here, the IR spectra of the pure components), and their respective concentrations, **C**:

$$\boldsymbol{D} = \boldsymbol{C}\boldsymbol{S}^{\boldsymbol{T}} + \boldsymbol{E} \tag{5.23}$$

The error matrix, **E**, which should be minimized, accounts for the part of the measured data that cannot be explained by the model. Alternating least square (ALS) is a popular method whereby the bilinear decomposition of **D** is based upon minimizing **E** via an iterative least-squares process. MCR-ALS requires initial estimates for **C** and $\boldsymbol{S}$, which, for a given number of components, are typically derived via evolving factor analysis (EFA). For a more detailed introduction to MCR-ALS, see Ref. [327]. MCR-ALS to extract time-dependent concentration profiles for different Pt loadings (0.7, 1.4, and 2.7 wt % Pt) was used to confirm the findings of the univariate data analysis from the previous sections and investigate possible correlations between different species. The results for the three different Pt loadings are given in **Figure 5.27**. Note that due to the strong spectral changes upon illumination (as discussed in the section 5.3.3), the single-channel spectrum of the dark setup (filled flow cell prior to UV illumination) was not suitable for use as the background spectrum for MCR-ALS. Instead, the spectra obtained at 4 min, *i.e.*, the time at which $t_{90\%}$ was reached (Figure 5.21), was chosen as the background spectrum. Note that after 4 min, the growth of Pt nanoparticles has not

Die approbierte gedruckte Originalversion dieser Dissertation ist an der TU Wien Bibliothek verfügbar.
The approved original version of this doctoral thesis is available in print at TU Wien Bibliothek.
TU Bibliothek WIEN Your knowledge hub

finished yet (as shown in the previous section), and thus an increase of the Pt^0–$CO_{(ads)}$ band still needs to be considered.

The left panel of **Figure 5.27** shows the concentration profiles for each component as determined via the MCR-ALS analysis as a function of time with marked $t_{100\%}$ values of Pt_{HUC} and Pt_{WC}. The corresponding spectra of the individual components, which were comprised of spectral features of different intermediates, are shown on the right side. Bands critical to the identification of intermediates are highlighted in the component spectra: bands associated with methyl formate/formic acid and adsorbed formate are highlighted in orange, and bands associated with formaldehyde and methoxy methanol are highlighted in yellow.

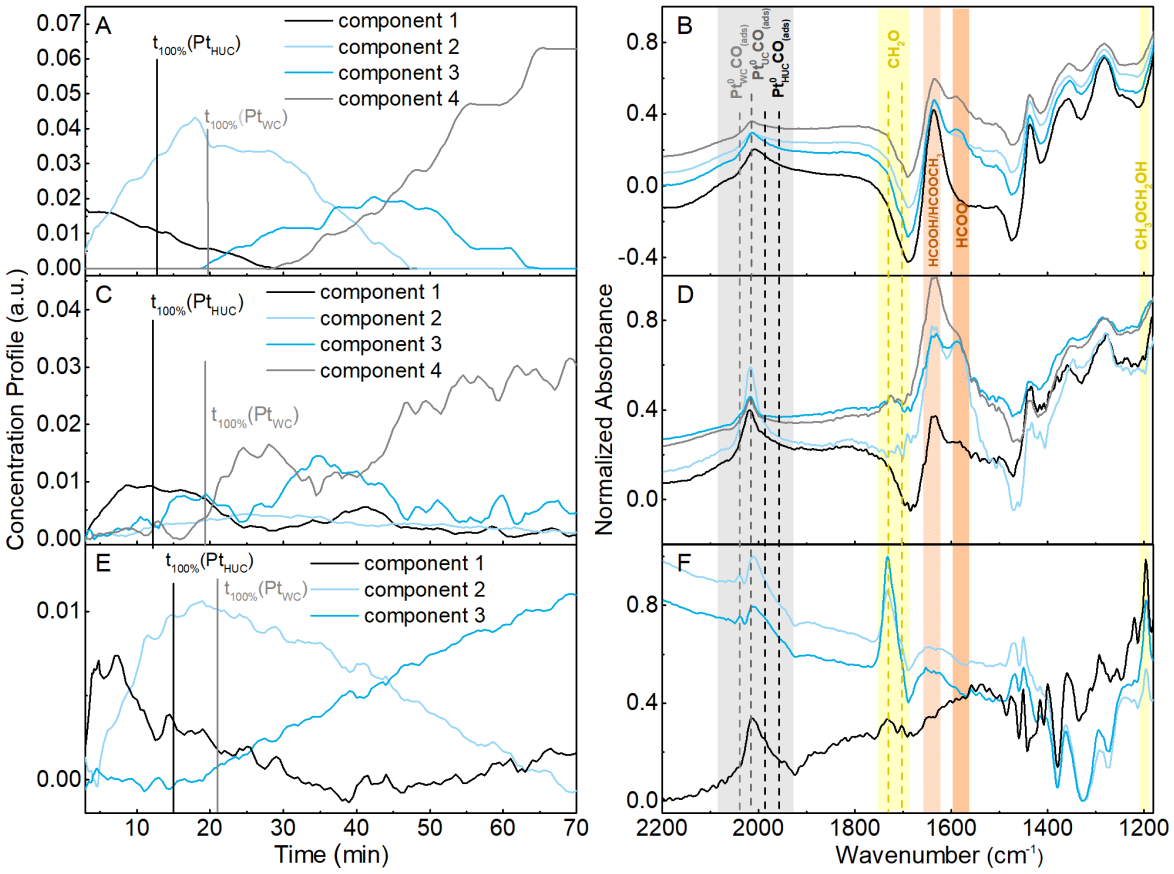

Figure 5.27: MCR-ALS of the *in situ* photodeposition of Pt and simultaneous photooxidation of methanol: (A-B) 0.7 wt.% Pt, component 1 (C1): Pt^0_{UC}-$CO_{(ads)}$ and formic acid/methyl formate, C2: mainly adsorbed formate and Pt_{WC}, C3: formate and formic acid/methyl formate, C4: formic acid/methyl formate and Pt_{WC}; (C-D): 1.4 wt.% Pt, C1: Pt_{HUC}, Pt_{UC} and formic acid/methyl formate, C2: adsorbed formate and formic acid/methyl formate and Pt_{WC}, C3: as C2 but with increasing formaldehyde, C4: formaldehyde and formic acid/methyl formate; (E-F): 2.7 wt.% Pt, C1: Pt_{HUC}, Pt_{UC} and methoxy methanol, C2: Pt_{WC} and chemisorbed and physisorbed formaldehyde, C3: increasing physisorbed formaldehyde and methoxy methanol.

For **0.7 wt % Pt** on TiO_2, four components were selected as the input parameters for MCR-ALS (Figure 5.27A and B): The concentration of component 1 (black trace), consisting of spectral features associated with Pt^0_{UC}–$CO_{(ads)}$ at 2018 cm^{-1} and formic acid/methyl formate at 1635 cm^{-1}, 1437 cm^{-1}, and 1280 cm^{-1}, increases immediately. From this, it was concluded that formic acid/methyl formate, CO, and Pt particles form simultaneously. Interestingly, the

Die approbierte gedruckte Originalversion dieser Dissertation ist an der TU Wien Bibliothek verfügbar.
The approved original version of this doctoral thesis is available in print at TU Wien Bibliothek.
TU Bibliothek Your knowledge hub WIEN

concentration profile of component 1 flattens out upon reaching $t_{100\%}(Pt_{HUC})$ and starts decreasing from $t_{100\%}(Pt_{WC})$ onward. This indicates that as soon as Pt nanoparticle growth begins to decline, the formic acid/methyl formate concentration decreases as well. With decreasing formic acid/methyl formate concentration and at $t_{100\%}(Pt_{WC})$, component 2 (light blue trace), which mainly includes features of adsorbed formate at 1587 cm^{-1} and 1360 cm^{-1}, smaller bands corresponding to formic acid/methyl formate at 1450 cm^{-1}, and a shoulder of the Pt^0–$CO_{(ads)}$ band at 2038 cm^{-1} corresponding to $Pt_{WC,}$ start to increase. Pt particles are now well-coordinated and formate species are dominantly produced. The sequence of observing first methyl formate and then formate species corresponds well to the indirect methyl formate pathway described above (equations (5.21) and (5.22).

At ~30 min, component 3 (blue trace) starts to increase. Similar to component 2, component 3 mainly shows bands of formate but also exhibited an increasing shoulder at 1635 cm^{-1} corresponding to formic acid/methyl formate. Furthermore, bands associated with chemisorbed formaldehyde at 1703 cm^{-1} and 1732 cm^{-1} starts to appear. No bands corresponding to the hydrated forms of formaldehyde (DOM/methoxy methanol) are visible. The final component, component 4, emerges after 40 min. Its spectrum is composed of the same features as component 3 except for an even more distinct shoulder at 1635 cm^{-1}, stemming from formic acid/methyl formate. The formation of, first, formaldehyde in component 2, followed by increased generation of formic acid in component 3 and then in component 4, is in line with the direct pathway for methanol photooxidation (equation ((5.20). Note that the Pt^0–$CO_{(ads)}$ band in the spectrum for component 4 showes the lowest intensity due to the near completion of particle growth.

From these findings, it was concluded that during the first 15 min of the experiment, the mechanistic pathway via methyl formate dominated until Pt nanoparticle growth is complete (components 1 and 2). At about 30 min, the direct photooxidation pathway, including formaldehyde (component 3 and 4) intermediates, increasingly impacts the overall reaction.

MCR-ALS analysis of **1.4 wt % Pt** on TiO_2 resulted in four components that were analogous to those found for the 0.7 wt % loading (Figure 5.27C and D). The spectrum that corresponds to component 1 (C, D, black traces) shows strong bands of Pt^0–$CO_{(ads)}$ (especially a shoulder of Pt_{HUC} at 1956 – 1986 cm^{-1}) and formic acid/methyl formate but also of adsorbed formate. In contrast to the experiment with 0.7 wt % Pt loading, the band of formic acid/methyl formate is more intense than the band of adsorbed formate in component 2, appearing after only 10 min of reaction. For components 3 and 4, in contrast to the lower Pt loading, the fraction of adsorbed formate decreases and appears solely as a shoulder of the formic acid/methyl formate band. This could indicate that the influence of the indirect methyl formate pathway on the overall reaction diminishes more strongly for the 1.4 wt % loading compared to 0.7 wt % Pt. However, no corresponding increase in the formaldehyde bands is observed. In general, the temporal progression of the 1.4 wt % Pt loading coincides with that of the 0.7 wt % Pt loading.

For **2.7 wt % Pt**, MCR-ALS resulted in three different components that exhibit distinctively

Die approbierte gedruckte Originalversion dieser Dissertation ist an der TU Wien Bibliothek verfügbar.
The approved original version of this doctoral thesis is available in print at TU Wien Bibliothek.
TU Bibliothek Your knowledge hub WIEN

different chemical composition and process evolution compared to the lower Pt loadings (Figure 5.27E and F). Here, component 1 reaches its maximal concentration right at the beginning of the photoreaction (black trace) and consists of bands that are assigned to Pt^0_{UC}–$CO_{(ads)}$, small features of chemisorbed formaldehyde at 1705 cm^{-1}, and more pronounced bands at 1293 cm^{-1} and 1196 cm^{-1} associated with methoxy methanol. The concentration of component 1 decays from 8 min onward, while the concentration of component 2 increases from 5 min onward, settles at $t_{100\%}(Pt_{HUC})$, and starts decaying after reaching $t_{100\%}(Pt_{WC})$. In contrast to component 1, the spectrum of component 2 (light blue trace) shows strong bands of formaldehyde at 1728 and 1705 cm^{-1} and smaller bands of methoxy methanol accompanying the Pt^0–$CO_{(ads)}$ shoulder (Pt_{WC}–$CO_{(ads)}$). The spectrum of component 3 shows a more intense band associated with physisorbed formaldehyde at 1728 cm^{-1} compared to the band associated with chemisorbed formaldehyde at 1703 cm^{-1}. The concentration of component 3 starts rising at $t_{100\%}(Pt_{WC})$, indicating that the final spectral composition starts appearing right after Pt particle growth is complete.

The observations made for 2.7 wt % Pt suggest that methanol oxidation proceeds solely via the direct oxidation pathway (equation (2)), in which methoxy methanol and chemisorbed formaldehyde dominate during the initial formation of Pt nanoparticles, while increasing amounts of physisorbed formaldehyde are found at later stages of the experiment, when well-coordinated Pt particles are present. However, although dissolved CO_2 is observed from 5 min onward (not shown in Figure 5.27), neither formic acid nor DOM are observed, which would be the immediately preceding intermediates for full mineralization of methanol to CO_2. It is possible that the reaction occurs too rapidly, resulting in signal intensity of formic acid/DOM that is too low to be observed via this setup.

Nevertheless, the dependence of the photooxidation pathway on the Pt loading was observed. For medium Pt loadings (0.7 wt % and 1.4 wt %), MCR-ALS suggests that the bimolecular side reaction to formate via a methyl formate intermediate dominates the first 30 min of the photoreaction, whereas bands associated with the direct oxidation pathway with formaldehyde as intermediate are only observed at later stages (*i.e.*, after 30 min). This shift in reaction pathways coincides with the $t_{100\%}(Pt_{WC})$, which would correspond to either completed Pt particle growth or complete coverage of Pt with CO.

In contrast, no bands corresponding to the indirect pathway for the highest Pt loading were observed. Here, formaldehyde formation was observed immediately, and dissolved CO_2 was observed from 5 min onward, indicating full mineralization of methanol. These results agree with the previous work of *Haselmann et al.*, in which they observed more stable H_2 evolution rates at higher Pt loadings. These differences in reaction selectivity were assigned to the differences in the total amount of Pt rather than to the growth dynamics of Pt particles or increasing CO coverage of Pt, as the development of the Pt^0–CO bands is almost identical in all cases. Although the oxidation is generally considered to take place on the TiO_2 surface, the triple-phase boundary of the liquid, metal oxide, and noble metal has been identified as the most reactive area.[328,329] In particular, *Fontelles-Carceller et al.* suggested a critical role of

Die approbierte gedruckte Originalversion dieser Dissertation ist an der TU Wien Bibliothek verfügbar.
The approved original version of this doctoral thesis is available in print at TU Wien Bibliothek.
TU Bibliothek WIEN Your knowledge hub

Pt in the complete mineralization of alcohols to CO_2.[329] Furthermore, *Haselmann et al.* previously stated that the ratio of defects (inherent or generated *in situ* through UV irradiation) to number of Pt particles may play a crucial role in the different H_2 evolution rates.[271] Defect sites are reactive centers and sites of adsorption in solids.[311,314,330] Fewer available Pt sites close to these adsorption centers might result in a higher likelihood of the adsorption of two methanol molecules next to each other, which would allow bimolecular reactions. The same process has been observed but with fixed Pt loading and increasing methanol concentrations.[265] Thus, at high enough Pt loadings, the direct oxidation pathway might be preferred over bimolecular side reactions. Previously, a drastic drop in the H_2 evolution rate after about 20 min to 30 min of a photocatalytic experiment was observed and suggested a shift to the bimolecular side reaction as evidenced by increasing CO generation.[271] In this study, increasing competition between the two reaction pathways after approximately the same amount of time were observed. However, in contrast to the previous suggestion of *Haselmann et al.* that the bimolecular pathway starts to dominate at this time, an increasing signal from intermediates belonging to the direct oxidation pathway was observed. The delayed observation of direct oxidation via formaldehyde for the lower Pt loadings could be due to different reaction kinetics of the two pathways. The methyl formate oxidation seemed to proceed more slowly than the formic acid decomposition and led to CO accumulation at the co-catalyst,[317] so that the available photogenerated holes might be preferably consumed by adsorbed methoxy groups for direct oxidation through the formaldehyde and formic acid intermediates.

These results, enabled by the dedicated ATR-FTIR setup, are the first showing that small changes in the number of Pt particles rather than changes in their size can have a drastic impact on the reaction selectivity for the photooxidation of methanol.

5.3.7 Conclusion

An *in situ* ATR-FTIR liquid-phase setup was developed that enabled real-time monitoring of the growth of co-catalyst particles (*e.g.*, Pt) during photodeposition and simultaneously provides mechanistic details regarding photocatalytic reactions (*e.g.*, photooxidation of methanol) over the entire lifetime of a photocatalyst in a highly reproducible manner. To the best of our knowledge, this has been realized for the first time.

Here, deconvolution of the Pt^0–$CO_{(ads)}$ band allowed the determination of different CO adsorption sites during Pt particle growth. Furthermore, in combination with MCR-ALS multivariate data analysis, it was confirmed that small changes in the Pt loading can lead to different methanol oxidation pathways at otherwise constant reaction conditions, which supports the previous work of *Haselmann et al.* on deactivation of the established reference system of Pt-loaded P25.[271] Lower Pt loadings showed spectral features that can be correlated to the methyl formate pathway, whereas higher Pt loadings lacked these bands, instead showing mainly formaldehyde and dissolved CO_2, indicating that methanol decomposition proceeds via direct and complete oxidation to CO_2. The dependence of the reaction selectivity

Die approbierte gedruckte Originalversion dieser Dissertation ist an der TU Wien Bibliothek verfügbar.
The approved original version of this doctoral thesis is available in print at TU Wien Bibliothek.
TU Bibliothek Your knowledge hub WIEN

was attributed on Pt loading to the availability of active sites, both on Pt and defects, for the total mineralization of methanol to CO_2 rather than different growth dynamics or different coverage of Pt with CO, as evidenced by the similar Pt^0–CO band development in all cases. However, defect species (*i.e.*, oxygen vacancies) are elusive species and only recently have *in situ* monitoring methods been reported (*e.g.*, by *in situ* EPR[331,332] and *in situ* XPS[333,334]). Further implementation of these methods is needed to correlate the actual defect concentration with the performance and reaction selectivities of (photo)catalysts during their application and is beyond the scope of this work.

The *in situ* liquid-phase ATR-FTIR system in combination with multivariate data analysis presents a powerful tool for understanding reaction mechanisms; it can be applied to a variety of systems and research questions and opens up possibilities for investigating aqueous systems at close-to-application conditions.

Die approbierte gedruckte Originalversion dieser Dissertation ist an der TU Wien Bibliothek verfügbar.
The approved original version of this doctoral thesis is available in print at TU Wien Bibliothek.
TU Bibliothek Your knowledge hub WIEN

Die approbierte gedruckte Originalversion dieser Dissertation ist an der TU Wien Bibliothek verfügbar.
The approved original version of this doctoral thesis is available in print at TU Wien Bibliothek.

Chapter 6 Advances in Instrumentation for ATR Spectroscopy

Since its introduction in the 1980s, 3D-printing has evolved into a versatile platform for rapid manufacturing of customized parts made of metals, ceramics and polymers. Nowadays commercially available 3D-printers cost less than $500, enabling fabrication at home or in every lab.[335] Recently, high-end applications ranging from 3D-printing cells for replacement of defective organs to the implementation of 3D-printers as spare part supplier on space trips have been reported.[336] Scientific instrumentation has been improved due to the freedom of design typical for 3D-printing. High performance laboratory equipment like a flexure translation stage microscope,[337] enhanced sample handling for analytical ultracentrifugation,[338] complex liquid handling,[339–341] innovative chemical reactionware[342] and acoustic lenses[343] are among a vast amount of examples difficult to produce with common manufacturing techniques. Several application of 3D-printing auxiliary optical equipment like chopper wheels, rails[344] and cage systems[345] have been reported. Parts of optical setups *e.g.* gas cells,[346,347] entire ultra-violet/visible (UV/VIS) spectrometers[348] as well as active optical components in the UV-Vis, IR[349] and terahertz[350] regime have already been 3D-printed.

This chapter presents the efforts toward new instrumentation for ATR spectroscopy in making use of the great possibilities of 3D printing. **Section 6.1** presents the 3D-printed twin of *Clipsi* (also compatible with Bruker FTIR spectrometers), its characterization and showcase applications. As a next step, the FTIR spectrometer was replaced by a pulsed light source and a FPI filter. Their combination in a 3D-printed mini-spectrometer with the dimension of 120 × 90 × 80 mm (length × width × height) as well as its application for nitrate sensing is presented in **section 6.2**.

6.1 Characterization of a 3D-printed ATR Module

Complimentary to commercial, costly ATR prisms, crystals prepared from double-side polished silicon wafer have emerged,[180] and have also been used in this thesis. Besides an

increased number of active reflections and hence effective path length, these crystals allow for fast screening by parallel preparation or complete disposal due their low-costs and availability. In addition, ATR spectroscopy was further enhanced by microstructuring of silicon for *e.g.* nanofluidic sensing,[351] or electrochemical investigations.[352] Furthermore, microstructured single-bounce ATR crystals make use of the easy access to silicon fabrication, while allowing to extending the IR transmission of silicon beyond multireflection elements.[353]

To further exploit ATR spectroscopy in fields were disposable low-cost equipment is needed, 3D-printing was combined with hand-crafted and commercially available low-cost silicon and germanium ATR crystals. The 3D-printed module was designed to fit in commercial FTIR spectrometers and its figures of merit bear comparison with a similar setup built from commercial optomechanics (see *Clipsi,* section 2.1).

6.1.1 Characterization and Iterative Optimization of the 3D-Printed ATR Unit

The 3D-printed ATR setup was placed in the beam path of a FTIR spectrometer and the gold mirrors were adjusted to maximum signal at the detector (see section 2.1.4 for further experimental details and design). The ATR body was designed to avoid stray light from direct reflection of the lower surface of the ATR crystal. This was verified by blocking the crystal's rear facet. Thereby, the detector signal was completely suppressed, hence, only light passing through the ATR crystal is reaching the detector. To showcase the versatility of the setup, three different ATR crystals were inserted, and the corresponding single channel spectra are given in **Figure 6.1A**.

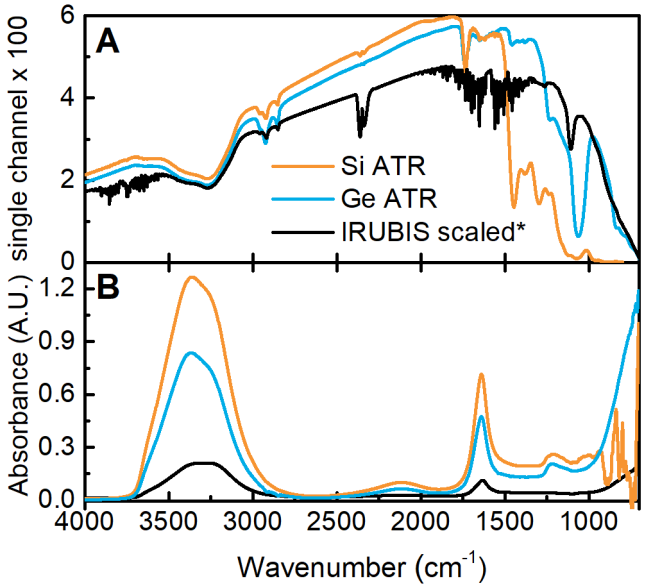

Figure 6.1: (A) Single Channel spectra of a Germanium crystal, silicon crystal and Si IRUBIS ATR crystals, all shown for angle of incidence = 45 °. *Spectra of IRUBIS is divided by 5. (B) Water spectra on corresponding ATR crystals. Absorbance is highly affected by the number of active bounces and material of the ATR element.

The single-bounce ATR crystal (IRUBIS) and the Ge ATR crystal provides the highest transmission down to 700 cm^{-1}, while the Si crystal is transparent to 1200 cm^{-1}. Bands at 1447 cm^{-1}, 1385 cm^{-1} and 1296 cm^{-1} are associated with phonons in silicon.[181] The band at 1066 cm^{-1} stems from Si-O-Si vibrations. The carbonyl stretching vibration of the polylactic

Die approbierte gedruckte Originalversion dieser Dissertation ist an der TU Wien Bibliothek verfügbar.
The approved original version of this doctoral thesis is available in print at TU Wien Bibliothek.
TU Bibliothek Your knowledge hub WIEN

acid of the filament is located at 1732 cm^{-1} and it is visible in the spectra because it is the supporting surface for the ATR crystals. The RMS noise of all crystals for 4 s integration time (32 scans) are between 3 - 5 10^{-5} A.U. obtained from 100 % lines between 2000 cm^{-1} to 1300 cm^{-1}. Furthermore, the effective path length d_e of the home-built Si and Ge ATR crystals, comparable with the thickness of a transmission measurements can be derived from the absorbance of water by inserting into Lambert-Beer's law.[5,9] For weakly absorbing samples, the effective pathlength can be approximated (see section 1.1.3). For the blank Si and Ge ATR crystal with $N = 15$, $\theta = 45°$, $n_1 = 3.42$ or $n_1 = 4.01$,[354,355] respectively, $n_2 = 1.32$ (water[11]) and $\lambda_0 = 6.1$ µm, equations (1.21)-(1.23) yield $N \cdot d_e$ (1640 cm^{-1}) =6.91 µm and 4.57 µm for Si and Ge, respectively. Note that the special microstructured geometry of the IRUBIS ATR crystals did not allow for these calculations.

Water spectra recorded using those different ATR crystals are given in **Figure 6.1B** and nicely illustrate the material and number of active bounces dependent depth of penetration: While the single-bounce ATR crystal from IRUBIS shows the lowest absorbance, the high number of bounces for the Ge and Si ATR crystal lead to considerably higher absorbances. These spectra can be further used to characterize the 3D-printed ATR module and determine the effective path length experimentally. To this end, the intensities of the bending vibration of water at 1640 cm^{-1}, the corresponding absorption coefficient $\varepsilon = 21.4$ L cm^{-1} mol^{-1} (obtained from a water transmission spectrum obtained with a defined path length), and $c = 55.56$ mol L^{-1} inserted into Lambert-Beer's law. This yielded a $d_{e,exp}$(Si ATR) = 5.97 µm and $d_{e,exp}$(Ge ATR) = 3.95 µm, which is equivalent for both films to 86.4 % of the theoretically obtained values reported above. To determine the source for this intriguingly reproducible deviation, the same ATR crystals and ATR fixture were used in the ATR setup built from commercial available optomechanics including xyz-stages and rotation mounts allowing for precisely adjusting the angle of incident (*Clipsi*) used in throughout this thesis. From this experiment, it was found that the $d_{e,exp}$ values for both crystals in combination with the 3D printed liquid compartment exactly match the theoretically obtained values. For this reason and due to the exact same deviation for both ATR materials, the small inaccuracies in dimension of the 3D-printed mirror mounts were assumed to result from a deviation of the angle of incidence, which highly affects the effective path length.

Table 6.1: Calculated and theoretical derived effective path length for different ATR crystals.

	Si ATR crystal	Ge ATR crystal	IRUBIS ATR crystal
d_p	0.48	0.39	
$d_{e,theo}$ (N=15; θ=45°)	7.24	4.57	
$d_{e,exp}$ first print	5.97	3.95	1.01
$d_{e,exp}$ final print	7.07	4.49	0.95

If inserting into equation (1.21)-(1.23), the obtained $d_{e,exp}$ values correspond to $\theta = 48.8°$ if holding all other parameter fixed. Here, the rapid prototyped nature of 3D-printing easily

Die approbierte gedruckte Originalversion dieser Dissertation ist an der TU Wien Bibliothek verfügbar.
The approved original version of this doctoral thesis is available in print at TU Wien Bibliothek.

allowed for correction by adapting the angle of the facet of the mirror mounts. This adjustment and reprint of the mirror mount, enabled to account for the printer-induced deviations and $d_{e,exp}$ were in very good agreement with theory, being just 0.5° off. In addition, the mechanical stability of the 3D-printed ATR module was tested by removing the entire system from the spectrometer's sample compartment, removing the ATR crystals and as well as pushing the mirror mounts by hand while recording water spectra. For all three test situations, the deviation of the intensity of the water band was < 4 %. Lastly, the entire ATR setup was inserted into another spectrometer (Bruker Tensor 37). Owing to the standardized sample compartment dimensions and beam height, no adjustments were needed, and the ATR module was immediately ready to use. However, in contrast to the high-end spectrometer, here a slightly higher RMS noise of $8 \cdot 10^{-5}$ A.U was obtained.

6.1.2 Exemplary Use Cases

The excellent mechanical stability and the high-quality spectra obtained with the 3D-printed ATR module, paired with the low-cost disposable character of the entire setup as well as the removable character of the ATR crystals will be further explored in the following sections.

6.1.2.1 Biological samples

Handling of biogenic samples typically involves cumbersome instrument cleaning protocols to avoid cross-contamination and therefore often relies on disposable equipment, additionally such samples often feature hazardous characteristics. In the presented setup, the only parts getting in contact with the sample are either the low-cost commercial IRUBIS ATR crystals or hand-crafted ATR crystals made from wafers as well as the fully 3D-printed ATR module. Therefore, cross-contaminations can be avoided due to the disposable nature of the proposed setup.

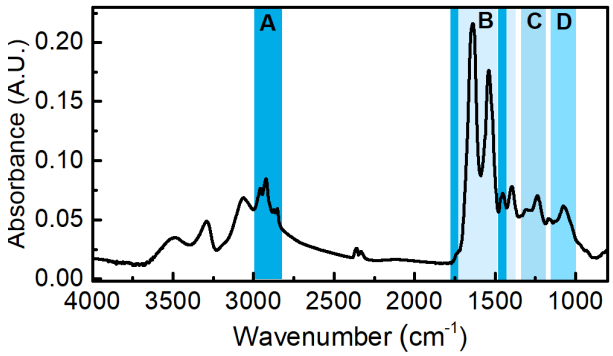

Figure 6.2: FTIR spectra of *E. coli* dried on IRUBIS ATR crystal. Bands for different species found in biological samples are highlighted: (A) lipids, (B) protein, (C) phosphates of the DNA backbone and carbohydrates (D).

Potential hazardous samples were mimicked by *E. coli* suspension pipetted on an IRUBIS ATR crystal, dried overnight at room temperature and re-placed in the 3D-printed ATR setup. The resulting IR spectrum is given in **Figure 6.2**, showing a high-quality bacteria spectrum including bands typically found in biological samples. Bands associated with lipids (region A, Figure 6.2), protein at 1641 and 1536 cm^{-1} (region B) and bands corresponding to the DNA backbone at 1237 cm^{-1} (region C) and carbohydrates at 1070 cm^{-1} (region D) are in good accordance with literature.[356] Besides for bacteria, IR spectroscopy is frequently

Die approbierte gedruckte Originalversion dieser Dissertation ist an der TU Wien Bibliothek verfügbar.
The approved original version of this doctoral thesis is available in print at TU Wien Bibliothek.
TU Bibliothek Your knowledge hub WIEN

employed for spectroscopic studies of proteins.[7] The typically employed ATR configurations with only one active bounce however impede the application of ATR spectroscopy for low concentration protein measurements. The herein presented multibounce ATR crystals have effective path lengths of up to 7 µm at 1640 cm^{-1}, being in the range of transmission cells employed for the same purpose but being difficult to handle.[357] In **Figure 6.3A**, the spectra of the model protein Bovine Serum Albumin (BSA) in aqueous solutions for different concentrations are shown. The amide I band at 1653 cm^{-1} and the amide II band at 1543 cm^{-1} are well resolved. The height of the amide II band as a function of BSA concentration is given in Figure 6.3B demonstrating linearity down to a concentration of 2 mg mL^{-1}. This underlines the potential usage of the setup for investigation in biological matrices *e.g.* blood or milk.

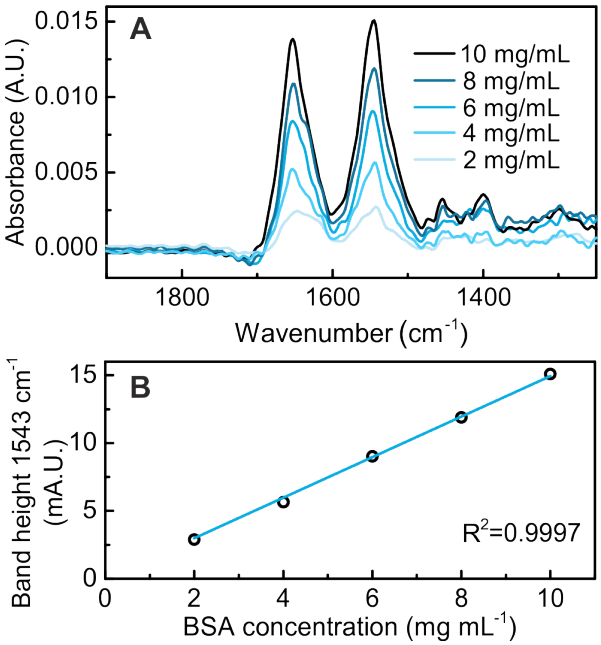

Figure 6.3: (A) FTIR spectra of BSA solutions with different concentration recorded on a Si ATR crystal. Background spectrum was recorded one for all spectra using pure water. (B) Calibration curve using amide II band height.

6.1.2.2 Monitoring Polymerization Processes

IR spectroscopy has proven a great tool to study polymerization processes as it probes the characteristic vibrations of the molecule.[358,359] Since the curing processes is strongly influenced by the applied film thickness, the possibility of reproducible deposition of the probed film is highly desired. In contrast to fiber optics or commercial single-bounce ATR setups, the presented exchangeable ATR crystals provide this degree of freedom. Due to their small footprint and low weight, they can be inserted into spin or dip-coating devices allowing for controlled film deposition. In addition, these ATR crystals can be heated to 400 °C overnight without decrease in performance (compare calcination temperatures given in section 2.3.3). This is a crucial requirement as many adhesive cure upon heat treatment.

By means of spin coating, a commercial two-component epoxy resin was applied to a Si ATR crystal and spectra were recorded immediately after deposition, after 30 min of curing at 100 °C, as suggested by the supplier, and after further curing for 24 h (see **Figure 6.4**).

Die approbierte gedruckte Originalversion dieser Dissertation ist an der TU Wien Bibliothek verfügbar.
The approved original version of this doctoral thesis is available in print at TU Wien Bibliothek.
TU Bibliothek Your knowledge hub WIEN

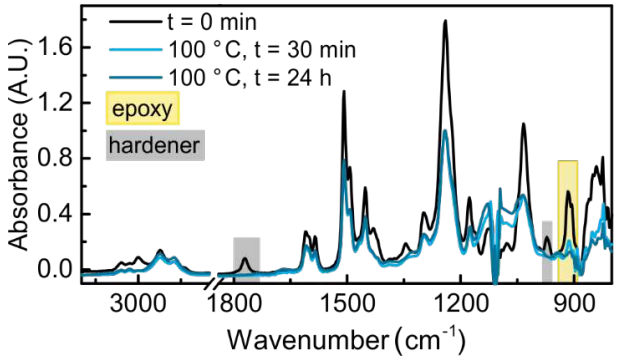

Figure 6.4: FTIR spectra of just-deposited and cured epoxy resin on a Si ATR crystal for different curing times. Background spectrum was recorded for blank Si ATR crystal.

After 30 min of curing, the band at 912 cm^{-1} associated with the epoxy ring has almost vanished, while the bands associated with the anhydride hardener at 1770 cm^{-1} and 971 cm^{-1} are not visible anymore (Figure 6.4). After 24 h of curing, no band at 912 cm^{-1} is visible and a full conversion of the epoxy group can be concluded.

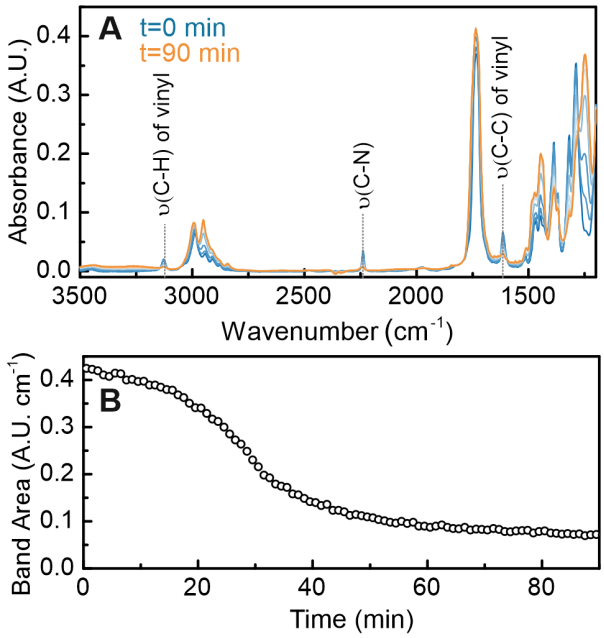

Figure 6.5: (A) FTIR spectra of super glue and (B) temporal progression of the area of the C-H stretching vibration of the vinyl group.

In addition to the heat curing adhesive, the ionic polymerization of a cyanoacrylate adhesive ("superglue") initiated by water in ambient air was monitored. To this end, the adhesive was applied to a Si ATR crystal into the open sample compartment with ca. 40 % relative humidity. As the polymerization progressed, the vinyl group was consumed leading to decreasing bands that are associated with the C-H and C=C stretching vibration of this group at 3126 cm^{-1} and 1613 cm^{-1}, respectively (compare **Figure 6.5A**). The area of the C-H stretching vibration was used to monitor the polymerization process and the evolution of the band area over time is given in **Figure 6.5B**. The reaction proceeded faster within the first 30 min, after which the reaction slowed down, and the profile flattened out. In addition, the band of the adjacent nitrile moiety is shifted to higher wavenumbers from 2237 cm^{-1} to 2251 cm^{-1} due to the change in the electronic environment. All these findings are in good agreement with a previous report on a similar adhesive.[360]

Die approbierte gedruckte Originalversion dieser Dissertation ist an der TU Wien Bibliothek verfügbar.
The approved original version of this doctoral thesis is available in print at TU Wien Bibliothek.
TU Bibliothek Your knowledge hub WIEN

6.1.3 Conclusion and Costs

The combination of a 3D-printed ATR module using different low-cost and easily exchangeable ATR crystals embedded into commercial FTIR spectrometer was demonstrated. The low noise levels and high path lengths of the multibounce ATR crystals allow for high quality spectra acquisition beyond commercial ATR units. Processing a wide variety of samples, with the setup underlined the versatile nature of 3D-printed instrumentation: The ATR crystals withstand high temperatures, allowing for monitoring of polymerization processes. The easiness of exchanging the ATR elements indicates the implementation in applications requiring high sample throughput or complex sample handing. Moreover, the disposable character of the ATR elements and the overall ATR suggest the use in studies involving hazardous samples.

Table 6.2: Summary of costs for the 3D-printed ATR module. [a]up to 50 ATR crystals can be prepared form one wafer; [b]in this study, gold-sputtered microscopy slides were used. [c]depending on used ATR crystal

	Supplier	**Prize [€]**
ATR crystal	Si: Double-side polished Si wafer, *e.g.* microchemicals, 100 mm	24[a]
	Ge: Double-side polished Ge wafer, *e.g.* from universitywafer, 50 mm	200[a]
	IRUBIS	70
27 m filament	*e.g.* Prusament, Prusa	2
Adapter plate	Bruker	223
2 x Gold mirrors[b]	*e.g.* PFSQ10-03-M01 Thorlabs	108
4 x M6x10 mm screw	*e.g.* RS components	1
4 x M3x5 mm screw	*e.g.* RS components	1
2 x M2 nuts	*e.g.* RS components	1
FKM O-ring	*e.g.* Persicaner	1
Total		**361 - 537**[c]

Table 6.2 summarizes the costs of the used components and if assuming a 3D-printer is available as well as the spectrometer adapter plate that is typically delivered with the FTIR spectrometer for transmission measurements, this setup can be rebuilt overnight for less than 150 €. This low-budget setup allows for making the high versatility of ATR spectroscopy accessible to a broader audience. In addition, only minor alteration of the ATR module should allow for the incorporation into FTIR spectrometers of other manufactures. Lastly, the combination with novel light sources like quantum cascade lasers or pulsed small-footprint thermal emitters coupled with novel detector systems such as Fabry-Pérot filters, would allow to further miniaturize and 3D-print entire IR spectrometers as it will be discussed in the following section.

Die approbierte gedruckte Originalversion dieser Dissertation ist an der TU Wien Bibliothek verfügbar.
The approved original version of this doctoral thesis is available in print at TU Wien Bibliothek.
TU Bibliothek Your knowledge hub WIEN

6.2 3D-Printed Mini ATR-IR Spectrometer

In the last decades, miniaturized MIR light sources and filters have emerged (see section 1.1.4.3 for further details) and in our group *A. Genner* and *C. Gasser* pioneered in this field.[26,361,362] They combined tunable Fabry-Pérot (FP) filters with a pulsed MIR source for monitoring exhaust gas in IR transmission measurements. Furthermore, FP filters have been coupled with a supercontinuum broadband laser in ATR configuration for hydrogen peroxide detection.[362] Based on these schemes, a 3D-printed ATR unit that houses a pulsed MIR light source, a FP filter and the home-made ATR crystals was designed and fabricated. This setup was combination with the mesoporous ion exchange coated ATR crystals presented in section 4.3.

6.2.1 Design of a Mini ATR-IR Spectrometer

A pulsed light source (601.612, EMIRS200_AT01T_BR080_CCa00V incl. Burn-In with Reflector 3 and CaF_2 window, front-vented, *Axetrix,* Switzerland*)* was combined with a spectrally tunable pyroelectric detector (LFP-5580C-337, TO8 housing, *InfraTec*, Germany) covering a spectral range between 1900 cm^{-1} - 1200 cm^{-1} and corresponding preamplifier electronics from *InfraTec*. All parts were integrated in a 3D-printed ATR unit that houses the ATR crystal and defines the angle of incidence for ATR crystal to be 45°, see **Figure 6.6**.

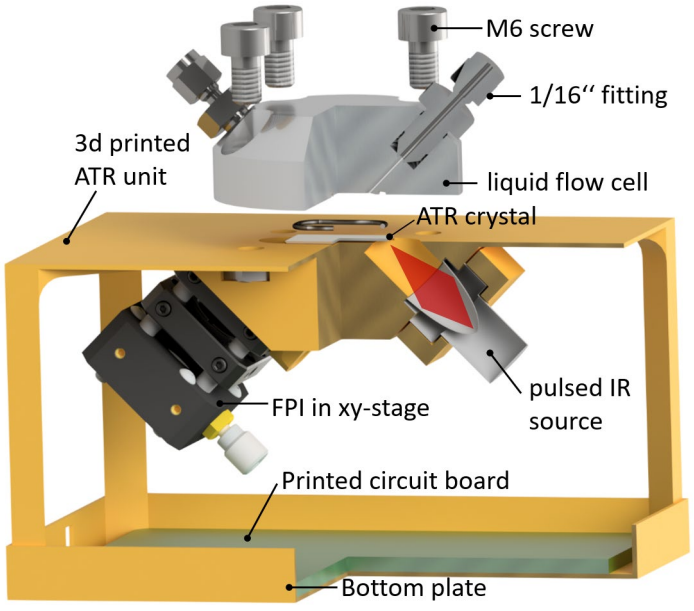

Figure 6.6: Exploded view of the 3D-printed mini-spectrometer with a footprint of 80 × 120 × 70 mm.

The pulsed light source is accommodated in a dedicated, 3D-printed cartridge, which is fixed with two M3 screws and triangular slots without the need of any further optical components. The distance between light source and the facet of the ATR crystal was designed to meet the focal point of the source of 25 mm. On the filter side, a 16 mm cage system (*Thorlabs GmbH*, Germany) is fixed to the ATR unit with a M2 countersunk screw. The cage system comprises a ZnSe lens (1/2'', F = 12 mm) focusing the MIR beam to the FP filter that is placed in a x-y stage. Strong absorption of PLA of which the ATR unit consist off, were avoided by

Die approbierte gedruckte Originalversion dieser Dissertation ist an der TU Wien Bibliothek verfügbar.
The approved original version of this doctoral thesis is available in print at TU Wien Bibliothek.
TU Bibliothek WIEN Your knowledge hub

placing a small piece of glass between ATR crystal and ATR unit. The bottom plate was designed to hold the props of the ATR unit and to house the preamplifier board, which controls source and filter. The board was supplied with 5 V and connected to a PC via USB. Four M6 nuts were sunk in slits enabling mounting of the standard liquid flow cell (see section 2.1.3 for further details on the flow cell). The flow cell was connected to a peristaltic pump for experiments with nitrate solutions.

6.2.2 Noise Characterization

A Ge ATR crystal was used to increase the throughput of the MIR irradiation for lower wavenumbers (compare section 2.1.5 for Si and Ge ATR transmittance). For characterizing the setup and finding optimum conditions, the light source was operated with different current and the FP filter software was set to different number of data points averaged per wavelength (= avg) between 1 and 16. The noise was derived by means of 100 % lines for different settings and the corresponding spectra are given in **Figure 6.7**. The lowest RMS noise for the entire spectral region was found to be $2.2 \cdot 10^{-3}$ A.U for a current of 100 mA and maximum averaging of avg=16. Therefore, all experiments were performed with these settings. As averaging scales inversely with scanning time, the time needed to record a spectrum with avg = 16 was ca. 2 min.

The single channel spectrum obtained from 100 mA and avg = 16 is also given in Figure 6.7, right y-axis.

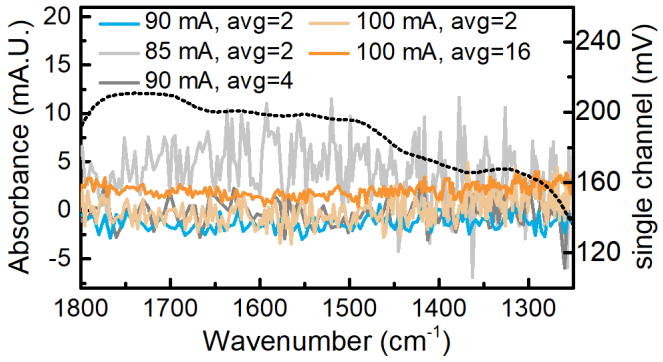

Figure 6.7: Light source was driven with different current. The corresponding 100 % lines show lower noise levels for higher current. A single channel spectrum for 100 mA, avg=16 is also given (dotted line, right y-axis)

6.2.3 Show-Case Application: Determination of Nitrate in Water

Due to the high RMS noise compared to the liquid nitrogen cooled spectrometers and the low spectral resolution of the FP filter ($\Delta\lambda$ =20 nm, > 5 cm^{-1}) determination of hydrocarbons enriched from aqueous or gas phase was not possible with this setup. However, the high absorption coefficient and broad band of NO_3^- seemed suitable for this setup. Therefore, the TMAC functionalized CTAB film was also used for measurements with the mini-spectrometer (see section 4.3.3 for further details on the film). In contrast to the measurements with a Vertex 80v FTIR spectrometer, recording of one spectrum (averaging of 16 measurements for each data point, 10 Hz) takes 2 min. Therefore, no time profiles were retrieved, but a spectrum

Die approbierte gedruckte Originalversion dieser Dissertation ist an der TU Wien Bibliothek verfügbar.
The approved original version of this doctoral thesis is available in print at TU Wien Bibliothek.
TU Bibliothek Your knowledge hub WIEN

after the application of 5 mL $NaNO_3$ solution with 1 mL min^{-1} flow velocity was recorded. Spectra obtained for different $NaNO_3$ concentrations are given in **Figure 6.8, left** and clearly show that a concentration of 5 mg L^{-1} is still detectable.

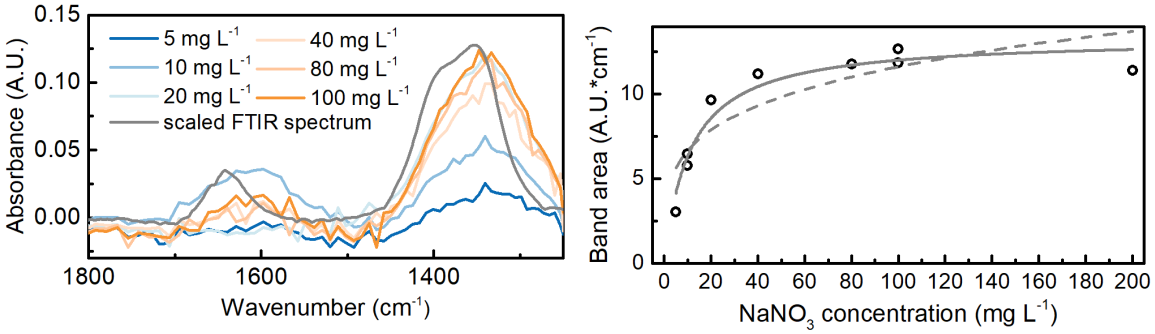

Figure 6.8: (Left) IR spectra obtained with the mini-spectrometer for different $NaNO_3$ concentrations. The background spectrum was recorded with distilled water.(Right) Isotherms obtained from CTAB 3d hexagonal coated on a Ge ATR crystal placed in the mini-spectrometer. Isotherm data points were fitted with the *Langmuir* function (solid line) and *Freundlich* function (dashed line).

The band areas were obtained between 1260 cm^{-1} and 1475 cm^{-1} and the resulting data points are depicted in **Figure 6.8, right**. As for the calibration curve obtained with the Vertex 80v, the calibration series shows a similar progression and it was fitted with the *Langmuir* and *Freundlich* functions. The quality of the fit was evaluated by χ^2 values, which were lower for the *Langmuir* fit indicating a better fit for this function. According to quantitative considerations performed in section 4.3, the enriched amount of NO_3^- per volume was also derived from these experiments. The band area obtained from a 10 mg L^{-1} $NaNO_3$ solution corresponded to 14.9 g L^{-1}_{film}. This equaled to a trimethylammonium moiety consumption of 15 % and an enrichment factor of 1490. The maximum adsorption capacity obtained from the *Langmuir* fit q_m was calculated to be 11.2 A.U. cm^{-1} (equal to 37.2 g L^{-1}_{film}), which corresponded to trimethylammonium moiety consumption of 37 %. This result indicates that only a fraction of the trimethylammonium moieties in the film was available for ion exchange. These results were compared with nitrate enrichment experiments performed from batch solutions using powdered mesoporous materials in literature. Here, the enriched amount is generally given in mg g_{SiO2}^{-1}. To convert the obtained capacity in g L^{-1}_{film} the film density of ρ=1.32 g cm^{-3} was calculated as the weighted average density from density of bulk silica and the porosity of the film $P = 50$ %. Thereby, a maximum absorption capacity of 28 mg g_{SiO2}^{-1} was obtained. This is in accordance with values obtained for batch experiments after 1 h of equilibration time for similar materials.[210,363]

The maximal nitrate concentration allowed in drinking water suggested by the WHO is 50 mg L^{-1}. The steep slope of the *Langmuir* function up to 40 mg L^{-1} make this setup in combination with TMAC functionalized mesoporous silica films an interesting candidate for a portable (due to the low power consumption of the system, battery operation is possible) sensor for monitoring drinking water quality.

Die approbierte gedruckte Originalversion dieser Dissertation ist an der TU Wien Bibliothek verfügbar.
The approved original version of this doctoral thesis is available in print at TU Wien Bibliothek.
TU Bibliothek Your knowledge hub WIEN

Die approbierte gedruckte Originalversion dieser Dissertation ist an der TU Wien Bibliothek verfügbar.
The approved original version of this doctoral thesis is available in print at TU Wien Bibliothek.

Chapter 7 Summary and Outlook

This thesis demonstrates the advantageous properties of mesoporous silica as enrichment material in trace chemical analysis when combined with ATR-IR spectroscopy and, inversely, that ATR-IR spectroscopy is a powerful tool to characterize porous materials and study chemical and physical processes within them.

For sensing, the great versatility of mesoporous silica in terms of pore size and surface functionalization was exploited. Tuning the surface chemistry of porous silica allows for introducing various functionalities *e.g.* hydrophobicity or ion exchange groups. The synthetic procedures are straight forward and routinely used for chromatography column materials. Their widespread application in chromatography comes with two benefits: many organosilanes are commercially available at rather low cost and the established knowledge in this field can be transferred, adapted and utilized for IR spectroscopy-based sensing.
Mesoporous silica films with different pore sizes and different functional groups were synthesized and used for enrichment of target analytes from gas and aqueous phase in the evanescent field of ATR crystals. Thereby, numerous advantages of these materials as compared to commonly employed polymer films were shown:

- fast diffusion into porous materials is reflected in low response times of less than 5 s
- fast regeneration is achieved without the need of thermal treatments
- calibration curves follow *Langmuir* or *Freundlich* functions that are beneficial for sensing due to their high slope at low concentrations
- mesoporous silica is covalently attached to the oxide surface of the ATR crystal, which enhanced mechanical stability and the same film could be used over months of intense experimenting
- high enrichment factors between 200 - 1800 from aqueous phase and up to 32000 from gas phase, depending on the analyte, were obtained

For studying adsorption and desorption processes, *in situ* monitoring at a temporal resolution

of seconds delivered valuable information for the development and understanding of porous materials. In this context, IR spectroscopy with multibounce ATR crystals stands out for its high sensitivity and rich spectral information as well as its applicability to the conditions of real-world experiments. Furthermore, ATR-IR spectroscopy in combination with multivariate data analysis proved a powerful tool for understanding reaction mechanisms.

Based on these results, a possible next step is the investigation of porous films of other materials such as TiO_2, which would increase the IR transparency compared to silica at wavenumbers below 1250 cm^{-1}. In addition, newly emerging porous films such as metal organic frameworks or covalent organic frameworks could be combined with ATR-IR spectroscopy to investigate different processes in these materials, *e.g.* adsorption or catalysis.[364–366]
Furthermore, the low, tunable refractive index of mesoporous materials makes them promising candidates for cladding materials of integrated optics. Apart from this, new synthesis methods such as soft-NIL could pave the way to fully porous waveguides.[188]
The sensitivity for sensing can be further increased by replacing the ATR crystal with waveguides. Successful coating of waveguide structures has been shown in this thesis and an outlook for the combination of mesoporous silica with integrated optics is given in the following section.

7.1 Mesoporous Silica Cladding on Ge-based Integrated Optics

A few weeks before this thesis was finalized, H2020 project partners from IMEC/ Ghent University provided integrated optic circuit (IOC) chips designed for mid-IR spectroscopy and chemical sensing. The first results will be shortly summarized in this final section. The Ge-based IOC chip comprised two grating couplers for in- and out-coupling to/from a single mode waveguide that is in contact with the sample covering the surface of the chip. Two micro-lenses were fabricated on the backside of the chip to focus the beam on the grating couplers. The IOC chip with a footprint of 15 × 20 mm was inserted into a dedicated aluminum cartridge that enabled positioning of the chip with the help of dowel pins and flexible pressure fittings (**Figure 7.1, right**).

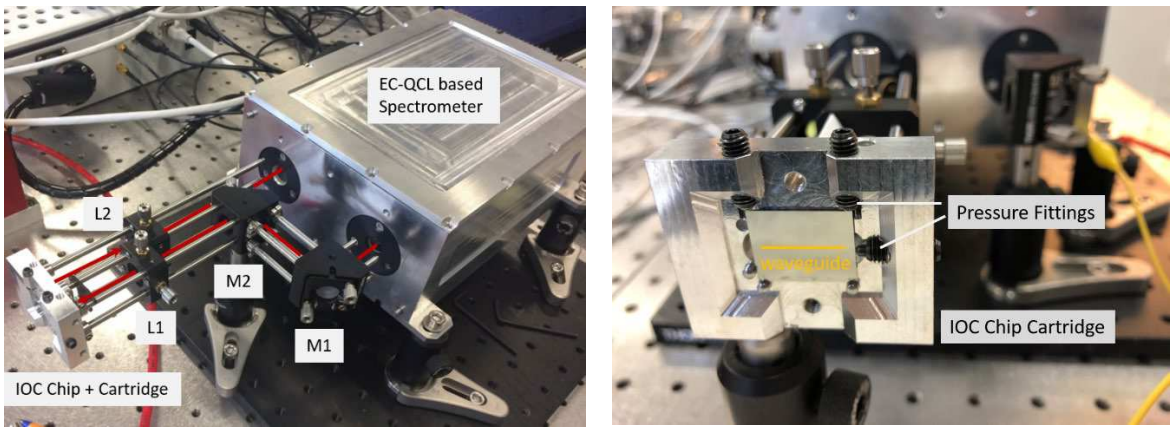

Figure 7.1: (Left) Aquarius EC-QCL based spectrometer with cage system and IOC chip cartridge. L..lens, M..mirror (Right) Close up on the cartridge holding the IOC chip.

Die approbierte gedruckte Originalversion dieser Dissertation ist an der TU Wien Bibliothek verfügbar.
The approved original version of this doctoral thesis is available in print at TU Wien Bibliothek.
TU Bibliothek Your knowledge hub WIEN

The pressure fittings and dowel pins allowed for a ca. 5 µm replacement tolerance, which is smaller then the micro-lens tolerances of ca. 50 µm. The distance between the incouple and outcouple micro-lenses and hence the length of the waveguide corresponded to 16 mm. This allowed the use of a commercially available 16 mm cage system of *Thorlabs*. This cage system interfaced the cartridge holding the IOC chip with the Aquarius spectrometer (Figure 7.1, left). The system comprised two Au mirrors in kinematic tip and tilt mounts and lenses (F = 50 mm, ZnSe, *Edmund Optics*) to focus the beam onto the micro-lenses. A dedicated aluminum flow cell was placed on top of the IOC chip, which covered 8 mm of the waveguide. The dimensions of the flow cell reservoir limited the effective interaction path length of the waveguide with the sample to ca. 80 µm (By design, one percent of the power of the guided mode extended into the sample).

Incoupling into the IOC chip was successful and the transmission spectrum of the waveguide is given in **Figure 7.2,** left. It showed a broadband transmission between 1520 - 1350 cm^{-1}. The RMS noise was derived by means of 100 % lines and corresponded to ca. 10 mA.U., approximately two orders of magnitude higher compared to commercial FTIR spectrometers used throughout this thesis. The spectra of cyclohexane (CH) in dichloromethane (DCM) obtained from the uncoated chip are depicted in Figure 7.2, right, and show a linear response with increasing CH concentration.

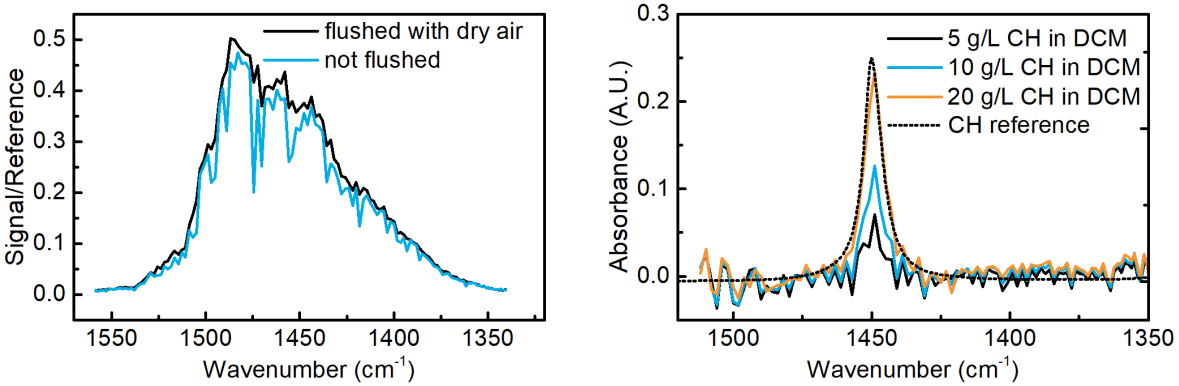

Figure 7.2: (Left) Transmission spectrum of the IOC chip with and without flushing of the measurement area with dry air. (Right) IR spectra obtained from cyclohexane (CH) in dichloromethane (DCM) solutions.

As shown in chapter 3 for Ge test structures, the IOC chip was coated with three layers of CTAB 3d hexagonal films to cover the trenched waveguide structures. Subsequently, the film was functionalized with HMDS.

The spectrum of a successful enrichment experiment from an aqueous *p*-xylene solution with a concentration of 62 mg L^{-1} is given in **Figure 7.3.** Note that the noise floor of this spectrum was higher compared to the uncoated IOC chip due to additional losses of the coated waveguide and very low power levels at the detector (both with and without coating). Absorption by the mesoporous silica film itself led to a decrease of the transmitted intensity by 60 %. Additionally, a small fraction of water inevitably penetrated the film (as shown *e.g.* in section 4.1 or 4.4.) that also caused considerable absorption in the probed spectral region.

Die approbierte gedruckte Originalversion dieser Dissertation ist an der TU Wien Bibliothek verfügbar.
The approved original version of this doctoral thesis is available in print at TU Wien Bibliothek.
TU Bibliothek Your knowledge hub WIEN

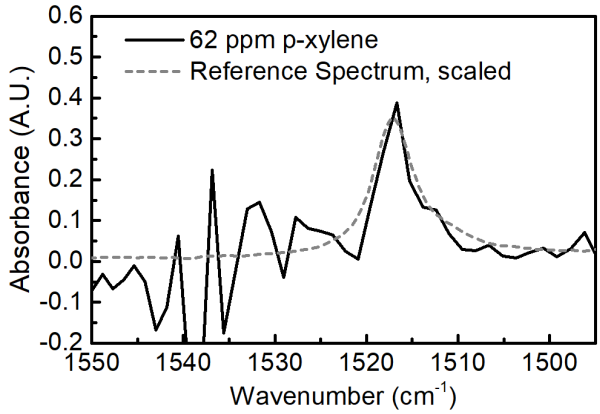

Figure 7.3: IR spectrum obtained from the enrichment of a 62 mg L^{-1} *p*-xylene solution compared with a reference FTIR spectrum. High noise floor for > 1530 cm^{-1} is due to low transmission of the IOC chip for this region, compare Figure 7.2, left.

Comparable enrichment experiments performed on ATR crystals with an effective path length of 5.6 µm (see section 4.2.5, Ge ATR crystal at 1520 cm^{-1}), being 7 % of the effective path length of the IOC chip, yielded an absorbance of 0.028 A.U. This absorbance corresponds to 7 % of the obtained IOC chip absorbance of 0.4 A.U. The agreement between effective pathlength and absorbance for these two measurements indicates that the same enrichment factor as found for the measurements performed on single layer mesoporous films on ATR crystals were achieved.

Given these results, we could successfully transfer the enrichment properties of mesoporous silica to structured IOC surfaces. However, the noise floor of the Aquarius spectrometer left room for improvements and suffered from low power levels at the detector. Using a state of the art EC-QCL with high power and low noise emission, *Schwaighofer et al.* recently achieved an RMS noise level of $6 \cdot 10^{-5}$ A.U. for a comparable EC-QCL-based spectrometer.[367] Assuming this noise floor and a signal level of 0.4 A.U. for 62 ppm shown above, limits of detection below 10 ppb would be achievable.

Die approbierte gedruckte Originalversion dieser Dissertation ist an der TU Wien Bibliothek verfügbar.
The approved original version of this doctoral thesis is available in print at TU Wien Bibliothek.
TU Bibliothek Your knowledge hub WIEN

Bibliography

1. Baumgartner, B., Hayden, J., Loizillon, J., Steinbacher, S., Grosso, D. & Lendl, B. Pore Size-Dependent Structure of Confined Water in Mesoporous Silica Films from Water Adsorption/Desorption Using ATR–FTIR Spectroscopy. *Langmuir* **35**, 11986–11994 (2019).
2. Baumgartner, B., Hayden, J., Schwaighofer, A. & Lendl, B. In Situ IR Spectroscopy of Mesoporous Silica Films for Monitoring Adsorption Processes and Trace Analysis . *ACS Appl. Nano Mater.* **1**, 7083–7091 (2018).
3. Baumgartner, B., Hayden, J. & Lendl, B. Mesoporous silica films for sensing volatile organic compounds using attenuated total reflection spectroscopy. *Sensors Actuators B Chem.* **302**, 127194 (2020).
4. Griffiths, P. R. & de Hasseth, J. A. *Fourier Transform Infrared Spectrometry (FTIR).* **222**, (Wiley-Interscience, 2015).
5. Mirabella, F. M. *Internal Reflection Spectroscopy: Theory and Applications*. (Marcel Dekker, 1993).
6. Beer. Bestimmung der Absorption des rothen Lichts in farbigen Flüssigkeiten. *Ann. der Phys. und Chemie* **162**, 78–88 (1852).
7. Vigano, C., Manciu, L., Buyse, F., Goormaghtigh, E. & Ruysschaert, J. M. Attenuated total reflection IR spectroscopy as a tool to investigate the structure, orientation and tertiary structure changes in peptides and membrane proteins. *Biopolymers - Peptide Science Section* **55**, 373–380 (2000).
8. Pollack, G. L. & Stump, D. R. *Electromagnetism*. (Addison Wesley, 2002).
9. Ramer, G. & Lendl, B. Attenuated Total Reflection Fourier Transform Infrared Spectroscopy. in *Encyclopedia of Analytical Chemistry* (John Wiley & Sons, Ltd, 2013).
10. Kischkat, J., Peters, S., Gruska, B., Semtsiv, M., Chashnikova, M., Klinkmüller, M., Fedosenko, O., Machulik, S., Aleksandrova, A., Monastyrskyi, G., Flores, Y. & Ted Masselink, W. Mid-Infrared Optical Properties of Thin Films of Aluminum Oxide, Titanium Dioxide, Silicon Dioxide, Aluminum Nitride, and Silicon Nitride. *Appl. Opt.* **51**, 6789–6798 (2012).
11. Hale, G. M. & Querry, M. R. Optical Constants of Water in the 200-nm to 200-μm Wavelength Region. *Appl. Opt.* **12**, 555 (1973).
12. Evanescent field. Available at: https://www.wikiwand.com/en/Evanescent_field.
13. Harrick, N. J. Electric Field Strengths at Totally Reflecting Interfaces. *J. Opt. Soc. Am.* **55**, 851 (1965).
14. Harrick, N. J. & du Pré, F. K. Effective Thickness of Bulk Materials and of Thin Films for Internal Reflection Spectroscopy. *Appl. Opt.* **5**, 1739 (1966).
15. Mirabella, F. M. Strength of interaction and penetration of infrared radiation for polymer films in internal reflection spectroscopy. *J. Polym. Sci. Polym. Phys. Ed.* **21**, 2403–2417 (1983).
16. Milosevic, M. *Internal Reflection and ATR Spectroscopy*. (John Wiley & Sons, Inc., 2012). doi:10.1002/9781118309742
17. Harrick, N. J. & Carlson, A. I. Internal Reflection Spectroscopy: Validity of Effective Thickness Equations. *Appl. Opt.* **10**, 19 (1971).
18. Mizaikoff, B. & Lendl, B. Sensor Systems Based on Mid-Infrared Transparent Fibers. in *Handbook of Vibrational Spectroscopy* (ed. Griffiths, P. R.) (John Wiley & Sons, Ltd, 2006). doi:10.1002/0470027320.s2704
19. Schaedle, T., Mizaikoff, B., Schädle, T. & Mizaikoff, B. Mid-Infrared Waveguides: A Perspective. *Appl. Spectrosc.* **70**, 1625–1638 (2016).
20. Sieger, M., Haas, J., Jetter, M., Michler, P., Godejohann, M. & Mizaikoff, B. Mid-Infrared Spectroscopy Platform Based on GaAs/AlGaAs Thin-Film Waveguides and Quantum Cascade Lasers. *Anal. Chem.* **88**, 2558–2562 (2016).
21. Charlton, C., Giovannini, M., Faist, J. & Mizaikoff, B. Fabrication and characterization of molecular beam epitaxy grown thin-film GaAs waveguides for mid-infrared evanescent field chemical sensing. *Anal. Chem.* **78**, 4224–4227 (2006).
22. Brandstetter, M., Genner, A., Anic, K. & Lendl, B. Tunable external cavity quantum cascade laser for the simultaneous determination of glucose and lactate in aqueous phase. in *Analyst* **135**, 3260–3265 (The Royal Society of Chemistry, 2010).
23. Lainé, D. C., Ai-Jourani, M. M., Carpenter, S. & Sedgbeer, M. Pulsed wideband IR thermal source. *IEE Proc. Optoelectron.* **144**, 315–322 (1997).
24. Inoue, T., De Zoysa, M., Asano, T. & Noda, S. High-Q mid-infrared thermal emitters operating with high power-utilization efficiency. *Opt. Express* **24**, 15101 (2016).
25. Puton, J., Jasek, K., Siodłowski, B., Knap, A. & Wiśniewski, K. Optimisation of a pulsed IR source for

Die approbierte gedruckte Originalversion dieser Dissertation ist an der TU Wien Bibliothek verfügbar.
The approved original version of this doctoral thesis is available in print at TU Wien Bibliothek.
TU Bibliothek Your knowledge hub WIEN

NDIR gas analysers. *Opto-electronics Rev.* **10**, 97–103 (2002).

26. Genner, A., Gasser, C., Moser, H., Ofner, J., Schreiber, J. & Lendl, B. On-line monitoring of methanol and methyl formate in the exhaust gas of an industrial formaldehyde production plant by a mid-IR gas sensor based on tunable Fabry-Pérot filter technology. *Anal. Bioanal. Chem.* **409**, 753–761 (2017).
27. Polyanskiy, M. N., Babzien, M. & Pogorelsky, I. V. Chirped-pulse amplification in a CO_2 laser. *Optica* **2**, 675–681 (2015).
28. Singh, V. *et al.* Mid-infrared materials and devices on a Si platform for optical sensing. *Science and Technology of Advanced Materials* **15**, 014603 (2014).
29. Capasso, F. Band-Gap Engeneering: From Physics and Materials to New Semiconductor Devices. *Science (80-.).* **235**, 172–176 (1987).
30. Capasso, F., Gmachl, C., Sivco, D. L. & Cho, A. Y. Quantum Cascade Lasers. *Phys. Today* **55**, 34–40 (2002).
31. Yang, R. Q. Infrared laser based on intersubband transitions in quantum wells. *Superlattices Microstruct.* **17**, 77–83 (1995).
32. Meyer, J. R., Vurgaftman, I., Yang, R. Q. & Ram-Mohan, L. R. Type-II and type-I interband cascade lasers. *Electron. Lett.* **32**, 45–46 (1996).
33. Michelson, A. A. Visibility of interference-fringes in the focus of a telescope. *London, Edinburgh, Dublin Philos. Mag. J. Sci.* **31**, 256–259 (1891).
34. Soref, R. Mid-infrared photonics in silicon and germanium. *Nat. Photonics* **4**, 495–497 (2010).
35. Kita, D. M., Miranda, B., Favela, D., Bono, D., Michon, J., Lin, H., Gu, T. & Hu, J. High-performance and scalable on-chip digital Fourier transform spectroscopy. *Nat. Commun.* **9**, 4405 (2018).
36. Miller, S. A., Yu, M., Ji, X., Griffith, A. G., Cardenas, J., Gaeta, A. L. & Lipson, M. Low-loss silicon platform for broadband mid-infrared photonics. *Optica* **4**, 707–712 (2017).
37. Schwarz, B., Reininger, P., Ristanić, D., Detz, H., Andrews, A. M., Schrenk, W. & Strasser, G. Monolithically integrated mid-infrared lab-on-a-chip using plasmonics and quantum cascade structures. *Nat. Commun.* **5:4085**, (2014).
38. Kumari, B., Barh, A., Varshney, R. K. & Pal, B. P. Silicon-on-nitride slot waveguide: A promising platform as mid-IR trace gas sensor. *Sensors Actuators, B Chem.* **236**, 759–764 (2016).
39. Liu, Q., Ramirez, J. M., Vakarin, V., Le Roux, X., Ballabio, A., Frigerio, J., Chrastina, D., Isella, G., Bouville, D., Vivien, L., Ramos, C. A. & Marris-Morini, D. Mid-infrared sensing between 5.2 and 6.6 µm wavelengths using Ge-rich SiGe waveguides. *Opt. Mater. Express* **8**, 1305–1312 (2018).
40. Robinson, J. T., Chen, L. & Lipson, M. On-chip gas detection in silicon optical microcavities. in *2008 Conference on Quantum Electronics and Laser Science Conference on Lasers and Electro-Optics, CLEO/QELS* **16**, 4296 (Optical Society of America, 2008).
41. Muneeb, M., Chen, X., Verheyen, P., Lepage, G., Pathak, S., Ryckeboer, E., Malik, A., Kuyken, B., Nedeljkovic, M., Van Campenhout, J., Mashanovich, G. Z. & Roelkens, G. Demonstration of Silicon-on-insulator mid-infrared spectrometers operating at 3.8 µm. *Opt. Express* **21**, 11659–11669 (2013).
42. Yu, M., Okawachi, Y., Griffith, A. G., Picqué, N., Lipson, M. & Gaeta, A. L. Silicon-chip-based mid-infrared dual-comb spectroscopy. *Nat. Commun.* **9**, 1869 (2018).
43. Holmstrom, S. A., Stievater, T. H., Kozak, D. A., Pruessner, M. W., Tyndall, N., Rabinovich, W. S., Andrew McGill, R. & Khurgin, J. B. Trace gas Raman spectroscopy using functionalized waveguides. *Optica* **3**, 891–896 (2016).
44. Tyndall, N. F., Stievater, T. H., Kozak, D. A., Koo, K., McGill, R. A., Pruessner, M. W., Rabinovich, W. S. & Holmstrom, S. A. Waveguide-enhanced Raman spectroscopy of trace chemical warfare agent simulants. *Opt. Lett.* **43**, 4803–4806 (2018).
45. Vasiliev, A., Malik, A., Muneeb, M., Kuyken, B., Baets, R. & Roelkens, G. On-Chip Mid-Infrared Photothermal Spectroscopy Using Suspended Silicon-on-Insulator Microring Resonators. *ACS Sensors* **1**, 1301–1307 (2016).
46. Ramirez, J. M., Liu, Q., Vakarin, V., Frigerio, J., Ballabio, A., Le Roux, X., Bouville, D., Vivien, L., Isella, G. & Marris-Morini, D. Graded SiGe waveguides with broadband low-loss propagation in the mid infrared. *Opt. Express* **26**, 870–877 (2018).
47. Younis, U., Luo, X., Dong, B., Huang, L., Vanga, S., Lim, E.-J., Lo, G.-Q., Lee, C., Bettiol, A. A. & Ang, K.-W. Towards low-loss waveguides in SOI and Ge-on-SOI for mid-IR sensing. *J. Phys. Commun.* **2**, 045029 (2018).
48. Mashanovich, G. Z., Mitchell, C. J., Penades, J. S., Khokhar, A. Z., Littlejohns, C. G., Cao, W., Qu, Z., Stanković, S., Gardes, F. Y., Masaud, T. Ben, Chong, H. M. H., Mittal, V., Murugan, G. S., Wilkinson,

Die approbierte gedruckte Originalversion dieser Dissertation ist an der TU Wien Bibliothek verfügbar.
The approved original version of this doctoral thesis is available in print at TU Wien Bibliothek.
TU Bibliothek Your knowledge hub WIEN

J. S., Peacock, A. C. & Nedeljkovic, M. Germanium Mid-Infrared Photonic Devices. *J. Light. Technol.* **35**, 624–630 (2017).

49. Chang, Y.-C., Paeder, V., Hvozdara, L., Hartmann, J.-M. & Herzig, H. P. Low-loss germanium strip waveguides on silicon for the mid-infrared. *Opt. Lett.* **37**, 2883–2885 (2012).
50. Wilks, P. Infrared Filtometers. in *Handbook of Vibrational Spectroscopy* (eds. Chalmers, J. M. & Griffiths, P. R.) (J. Wiley, 2006). doi:10.1002/0470027320.s0203
51. Jerman, J. H., Clift, D. J. & Mallinson, S. R. A miniature Fabry-Perot interferometer with a corrugated silicon diaphragm support. *Sensors Actuators A. Phys.* **29**, 151–158 (1991).
52. InfraTec. Durchstimmbare Detektoren (FPI Detektor) von InfraTec. Available at: https://www.infratec.at/sensorik/fpi-detektoren/. (Accessed: 13th September 2019)
53. Neumann, N., Ebermann, M., Hiller, K. & Kurth, S. Tunable infrared detector with integrated micromachined Fabry-Perot filter. in *MOEMS and Miniaturized Systems VI* (eds. Dickensheets, D. L., Gogoi, B. P. & Schenk, H.) **6466**, 646606 (International Society for Optics and Photonics, 2007).
54. Kurth, S., Hiller, K., Neumann, N., Heinze, M., Doetzel, W. & Gessner, T. Tunable Fabry-Perot-Interferometer for 3-5 µm wavelength with bulk micromachined reflector carrier. in *SPIE 4983, MOEMS and Miniaturized Systems III* (ed. Smith, J. H.) **4983**, 215 (International Society for Optics and Photonics, 2003).
55. Yanagisawa, T., Shimizu, T., Kuroda, K. & Kato, C. The Preparation of Alkyltriinethylaininonium–Kaneinite Complexes and Their Conversion to Microporous Materials. *Bull. Chem. Soc. Jpn.* **63**, 988–992 (1990).
56. Hoffmann, F., Cornelius, M., Morell, J. & Fröba, M. Silica-Based Mesoporous Organic-Inorganic Hybrid Materials. *Angewandte Chemie - International Edition* **45**, 3216–3251 (2006).
57. Wan, Y. & Zhao, D. On the Controllable Soft-Templating Approach to Mesoporous Silicates. *Chemical Reviews* **107**, 2821–2860 (2007).
58. Nicole, L., Boissière, C., Grosso, D., Quach, A. & Sanchez, C. Mesostructured Hybrid Organic–Inorganic Thin Films. *J. Mater. Chem.* **15**, 3598–3627 (2005).
59. Rouquerol, J., Avnir, D., Fairbridge, C. W., Everett, D. H., Haynes, J. M., Pernicone, N., Ramsay, J. D. F., Sing, K. S. W. & Unger, K. K. Recommendations for the Characterization of Porous Solids. *Pure Appl. Chem.* **66**, 1739–1758 (1994).
60. Brunel, D., Blanc, A. C., Galarneau, A. & Fajula, F. New Trends in the Design of Supported Catalysts on Mesoporous Silicas and their Applications in Fine Chemicals. in *Catalysis Today* **73**, 139–152 (Elsevier, 2002).
61. Clark, J. H., Macquarrie, D. J. & Tavener, S. J. The Application of Modified Mesoporous Silicas in Liquid Phase Catalysis. *Dalt. Trans.* **0**, 4297 (2006).
62. Macquarrie, D. J. Organically Modified Micelle Templated Silicas in Green Chemistry. *Topics in Catalysis* **52**, 1640–1650 (2009).
63. Walcarius, A. & Collinson, M. M. Analytical Chemistry with Silica Sol-Gels: Traditional Routes to New Materials for Chemical Analysis. *Annu. Rev. Anal. Chem.* **2**, 121–143 (2009).
64. Walcarius, A., Mandler, D., Cox, J. A., Collinson, M. & Lev, O. Exciting new directions in the intersection of functionalized sol–gel materials with electrochemistry. *J. Mater. Chem.* **15**, 3663 (2005).
65. Melde, B. J., Johnson, B. J. & Charles, P. T. Mesoporous Silicate Materials in Sensing. *Sensors* **8**, 5202–5228 (2008).
66. Scott, B. J., Wirnsberger, G. & Stucky, G. D. Mesoporous and Mesostructured Materials for Optical Applications Mesoporous and Mesostructured Materials for Optical Applications. *Chem. Mater.* **13**, 3140–3150 (2001).
67. Clark, J. H., Macquarrie, D. J. & Wilson, K. Functionalised Mesoporous Materials for Green Chemistry. *Stud. Surf. Sci. Catal.* **129**, 251–264 (2000).
68. Ulrich Schubert, N. H. *Synthesis of Inorganic Materials*. (2012).
69. Brinker, C. J. J., Sehgal, R., Hietala, S. L. L., Deshpande, R., Smith, D. M. M., Loy, D. & Ashley, C. S. S. Sol-gel strategies for controlled porosity inorganic materials. *J. Memb. Sci.* **94**, 85–102 (1994).
70. Kresge, C., Leonowicz, M., Roth, W. & Vartuli, J. Ordered Mesoporous Molecular Sieves Synthesized by a Liquid-Crystal Template Mechanism. *Nature* **359**, 710–712 (1992).
71. Fan, J., Yu, C., Lei, J., Zhang, Q., Li, T., Tu, B., Zhou, W. & Zhao, D. Low-temperature strategy to synthesize highly ordered mesoporous silicas with very large pores. *J. Am. Chem. Soc.* **127**, 10794–10795 (2005).
72. Deng, Y., Wei, J., Sun, Z. & Zhao, D. Large-pore ordered mesoporous materials templated from non-

Die approbierte gedruckte Originalversion dieser Dissertation ist an der TU Wien Bibliothek verfügbar.
The approved original version of this doctoral thesis is available in print at TU Wien Bibliothek.
TU Bibliothek Your knowledge hub WIEN

Pluronic amphiphilic block copolymers. *Chemical Society Reviews* **42**, 4054–4070 (2013).

73. Brinker, J. C., Lu, Y., Sellinger, A. & Fan, H. Evaporation-Induced Self-Assembly: Nanostructures Made Easy. *Adv. Mater.* **11**, 579–585 (1999).
74. Schneller, T. & Waser, R. *Chemical Solution Deposition of Functional Oxide Thin Films*. (Springer Berlin Heidelberg, 2013).
75. Grosso, D., Cagnol, F., Soler-Illia, G. J. D. A. A., Crepaldi, E. L., Amenitsch, H., Brunet-Bruneau, A., Bourgeois, A. & Sanchez, C. Fundamentals of mesostructuring through evaporation-induced self-assembly. *Adv. Funct. Mater.* **14**, 309–322 (2004).
76. Holmqvist, P., Alexandridis, P. & Lindman, B. Modification of the microstructure in block copolymer-water-"oil" systems by varying the copolymer composition and the 'oil' type: Small-angle X-ray scattering and deuterium-NMR investigation. *J. Phys. Chem. B* **102**, 1149–1158 (1998).
77. Barczak, M. Template removal from mesoporous silicas using different methods as a tool for adjusting their properties. *New J. Chem.* **42**, 4182–4191 (2018).
78. Dunphy, D. R., Sheth, P. H., Garcia, F. L. & Brinker, C. J. Enlarged pore size in mesoporous silica films templated by pluronic F127: Use of poloxamer mixtures and increased template/SiO_2 ratios in materials synthesized by evaporation-induced self-assembly. *Chem. Mater.* **27**, 75–84 (2015).
79. Imperor-Clerc, M., Davidson, P. & Davidson, A. Existence of a microporous corona around the mesopores of silica-based SBA-15 materials templated by triblock copolymers. *J. Am. Chem. Soc.* **122**, 11925–11933 (2000).
80. Soler-Illia, G. J. A. A., Angelomé, P. C., Fuertes, M. C., Calvo, A., Wolosiuk, A., Zelcer, A., Bellino, M. G. & Martínez, E. D. Mesoporous hybrid and nanocomposite thin films. A sol-gel toolbox to create nanoconfined systems with localized chemical properties. in *Journal of Sol-Gel Science and Technology* **57**, 299–312 (Springer US, 2011).
81. Athens, G. L., Shayib, R. M. & Chmelka, B. F. Functionalization of mesostructured inorganic-organic and porous inorganic materials. *Current Opinion in Colloid and Interface Science* **14**, 281–292 (2009).
82. Deschner, T., Liang, Y. & Anwander, R. Silylation efficiency of chorosilanes, alkoxysilanes, and monosilazanes on periodic mesoporous silica. *J. Phys. Chem. C* **114**, 22603–22609 (2010).
83. *Handbook of Porous Solids. Handbook of Porous Solids* (Wiley, 2002). doi:10.1002/9783527618286
84. Neimark, A. V., Thommes, M., Sing, K. S. W., Rodriguez-Reinoso, F., Olivier, J. P., Kaneko, K. & Rouquerol, J. Physisorption of gases, with special reference to the evaluation of surface area and pore size distribution (IUPAC Technical Report). *Pure Appl. Chem.* **87**, (2015).
85. Sing, K. S. W., Everett, D. H., Haul, R. A. W., Moscou, L., Pierotti, R. A., Rouquerol, J. & Siemieniewska, T. Reporting Physisorption Data for Gas/Solid Systems with Special Reference to the Determination of Surface Area and Porosity. *Pure Appl. Chem.* **57**, 603–619 (1985).
86. Monson, P. A. Understanding adsorption/desorption hysteresis for fluids in mesoporous materials using simple molecular models and classical density functional theory. *Microporous Mesoporous Mater.* **160**, 47–66 (2012).
87. Landers, J., Gor, G. Y. & Neimark, A. V. Density functional theory methods for characterization of porous materials. *Colloids Surfaces A Physicochem. Eng. Asp.* **437**, 3–32 (2013).
88. Maréchal, Y., Vasylieva, A., Doroshenko, I., Vaskivskyi, Y., Chernolevska, Y., Pogorelov, V., Mallamace, F., Broccio, M., Corsaro, C., Faraone, A., Majolino, D., Venuti, V., Liu, L., Mou, C.-Y., Chen, S.-H., Kocherbitov, V. & Alfredsson, V. FTIR study of condensed water structure. *J. Mol. Struct.* **111**, 146–155 (2007).
89. Mallamace, F., Broccio, M., Corsaro, C., Faraone, A., Majolino, D., Venuti, V., Liu, L., Mou, C.-Y. & Chen, S.-H. Evidence of the existence of the low-density liquid phase in supercooled, confined water. *Proc. Natl. Acad. Sci.* **104**, 424–428 (2007).
90. Baumgartner, B., Hayden, J., Loizillon, J., Steinbacher, S., Grosso, D. & Lendl, B. Pore Size-Dependent Structure of Confined Water in Mesoporous Silica Films from Water Adsorption-Desorption using ATR-FTIR Spectroscopy. *Langmuir* (2019). doi:10.1021/acs.langmuir.9b01435
91. Boissiere, C., Grosso, D., Lepoutre, S., Nicole, L., Bruneau, A. B. & Sanchez, C. Porosity and mechanical properties of mesoporous thin films assessed by environmental ellipsometric porosimetry. *Langmuir* **21**, 12362–12371 (2005).
92. Hwang, J., Kataoka, S., Endo, A. & Daiguji, H. Adsorption and Desorption of Water in Two-Dimensional Hexagonal Mesoporous Silica with Different Pore Dimensions. *J. Phys. Chem. C* **119**, 26171–26182 (2015).
93. Dubreuil, O., Dewalque, J., Chêne, G., Mathis, F., Spronck, G., Strivay, D., Cloots, R. & Henrist, C. TiO2 mesoporous thin films studied by Atmospheric Ellipsometric Porosimetry: A case of contamination.

Die approbierte gedruckte Originalversion dieser Dissertation ist an der TU Wien Bibliothek verfügbar.
The approved original version of this doctoral thesis is available in print at TU Wien Bibliothek.
TU Bibliothek WIEN Your knowledge hub

Microporous Mesoporous Mater. **145**, 1–8 (2011).

94. Baklanov, M. R., Mogilnikov, K. P., Polovinkin, V. G. & Dultsev, F. N. Determination of pore size distribution in thin films by ellipsometric porosimetry. *J. Vac. Sci. Technol. B Microelectron. Nanom. Struct.* **18**, 1385 (2002).
95. Barrett, E. P., Joyner, L. G. & Halenda, P. P. The Determination of Pore Volume and Area Distributions in Porous Substances. I. Computations from Nitrogen Isotherms. *J. Am. Chem. Soc.* **73**, 373–380 (1951).
96. Halsey, G. Physical Adsorption on Non-Uniform Surfaces. *J. Chem. Phys.* **16**, 931–937 (1948).
97. Kruk, M., Jaroniec, M. & Sayari, A. Application of Large Pore MCM-41 Molecular Sieves To Improve Pore Size Analysis Using Nitrogen Adsorption Measurements. *Langmuir* **13**, 6267–6273 (2002).
98. Lu, H. M. & Jiang, Q. Size-dependent surface tension and Tolman's length of droplets. *Langmuir* **21**, 779–781 (2005).
99. Tolman, R. C. The effect of droplet size on surface tension. *J. Chem. Phys.* **17**, 333–337 (1949).
100. Zhu, D., Zhang, H., Tao, Q., Xu, Z. & Zheng, S. Surface Functionalized Mesoporous Silicas as Adsorbents for Aromatic Contaminants in Aqueous Solution. *Environ. Toxicol. Chem.* **28**, 1400–1408 (2009).
101. Qin, Q. & Xu, Y. Enhanced Nitrobenzene Adsorption in Aqueous Solution by Surface Silylated MCM-41. *Microporous Mesoporous Mater.* **232**, 143–150 (2016).
102. Sepehrian, H., Fasihi, J. & Khayatzadeh Mahani, M. Adsorption Behavior Studies of Picric Acid on Mesoporous MCM-41. *Ind. Eng. Chem. Res.* **48**, 6772–6775 (2009).
103. Anbia, M. & Lashgari, M. Synthesis of Amino-Modified Ordered Mesoporous Silica as a New Nano Sorbent for the Removal of Chlorophenols from Aqueous Media. *Chem. Eng. J.* **150**, 555–560 (2009).
104. Langmuir, I. The consitution and fundamental properties of solids and liquids. Part I. solids. *J. Am. Chem. Soc.* **38**, 2221–2295 (1916).
105. Giles, C. H., Smith, D. & Huitson, A. A general treatment and classification of the solute adsorption isotherm. I. Theoretical. *J. Colloid Interface Sci.* **47**, 755–765 (1974).
106. Meziani, M. J., Zajac, J., Jones, D. J., Rozière, J. & Partyka, S. Surface characterization of mesoporous silicoalurninates of the MCM-41 type: Evaluation of polar surface sites using flow calorimetry, adsorption of a cationic surfactant as a function of pore size and aluminum content. *Langmuir* **13**, 5409–5417 (1997).
107. Corma, A. Inorganic Solid Acids and Their Use in Acid-Catalyzed Hydrocarbon Reactions. *Chem. Rev.* **95**, 559–614 (1995).
108. Delage, F., Pre, P. & Le Cloirec, P. Mass transfer and warming during adsorption of high concentrations of VOCs on an activated carbon bed: Experimental and theoretical analysis. *Environ. Sci. Technol.* **34**, 4816–4821 (2000).
109. Lin, W. & Li, Z. Detection and Quantification of Trace Organic Contaminants in Water Using the FT-IR-Attenuated Total Reflectance Technique. *Anal. Chem.* **82**, 505–515 (2010).
110. Regan, F., Meaney, M., Vos, J. G., MacCraith, B. D. & Walsh, J. E. Determination of pesticides in water using ATR-FTIR spectroscopy on PVC/chloroparaffin coatings. *Anal. Chim. Acta* **334**, 85–92 (1996).
111. Göbel, R., Krska, R., Kellner, R., Seitz, R. W. & Tomellini, S. A. Investigation of Different Polymers as Coating Materials for IR/ATR Spectroscopic Trace Analysis of Chlorinated Hydrocarbons in Water. *Appl. Spectrosc.* **48**, 678–683 (1994).
112. Flavin, K., Hughes, H., Dobbyn, V., Kirwan, P., Murphy, K., Steiner, H., Mizaikoff, B. & Mcloughlin, P. A comparison of polymeric materials as pre-concentrating media for use with ATR/FTIR sensing. *Int. J. Environ. Anal. Chem.* **86**, 401–415 (2006).
113. Murphy, B., Kirwan, P. & McLoughlin, P. Investigation into polymer-diffusant interactions using ATR-FTIR spectroscopy. *Vib. Spectrosc.* **33**, 75–82 (2003).
114. Murphy, B., Kirwan, P. & McLoughlin, P. Study of the impact of penetrant characteristics upon diffusion into Teflon membranes to further assess the performance of an ATR/FTIR sensor. *Anal. Bioanal. Chem.* **377**, 195–202 (2003).
115. Lu, Y., Han, L., Brinker, C. J., Niemczyk, T. M. & Lopez, G. P. Chemical sensors based on hydrophobic porous sol-gel films and ATR-FTIR spectroscopy. *Sensors Actuators B Chem.* **36**, 517–521 (1996).
116. Han, L., Niemczyk, T. M., Haaland, D. M. & Lopez, G. P. Enhancing IR detection limits for trace polar organics in aqueous solutions with surface-modified sol-gel-coated ATR sensors. *Appl. Spectrosc.* **53**, 381–389 (1999).
117. Janotta, M., Karlowatz, M., Vogt, F. & Mizaikoff, B. Sol-gel Based Mid-Infrared Evanescent Wave Sensors for Detection of Organophosphate Pesticides in Aqueous Solution. *Anal. Chim. Acta* **496**, 339–348 (2003).
118. Flavin, K., Mullowney, J., Murphy, B., Owens, E., Kirwan, P., Murphy, K., Hughes, H. & McLoughlin, P. The development of novel organically modified sol-gel media for use with ATR/FTIR sensing. *Analyst*

Die approbierte gedruckte Originalversion dieser Dissertation ist an der TU Wien Bibliothek verfügbar.
The approved original version of this doctoral thesis is available in print at TU Wien Bibliothek.
TU Bibliothek Your knowledge hub WIEN

132, 224–9 (2007).

119. Karlowatz, M., Kraft, M. & Mizalkoff, B. Simultaneous Quantitative Determination of Benzene, Toluene, and Xylenes in Water Using Mid-Infrared Evanescent Field Spectroscopy. *Anal. Chem.* **76**, 2643–2648 (2004).
120. Roy, G. & Mielczarski, J. A. Infrared detection of chlorinated hydrocarbons in water at ppb levels of concentrations. *Water Res.* **36**, 1902–1908 (2002).
121. Yang, J. & Huang, Y. S. IR chemical sensor for detection of aromatic compounds in aqueous solutions using alkylated polystyrene-coated ATR waveguides. *Appl. Spectrosc.* **54**, 202–208 (2000).
122. Schädle, T., Pejcic, B., Myers, M. & Mizaikoff, B. Fingerprinting Oils in Water via their Dissolved VOC Pattern using Mid-Infrared Sensors. *Anal. Chem.* **86**, 9512–9517 (2014).
123. Yang, J. & Cheng, M. L. Development of an SPME/ATR-IR Chemical Sensor for Detection of Phenol Type Compounds in Aqueous Solutions. *Analyst* **126**, 881–886 (2001).
124. Acha, V., Meurens, M., Naveau, H. & Agathos, S. N. ATR-FTIR sensor development for continuous on-line monitoring of chlorinated aliphatic hydrocarbons in a fixed-bed bioreactor. *Biotechnol. Bioeng.* **68**, 473–487 (2000).
125. Rauh, F., Schwenk, M., Pejcic, B., Myers, M., Ho, K. B., Stalker, L. & Mizaikoff, B. A mid-infrared sensor for the determination of perfluorocarbon-based compounds in aquatic systems for geosequestration purposes. *Talanta* **130**, 527–535 (2014).
126. Stach, R., Pejcic, B., Crooke, E., Myers, M. & Mizaikoff, B. Mid-Infrared Spectroscopic Method for the Identification and Quantification of Dissolved Oil Components in Marine Environments. *Anal. Chem.* **87**, 12306–12312 (2015).
127. Jakusch, M., Mizaikoff, B., Kellner, R. & Katzir, a. Optimized sensitive coatings for MIR fiber optic sensors. *Proc. SPIE* **3105**, 283–288 (1997).
128. Pejcic, B., Boyd, L., Myers, M., Ross, A., Raichlin, Y., Katzir, A., Lu, R. & Mizaikoff, B. Direct quantification of aromatic hydrocarbons in geochemical fluids with a mid-infrared attenuated total reflection sensor. *Org. Geochem.* **55**, 63–71 (2013).
129. Murphy, B. & Mcloughlin, P. Determination of Chlorinated Hydrocarbon Species in Aqueous Solution Using Teflon Coated ATR Waveguide/FTIR Spectroscopy. *Int. J. Environ. Anal. Chem.* **83**, 653–662 (2003).
130. Dobbs, G. T., Balu, B., Young, C., Kranz, C., Hess, D. W. & Mizaikoff, B. Mid-Infrared Chemical Sensors Utilizing Plasma-Deposited Fluorocarbon Membranes. **79**, 9566–9571 (2007).
131. McLoughlin, P., Flavin, K., Kirwan, P., Murphy, B. & Murphy, K. Modelling of Fickian diffusion to enhance polymer-modified sensor performance. *Sensors Actuators, B Chem.* **107**, 170–177 (2005).
132. Han, L., Niemczyk, T. M., Lu, Y. & Lopez, G. P. Chemical Sensors Based on Surface-Modified Sol-Gel-Coated Infrared Waveguides. *Appl. Spectrosc.* **52**, 119–122 (1998).
133. Haibach, F. G., Sanchez, A., Floro, J. A. & Niemczyk, T. M. Extended spectral range surface-modified sol-gel coated infrared waveguide sensors. *Appl. Spectrosc.* **56**, 398–400 (2002).
134. Göbel, R., Krska, R., Kellner, R. & Katzir, A. Development of protective polymer coatings for silver halide fibers and their application as threshold level sensors for chlorinated hydrocarbons in sea water. *Fresenius. J. Anal. Chem.* **348**, 780–781 (1994).
135. Howley, R., MacCraith, B. D., O'Dwyer, K., Kirwan, P. & McLoughlin, P. A study of the factors affecting the diffusion of chlorinated hydrocarbons into polyisobutylene and polyethylene-co-propylene for evanescent wave sensing. *Vib. Spectrosc.* **31**, 271–278 (2003).
136. Jakusch, M., Mizaikoff, B., Kellner, R. & Katzir, A. Towards a remote IR fiber-optic sensor system for the determination of chlorinated hydrocarbons in water. *Sensors Actuators B Chem.* **38**, 83–87 (1997).
137. Lu, R., Mizaikoff, B., Li, W.-W., Qian, C., Katzir, A., Raichlin, Y., Sheng, G.-P. & Yu, H.-Q. Determination of Chlorinated Hydrocarbons in Water Using Highly Sensitive Mid-Infrared Sensor Technology. *Sci. Rep.* **3**, 1–6 (2013).
138. Lu, R., Sheng, G., Li, W., Yu, H., Raichlin, Y., Katzir, A. & Mizaikoff, B. IR-ATR chemical sensors based on planar silver halide waveguides coated with an ethylene/propylene copolymer for detection of multiple organic contaminants in water. *Angew. Chemie - Int. Ed.* **52**, 2265–2268 (2013).
139. Mizaikoff, B., Kraft, M. & Jakusch, M. Water Monitoring Using Infrared Fiber Optic Sensors. *Ieee* **6**, 1401–1404 (1998).
140. Walsh, J. E., MacCraith, B. D., Meaney, M., Vos, J. G., Regan, F., Lancia, A. & Artjushenko, S. Sensing of chlorinated hydrocarbons and pesticides in water using polymer coated mid-infrared optical fibres. *Analyst* **121**, 789–792 (1996).

Die approbierte gedruckte Originalversion dieser Dissertation ist an der TU Wien Bibliothek verfügbar.
The approved original version of this doctoral thesis is available in print at TU Wien Bibliothek.
TU Bibliothek Your knowledge hub WIEN

141. Beyer, T., Hahn, P., Hartwig, S., Konz, W., Scharring, S., Katzir, A., Steiner, H., Jakusch, M., Kraft, M. & Mizaikoff, B. Mini spectrometer with silver halide sensor fiber for in situ detection of chlorinated hydrocarbons. *Sensors Actuators, B Chem.* **90**, 319–323 (2003).
142. McCue, R. P., Walsh, J. E., Walsh, F. & Regan, F. Modular fibre optic sensor for the detection of hydrocarbons in water. *Sensors Actuators, B Chem.* **114**, 438–444 (2006).
143. Janotta, M. A., Katzir, A. & Izaikoff, B. M. Sol-Gel-Coated Mid-Infrared Fiber-Optic Sensors. *Appl. Spectrosc.* **57**, 823–828 (2003).
144. Howley, R., MacCraith, B. D., O'Dwyer, K., Masterson, H., Kirwan, P. & McLoughlin, P. Determination of hydrocarbons using sapphire fibers coated with poly(dimethylsiloxane). *Appl. Spectrosc.* **57**, 400–406 (2003).
145. Krska, R., Taga, K. & Kellner, R. New IR Fiber-Optic Chemical Sensor for In Situ Measurements of Chlorinated Hydrocarbons in Water. *Appl. Spectrosc.* **47**, 1484–1487 (1993).
146. Krska, R., Kellner, R., Schiessl, U., Tacke, M. & Katzir, A. Fiber optic sensor for chlorinated hydrocarbons in water based on infrared fibers and tunable diode lasers. *Appl. Phys. Lett.* **63**, 1868–1870 (1993).
147. Blair, D. S., Burgess, L. W. & Brodsky, A. M. Monitoring Volatile Organic Compounds in Water. *Anal. Chem.* **69**, 2238–2246 (1997).
148. Bormashenko, E., Sheshnev, A., Pogreb, R., Sutovsk, S., Reichlin, Y., Shulzinger, E. & Katzir, A. Study of water diffusion in polyacrylonitrile using IR fiber optic evanescent wave spectroscopy. *Emami, S. H.* **13**, 1039–1045 (2002).
149. Eytan, O., Bormashenko, E., Pogreb, R., Sutovski, S., Sela, B. & Katzir, A. Fiberoptic Evanescent Wave Spectroscopy (FEWS) for Blood Diagnosis : The Use ofPolymer Coated AgC1Br Fibers and Neural Network Analysis. *Proc. SPIE* **3596**, 74–81 (1999).
150. Regan, F., MacCraith, B. D., Walsh, J. E., Dwyer, K. O., Vos, J. G. & Meaney, M. Novel Teflon-coated optical fibres for TCE determination using FTIR spectroscopy. *Vib. Spectrosc.* **14**, 239–246 (1997).
151. Ruddy, V. & McCabe, S. Detection of Propane by IR-ATR in a Teflon-Clad Fluoride Glass Optical Fiber. *Appl. Spectrosc.* **44**, 1461–1463 (1990).
152. Erickson, T. A. & Lear, K. L. An integrated optoelectronic chip for sensing aromatic hydrocarbon contaminants in groundwater. *Sensors Actuators, B Chem.* **204**, 421–428 (2014).
153. Erickson, T. A., Nijjar, R., Kipper, M. J. & Lear, K. L. Characterization of plasma-enhanced teflon AF for sensing benzene, toluene, and xylenes in water with near-IR surface plasmon resonance. *Talanta* **119**, 151–155 (2014).
154. Dullo, F. T., Lindecrantz, S., Jágerská, J., Hansen, J. H., Engqvist, M., Solbø, S. A. & Hellesø, O. G. Sensitive on-chip methane detection with a cryptophane-A cladded Mach-Zehnder interferometer. *Opt. Express* **23**, 31564 (2015).
155. Siarkowski, A. L. Sensing based on Mach-Zehnder interferometer and hydrophobic thin films used on volatile organic compounds detection. *Opt. Eng.* **51**, 054401 (2012).
156. Yang, J., Che, X., Shen, R., Wang, C., Li, X. & Chen, W. High-sensitivity photonic crystal fiber long-period grating methane sensor with cryptophane-A-6Me absorbed on a PAA-CNTs/PAH nanofilm. *Opt. Express* **25**, 20258 (2017).
157. Girschikofsky, M., Rosenberger, M., Belle, S., Brutschy, M., Waldvogel, S. R. & Hellmann, R. Highly sensitive detection of naphthalene in solvent vapor using a functionalized PBG refractive index sensor. *Sensors* **12**, 2018–2025 (2012).
158. Busse, S., DePaoli, M., Wenz, G. & Mittler, S. An integrated optical Mach-Zehnder interferometer functionalized by β-cyclodextrin to monitor binding reactions. *Sensors Actuators, B Chem.* **80**, 116–124 (2001).
159. Gauglitz, G. & Ingenhoff, J. Integrated optical sensors for halogenated and non-halogenated hydrocarbons. *Sensors Actuators B. Chem.* **11**, 207–212 (1993).
160. Lai, W. C., Chakravarty, S., Wang, X., Lin, C. & Chen, R. T. Photonic crystal slot waveguide absorption spectrometer for on-chip near-infrared spectroscopy of xylene in water. *Appl. Phys. Lett.* **98**, 023304 (2011).
161. Celo, D., Post, E., Summers, M., Smy, T., Brett, M. J. & Albert, J. Interferometric sensing platform with dielectric nanostructured thin films. *Opt. Express* **17**, 6655 (2009).
162. Zhang, J., Tang, X., Dong, J., Wei, T. & Xiao, H. Zeolite thin film-coated long period fiber grating sensor for measuring trace organic vapors. *Sensors Actuators, B Chem.* **135**, 420–425 (2009).
163. Miller, L. W., Tejedor, M. I., Nelson, B. P. & Anderson, M. A. Mesoporous Metal Oxide Semiconductor-Clad Waveguides. *J. Phys. Chem. B* **103**, 8490–8492 (1999).
164. Wan, X., Lu, D. F., Gao, R., Cheng, J. & Qi, Z. M. Metal-Clad Waveguide Resonance Sensor Using a

Die approbierte gedruckte Originalversion dieser Dissertation ist an der TU Wien Bibliothek verfügbar.
The approved original version of this doctoral thesis is available in print at TU Wien Bibliothek.
TU Bibliothek Your knowledge hub WIEN

Mesoporous TiO2 Thin Film as the Chemical Sensitive Core Layer. *J. Phys. Chem. C* **121**, 19173–19181 (2017).

165. Qi, Z. M., Honma, I. & Zhou, H. Fabrication of ordered mesoporous thin films for optical waveguiding and interferometric chemical sensing. *J. Phys. Chem. B* **110**, 10590–10594 (2006).
166. Korposh, S., James, S. W., Lee, S.-W., Topliss, S., Cheung, S. C., Batty, W. J. & Tatam, R. P. Fiber optic long period grating sensors with a nanoassembled mesoporous film of SiO_2 nanoparticles. *Opt. Express* **18**, 13227 (2010).
167. Zhou, G., Niu, L., Jiang, Y., Liu, H., Xie, X., Yan, H., Yan, L., Liu, J., Chen, J., Miao, X., Zhou, H., Jiang, X. & Lv, H. Sensing of airborne molecular contaminants based on microfiber coupler with mesoporous silica coating. *Sensors Actuators, A Phys.* **287**, 1–7 (2019).
168. Walcarius, A. & Mercier, L. Mesoporous Organosilica Adsorbents: Nanoengineered Materials for Removal of Organic and Inorganic Pollutants. *J. Mater. Chem.* **20**, 4478–4511 (2010).
169. Wu, Z. & Zhao, D. Ordered mesoporous materials as adsorbents. *Chem. Commun.* **47**, 3332 (2011).
170. Wagner, T., Haffer, S., Weinberger, C., Klaus, D. & Tiemann, M. Mesoporous materials as gas sensors. *Chemical Society Reviews* **42**, 4036–4053 (2013).
171. Melde, B. J., Johnson, B. J. & Charles, P. T. Mesoporous silicat materials in sensing. *Sensors* **8**, 5202–5228 (2008).
172. Gibson, L. T. Mesosilica materials and organic pollutant adsorption: Part A removal from air. *Chemical Society Reviews* **43**, 5163–5172 (2014).
173. Wales, D. J., Grand, J., Ting, V. P., Burke, R. D., Edler, K. J., Bowen, C. R., Mintova, S. & Burrows, A. D. Gas sensing using porous materials for automotive applications. *Chem. Soc. Rev.* **44**, 4290–4321 (2015).
174. Gibson, L. T. Mesosilica materials and organic pollutant adsorption: Part A removal from air. *Chemical Society Reviews* **43**, 5163–5172 (2014).
175. Wang, J., Ma, Q., Wang, Y., Li, Z. Z., Li, Z. Z. & Yuan, Q. New insights into the structure-performance relationships of mesoporous materials in analytical science. *Chemical Society Reviews* **47**, 8766–8803 (2018).
176. Kosuge, K., Kubo, S., Kikukawa, N. & Takemori, M. Effect of pore structure in mesoporous silicas on VOC dynamic adsorption/desorption performance. *Langmuir* **23**, 3095–3102 (2007).
177. Soler-Illia, G. J. D. A. A., Sanchez, C., Lebeau, B. & Patarin, J. Chemical strategies to design textured materials: From microporous and mesoporous oxides to nanonetworks and hierarchical structures. *Chem. Rev.* **102**, 4093–4138 (2002).
178. Innocenzi, P. & Malfatti, L. Mesoporous thin films: properties and applications. *Chem. Soc. Rev.* **42**, 4198–4216 (2013).
179. Sieger, M. & Mizaikoff, B. Toward On-Chip Mid-Infrared Sensors. *Anal. Chem.* **88**, 5562–5573 (2016).
180. Karabudak, E., Kas, R., Ogieglo, W., Rafieian, D., Schlautmann, S., Lammertink, R. G. H. H., Gardeniers, H. J. G. E. G. E. & Mul, G. Disposable attenuated total reflection-infrared crystals from silicon wafer: A versatile approach to surface infrared spectroscopy. *Anal. Chem.* **85**, 33–38 (2013).
181. Karabudak, E., Yüce, E., Schlautmann, S., Hansen, O., Mul, G. & Gardeniers, H. (J. G. E. . On the pathway of photoexcited electrons: Probing photon-to-electron and photon-to-phonon conversions in silicon by ATR-IR. *Phys. Chem. Chem. Phys.* **14**, 10882–10885 (2012).
182. Wagner, C., Genner, A., Ramer, G. & Lendl, B. Advanced Total Lab Automation System (ATLAS). in *Modeling, Programming and Simulations Using LabVIEW Software* 1–20 (2010).
183. Besson, S., Gacoin, T., Ricolleau, C., Jacquiod, C. & Boilot, J.-P. Phase Diagram for Mesoporous CTAB–Silica Films Prepared Under Dynamic Conditions. *J. Mater. Chem.* **13**, 404–409 (2002).
184. Matheron, M., Bourgeois, A., Brunet-Bruneau, A., Albouy, P.-A., Biteau, J., Gacoin, T. & Boilot, J.-P. Highly Ordered CTAB-Templated Organosilicate Films. *J. Mater. Chem.* **15**, 4741–4745 (2005).
185. Matheron, M., Gacoin, T. & Boilot, J.-P. Stabilization of Well-Organized Transient Micellar Phases in CTAB-Templated Silica and Organosilica Thin Films. *Soft Matter* **3**, 223–229 (2007).
186. Borodina, E., Karpov, S. I., Selemenev, V. F., Schwieger, W., Maracke, S., Fröba, M. & Rößner, F. Surface and texture properties of mesoporous silica materials modified by silicon-organic compounds containing quaternary amino groups for their application in base-catalyzed reactions. *Microporous Mesoporous Mater.* **203**, 224–231 (2015).
187. Krishna, N. V., Anuradha, S., Ganesh, R., Kumar, V. V. & Selvam, P. Sulfonic Acid Functionalized Ordered Mesoporous Silica and their Application as Highly Efficient and Selective Heterogeneous Catalysts in the Formation of 1,2-Monoacetone-D-glucose. *ChemCatChem* **10**, 5610–5618 (2018).

Die approbierte gedruckte Originalversion dieser Dissertation ist an der TU Wien Bibliothek verfügbar.
The approved original version of this doctoral thesis is available in print at TU Wien Bibliothek.
TU Bibliothek Your knowledge hub WIEN

188. Bottein, T., Dalstein, O., Putero, M., Cattoni, A., Faustini, M., Abbarchi, M. & Grosso, D. Environment-controlled sol-gel soft-NIL processing for optimized titania, alumina, silica and yttria-zirconia imprinting at sub-micron dimensions. *Nanoscale* **10**, 1420–1431 (2018).
189. Besson, S., Gacoin, T., Jacquiod, C., Ricolleau, C., Babonneau, D. & Boilot, J.-P. Structural study of 3D-hexagonal mesoporous spin-coated sol–gel films. *J. Mater. Chem.* **10**, 1331–1336 (2000).
190. Besson, S., Ricolleau, C., Gacoin, T., Jacquiod, C. & Boilot, J.-P. A New 3D Organization of Mesopores in Oriented CTAB Silica Films. *J. Phys. Chem. B* **104**, 12095–12097 (2000).
191. Matheron, M., Bourgeois, A., Gacoin, T., Brunet-Bruneau, A., Albouy, P. A., Boilot, J. P., Biteau, J. & Lacan, P. Mesoporous 3D-hexagonal organosilicate films: Post-synthesis grafting vs. direct synthesis. in *Thin Solid Films* **495**, 175–179 (2006).
192. Alberius, P. C. A., Frindell, K. L., Hayward, R. C., Kramer, E. J., Stucky, G. D. & Chmelka, B. F. General predictive syntheses of cubic, hexagonal, and lamellar silica and titania mesostructured thin films. *Chem. Mater.* **14**, 3284–3294 (2002).
193. Meynen, V., Cool, P. & Vansant, E. F. Verified syntheses of mesoporous materials. *Microporous Mesoporous Mater.* **125**, 170–223 (2009).
194. Spin Coater – Stefik Group. (2019). Available at: http://www.stefikgroup.com/spin-coater/. (Accessed: 19th September 2019)
195. Dourdain, S., Mehdi, A., Bardeau, J. F. & Gibaud, A. Determination of porosity of mesoporous silica thin films by quantitative X-ray reflectivity analysis and GISAXS. in *Thin Solid Films* **495**, 205–209 (Elsevier, 2006).
196. Dunphy, D. R., Singer, S., Cook, A. W., Smarsly, B., Doshi, D. A. & Blinker, C. J. Aqueous Stability of Mesoporous Silica Films Doped or Grafted with Aluminum Oxide. *Langmuir* **19**, 10403–10408 (2003).
197. Galarneau, A., Nader, M., Guenneau, F., Di Renzo, F. & Gedeon, A. Understanding the stability in water of mesoporous SBA-15 and M CM-41. *J. Phys. Chem. C* **111**, 8268–8277 (2007).
198. Zhao, H., Raza, A., Baumgartner, B., Clemmen, S., Lendl, B., Skirtach, A. & Baets, R. Waveguide-Enhanced Raman Spectroscopy Using a Mesoporous Silica Sorbent Layer for Volatile Organic Compound (VOC) Sensing. in *Conference on Lasers and Electro-Optics* STh1F.7 (OSA, 2019). doi:10.1364/cleo_si.2019.sth1f.7
199. Bruggeman, D. A. G. Berechnung verschiedener physikalischer Konstanten von heterogenen Substanzen. I. Dielektrizitätskonstanten und Leitfähigkeiten der Mischkörper aus isotropen Substanzen. *Ann. Phys.* **416**, 636–664 (1935).
200. Gao, L. & Gu, J. Z. Effective dielectric constant of a two-component material with shape distribution. *J. Phys. D. Appl. Phys.* **35**, 267–271 (2002).
201. Wang, M. & Pan, N. Predictions of effective physical properties of complex multiphase materials. *Mater. Sci. Eng. R Reports* **63**, 1–30 (2008).
202. Ho, Y. S. Selection of Optimum Sorption Isotherm. *Carbon N. Y.* **42**, 2115–2116 (2004).
203. ASTM D7678-17, Standard Test Method for Total Oil and Grease (TOG) and Total Petroleum Hydrocarbons (TPH) in Water and Wastewater with Solvent Extraction using Mid-IR Laser Spectroscopy. *ASTM Int.* (2013). doi:10.1520/D7678
204. Taniguchi, M. & Lindsey, J. S. Database of Absorption and Fluorescence Spectra of >300 Common Compounds for use in PhotochemCAD. *Photochem. Photobiol.* **94**, 290–327 (2018).
205. Laue, W., Thiemann, M., Scheibler, E. & Wiegand, K. W. Nitrates and Nitrites. in *Ullmann's Encyclopedia of Industrial Chemistry* (Wiley-VCH Verlag GmbH & Co. KGaA, 2000). doi:10.1002/14356007.a17_265
206. Council Directive. Protection of water against pollution caused by nitrates from agricultural sources. *Off. J. Eur. Communities* **L 269**, 1–15 (2000).
207. Patton, C. J. & Kryskalla, J. R. Analytical Properties of Some Commercially Available Nitrate Reductase Enzymes Evaluated as Replacements for Cadmium in Automated , Semiautomated , and Manual Colorimetric Methods for Determination of Nitrate Plus Nitrite in Water Model of Nitrate Reducta. *Sci. Investig. Rep. 2013–5033* (2013).
208. Zhu, M., Lerum, M. Z. & Chen, W. How to prepare reproducible, homogeneous, and hydrolytically stable aminosilane-derived layers on silica. *Langmuir* **28**, 416–423 (2012).
209. Wong, E. M., Markowitz, M. A., Qadri, S. B., Golledge, S., Castner, D. G. & Gaber, B. P. Hybrid organic-inorganic quaternary ammonium organosilane functionalized mesoporous thin films. *J. Phys. Chem. B* **106**, 6652–6658 (2002).
210. Dioum, A. & Hamoudi, S. Mono- and quaternary-ammonium functionalized mesoporous silica materials for nitrate adsorptive removal from water and wastewaters. *J. Porous Mater.* **21**, 685–690 (2014).

Die approbierte gedruckte Originalversion dieser Dissertation ist an der TU Wien Bibliothek verfügbar.
The approved original version of this doctoral thesis is available in print at TU Wien Bibliothek.
TU Bibliothek WIEN Your knowledge hub

211. Saad, R., Hamoudi, S. & Belkacemi, K. Adsorption of phosphate and nitrate anions on ammonium-functionnalized mesoporous silicas. *J. Porous Mater.* **15**, 315–323 (2008).
212. Jia, C., Batterman, S. & Godwin, C. VOCs in industrial, urban and suburban neighborhoods, Part 1: Indoor and outdoor concentrations, variation, and risk drivers. *Atmos. Environ.* **42**, 2083–2100 (2008).
213. Guo, H., Lee, S. C., Chan, L. Y. & Li, W. M. Risk assessment of exposure to volatile organic compounds in different indoor environments. *Environ. Res.* **94**, 57–66 (2004).
214. Destaillats, H., Maddalena, R. L., Singer, B. C., Hodgson, A. T. & McKone, T. E. Indoor pollutants emitted by office equipment: A review of reported data and information needs. *Atmospheric Environment* **42**, 1371–1388 (2008).
215. Lee, C. W., Dai, Y. T., Chien, C. H. & Hsu, D. J. Characteristics and health impacts of volatile organic compounds in photocopy centers. *Environ. Res.* **100**, 139–149 (2006).
216. Spinelle, L., Gerboles, M., Kok, G., Persijn, S. & Sauerwald, T. Review of portable and low-cost sensors for the ambient air monitoring of benzene and other volatile organic compounds. *Sensors* **17**, 1–30 (2017).
217. Hasegawa, T. *Quantitative infrared spectroscopy for understanding of a condensed matter. Springer Japan* (Springer Japan, 2017). doi:10.1007/978-4-431-56493-5
218. Sydoryk, I., Lim, A., Jäger, W., Tulip, J. & Parsons, M. T. Detection of benzene and toluene gases using a mid-infrared continuous-wave external cavity quantum cascade laser at atmospheric pressure. *Appl. Opt.* **49**, 945 (2010).
219. Jelassi, J., Grosz, T., Bako, I., Bellissent-Funel, M. C., Dore, J. C., Castricum, H. L. & Sridi-Dorbez, R. Structural studies of water in hydrophilic and hydrophobic mesoporous silicas: An x-ray and neutron diffraction study at 297 K. *J. Chem. Phys.* **134**, 064509 (2011).
220. Liu, Y. & Ojamäe, L. Raman and IR Spectra of Ice Ih and Ice XI with an Assessment of DFT Methods. *J. Phys. Chem. B* **120**, 11043–11051 (2016).
221. Verdaguer, A., Sacha, G. M., Bluhm, H. & Salmeron, M. Molecular Structure of Water at Interfaces: Wetting at the Nanometer Scale. *Chem. Rev.* **106**, 1478–1510 (2006).
222. Shimizu, T. K., Maier, S., Verdaguer, A., Velasco-Velez, J. J. & Salmeron, M. Water at surfaces and interfaces: From molecules to ice and bulk liquid. *Progress in Surface Science* **93**, 87–107 (2018).
223. Thiel, P. A. & Madey, T. E. The interaction of water with solid surfaces: Fundamental aspects. *Surface Science Reports* **7**, 211–385 (1987).
224. Ewing, G. E. Ambient Thin Film Water on Insulator Surfaces. *Chem. Rev.* **106**, 1511–1526 (2006).
225. Verdaguer, A., Weis, C., Oncins, G., Ketteler, G., Bluhm, H., Salmero, M. & Salmeron, M. Growth and Structure of Water on SiO_2 Films on Si Investigated by Kelvin Probe Microscopy and in Situ X-ray Spectroscopies. *Langmuir* **23**, 9699–9703 (2007).
226. Buck, U. & Huisken, F. Infrared spectroscopy of size-selected water and methanol clusters. *Chem. Rev.* **100**, 3863–3890 (2000).
227. Chen, L., He, X., Liu, H., Qian, L. & Kim, S. H. Water Adsorption on Hydrophilic and Hydrophobic Surfaces of Silicon. *J. Phys. Chem. C* **122**, 11385–11391 (2018).
228. Soper, A. K. & Ricci, M. A. Structures of high-density and low-density water. *Phys. Rev. Lett.* **84**, 2881–2884 (2000).
229. Asay, D. B. & Kim, S. H. Evolution of the adsorbed water layer structure on silicon oxide at room temperature. *J. Phys. Chem. B* **109**, 16760–16763 (2005).
230. Asay, D. B., Barnette, A. L. & Kim, S. H. Effects of surface chemistry on structure and thermodynamics of water layers at solid-vapor interfaces. *J. Phys. Chem. C* **113**, 2128–2133 (2009).
231. Barnette, A. L. & Kim, S. H. Attenuated total reflectance infrared spectroscopy study of hysteresis of water and n-alcohol coadsorption on silicon oxide. *Langmuir* **28**, 15529–15536 (2012).
232. Horikawa, T., Do, D. D. & Nicholson, D. Capillary condensation of adsorbates in porous materials. *Advances in Colloid and Interface Science* **169**, 40–58 (2011).
233. Kocherbitov, V. & Alfredsson, V. Hydration of MCM-41 studied by sorption calorimetry. *J. Phys. Chem. C* **111**, 12906–12913 (2007).
234. Groen, J. C., Peffer, L. A. A. & Pérez-Ramírez, J. Pore size determination in modified micro- and mesoporous materials. Pitfalls and limitations in gas adsorption data analysis. *Microporous Mesoporous Mater.* **60**, 1–17 (2003).
235. Davis, K. M. & Tomozawa, M. An infrared spectroscopic study of water-related species in silica glasses. *J. Non. Cryst. Solids* **201**, 177–198 (1996).
236. De Aragão, B. J. G. & Messaddeq, Y. Peak separation by derivative spectroscopy applied to FTIR analysis of hydrolized silica. *J. Braz. Chem. Soc.* **19**, 1582–1594 (2008).

Die approbierte gedruckte Originalversion dieser Dissertation ist an der TU Wien Bibliothek verfügbar.
The approved original version of this doctoral thesis is available in print at TU Wien Bibliothek.
TU Bibliothek WIEN Your knowledge hub

237. Brubach, J. B., Mermet, A., Filabozzi, A., Gerschel, A. & Roy, P. Signatures of the hydrogen bonding in the infrared bands of water. *J. Chem. Phys.* **122**, (2005).
238. Davis, K. M., Agarwal, A., Tomozawa, M. & Hirao, K. Quantitative infrared spectroscopic measurement of hydroxyl concentrations in silica glass. *J. Non. Cryst. Solids* **203**, 27–36 (1996).
239. Gallas, J. P., Goupil, J. M., Vimont, A., Lavalley, J. C., Gil, B., Gilson, J. P. & Miserque, O. Quantification of water and silanol species on various silicas by coupling IR spectroscopy and in-situ thermogravimetry. *Langmuir* **25**, 5825–5834 (2009).
240. Carteret, C. Mid- and near-infrared study of hydroxyl Groups at a silica surface: H-Bond effect. *J. Phys. Chem. C* **113**, 13300–13308 (2009).
241. Israelachvili, J. N. *Intermolecular and surface forces.* (Academic Press, 2011).
242. Weast, R. C. *CRC Handbook of chemistry and physics: A ready-reference book of chemical and physical data. Boca Raton, Florida, USA* (1986).
243. Coasne, B., Galarneau, A., Pellenq, R. J. M. & Di Renzo, F. Adsorption, intrusion and freezing in porous silica: The view from the nanoscale. *Chemical Society Reviews* **42**, 4141–4171 (2013).
244. Digilov, R. Kelvin equation for meniscuses of nanosize dimensions. *Langmuir* **16**, 1424–1427 (2000).
245. Ravikovitch, P. I. & Neimark, A. V. Experimental confirmation of different mechanisms of evaporation from ink-bottle type pores: Equilibrium, pore blocking, and cavitation. *Langmuir* **18**, 9830–9837 (2002).
246. Pettersen, M. S., Balibar, S. & Maris, H. J. Experimental investigation of cavitation in superfluid He_4. *Phys. Rev. B* **49**, 12062–12070 (1994).
247. Grosman, A. & Ortega, C. Cavitation in metastable fluids confined to linear mesopores. *Langmuir* **27**, 2364–2374 (2011).
248. Caupin, F. & Herbert, E. Cavitation in water: a review. *Comptes Rendus Physique* **7**, 1000–1017 (2006).
249. Kalikmanov, V. I. Semiphenomenological theory of the Tolman length. *Phys. Rev. E* **55**, 3068–3071 (1997).
250. Bowen, T. C., Li, S., Noble, R. D. & Falconer, J. L. Driving force for pervaporation through zeolite membranes. *J. Memb. Sci.* **225**, 165–176 (2003).
251. Mehio, N., Dai, S. & Jiang, D. E. Quantum mechanical basis for kinetic diameters of small gaseous molecules. *J. Phys. Chem. A* **118**, 1150–1154 (2014).
252. Lei, Y. A., Bykov, T., Yoo, S. & Zeng, X. C. The Tolman length: Is it positive or negative? *J. Am. Chem. Soc.* **127**, 15346–15347 (2005).
253. Protasova, L. N., Rebrov, E. V., Ismagilov, Z. R. & Schouten, J. C. Determination of the Tolman length in the improved Derjaguin-Broekhoff-de Boer theory for capillary condensation of ethanol in mesoporous thin films by ellipsometric porosimetry. *Microporous Mesoporous Mater.* **123**, 243–252 (2009).
254. Dewar, M. J. S., Zoebisch, E. G., Healy, E. F. & Stewart, J. J. P. AM1: A New General Purpose Quantum Mechanical Molecular Model1. *J. Am. Chem. Soc.* **107**, 3902–3909 (1985).
255. Lewis, N. S. & Nocera, D. G. Powering the planet: Chemical challenges in solar energy utilization. *Proceedings of the National Academy of Sciences of the United States of America* **103**, 15729–15735 (2006).
256. Møller, K. T., Jensen, T. R., Akiba, E. & Li, H. W. Hydrogen - A sustainable energy carrier. *Prog. Nat. Sci. Mater. Int.* **27**, 34–40 (2017).
257. Ni, M., Leung, M. K. H., Sumathy, K. & Leung, D. Y. C. Potential of renewable hydrogen production for energy supply in Hong Kong. *Int. J. Hydrogen Energy* **31**, 1401–1412 (2006).
258. Holladay, J. D., Hu, J., King, D. L. & Wang, Y. An overview of hydrogen production technologies. *Catalysis Today* **139**, 244–260 (2009).
259. Fujishima, A., Zhang, X. & Tryk, D. A. Heterogeneous photocatalysis: From water photolysis to applications in environmental cleanup. *Int. J. Hydrogen Energy* **32**, 2664–2672 (2007).
260. Schneider, J., Matsuoka, M., Takeuchi, M., Zhang, J., Horiuchi, Y., Anpo, M. & Bahnemann, D. W. Understanding TiO_2 Photocatalysis: Mechanisms and Materials. *Chem. Rev.* **114**, 9919–9986 (2014).
261. Thompson, T. L. & Yates, J. T. TiO_2-based Photocatalysis: Surface Defects, Oxygen and Charge Transfer. *Top. Catal.* **35**, 197–210 (2005).
262. Fujishima, A., Zhang, X. & Tryk, D. A. TiO_2 photocatalysis and related surface phenomena. *Surf. Sci. Rep.* **63**, 515–582 (2008).
263. Nakata, K. & Fujishima, A. TiO_2 photocatalysis: Design and applications. *Journal of Photochemistry and Photobiology C: Photochemistry Reviews* **13**, 169–189 (2012).
264. Christoforidis, K. C. & Fornasiero, P. Photocatalytic Hydrogen Production: A Rift into the Future Energy Supply. *ChemCatChem* **9**, 1523–1544 (2017).
265. Chiarello, G. L., Ferri, D. & Selli, E. In situ attenuated total reflection infrared spectroscopy study of the

Die approbierte gedruckte Originalversion dieser Dissertation ist an der TU Wien Bibliothek verfügbar.
The approved original version of this doctoral thesis is available in print at TU Wien Bibliothek.
TU Bibliothek Your knowledge hub WIEN

photocatalytic steam reforming of methanol on Pt/TiO_2. *Appl. Surf. Sci.* **450**, 146–154 (2018).

266. Highfield, J. G., Chen, M. H., Nguyen, P. T. & Chen, Z. Mechanistic investigations of photo-driven processes over TiO_2 by in-situ DRIFTS-MS: Part 1. Platinization and methanol reforming. *Energy Environ. Sci.* **2**, 991 (2009).
267. Chiarello, G. L., Aguirre, M. H. & Selli, E. Hydrogen production by photocatalytic steam reforming of methanol on noble metal-modified TiO_2. *J. Catal.* **273**, 182–190 (2010).
268. El-Roz, M., Bazin, P., Daturi, M. & Thibault-Starzyk, F. On the mechanism of methanol photooxidation to methylformate and carbon dioxide on TiO_2: An operando-FTIR study. *Phys. Chem. Chem. Phys.* **17**, 11277–11283 (2015).
269. Schneider, J. & Bahnemann, D. W. Undesired role of sacrificial reagents in photocatalysis. *Journal of Physical Chemistry Letters* **4**, 3479–3483 (2013).
270. Kawai, T. & Sakata, T. Photocatalytic hydrogen production from liquid methanol and water. *J. Chem. Soc. Chem. Commun.* 694 (1980). doi:10.1039/c39800000694
271. Haselmann, G. M. & Eder, D. Early-Stage Deactivation of Platinum-Loaded TiO_2 Using in Situ Photodeposition during Photocatalytic Hydrogen Evolution. *ACS Catal.* **7**, 4668–4675 (2017).
272. Pichat, P. Representative examples of infrared spectroscopy uses in semiconductor photocatalysis. *Catal. Today* **224**, 251–257 (2014).
273. Bürgi, T. & Baiker, A. Attenuated Total Reflection Infrared Spectroscopy of Solid Catalysts Functioning in the Presence of Liquid-Phase Reactants. *Adv. Catal.* **50**, 227–283 (2006).
274. Hauchecorne, B. & Lenaerts, S. Unravelling the mysteries of gas phase photocatalytic reaction pathways by studying the catalyst surface: A literature review of different Fourier transform infrared spectroscopic reaction cells used in the field. *Journal of Photochemistry and Photobiology C: Photochemistry Reviews* **14**, 72–85 (2013).
275. Nomikos, G. N., Panagiotopoulou, P., Kondarides, D. I. & Verykios, X. E. Kinetic and mechanistic study of the photocatalytic reforming of methanol over Pt/TiO_2 catalyst. *Appl. Catal. B Environ.* **146**, 249–257 (2014).
276. Gazsi, A., Schubert, G., Bánsági, T. & Solymosi, F. Photocatalytic decompositions of methanol and ethanol on Au supported by pure or N-doped TiO_2. *J. Photochem. Photobiol. A Chem.* **271**, 45–55 (2013).
277. Chen, T., Feng, Z., Wu, G., Shi, J., Ma, G., Ying, P. & Li, C. Mechanistic studies of photocatalytic reaction of methanol for hydrogen production on Pt/TiO_2 by in situ fourier transform IR and time-resolved IR spectroscopy. *J. Phys. Chem. C* **111**, 8005–8014 (2007).
278. Halasi, G., Schubert, G. & Solymosi, F. Comparative study on the photocatalytic decomposition of methanol on TiO_2 modified by N and promoted by metals. *J. Catal.* **294**, 199–206 (2012).
279. Liao, L. F., Wu, W. C., Chen, C. Y. & Lin, J. L. Photooxidation of formic acid vs formate and ethanol vs ethoxy on TiO_2 and effect of adsorbed water on the rates of formate and formic acid photooxidation. *J. Phys. Chem. B* **105**, 7678–7685 (2001).
280. Kim, G. J., Lee, S. M., Chang Hong, S. & Kim, S. S. Active oxygen species adsorbed on the catalyst surface and its effect on formaldehyde oxidation over Pt/TiO_2 catalysts at room temperature; Role of the Pt valence state on this reaction? *RSC Adv.* **8**, 3626–3636 (2018).
281. Mojet, B. L., Ebbesen, S. D. & Lefferts, L. Light at the interface: The potential of attenuated total reflection infrared spectroscopy for understanding heterogeneous catalysis in water. *Chemical Society Reviews* **39**, 4643–4655 (2010).
282. Shirley, D. A. High-resolution x-ray photoemission spectrum of the valence bands of gold. *Phys. Rev. B* **5**, 4709–4714 (1972).
283. Briggs, D., Grant, J. T. & Oelhafen, P. *Practical surface analysis by auger and X-ray photoelectron spectroscopy. Journal of Electron Spectroscopy and Related Phenomena* **34**, (IM Publications, 1984).
284. Scofield, J. H. Hartree-Slater subshell photoionization cross-sections at 1254 and 1487 eV. *J. Electron Spectros. Relat. Phenomena* **8**, 129–137 (1976).
285. Jaumot, J., Gargallo, R., De Juan, A. & Tauler, R. A graphical user-friendly interface for MCR-ALS: A new tool for multivariate curve resolution in MATLAB. *Chemom. Intell. Lab. Syst.* **76**, 101–110 (2005).
286. Ohtani, B., Iwai, K., Nishimoto, S. I. & Sato, S. Role of platinum deposits on titanium(IV) oxide particles: Structural and kinetic analyses of photocatalytic reaction in aqueous alcohol and amino acid solutions. *J. Phys. Chem. B* **101**, 3349–3359 (1997).
287. Janin, E., Björkqvist, M., Grehk, T. M., Göthelid, M., Pradier, C. M., Karlsson, U. O. & Rosengren, A. Hydrogen adsorption on the Pt(111) ($\sqrt{3} \times \sqrt{3}$) R30°-Sn surface alloy studied by high resolution core level photoelectron spectroscopy. *Appl. Surf. Sci.* **99**, 371–378 (1996).

Die approbierte gedruckte Originalversion dieser Dissertation ist an der TU Wien Bibliothek verfügbar.
The approved original version of this doctoral thesis is available in print at TU Wien Bibliothek.
TU Bibliothek Your knowledge hub WIEN

288. Koudelka, M., Monnier, A., Sanchez, J. & Augustynski, J. Correlation between the surface composition of Pt/TiO_2 catalysts and their adsorption behaviour in aqueous solutions. *J. Mol. Catal.* **25**, 295–305 (1984).
289. Szczepankiewicz, S. H., Colussi, A. J. & Hoffmann, M. R. Infrared Spectra of Photoinduced Species on Hydroxylated Titania Surfaces. *J. Phys. Chem. B* **104**, 9842–9850 (2002).
290. Warren, D. S. & McQuillan, A. J. Influence of adsorbed water on phonon and UV-induced IR absorptions of TiO_2 photocatalytic particle films. *J. Phys. Chem. B* **108**, 19373–19379 (2004).
291. Litke, A., Hensen, E. J. M. & Hofmann, J. P. Role of Dissociatively Adsorbed Water on the Formation of Shallow Trapped Electrons in TiO_2 Photocatalysts. *J. Phys. Chem. C* **121**, 10153–10162 (2017).
292. Litke, A., Su, Y., Tranca, I., Weber, T., Hensen, E. J. M. & Hofmann, J. P. Role of Adsorbed Water on Charge Carrier Dynamics in Photoexcited TiO_2. *J. Phys. Chem. C* **121**, 7514–7524 (2017).
293. Savory, D. M. & McQuillan, A. J. Influence of formate adsorption and protons on shallow trap infrared absorption (STIRA) of anatase TiO_2 during photocatalysis. *J. Phys. Chem. C* **117**, 23645–23656 (2013).
294. Schaden, S., Haberkorn, M., Frank, J., Baena, J. R. & Lendl, B. Direct determination of carbon dioxide in aqueous solution using mid-infrared quantum cascade lasers. *Appl. Spectrosc.* **58**, 667–670 (2004).
295. Chen, X., Su, X., Duan, H., Liang, B., Huang, Y. & Zhang, T. Catalytic performance of the Pt/TiO_2 catalysts in reverse water gas shift reaction: Controlled product selectivity and a mechanism study. *Catal. Today* **281**, 312–318 (2017).
296. Ivanova, E., Mihaylov, M., Thibault-Starzyk, F., Daturi, M. & Hadjiivanov, K. FTIR spectroscopy study of CO and NO adsorption and co-adsorption on Pt/TiO_2. *J. Mol. Catal. A Chem.* **274**, 179–184 (2007).
297. Primet, M., Basset, J. M., Mathieu, M. V. & Prettre, M. Infrared Study of CO Adsorbed on Pt/Al_2O_3. A method for determining metal-adsorbate interactions. *J. Catal.* **29**, 213–223 (1973).
298. Rotzinger, F. P., Kesselman-Truttmann, J. M., Hug, S. J., Shklover, V. & Grätzel, M. Structure and Vibrational Spectrum of Formate and Acetate Adsorbed from Aqueous Solution onto the TiO_2 Rutile (110) Surface. *J. Phys. Chem. B* **108**, 5004–5017 (2004).
299. Popova, G. Y., Andrushkevich, T. V., Chesalov, Y. A. & Stoyanov, E. S. In situ FTIR Study of the Adsorption of Formaldehyde, Formic Acid, and Methyl Formiate at the Surface of TiO_2 (Anatase). *Kinet. Catal.* **41**, 885–891 (2000).
300. Chuang, C.-C., Wu, W.-C., Huang, M.-C., Huang, I.-C. & Lin, J.-L. FTIR Study of Adsorption and Reactions of Methyl Formate on Powdered TiO_2. *J. Catal.* **185**, 423–434 (1999).
301. Lentz, C., Jand, S. P., Melke, J., Roth, C. & Kaghazchi, P. DRIFTS study of CO adsorption on Pt nanoparticles supported by DFT calculations. *J. Mol. Catal. A Chem.* **426**, 1–9 (2017).
302. Garnier, A., Sall, S., Garin, F., Chetcuti, M. J. & Petit, C. Site effects in the adsorption of carbon monoxide on real 1.8 nm Pt nanoparticles: An Infrared investigation in time and temperature. *J. Mol. Catal. A Chem.* **373**, 127–134 (2013).
303. Avanesian, T., Dai, S., Kale, M. J., Graham, G. W., Pan, X. & Christopher, P. Quantitative and Atomic-Scale View of CO-Induced Pt Nanoparticle Surface Reconstruction at Saturation Coverage via DFT Calculations Coupled with in Situ TEM and IR. *J. Am. Chem. Soc.* **139**, 4551–4558 (2017).
304. Kale, M. J. & Christopher, P. Utilizing Quantitative in Situ FTIR Spectroscopy To Identify Well-Coordinated Pt Atoms as the Active Site for CO Oxidation on Al_2O_3-Supported Pt Catalysts. *ACS Catal.* **6**, 5599–5609 (2016).
305. Yoshinobu, J., Tsukahara, N., Yasui, F., Mukai, K. & Yamashita, Y. Lateral Displacement by Transient Mobility in Chemisorption of CO on Pt(997). *Phys. Rev. Lett.* **90**, 4 (2003).
306. Hayden, B. E., Kretzschmar, K., Bradshaw, A. M. & Greenler, R. G. An infrared study of the adsorption of CO on a stepped platinum surface. *Surf. Sci.* **149**, 394–406 (1985).
307. Ebbesen, S. D., Mojet, B. L. & Lefferts, L. In situ ATR-IR study of CO adsorption and oxidation over Pt/Al_2O_3 in gas and aqueous phase: Promotion effects by water and pH. *J. Catal.* **246**, 66–73 (2007).
308. Hendrickx, H. A. C. M., des Bouvrie, C. & Ponec, V. On the electronic competition effect upon CO adsorption on metals. *J. Catal.* **109**, 120–125 (1988).
309. Chang, S. C. & Weaver, M. J. Coverage-dependent dipole coupling for carbon monoxide adsorbed at ordered platinum(111)-aqueous interfaces: Structural and electrochemical implications. *J. Chem. Phys.* **92**, 4582–4594 (1990).
310. Primet, M. Electronic transfer and ligand effects in the infrared spectra of adsorbed carbon monoxide. *J. Catal.* **88**, 273–282 (1984).
311. Han, Y., Liu, C. J. & Ge, Q. Effect of Pt clusters on methanol adsorption and dissociation over perfect and defective anatase TiO_2 (101) surface. *J. Phys. Chem. C* **113**, 20674–20682 (2009).
312. Henderson, M. A., Otero-Tapia, S. & Castro, M. E. The chemistry of methanol on the TiO_2(110) surface:

Die approbierte gedruckte Originalversion dieser Dissertation ist an der TU Wien Bibliothek verfügbar.
The approved original version of this doctoral thesis is available in print at TU Wien Bibliothek.
TU Bibliothek Your knowledge hub WIEN

the influence of vacancies and coadsorbed species. *Faraday Discuss.* **114**, 313–329 (1999).

313. Schaub, R., Thostrup, P., Lopez, N., Lægsgaard, E., Stensgaard, I., Nørskov, J. K. & Besenbacher, F. Oxygen vacancies as active sites for water dissociation on rutile TiO_2(110). *Phys. Rev. Lett.* **87**, 266104-1-266104–4 (2001).
314. Wendt, S., Schaub, R., Matthiesen, J., Vestergaard, E. K., Wahlström, E., Rasmussen, M. D., Thostrup, P., Molina, L. M., Lægsgaard, E., Stensgaard, I., Hammer, B. & Besenbacher, F. Oxygen vacancies on TiO_2(1 1 0) and their interaction with H_2O and O_2: A combined high-resolution STM and DFT study. *Surf. Sci.* **598**, 226–245 (2005).
315. Guo, Q., Xu, C., Yang, W., Ren, Z., Ma, Z., Dai, D., Minton, T. K. & Yang, X. Methyl formate production on TiO_2(110), initiated by methanol photocatalysis at 400 nm. *J. Phys. Chem. C* **117**, 5293–5300 (2013).
316. Li, C., Domen, K., Maruya, K. ichi & Onishi, T. Spectroscopic identification of adsorbed species derived from adsorption and decomposition of formic acid, methanol, and formaldehyde on cerium oxide. *J. Catal.* **125**, 445–455 (1990).
317. Schubert, G., Bánsági, T. & Solymosi, F. Photocatalytic decomposition of methyl formate over TiO_2-supported Pt metals. *J. Phys. Chem. C* **117**, 22797–22804 (2013).
318. Phillips, K. R., Jensen, S. C., Baron, M., Li, S. C. & Friend, C. M. Sequential photo-oxidation of methanol to methyl formate on TiO_2(110). *J. Am. Chem. Soc.* **135**, 574–577 (2013).
319. Yu, X., Zhang, Z., Yang, C., Bebensee, F., Heissler, S., Nefedov, A., Tang, M., Ge, Q., Chen, L., Kay, B. D., Dohnálek, Z., Wang, Y. & Wöll, C. Interaction of Formaldehyde with the Rutile TiO_2(110) Surface: A Combined Experimental and Theoretical Study. *J. Phys. Chem. C* **120**, 12626–12636 (2016).
320. Gaca-Zając, K. Z., Smith, B. R., Nordon, A., Fletcher, A. J., Johnston, K. & Sefcik, J. Investigation of IR and Raman spectra of species present in formaldehyde-water-methanol systems. *Vib. Spectrosc.* **97**, 44–54 (2018).
321. Fanetti, S., Ceppatelli, M., Citroni, M. & Bini, R. High-pressure photoinduced reactivity of CH_3OH and CD_3OH. *J. Phys. Chem. C* **116**, 2108–2115 (2012).
322. Busca, G., Lamotte, J., Lavalley, J.-C. & Lorenzelli, V. FT-IR study of the adsorption and transformation of formaldehyde on oxide surfaces. *J. Am. Chem. Soc.* **109**, 5197–5202 (1987).
323. Kecskés, T., Raskó, J. & Kiss, J. FTIR and mass spectrometric studies on the interaction of formaldehyde with TiO_2 supported Pt and Au catalysts. *Appl. Catal. A Gen.* **273**, 55–62 (2004).
324. Li, Y., Lu, G. & Li, S. Photocatalytic production of hydrogen in single component and mixture systems of electron donors and monitoring adsorption of donors by in situ infrared spectroscopy. *Chemosphere* **52**, 843–850 (2003).
325. Araña, J., Doña-Rodríguez, J. M., Cabo, C. G. I., González-Díaz, O., Herrera-Melián, J. A. & Pérez-Peña, J. FTIR study of gas-phase alcohols photocatalytic degradation with TiO_2 and AC-TiO_2. *Appl. Catal. B Environ.* **53**, 221–232 (2004).
326. El-Roz, M., Kus, M., Cool, P. & Thibault-Starzyk, F. New operando IR technique to study the photocatalytic activity and selectivity of TiO_2 nanotubes in air purification: Influence of temperature, UV intensity, and VOC concentration. *J. Phys. Chem. C* **116**, 13252–13263 (2012).
327. De Juan, A., Jaumot, J. & Tauler, R. Multivariate Curve Resolution (MCR). Solving the mixture analysis problem. *Anal. Methods* **6**, 4964–4976 (2014).
328. Halasi, G., Schubert, G. & Solymosi, F. Photodecomposition of formic acid on N-doped and metal-promoted TiO_2 production of CO-free H_2. *J. Phys. Chem. C* **116**, 15396–15405 (2012).
329. Fontelles-Carceller, O., Muñoz-Batista, M. J., Rodríguez-Castellón, E., Conesa, J. C., Fernández-García, M. & Kubacka, A. Measuring and interpreting quantum efficiency for hydrogen photo-production using Pt-titania catalysts. *J. Catal.* **347**, 157–169 (2017).
330. Pacchioni, G. Oxygen Vacancy: The Invisible Agent on Oxide Surfaces. *ChemPhysChem* **4**, 1041–1047 (2003).
331. Priebe, J. B., Radnik, J., Lennox, A. J. J., Pohl, M. M., Karnahl, M., Hollmann, D., Grabow, K., Bentrup, U., Junge, H., Beller, M. & Brückner, A. Solar Hydrogen Production by Plasmonic Au-TiO_2 Catalysts: Impact of Synthesis Protocol and TiO_2 Phase on Charge Transfer Efficiency and H_2 Evolution Rates. *ACS Catal.* **5**, 2137–2148 (2015).
332. Priebe, J. B., Karnahl, M., Junge, H., Beller, M., Hollmann, D. & Brückner, A. Water reduction with visible light: Synergy between optical transitions and electron transfer in Au-TiO_2 catalysts visualized by in situ EPR spectroscopy. *Angew. Chemie - Int. Ed.* **52**, 11420–11424 (2013).
333. Krishnan, P., Liu, M., Itty, P. A., Liu, Z., Rheinheimer, V., Zhang, M. H., Monteiro, P. J. M. & Yu, L. E. Characterization of photocatalytic TiO_2 powder under varied environments using near ambient pressure

Die approbierte gedruckte Originalversion dieser Dissertation ist an der TU Wien Bibliothek verfügbar.
The approved original version of this doctoral thesis is available in print at TU Wien Bibliothek.
TU Bibliothek WIEN Your knowledge hub

X-ray photoelectron spectroscopy. *Sci. Rep.* **7**, 43298 (2017).

334. Feng, N., Wang, Q., Zheng, A., Zhang, Z., Fan, J., Liu, S. Bin, Amoureux, J. P. & Deng, F. Understanding the high photocatalytic activity of (B, Ag)-codoped TiO_2. *J. Am. Chem. Soc.* **135**, 1607–1616 (2013).
335. Ligon, S. C., Liska, R., Stampfl, J., Gurr, M. & Mülhaupt, R. Polymers for 3D Printing and Customized Additive Manufacturing. *Chemical Reviews* **117**, 10212–10290 (2017).
336. Schubert, C., Van Langeveld, M. C. & Donoso, L. A. Innovations in 3D printing: A 3D overview from optics to organs. *Br. J. Ophthalmol.* **98**, 159–161 (2014).
337. Sharkey, J. P., Foo, D. C. W., Kabla, A., Baumberg, J. J. & Bowman, R. W. A one-piece 3D printed flexure translation stage for open-source microscopy. *Rev. Sci. Instrum.* **87**, 025104 (2016).
338. To, S. C., Brautigam, C. A., Chaturvedi, S. K., Bollard, M. T., Krynitsky, J., Kakareka, J. W., Pohida, T. J., Zhao, H. & Schuck, P. Enhanced Sample Handling for Analytical Ultracentrifugation with 3D-Printed Centerpieces. *Anal. Chem.* **91**, 5866–5873 (2019).
339. Cocovi-Solberg, D. J., Rosende, M., Michalec, M. & Miró, M. 3D Printing: The Second Dawn of Lab-On-Valve Fluidic Platforms for Automatic (Bio)Chemical Assays. *Anal. Chem.* **91**, 1140–1149 (2019).
340. Kitson, P. J., Rosnes, M. H., Sans, V., Dragone, V. & Cronin, L. Configurable 3D-Printed millifluidic and microfluidic 'lab on a chip' reactionware devices. *Lab Chip* **12**, 3267–3271 (2012).
341. Fujisaki, S., Shibata, H., Yamada, K., Suzuki, K. & Citterio, D. Printed low-cost microfluidic analytical devices based on a transparent substrate. *Analyst* **144**, 2746–2754 (2019).
342. Symes, M. D., Kitson, P. J., Yan, J., Richmond, C. J., Cooper, G. J. T., Bowman, R. W., Vilbrandt, T. & Cronin, L. Integrated 3D-printed reactionware for chemical synthesis and analysis. *Nat. Chem.* **4**, 349–354 (2012).
343. Franklin, A., Marzo, A., Malkin, R. & Drinkwater, B. W. Three-dimensional ultrasonic trapping of micro-particles in water with a simple and compact two-element transducer. *Appl. Phys. Lett.* **111**, 094101 (2017).
344. Zhang, C., Anzalone, N. C., Faria, R. P. & Pearce, J. M. Open-Source 3D-Printable Optics Equipment. *PLoS One* **8**, e59840 (2013).
345. Winters, B. J. & Shepler, D. 3D printable optomechanical cage system with enclosure. *HardwareX* **3**, 62–81 (2018).
346. Bauer, R., Stewart, G., Johnstone, W., Boyd, E. & Lengden, M. 3D-printed miniature gas cell for photoacoustic spectroscopy of trace gases. *Opt. Lett.* **39**, 4796 (2014).
347. Bonilla-Manrique, O. E., Moser, H., Martín-Mateos, P., Lendl, B. & Ruiz-Llata, M. Hydrogen sulfide detection in the midinfrared using a 3d-printed resonant gas cell. *J. Sensors* **2019**, 1–7 (2019).
348. Grasse, E. K., Torcasio, M. H. & Smith, A. W. Teaching UV-Vis Spectroscopy with a 3D-Printable Smartphone Spectrophotometer. *J. Chem. Educ.* **93**, 146–151 (2016).
349. Willis, K., Brockmeyer, E., Hudson, S. & Poupyrev, I. Printed optics. in *Proceedings of the 25th annual ACM symposium on User interface software and technology - UIST '12* 589 (ACM Press, 2012). doi:10.1145/2380116.2380190
350. Pandey, S., Gupta, B. & Nahata, A. Terahertz plasmonic waveguides created via 3D printing. *Opt. Express* **21**, 24422 (2013).
351. Karabudak, E., Mojet, B. L., Schlautmann, S., Mul, G. & Gardeniers, H. J. G. E. Attenuated total reflection-infrared nanofluidic chip with 71 nL detection volume for in situ spectroscopic analysis of chemical reaction intermediates. *Anal. Chem.* **84**, 3132–3137 (2012).
352. Morhart, T. A., Unni, B., Lardner, M. J. & Burgess, I. J. Electrochemical ATR-SEIRAS Using Low-Cost, Micromachined Si Wafers. *Anal. Chem.* **89**, 11818–11824 (2017).
353. Schumacher, H., Künzelmann, U., Vasilev, B., Eichhorn, K. J. & Bartha, J. W. Applications of microstructured silicon wafers as internal reflection elements in attenuated total reflection Fourier transform infrared spectroscopy. *Appl. Spectrosc.* **64**, 1022–1027 (2010).
354. Edwards, D. F. & Ochoa, E. Infrared refractive index of silicon. *Appl. Opt.* **19**, 4130 (1980).
355. Burnett, J. H., Kaplan, S. G., Stover, E., Phenis, A., Optics, A. M. P. & Rd, M. Refractive index measurements of Ge. **9974**, 1–10 (1949).
356. Baker, M. J. *et al.* Using Fourier transform IR spectroscopy to analyze biological materials. *Nat. Protoc.* **9**, 1771–1791 (2014).
357. Yang, H., Yang, S., Kong, J., Dong, A. & Yu, S. Obtaining information about protein secondary structures in aqueous solution using Fourier transform IR spectroscopy. *Nat. Protoc.* **10**, 382–396 (2015).
358. Scherzer, T., Tauber, A. & Mehnert, R. UV curing of pressure sensitive adhesives studied by real-time FTIR-ATR spectroscopy. *Vib. Spectrosc.* **29**, 125–131 (2002).

Die approbierte gedruckte Originalversion dieser Dissertation ist an der TU Wien Bibliothek verfügbar.
The approved original version of this doctoral thesis is available in print at TU Wien Bibliothek.
TU Bibliothek Your knowledge hub WIEN

359. Margalit, E., Katzir, A., Dodiuk, H. & Kosower, E. M. Silver halide infrared fibre-optic evanescent wave spectroscopy for in situ monitoring of the chemical processes in adhesive curing. *Surf. Interface Anal.* **15**, 473–478 (1990).

360. Tomlinson, S. K., Ghita, O. R., Hooper, R. M. & Evans, K. E. The use of near-infrared spectroscopy for the cure monitoring of an ethyl cyanoacrylate adhesive. *Vib. Spectrosc.* **40**, 133–141 (2006).

361. Gasser, C., Genner, A., Moser, H., Ofner, J. & Lendl, B. Application of a tunable Fabry-Pérot filtometer to mid-infrared gas sensing. *Sensors Actuators, B Chem.* **242**, 9–14 (2017).

362. Gasser, C., Kilgus, J., Harasek, M., Lendl, B. & Brandstetter, M. Enhanced mid-infrared multi-bounce ATR spectroscopy for online detection of hydrogen peroxide using a supercontinuum laser. *Opt. Express* **26**, 12169 (2018).

363. Hamoudi, S. & Belkacemi, K. Adsorption of nitrate and phosphate ions from aqueous solutions using organically-functionalized silica materials: Kinetic modeling. *Fuel* **110**, 107–113 (2013).

364. Ikigaki, K., Okada, K., Tokudome, Y., Toyao, T., Falcaro, P., Doonan, C. J. & Takahashi, M. MOF-on-MOF: Oriented Growth of Multiple Layered Thin Films of Metal-Organic Frameworks. *Angew. Chemie Int. Ed.* **58**, 6886–6890 (2019).

365. Falcaro, P., Okada, K., Hara, T., Ikigaki, K., Tokudome, Y., Thornton, A. W., Hill, A. J., Williams, T., Doonan, C. & Takahashi, M. Centimetre-scale micropore alignment in oriented polycrystalline metal–organic framework films via heteroepitaxial growth. *Nat. Mater.* **16**, 342–348 (2017).

366. Sick, T., Hufnagel, A. G., Kampmann, J., Kondofersky, I., Calik, M., Rotter, J. M., Evans, A., Döblinger, M., Herbert, S., Peters, K., Böhm, D., Knochel, P., Medina, D. D., Fattakhova-Rohlfing, D. & Bein, T. Oriented films of conjugated 2D covalent organic frameworks as photocathodes for water splitting. *J. Am. Chem. Soc.* **140**, 2085–2092 (2018).

367. Schwaighofer, A., Montemurro, M., Freitag, S., Kristament, C., Culzoni, M. J. & Lendl, B. Beyond Fourier Transform Infrared Spectroscopy: External Cavity Quantum Cascade Laser-Based Mid-infrared Transmission Spectroscopy of Proteins in the Amide i and Amide II Region. *Anal. Chem.* **90**, 7072–7079 (2018).

368. Chiola, V., Ritsko, J. E. & Vanderpool, C. D. Process for producing low-bulk density silica. *United States Patent Office* 1–3 (1971).

369. Jamois, C., Wehrspohn, R. B., Andreani, L. C., Hermann, C., Hess, O. & Gösele, U. Silicon-based two-dimensional photonic crystal waveguides. *Photonics and Nanostructures - Fundamentals and Applications* **1**, 1–13 (2003).

Die approbierte gedruckte Originalversion dieser Dissertation ist an der TU Wien Bibliothek verfügbar.
The approved original version of this doctoral thesis is available in print at TU Wien Bibliothek.
TU Bibliothek Your knowledge hub WIEN

Die approbierte gedruckte Originalversion dieser Dissertation ist an der TU Wien Bibliothek verfügbar.
The approved original version of this doctoral thesis is available in print at TU Wien Bibliothek.

Appendix

A. Abstract of Published Works

Publication I

In Situ IR Spectroscopy of Mesoporous Silica Films for Monitoring Adsorption Processes and Trace Analysis

Bettina Baumgartner, Jakob Hayden, Andreas Schwaighofer, Bernhard Lendl

ACS Appl. Nano Mater. **1**, 7083–7091 (2018)

Adsorption of molecules on high-surface-area materials is a fundamental process critical to many fields of basic and applied chemical research; for instance, it is among the simplest and most efficient principles for separating and remediating polluted water. However, established experimental approaches for investigating this fundamental process preclude *in situ* monitoring and thus obtaining real-time information about the ongoing processes. In this work, mid-infrared attenuated total reflection (ATR) spectroscopy is introduced as a powerful technique for quantitative *in situ* monitoring of adsorption processes and thus enrichment of traces of organic pollutants from aqueous solution in ordered mesoporous silica films. The synthesis, functionalization, and characterization of two silica films with 3D hexagonal and cubic pore structure on silicon ATR crystals are presented. Benzonitrile and valeronitrile as model compounds for aromatic and aliphatic water pollutants are enriched in hydrophobic films, while the matrix, water, is excluded from the volume probed by the evanescent field. Enrichment times of <5 s are observed during *in situ* measurements of benzonitrile adsorbing onto the film from aqueous solution. The sensing system is calibrated using the Freundlich adsorption equation as calibration function. Enrichment factors of benzonitrile and valeronitrile within the film were determined to be >200 and >100, respectively, yielding detection limits in the low ppm range. Furthermore, fast and complete desorption of the analyte, ensuring reliable regeneration of the sensor, was verified. Lastly, we derive and experimentally validate equations for ATR spectroscopy with thin film adsorption layers to quantify the absolute mass of adsorbed pollutant in the film. The excellent agreement between recorded absorptions at target wavenumbers of the target analytes and corresponding simulations corroborates the validity of the chosen approach.

Publication II

Pore Size-Dependent Structure of Confined Water in Mesoporous Silica Films from Water Adsorption-Desorption using ATR-FTIR Spectroscopy

Bettina Baumgartner, Jakob Hayden, Jérôme Loizillon, Sophia Steinbacher, David Grosso, and Bernhard Lendl

Langmuir **35**, 11986–11994 (2019)

The local structure of water on chemically and structurally different surfaces is subject of ongoing research. In particular, confined spaces as found in mesoporous silica have a

Die approbierte gedruckte Originalversion dieser Dissertation ist an der TU Wien Bibliothek verfügbar.
The approved original version of this doctoral thesis is available in print at TU Wien Bibliothek.
TU Bibliothek Your knowledge hub WIEN

pronounced effect on the interplay between adsorbate-adsorbate and adsorbate-surface interactions. Mid-infrared spectroscopy is ideally suited to quantitatively and qualitatively study such systems as the probed molecular vibrations are highly sensitive to intermolecular interactions. Here, the quantity and structure of water adsorbed from the gas phase into silica mesopores at different water vapor pressures was monitored using mid-infrared attenuated total reflection (ATR) spectroscopy. Germanium ATR crystals were coated with different mesoporous silica films prepared by evaporation induced self-assembly. Quantitative analysis of the water bending vibration at 1640 cm^{-1} at varying vapor pressure allowed for retrieving porosity and pore size distribution of the mesoporous films. The results were in excellent agreement with those obtained from ellipsometric porosimetry. In addition, different degrees of hydrogen bonding of water as reflected in the band position and shape of the stretching vibrations (3000 - 3750 cm^{-1}) were analyzed and attributed to high-density, unordered bulk and low-density, surface-induced ordered water. Thereby, the progression of surface-induced ordered water and bulk water as a function of water vapor pressure was studied for different pore sizes. Small pores with 5 nm diameter showed a number of two ordered monolayers, while for pores > 12 nm the number of ordered monolayers is significantly larger and agrees with the number observed on planar SiO_2 surfaces.

Publication III

An Acoustic Trap for Bead Injection Attenuated Total Reflection Infrared Spectroscopy

Stephan Freitag, Bettina Baumgartner, Stefan Tauber, Christoph Gasser, Stefan Radel, Andreas Schwaighofer, Bernhard Lendl

Anal. Chem. **91**, 7672–7678 (2019)

In this work, we introduce a system combining an acoustic trap for bead injection with attenuated total reflection (ATR) infrared (IR) spectroscopy. By mounting an acoustofluidic cell hosting an ultrasound source on top of a custom-built ATR fixture, we were able to trap beads labeled with the enzyme alkaline phosphatase without requiring any mechanical retention elements. Sequential injection analysis was employed for reproducible sample handling and bead injection into the acoustic trap. To showcase potential applications of the presented setup for kinetic studies, we monitored the conversion of *p*-nitrophenylphosphate into *p*-nitrophenol and phosphate via beads carrying the immobilized enzyme using ATR-IR spectroscopy. Retaining the labeled beads via ultrasound particle manipulation resulted in excellent experimental reproducibility (relative standard deviation, 3.91%). It was demonstrated that trapped beads remained stably restrained with up to eight cell volumes of liquid passing through the acoustofluidic cell. Beads could be discarded in a straightforward manner by switching off the ultrasound, in contrast to systems containing mechanical retention elements, which require backflushing. Multiple experiments were performed by employing different substrate concentrations with the same batch of trapped beads as well as varying the amount of enzyme present in the cell, enabling enzyme kinetic studies and

Die approbierte gedruckte Originalversion dieser Dissertation ist an der TU Wien Bibliothek verfügbar.
The approved original version of this doctoral thesis is available in print at TU Wien Bibliothek.
TU Bibliothek WIEN Your knowledge hub

emphasizing the application of the proposed setup in studies where enzymatic reuse is desired. This proves the potential of the acoustic trap combined with ATR-IR spectroscopy to monitor the activity of immobilized enzymes and its ability to perform complex bead-based assays.

Publication IV

In-depth study of coating multimodal porosity using ellipsometry porosimetry in desorption scanning mode

Jérôme Loizillon, Bettina Baumgartner, Christophe Sinturel, Marco Abbarchi, Bernhard Lendl, David Grosso

J. Phys. Chem. C **123**, 23464–23479 (2019)

Ellipsometry porosimetry provides full adsorption/desorption isotherms and is among the most accurate techniques to probe porosity in thin films. Here we address a novel technique based on desorption scanning for a precise assessment of the porosity features revealing the size distribution of interconnections between the various populations of pores in the coatings. This investigation was performed on model (multimodal) mesoporous silica films prepared by evaporation-induced self-assembly in presence of micellar templating agents, before and after pore network modification through chemical attack in NH_4F. The systems were also analyzed by Grazing Incidence Small Angle X-ray Scattering to confirm the multimodal periodic organization and homogeneity of the porosity. Conventional pore blocking effect could not explain by itself the unconventional behaviors observed in the desorption scans. We propose a new desorption mechanism, addressed as pore transit desorption, to justify the experimental features and provide a full description of the porous network complexity. Based on these, we discuss several model cases of porosities combining up to two populations of pores and 3 populations of interconnections. Overall, interpretations made in this work can be generalized and transposed to any mesoporous material.

Publication V

Mid-infrared sensing of CO at saturated absorption conditions using intracavity quartz-enhanced photoacoustic spectroscopy

Jakob Hayden, Bettina Baumgartner, Johannes P. Waclawek, Bernhard Lendl

Appl. Phys. B 125, (2019)

The sensitivity of quartz-enhanced photoacoustic spectroscopy (QEPAS) can be drastically increased using the power enhancement in high-finesse cavities. Here, low noise resonant power enhancement to 6.3 W was achieved in a linear Brewster window cavity by exploiting optical feedback locking of a quantum cascade laser. The high intracavity intensity of up to 73 W mm^{-2} in between the prongs of a custom tuning fork resulted in strong optical saturation of CO at 4.59 µm. Saturated absorption is discussed theoretically and experimentally for photoacoustic measurements in general and intracavity QEPAS (I-QEPAS) in particular. The saturation intensity of CO's R9 transition was retrieved from power-

Die approbierte gedruckte Originalversion dieser Dissertation ist an der TU Wien Bibliothek verfügbar.
The approved original version of this doctoral thesis is available in print at TU Wien Bibliothek.
TU Bibliothek WIEN Your knowledge hub

dependent I-QEPAS signals. This allowed for sensing CO independently from varying degrees of saturation caused by absorption induced changes of intracavity power. Figures of merit of the I-QEPAS setup for sensing of CO and H_2O are compared to standard wavelength modulation QEPAS without cavity enhancement. For H_2O, the sensitivity was increased by a factor of 230, practically identical to the power enhancement, while the sensitivity gain for CO detection was limited to 57 by optical saturation.

Publication VI

Mesoporous Silica Films for Sensing Volatile Organic Compounds using Attenuated Total Reflection Spectroscopy

Bettina Baumgartner, Jakob Hayden and Bernhard Lendl

Sensors Actuators B Chem. **302**, 127194 (2020).

Sensitivity of evanescent wave sensing of gaseous species can be vastly increased by enrichment materials that locally concentrate the analyte on the sensor. Here, we investigate functionalized mesoporous silica films as versatile enrichment layer for sensing volatile organic compounds (VOCs) from gas-phase. Attenuated total reflection (ATR) crystals were coated with silica films of different pore sizes and their capability to enrich three different aromatic hydrocarbons from a vapor stream was studied by means of FTIR spectroscopy. Thereby, single-digit ppmv limits of detection were achieved with an effective path length of only 6.3 µm. The selectivity introduced by the functionalization of the silica films effectively minimized interferences of water vapor, which gave access to the spectral fingerprint region between 1550 and 1450 cm^{-1}. This allowed to discriminate and quantify toluene, *p*-xylene and 1,2,4-trimethylbenzene in multicomponent mixtures at high humidity. Fast response and regeneration times and enrichment factors up to 32 000 showcase the high potential of this material for evanescent wave sensing.

Publication VII

3D-Printing for Low-Cost and Versatile Attenuated Total Reflection Infrared Spectroscopy

Bettina Baumgartner, Stephan Freitag, Bernhard Lendl

Submitted to Analytical Chemistry

In this work, we present a fully 3D-printed accessory for attenuated total reflection Fourier transform infrared (ATR-FTIR) spectroscopy ready for use in commercial FTIR spectrometers. The developed setup stands out in terms of robustness and ease of sample application. Rapid prototyping paired with theoretical considerations were employed to design and fabricate the accessory. Cost-efficient commercially available and silicon and germanium ATR crystals prepared from double-side polished wafers were mounted in the setup. While low-noise levels and stability bear comparison with commercial systems, the multibounce ATR crystal's long interaction path lengths as well as their interchangeability turns the presented

Die approbierte gedruckte Originalversion dieser Dissertation ist an der TU Wien Bibliothek verfügbar.
The approved original version of this doctoral thesis is available in print at TU Wien Bibliothek.
TU Bibliothek WIEN Your knowledge hub

ATR module into an even more sophisticated tool. The versatility of the proposed setup is demonstrated for various spectroscopic challenges: Curing of a cyanoacrylate and a two component epoxy based adhesive was monitored by tracking polymerization processes at room and high temperatures. To emphasize potential applications of the disposable ATR accessory in life science studies exploring potential bio-hazardous samples mid-IR spectra of *Escherichia coli* and bovine serum albumin were recorded The total printing time of the ATR module is 10.5 h enabling overnight fabrication at a total cost ranging from 150-613 € making the high versatility of ATR spectroscopy accessible to a broader audience. This proves the potential of 3D-printing to generate optical devices tailored to the needs of individual analytical problems.

Publication VIII

In situ Pt Photodeposition and Methanol Photooxidation on Pt/TiO_2: Pt-Loading-Dependent Photocatalytic Reaction Pathways Studied by Liquid-Phase Infrared Spectroscopy

Greta M. Haselmann[‡], Bettina Baumgartner[‡], Jia Wang, Karin Wieland, Tushar Gupta, Christopher Herzig, Andreas Limbeck, Bernhard Lendl, Dominik Eder

[‡] shared first-author

Submitted to ACS Catalysis

We developed a top-irradiated, liquid-phase attenuated total reflectance Fourier transform infrared (ATR-FTIR) setup that allows time-resolved investigations of both Pt particle growth during in situ photodeposition via monitoring of the Pt^0–CO_{ads} band on TiO_2 thin films as well as the photooxidation of methanol in aqueous environments. Obtained ATR-FTIR data sets were analyzed via multivariate curve resolution-alternating least squares (MCR-ALS), which enabled us to clearly differentiate various reaction pathways for different Pt loadings at otherwise fixed reaction conditions (*i.e.*, methanol concentration, UV intensity). At the highest Pt loading (nominal concentration of 2.7 wt %), photooxidation of methanol occurs via direct oxidation through a formaldehyde intermediate to CO_2, whereas the lower Pt loadings of 0.7 and 1.4 wt % favor a side reaction that includes methyl formate as an intermediate. These findings were correlated with the formation of different CO binding sites on Pt during photodeposition, and we presume that changes in the reaction pathway depend on the number rather than the nature of active available Pt sites. Complementary ex situ characterizations of the thin films by transmission electron microscopy (TEM), Raman spectroscopy, X-ray diffraction (XRD), X-ray photoelectron spectroscopy (XPS), and inductively coupled plasma mass spectrometry (ICP-MS) were performed, delivering information on the generated Pt nanoparticles and structural changes of TiO_2. The presented optical setup paves the way for fundamental studies of heterogeneous catalytic reactions as close as possible to their actual use in aqueous systems.

Die approbierte gedruckte Originalversion dieser Dissertation ist an der TU Wien Bibliothek verfügbar.
The approved original version of this doctoral thesis is available in print at TU Wien Bibliothek.
TU Bibliothek Your knowledge hub WIEN

Publication IX

Multiplex Volatile Organic Compound (VOC) Sensing with Nanophotonic Slot Waveguides Functionalized with a Mesoporous Silica Sorbent Layer

Haolan Zhao, Bettina Baumgartner, Ali Raza, Bernhard Lendl, Roel Baets

Submitted to Optics Letters

We report a Raman sensor for broadband vapor-phase volatile organic compounds (VOCs) based on SiN waveguides functionalized with a mesoporous silica top-cladding. The Raman response of low-concentration VOC gases are evanescently probed via a centimeter-long functionalized slot waveguide. Thanks to the five orders of magnitude concentration factor offered by the mesoporous coating, the detection limit of acetone, ethanol and isopropyl alcohol (IPA) is determined to be 594 ppm, 157 ppm, and 53 ppm respectively with 1 s measurement time in the current setup. Capable of multiplex gas sensing in a complex matrix through fast and reversible adsorption, the demonstration paves the way to on-site continuous VOC monitoring.

Publication X

A Pocket-Sized 3D-printed Attenuated Total Reflection Infrared-Filtometer combined with Functionalized Silica Films for Nitrate Sensing in Water

Bettina Baumgartner, Stephan Freitag, Christoph Gasser, Bernhard Lendl

In preparation

In this contribution, a Fabry-Pérot (FP) filter and a miniaturized thermal emitter housed in a mini-ATR-spectrometer combined with trimethylammonium-functionalized mesoporous silica films on germanium ATR crystals for nitrate sensing is presented. The sensing performance of the functionalized films was investigated using FTIR spectroscopy and revealed fast response times of less than 1 min and high enrichment factors of up to 1490, depending on the concentration. The coated ATR crystals were transferred into a dedicated 3D-printed ATR unit comprising light source, FP filter and printed circuit board with a footprint of only 80 × 120 × 70 mm. Although having a lower signal to noise ratio and smaller spectral coverage compared to FTIR spectrometers, the high enrichment factors of the functionalized ATR crystals allowed for sensing NO_3^- concentrations as low as 5 mg L^{-1}. Given the high versatility of silica and low cost of the FP filters, this results demonstrate the high potential of functionalized mesoporous materials in combination with filtometers for water monitoring.

Die approbierte gedruckte Originalversion dieser Dissertation ist an der TU Wien Bibliothek verfügbar.
The approved original version of this doctoral thesis is available in print at TU Wien Bibliothek.
TU Bibliothek Your knowledge hub WIEN

Publication XI

Anomalous Humidity Dependence in Photoacoustic Spectroscopy of CO Explained by Kinetic Cooling

Jakob Hayden, Bettina Baumgartner, Bernhard Lendl

In preparation

Water affects the amplitude of photoacoustic signals from many gas phase molecules. In quartz-enhanced photoacoustic (QEPAS) measurements of CO excited at the fundamental vibrational resonance of CO, the photoacoustic signal decreases with increasing humidity, reaches a pronounced minimum at ~ 0.25 $\%_V$ and increases with humidity for higher water contents. This peculiar trend is explained by competing endothermal and exothermal pathways of vibrational relaxation of CO in N_2 and H_2O. Near-resonant vibrational-vibrational transfer from CO to N_2, whose vibrational frequency is 188 cm^{-1} higher than in CO, consumes thermal energy, yielding a kinetic cooling effect. In contrast, vibrational relaxation via H_2O is fast and exothermal and hence counteracts kinetic cooling, explaining the observed trend. A detailed kinetic model for collisional relaxation of CO in N_2 and H_2O is presented. Simulations using rate constants obtained from literature are performed and compared to humidity dependent QEPAS experiments at varying pressure. Agreement between experiments and simulations confirms the validity of the model. The kinetic model could be used to identify optimized experimental conditions for sensing of CO and can be readily adapted to include further collision partners.

Die approbierte gedruckte Originalversion dieser Dissertation ist an der TU Wien Bibliothek verfügbar.
The approved original version of this doctoral thesis is available in print at TU Wien Bibliothek.
TU Bibliothek Your knowledge hub WIEN

B. MATLAB scripts

B.1 Porosimetry and PSD

```
    filename = 'ads_isotherm_correcrted';
    filename2=[filename, '.txt'];
    filename_des = 'des_isotherm_correcrted';
    filename_des2=[filename_des, '.txt'];
   rk0=3*10^-10;
   pans=1.33; % anisotropy obtained from shrinkage of porous and dense film; for 1 add
1.0000001
```

input

```
clearvars -except filename filename2 filename_des filename_des2 rk0 pans
p0=1;
theta=27; %wetting angle
vmol=18.0428*10^-6; %molare volume m3/mol
surft0=72.8*10^-3; %surface tension y0 J/m2-> modified with tolman length
R=8.314; %  gaskonstante 8.314 kg m2 /(s2 mol K)
T=298; % temperature K
h=0.096*10^-9; % atomic diameter in m for H2O
presraw=load(filename2);
pres=(presraw(2:end-1,1))*0.95;
waterthick=[((4.0189)*pres.^3-5.5774*pres.^2+3.7315*pres)*10^-9]';
E=sqrt(pans^2-1)/pans;
C=log((1+E)/(1-E))/E;
Geo=1+(C/(2*pans^2)); % geometric factor
```

Newtonian approximation

```
i0=0; %initialise the number of iterations
delta0=10^-8;
for kk=1:size(pres)
    uu=kk;
    rk=rk0;
    delta=delta0;
    i=i0;
    while (delta > 10^-20)
        y=R*T*log(pres(uu))-1.04167*10^10*surft0*vmol*Geo*cosd(theta)/(Geo
1.04167*10^10*rk);
        dy=-1.08507*10^20*surft0*Geo*vmol*cosd(theta)/(Geo-1.04167*10^10*rk)^2;
        NewX = rk - y/dy; %calculate the new value of x
        delta=abs(rk-NewX); %calculate the change in succesive terms
        rk=NewX; % update the nuew value for x
        i = i + 1; % uptdate the number of iterations
    end
    sprintf('After iteration %2.0d the delta is %3.18f',i,delta)
    rkv(uu)=rk;
end

rkv1=rkv';
rkv(isnan(rkv))=0;
bpore=((rkv+waterthick)*2)'; % calcualte pore diameter
figure(112)
hold on
plot(pres,rkv)
plot(pres,waterthick)
```

Die approbierte gedruckte Originalversion dieser Dissertation ist an der TU Wien Bibliothek verfügbar.
The approved original version of this doctoral thesis is available in print at TU Wien Bibliothek.
TU Bibliothek Your knowledge hub WIEN

```
plot(pres,bpore)
```

load Vwater/Vfilm data

```
vporeadsraw=presraw;
vpore=((vporeadsraw(2:end-1,2)));
```

```
figure(32)
plot(waterthick,vpore)
figure(34)
plot(pres,vpore)
```

PSD adsorption

```
bporemean=(bpore(1:end-1)+diff(bpore)./2)*10^9; %um werte zwischen den punkten zu erzeugen
differenz=diff(vpore-1)./diff(bpore);
figure(44)
hold on
plot(bporemean,differenz,'-o')
```

save adsorption

```
    differenzshort=differenz/10^7;
    PSDadssave=[bporemean differenzshort];
    save([filename,'_PSDads_fixedD_ATR.txt'],'PSDadssave','-ascii')
```

input desorption

```
clearvars -except filename filename2 filename_des filename_des2 rk0 pans
p0=1;
theta=27; %wetting angle
vmol=18.0428*10^-6; %molare volume m3/mol
surft0=72.8*10^-3; %surface tension y0 J/m2-> modified with tolman length
R=8.314; %  gaskonstante 8.314 kg m2 /(s2 mol K)
T=298; % temperature K
h=0.096*10^-9; % atomic diameter in m for H2O
presraw=load(filename_des2);
pres=(presraw(1:end-1,1))*0.95;
waterthick=[((6.1033)*pres.^3-9.0457*pres.^2+5.4176*pres-0.1641)*10^-9]';
E=sqrt(pans^2-1)/pans;
C=log((1+E)/(1-E))/E;
Geo=1+(C/(2*pans^2)); % geometric factor
```

Newtonian approximation

```
i0=0; %initialise the number of iterations
delta0=10^-7;
for kk=1:size(pres)
    uu=kk;
    rk=rk0;
    delta=delta0;
    i=i0;
    while (delta > 10^-20)
        y=R*T*log(pres(uu))-1.04167*10^10*surft0*vmol*Geo*cosd(theta)/(Geo-
1.04167*10^10*rk);
        dy=-1.08507*10^20*surft0*Geo*vmol*cosd(theta)/(Geo-1.04167*10^10*rk)^2;
        NewX = rk - y/dy; %calculate the new value of x
```

Die approbierte gedruckte Originalversion dieser Dissertation ist an der TU Wien Bibliothek verfügbar.
The approved original version of this doctoral thesis is available in print at TU Wien Bibliothek.
TU Bibliothek Your knowledge hub WIEN

```
        delta=abs(rk-NewX); %calculate the change in succesive terms
        rk=NewX; % update the nuew value for x
        i = i + 1; % uptdate the number of iterations
    end
    sprintf('After iteration %2.0d the delta is %3.18f',i,delta)
    rkv(uu)=rk;
end
```

```
rkv1=rkv';
rkv(isnan(rkv))=0;
bpore=((rkv+waterthick)*2)'; % calculate pore diameter
figure(112)
hold on
plot(pres,rkv)
plot(pres,waterthick)
plot(pres,bpore)
```

load Vwater/Vfilm data

```
vporeadsraw=presraw;
vpore=((vporeadsraw(1:end-1,2)));
```

PSD desoprtion

```
bporemean=(bpore(1:end-1)+diff(bpore)./2)*10^9; %um werte zwischen den punkten zu erzeugen
differenz=diff(vpore)./diff(bpore);
figure(44)
hold on
plot(bporemean,differenz,'-o')
```

save

```
    differenzshort=differenz/10^7;
    PSDadssave=[bporemean differenzshort];
    save([filename_des,'_PSDdes_fixedD_ATR.txt'],'PSDadssave','-ascii')
```

B.2 Gauss Fitting for Water Bands

Inputs

```
scantime=20; %time for one scan in opus in s
bgtime=30; %averaging time for background spectrum
upperlimit=1660;
navg=1;
navg2=6;
lowerlimit=1620;
neuladen=true;
saveresults=false;
addpath('S:\PHD\PHD\DATA\matlab\dp') %for natsort
```

Load all Spectra in folder

```
if neuladen
files = dir('*4.00*.txt');
filescells=struct2cell(files);
sortedfiles=string(natsortfiles(filescells(1,:))');
```

Die approbierte gedruckte Originalversion dieser Dissertation ist an der TU Wien Bibliothek verfügbar.
The approved original version of this doctoral thesis is available in print at TU Wien Bibliothek.
TU Bibliothek Your knowledge hub WIEN

```
raw=load(char(sortedfiles(1)));
wn=raw(:,1);
raw=[raw(:,2) zeros(length(files)-1,length(raw(:,2)))'];
for uu=2:length(files)
    temp=load(char(sortedfiles(uu)));
    raw(:,uu)=temp(:,2);
end
end
```

calculate spectrum

```
spectra=raw(:,2:end);
spectraavg=zeros(ceil(size(spectra,2)/navg),length(wn))';
for ii=1:length(wn)
    spectraavg(ii,:)=decimate(spectra(ii,:),navg,5);
end
```

Absorbance average

```
absocorr=spectraavg;
wnshort=wn(wn>lowerlimit & wn<upperlimit);
absoshort=absocorr(wn>lowerlimit & wn<upperlimit,:);
figure(77)
clf
plot(wn,absocorr)
```

define time axis

```
t=linspace(scantime*(navg/2),scantime*(size(raw,2)-navg/2),size(spectraavg,2));
```

find peak height

```
height=max(absoshort);
figure(25)
hold on
scatter(t,height)
```

average new - only platteau

```
r=6; % number of points per platteau
meannum=4; % number from which averaging starts in platteau
yy=reshape(height(1:fix(numel(height)/r)*r),r,[]); %reshape(conctol,6,[]);
yyt=reshape(t(1:fix(numel(t)/r)*r),r,[]);
yymean=mean(yy(6-meannum:end,:));
yytmean=mean(yyt(6-meannum:end,:));
figure(5)
hold on
plot(yyt,yy,'-x')
scatter(yytmean,yymean)
```

average - calculated spectrum

```
spectra2=raw(:,2:end);
spectraavg2=zeros(ceil(size(spectra2,2)/navg2),length(wn))';
```

Die approbierte gedruckte Originalversion dieser Dissertation ist an der TU Wien Bibliothek verfügbar.
The approved original version of this doctoral thesis is available in print at TU Wien Bibliothek.
TU Bibliothek Your knowledge hub WIEN

```
for uu=1:length(wn)
    spectraavg2(uu,:)=decimate(spectra2(uu,:),navg2,5);
end
```

BG correction

```
absocorr=spectraavg2-spectraavg2(wn>3800 & wn<3802,:);
figure(223)
plot(wn,absocorr)
```

abso short

```
absomcr=absocorr(wn>2400 & wn<4000,2:numads+1);
absomcrdes=absocorr(wn>2400 & wn<4000,numads+2:end-(afterzero));
wnmcr=wn(wn>2400 & wn<4000);
figure(222)
plot(wnmcr,absomcr)
```

Fit for width

```
    center=0;
    window=0;
    NumPeaks=6;
    NumTrials=5;
    autozero=1;
    shape=16;
position=[3140 3250 3395 3530 3630 3745];
for pp=1:size(absomcr,2)
    signal=[wnmcr absomcr(:,pp)];
   [FitResults, GOF, xi, yi] =
peakfit(signal,center,window,NumPeaks,shape,1,NumTrials,0,autozero,position,1,1);
   width1(pp)=FitResults(1,4);
   width2(pp)=FitResults(2,4);
  width3(pp)=FitResults(3,4);
   width4(pp)=FitResults(4,4);
   width5(pp)=FitResults(5,4);
   width6(pp)=FitResults(6,4);
end
```

mean of peak width

```
meanwidth1=mean(width1(3:end-2));
meanwidth2=mean(width2(3:end-2));
meanwidth3=mean(width3(3:end-2));
meanwidth4=mean(width4(3:end-2));
meanwidth5=mean(width5(3:end-2));
meanwidth6=mean(width6(3:end-2));
```

fit with fixed width

```
    center=0;
    window=0;
    NumPeaks=6;
    NumTrials=5;
    shape=50;
 position=[1 1 1 1 1 1;3140 3250 3395 3530 3630 3745; meanwidth1 meanwidth2 meanwidth3
```

Die approbierte gedruckte Originalversion dieser Dissertation ist an der TU Wien Bibliothek verfügbar.
The approved original version of this doctoral thesis is available in print at TU Wien Bibliothek.
TU Bibliothek WIEN Your knowledge hub

```
meanwidth4 meanwidth5 meanwidth6]';
for kk=1:size(absomcr,2)
    signal=[wnmcr absomcr(:,kk)];
   [FitResults, GOF, xi, yi] =
peakfit(signal,center,window,NumPeaks,shape,1,NumTrials,0,autozero,position,1,1);
   peak1_adsnorm(kk)=FitResults(1,5);
   peak2_adsnorm(kk)=FitResults(2,5);
   peak3_adsnorm(kk)=FitResults(3,5);
  peak4_adsnorm(kk)=FitResults(4,5);
   peak5_adsnorm(kk)=FitResults(5,5);
   peak6_adsnorm(kk)=FitResults(6,5);
   height1_adsnorm(kk)=FitResults(1,3);
   height2_adsnorm(kk)=FitResults(2,3);
   height3_adsnorm(kk)=FitResults(3,3);
  height4_adsnorm(kk)=FitResults(4,3);
   height5_adsnorm(kk)=FitResults(5,3);
   height6_adsnorm(kk)=FitResults(6,3);
end

for oo=1:size(absomcrdes,2)
    signal=[wnmcr absomcrdes(:,oo)];
   [FitResults, GOF, xi, yi] =
peakfit(signal,center,window,NumPeaks,shape,1,NumTrials,0,autozero,position,1,1);
   peak1_desnorm(oo)=FitResults(1,5);
   peak2_desnorm(oo)=FitResults(2,5);
   peak3_desnorm(oo)=FitResults(3,5);
   peak4_desnorm(oo)=FitResults(4,5);
   peak5_desnorm(oo)=FitResults(5,5);
   peak6_desnorm(oo)=FitResults(6,5);
      height1_desnorm(kk)=FitResults(1,3);
   height2_desnorm(kk)=FitResults(2,3);
   height3_desnorm(kk)=FitResults(3,3);
  height4_desnorm(kk)=FitResults(4,3);
   height5_desnorm(kk)=FitResults(5,3);
   height6_desnorm(kk)=FitResults(6,3);
end
```

saving height

```
allads=[height1_adsnorm' height2_adsnorm' height3_adsnorm' height4_adsnorm'
height5_adsnorm' height6_adsnorm'];
alldes=[height1_desnorm' height2_desnorm' height3_desnorm' height4_desnorm'
height5_desnorm' height6_desnorm'];
widhts= [meanwidth1 meanwidth2 meanwidth3 meanwidth4 meanwidth5 meanwidth6];
save('height_ads.txt','allads','-ascii')
save('height_des.txt','alldes','-ascii')
save('widths.txt','widhts','-ascii')
```

plot fitted values

```
figure(347)
plot(RH,peak1_adsnorm)
hold on
plot(RH,peak2_adsnorm,'-o')
plot(RH,peak3_adsnorm,'-x')
plot(RH,peak4_adsnorm)
plot(RH,peak5_adsnorm,'-o')
```

Die approbierte gedruckte Originalversion dieser Dissertation ist an der TU Wien Bibliothek verfügbar.
The approved original version of this doctoral thesis is available in print at TU Wien Bibliothek.
TU Bibliothek Your knowledge hub WIEN

```
plot(RH,peak6_adsnorm,'-x')
```

peak mix

```
LDW=peak1_adsnorm+peak2_adsnorm;
HDW=peak3_adsnorm+peak4_adsnorm+peak5_adsnorm;
figure(3125)
plot(RH,LDW)
hold on
plot(RH,HDW)
```

Plot Gauss functions

```
gaussx=[2400:1:4000];

usedspectra=35;

gaussy1=height1_adsnorm(:,usedspectra).*exp(-(gaussx-3140).^2./(2*(meanwidth1/2.3548)^2));
gaussy2=height2_adsnorm(:,usedspectra).*exp(-(gaussx-3250).^2./(2*(meanwidth2/2.35481)^2));
gaussy3=height3_adsnorm(:,usedspectra).*exp(-(gaussx-3400).^2./(2*(meanwidth3/2.3548)^2));
gaussy4=height4_adsnorm(:,usedspectra).*exp(-(gaussx-3530).^2./(2*(meanwidth4/2.3548)^2));
gaussy5=height5_adsnorm(:,usedspectra).*exp(-(gaussx-3630).^2./(2*(meanwidth5/2.3548)^2));
gaussy6=height6_adsnorm(:,usedspectra).*exp(-(gaussx-3745).^2./(2*(meanwidth6/2.3548)^2));

gaussum=gaussy1+gaussy2+gaussy3+gaussy4+gaussy5+gaussy6;
```

Die approbierte gedruckte Originalversion dieser Dissertation ist an der TU Wien Bibliothek verfügbar.
The approved original version of this doctoral thesis is available in print at TU Wien Bibliothek.
TU Bibliothek Your knowledge hub WIEN

B.3 *Bruggeman* Effective Medium Approximation

calculate $d_{efilm,0}$

```
th=0.4;
n1=3.42; %ATR crystal
n2=1.2; %sample 4.5 um_ 1.37;
theta=45;
n21=n2./n1;
lambda1=6.1; %um
bounces=20;
dp0=lambda1./(2.*pi.*(sqrt(n1^2.*sin(theta/360*2*pi).^2-n2.^2))); % dp in nm
desenk0=(lambda1./n1).*((n21.*cos(theta./360.*2.*pi))./(pi.*(1-
n21.^2).*sqrt(sin(theta/360.*2.*pi).^2-n21.^2)));
depar0=(lambda1./n1).*((n21.*cos(theta./360.*2.*pi).*(2.*sin(theta./360.*2.*pi).^2-
n21.^2))./(pi.*(1-n21.^2).*((1+n21.^2).*sin(theta./360*2.*pi).^2-
n21.^2).*sqrt(sin(theta./360*2.*pi)^2-n21.^2)));
de0=(desenk0+depar0)./2;
s=1-exp((-2*th)./dp0);
defilm0=s.*de0.*bounces;
```

inputs

```
nmo=1.2607; % add for bulk material and for iterative process add bruggemann solid + air
nwater=1.32;
nair=1;
rawads=load('ADS.txt');
pres=(rawads(:,1)./100)*0.95;
ads0=rawads(:,2);
rawdes=load('DES.txt');
presdes=(flipud(rawdes(:,1)./100))*0.95;
des0=flipud(rawdes(:,2));
```

calculation of g_{H2O}/V_{Film}

```
Absowater0=55.6.*21.4.*(defilm0*(10^-4));
absoads0=ads0./Absowater0;
absodes0=des0./Absowater0;
gH2O=(absoads0)./max(absoads0);
gH2Odes=(absodes0./max(absodes0));
figure(234)
plot(pres,absoads0)
hold on
plot(pres,absodes0)
```

```
porosity=0.51; %fractaion A, obtained from gH2O/VFilm
```

Bruggeman solid + water

```
nporouswater=1/2*sqrt(-nwater^2+3*porosity*nwater^2+2*nmo^2-
3*porosity*nmo^2+sqrt(8*nwater^2*nmo^2+(nwater^2-3*porosity*nwater^2-
2*nmo^2+3*porosity*nmo^2)^2));
```

bruggemann solid + air

```
nporous=1/2*sqrt(-nair^2+3*porosity*nair^2+2*nmo^2-
3*porosity*nmo^2+sqrt(8*nair^2*nmo^2+(nair^2-3*porosity*nair^2-
```

Die approbierte gedruckte Originalversion dieser Dissertation ist an der TU Wien Bibliothek verfügbar.
The approved original version of this doctoral thesis is available in print at TU Wien Bibliothek.
TU Bibliothek WIEN Your knowledge hub

```
2*nmo^2+3*porosity*nmo^2)^2));
```

bruggemann (solid+air) + water

```
nwaterair=1/2.*sqrt(-nwater^2+3.*gH2O*nwater^2+2.*nair^2-
3.*gH2O.*nair.^2+sqrt(8.*nwater.^2.*nair.^2+(nwater.^2-3.*gH2O.*nwater.^2-
2.*nair.^2+3.*gH2O.*nair.^2).^2));
nporouscorr=1/2.*sqrt(-nwaterair.^2+3.*porosity.*nwaterair.^2+2.*nmo.^2-
3.*porosity.*nmo.^2+sqrt(8.*nwaterair.^2.*nmo.^2+(nwaterair.^2-3.*porosity.*nwaterair.^2-
2.*nmo.^2+3.*porosity.*nmo.^2).^2));

nwaterairdes=1/2.*sqrt(-nwater^2+3.*gH2Odes*nwater^2+2.*nair^2-
3.*gH2Odes.*nair.^2+sqrt(8.*nwater.^2.*nair.^2+(nwater.^2-3.*gH2Odes.*nwater.^2-
2.*nair.^2+3.*gH2Odes.*nair.^2).^2));
nporouscorrdes=1/2.*sqrt(-nwaterairdes.^2+3.*porosity.*nwaterairdes.^2+2.*nmo.^2-
3.*porosity.*nmo.^2+sqrt(8.*nwaterairdes.^2.*nmo.^2+(nwaterairdes.^2-
3.*porosity.*nwaterairdes.^2-2.*nmo.^2+3.*porosity.*nmo.^2).^2));

figure(25)
clf
plot(pres,nwaterair)
hold on
 plot(pres,nporouscorr)
xlabel('RH')
ylabel('RI')
```

input parameter ATR

```
n1=4; %ATR crystal
n2=nporouscorr; %sample 4.5 um_ 1.37;
n2des=nporouscorrdes;
theta=45;
n21=n2./n1;
n21des=n2des./n1;
lambda1=6.45; %um
bounces=20;
```

depth of penetration

```
dp1=lambda1./(2.*pi.*(sqrt(n1^2.*sin(theta/360*2*pi).^2-n2.^2))); % dp in nm
dp1des=lambda1./(2.*pi.*(sqrt(n1^2.*sin(theta/360*2*pi).^2-n2des.^2))); % dp in nm
```

effective path length

```
desenk=(lambda1./n1).*((n21.*cos(theta./360.*2.*pi))./(pi.*(1-
n21.^2).*sqrt(sin(theta/360.*2.*pi).^2-n21.^2)));
depar=(lambda1./n1).*((n21.*cos(theta./360.*2.*pi).*(2.*sin(theta./360.*2.*pi).^2-
n21.^2))./(pi.*(1-n21.^2).*((1+n21.^2).*sin(theta./360*2.*pi).^2-
n21.^2).*sqrt(sin(theta./360*2.*pi)^2-n21.^2)));
de=(desenk+depar)./2;

desenkdes=(lambda1./n1).*((n21des.*cos(theta./360.*2.*pi))./(pi.*(1-
n21des.^2).*sqrt(sin(theta/360.*2.*pi).^2-n21des.^2)));
depardes=(lambda1./n1).*((n21des.*cos(theta./360.*2.*pi).*(2.*sin(theta./360.*2.*pi).^2-
n21des.^2))./(pi.*(1-n21des.^2).*((1+n21des.^2).*sin(theta./360*2.*pi).^2-
n21des.^2).*sqrt(sin(theta./360*2.*pi)^2-n21des.^2)));
```

Die approbierte gedruckte Originalversion dieser Dissertation ist an der TU Wien Bibliothek verfügbar.
The approved original version of this doctoral thesis is available in print at TU Wien Bibliothek.
TU Bibliothek Your knowledge hub WIEN

```
dedes=(desenkdes+depardes)./2;
```

fraction s

```
s=1-exp((-2*th)./dp1);
defilm=s.*de.*bounces;
degesamt=de.*bounces;

sdes=1-exp((-2*th)./dp1des);
defilmdes=sdes.*dedes.*bounces;
degesamtdes=dedes.*bounces;
```

new gH2O

```
Absowater=55.6.*21.4.*(defilm.*(10^-4));
Absowaterdes=55.6.*21.4.*(defilmdes.*(10^-4));
figure(22)
plot(pres,Absowater)
hold on
plot(presdes,Absowaterdes)

absoadscorr=ads0./Absowater;
absodescorr=des0./Absowaterdes;
figure(29)
clf
plot(pres,absoadscorr,'-o')
hold on
xlabel('RH')
ylabel('gH2O/VFilm (g/L')
plot(presdes,absodescorr,'-o')
scatter(pres,absoads0)
scatter(presdes,absodes0)
```

Die approbierte gedruckte Originalversion dieser Dissertation ist an der TU Wien Bibliothek verfügbar.
The approved original version of this doctoral thesis is available in print at TU Wien Bibliothek.
TU Bibliothek Your knowledge hub WIEN

B.4 BTEX Gas Phase Fitting

Inputs

```
scantime=10; %time for one scan in opus in s
bgtime=50; %averaging time for background spectrum
navg=1; %number of spectra to be averaged
neuladen=true;
saveresults=true;
gauss=true;
addpath 'S:\PHD\phd\DATA\matlab'
```

Load all Spectra in folder

```
if neuladen
files = dir('*2.00*.txt');
filescells=struct2cell(files);
sortedfiles=string(natsortfiles(filescells(1,:))');
raw=load(char(sortedfiles(1)));
wn=raw(:,1);
raw=[raw(:,2) zeros(length(files)-1,length(raw(:,2)))'];
for uu=2:length(files)
    temp=load(char(sortedfiles(uu)));
    raw(:,uu)=temp(:,2);
end
end
```

calculate Background spectrum

```
bg=mean(raw(:,1:floor(bgtime/scantime)),2);
spectra=raw;
spectraavg=zeros(ceil(size(spectra,2)/navg),length(wn))';
for ii=1:length(wn)
    spectraavg(ii,:)=decimate(spectra(ii,:),navg,5);
end
% Absorbance
abso=-log10(spectraavg./repmat(bg,1,size(spectraavg,2)));
figure(777)
plot(wn,abso)
wnshort=wn(wn>1300 & wn<3000);
absoshort=abso(wn>1300 & wn<3000,:);
% define time axis
t=linspace(scantime*(navg/2),scantime*(size(raw,2)-navg/2),size(spectraavg,2));
```

baseline correction

```
minabso=abso(wn>1801 & wn<1802,:);
corrabso=absoshort-minabso;
corrabso2=abso-minabso;
figure(78)
plot(wnshort,corrabso)
onlyads=corrabso(:,t>0 & t<450);
```

Fit preparation

```
fitshort=corrabso(wnshort>1350 & wnshort<1840,:);
wnfit=wn(wn>1350 & wn<1840);
```

Die approbierte gedruckte Originalversion dieser Dissertation ist an der TU Wien Bibliothek verfügbar.
The approved original version of this doctoral thesis is available in print at TU Wien Bibliothek.
TU Bibliothek Your knowledge hub WIEN

```
figure(23)
plot(wnfit,fitshort)
```

fit with fixed width

```
    center=0;
    window=0;
    NumPeaks=3;
    NumTrials=5;
    autozero=1;
    shape=50;
    position=[2 2 2;1496.5 1507 1517.5; 5.3 7.8 5.5]';
for kk=1:size(fitshort,2)
    signal=[wnfit fitshort(:,kk)];
   [FitResults, GOF, xi, yi] =
peakfit(signal,center,window,NumPeaks,shape,1,NumTrials,0,autozero,position,1,1);
   peak1_adsnorm(kk)=FitResults(1,5);
   peak2_adsnorm(kk)=FitResults(2,5);
   peak3_adsnorm(kk)=FitResults(3,5);
   height1_adsnorm(kk)=FitResults(1,3);
   height2_adsnorm(kk)=FitResults(2,3);
   height3_adsnorm(kk)=FitResults(3,3);
end
```

average platteau

```
r=6; % number of points per platteau
areabn=peak1_adsnorm;
meannum=2; % number from which averaging starts in platteau
yy=reshape(areabn(1:fix(numel(areabn)/r)*r),r,[]);
yyt=reshape(t(1:fix(numel(t)/r)*r),r,[]);
yymean_tol=mean(yy(meannum:end,:));
yymean_tol_error=(std(yy(meannum:end,:)))';
yytmean=mean(yyt(meannum:end,:));
figure(5)
plot(yyt,yy,'-x')
areabn2=peak2_adsnorm;
yy2=reshape(areabn2(1:fix(numel(areabn2)/r)*r),r,[]); %reshape(conctol,6,[]);
yyt2=reshape(t(1:fix(numel(t)/r)*r),r,[]);
yymean_TMB=mean(yy2(meannum:end,:));
yytmean2=mean(yyt2(meannum:end,:));
yymean_xyl_error=(std(yy2(meannum:end,:)))';
figure(5)
hold on
plot(yyt2,yy2,'-x')
scatter(yytmean2,yymean_TMB)
areabn3=peak3_adsnorm;
yy3=reshape(areabn3(1:fix(numel(areabn3)/r)*r),r,[]); %reshape(conctol,6,[]);
yyt3=reshape(t(1:fix(numel(t)/r)*r),r,[]);
yymean_xyl=mean(yy3(meannum:end,:));
yytmean3=mean(yyt3(meannum:end,:));
yymean_TMB_error=(std(yy3(meannum:end,:)))';
figure(5)
plot(yyt3,yy3,'-x')
scatter(yytmean,yymean_tol)
scatter(yytmean3,yymean_xyl)
```

Die approbierte gedruckte Originalversion dieser Dissertation ist an der TU Wien Bibliothek verfügbar.
The approved original version of this doctoral thesis is available in print at TU Wien Bibliothek.
TU Bibliothek Your knowledge hub WIEN

B.4 Cavitation Pressure

input

```
kb=1.38064852*10^-23;% Boltzmann constant J/K or m2 kg s-2 K-1
T=293.15; % temperture K
tau=1;% time intervall s
h=6.626*10^-34; %Planck constant m2 kg / s
nu=3.4*(10^16)*(10^-29); % probed pore volume in m3 (nm3 -> m3 = 10-27)
R=8.314; %  gaskonstante 8.314 kg m2 /(s2 mol K)
Navo=6.022*10^23; % avogardo constant
```

water

```
gamma0=72.8*10^-3; % surface tension in J/m2
Psat=206.5; %saturation pressure in Pa
Mmass=18; %g/mol
roh=1;
theta=25; %contact angle
h_diam=0.096*10^-9;
```

toluene

```
gamma0=28.52*10^-3; % surface tension in J/m2
Psat=2.89*10^3; %saturation pressure in Pa
Mmass=92.141; %g/mol
roh=0.87;
theta=0; %contact angle
h_diam=0.118*10^-9; %0.2*0.59 nm
```

isopropanol

```
gamma0=21.7400*10^-3; % surface tension in J/m2
Psat=4.21*10^3; %saturation pressure in Pa
Mmass=60.096; %g/mol
roh=0.786;
theta=0; %contact angle
h_diam= 0.094*10^-9;%0.15505*10^-9;
```

methanol

```
gamma0=22.70*10^-3; % surface tension in J/m2
Psat=12.9*10^3; %saturation pressure in Pa
Mmass=32.04; %g/mol
roh=0.79;
theta=0; %contact angle
h_diam=0.137*10^-9
```

liquid Nitrogen

```
gamma0=8.94*10^-3; % surface tension in J/m2
```

Die approbierte gedruckte Originalversion dieser Dissertation ist an der TU Wien Bibliothek verfügbar.
The approved original version of this doctoral thesis is available in print at TU Wien Bibliothek.
TU Bibliothek Your knowledge hub WIEN

```
Psat=57.90*10^3; %saturation pressure in Pa
Mmass=28; %g/mol
roh=0.807;
theta=0;
T=77;%contact angle
h_diam=0.0728*10^-9;
```

kinetic prefactor according ref. [247]

```
vmol=(Mmass/roh)*10^-6; %molare volume m3/mol
N0_2=(kb*T)/(h*(10^-6*(Mmass*roh/Navo)));
```

cavitation pressure

```
Pcav=-sqrt((16*pi*gamma0^3)/(3*kb*T*log(N0_2*nu*tau/log(2))))-Psat;
```

```
rcav=-(2*gamma0)/(Pcav-Psat);
```

```
p_p0=exp(((Pcav-Psat)*vmol)/(R*T))
```

corrected surface tension using *Tolman* length

```
rk=rcav;
G=1.33;
delta=h_diam; %tolman length
gammacorr=gamma0*(1/(1+(G*delta/rk)));
```

cavitation pressure with corrected surface tension

```
Pcav_corr=-sqrt((16*pi*gammacorr^3)/(3*kb*T*log((N0_2*nu*tau)/log(2))))-Psat;
```

```
p_p0_corr=exp(((Pcav_corr-Psat)*vmol*cosd(theta))/(R*T))
```

Die approbierte gedruckte Originalversion dieser Dissertation ist an der TU Wien Bibliothek verfügbar.
The approved original version of this doctoral thesis is available in print at TU Wien Bibliothek.
TU Bibliothek Your knowledge hub WIEN

C. Construction Drawings

C.1 ATR Crystal Cartridge

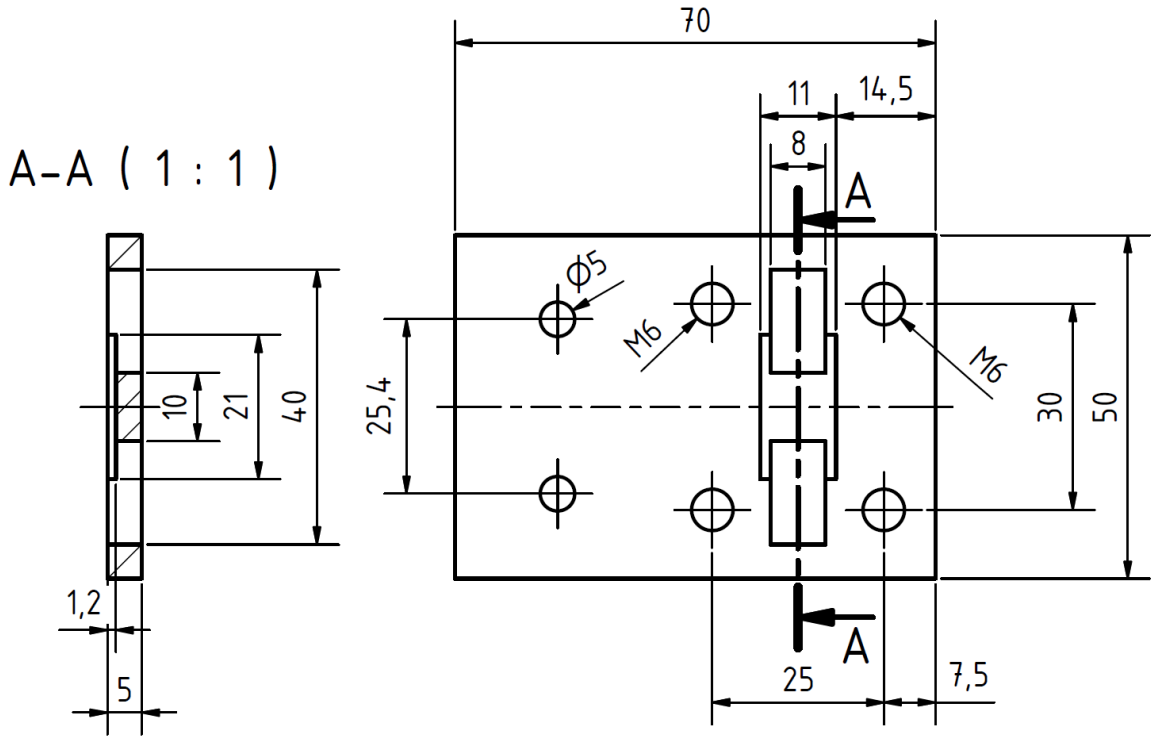

Material: Aluminum, Manufacturer: *Protolabs* (USA).

Die approbierte gedruckte Originalversion dieser Dissertation ist an der TU Wien Bibliothek verfügbar.
The approved original version of this doctoral thesis is available in print at TU Wien Bibliothek.
TU Bibliothek Your knowledge hub WIEN

C.2 Liquid Flow Cell

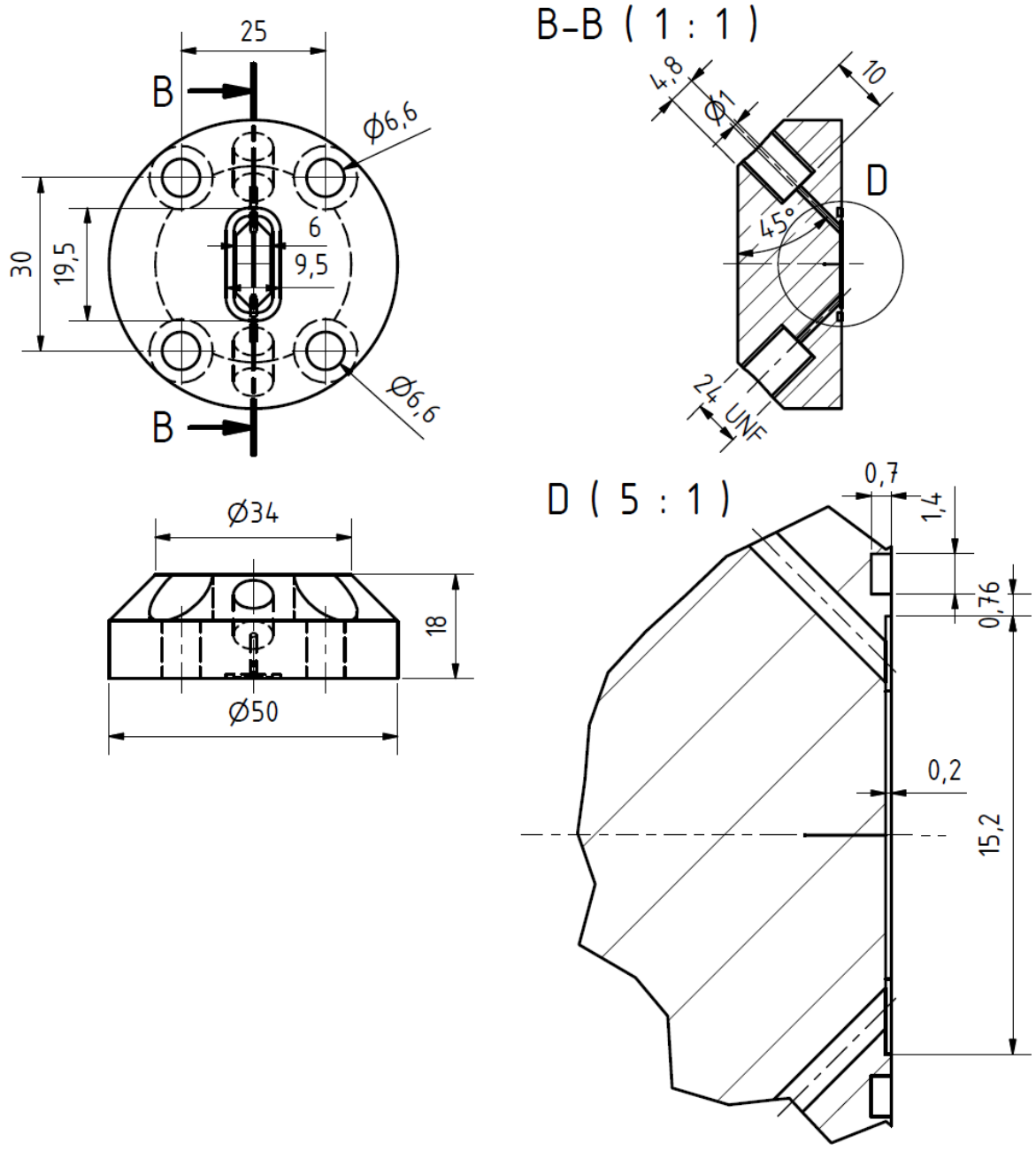

Material: Aluminum, Manufacturer: *Protolabs* (USA).

Die approbierte gedruckte Originalversion dieser Dissertation ist an der TU Wien Bibliothek verfügbar.
The approved original version of this doctoral thesis is available in print at TU Wien Bibliothek.
TU Bibliothek Your knowledge hub WIEN

C.3 Gas Flow Cell

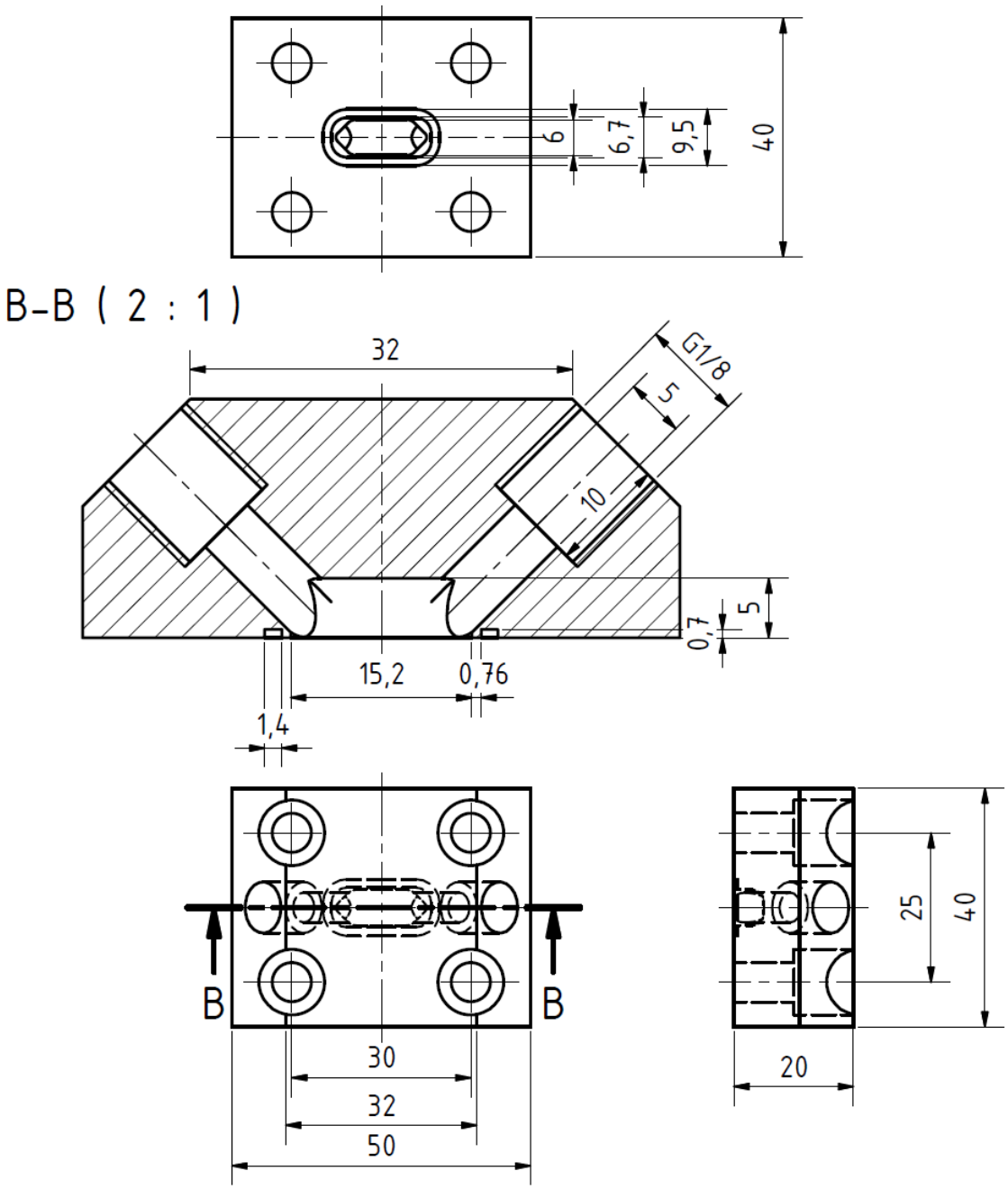

Material: Aluminum, Manufacturer: *Protolabs* (USA).

Die approbierte gedruckte Originalversion dieser Dissertation ist an der TU Wien Bibliothek verfügbar.
The approved original version of this doctoral thesis is available in print at TU Wien Bibliothek.

C.4 Flow Cell for Photocatalysis

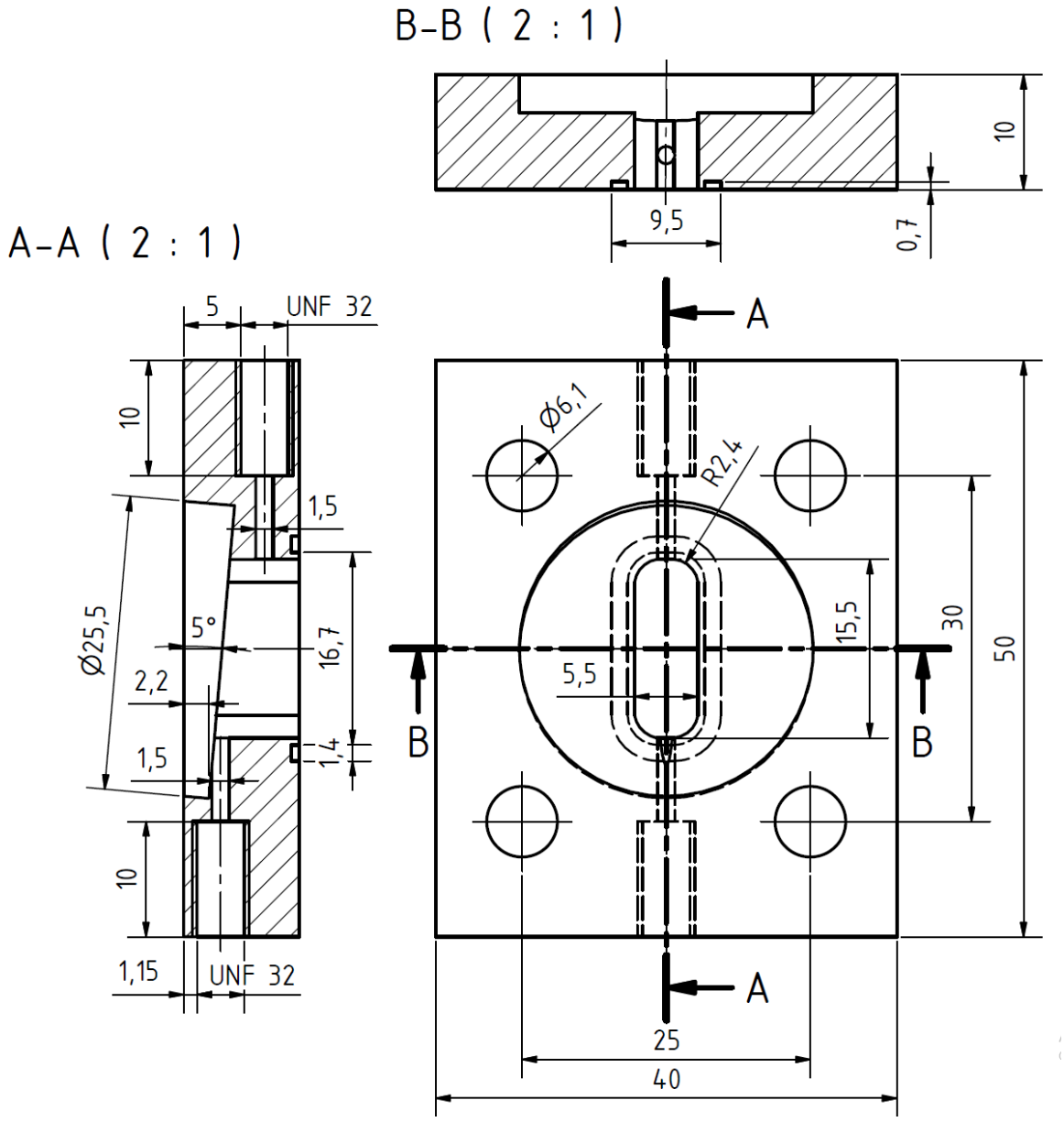

Material: PMMA, Manufacturer: *Protolabs* (USA).

Die approbierte gedruckte Originalversion dieser Dissertation ist an der TU Wien Bibliothek verfügbar.
The approved original version of this doctoral thesis is available in print at TU Wien Bibliothek.
TU Bibliothek Your knowledge hub WIEN

D. Curriculum Vitae

Bettina Baumgartner

Contact	bettina_baumgartner@gmx.net Laudongasse 18/3 1080 Wien
Nationality	Austrian
Date of Birth	October 12th 1990

Education

01|2017-12|2019	PhD Candidate at Institute of Chemical Technologies and Analytics, TU Wien. Topic: *Combining Mesoporous Materials with ATR Spectroscopy.* Supervisor: Prof. Bernhard Lendl.
03|2016- 12|2016	Research Associate at the Institute of Materials Chemistry, TU Wien. Supervisor: Dr. Miriam M. Unterlass.
10|2013- 01|2016	MSc in "Technical Chemistry" with specialization in Applied Synthetic Chemistry, TU Wien Master Thesis: *Hydrothermal Polymerization: Towards Highly Crystalline Polyimides.* Supervisor: Dr. Miriam M. Unterlass.
02|2014- 04|2014	Research Internship at Universitat Politécnica de Catalunya, Barcelona, Spain in the framework of Erasmus Programme Topic: Conducting Polymers for Batteries. Supervisor: Prof. Dr. Carlos Alemán.
09|2013	Research internship at TU Wien Topic: Modification of Polypropylene Surfaces. Supervisor: Prof. Dr. Simone Knaus.
10|2010- 07|2013	BSc in "Technical Chemistry", TU Wien BSc Thesis: *Modification of Titanium- and Zirconium-alkoxides with Tri- and Tetrafunctional Ligands.* Supervisor: Prof. Dr. Ulrich Schubert.
09|2004- 05|2010	Higher Technical College, TGM, Wien with specialization in Industrial Engineering

Work Experience

01|2017-12|2019	Project assistant at the Institute of Chemical Technologies and Analytics, TU Wien
03|2016-12|2016	Project assistant at the Institute of Materials Chemistry, TU Wien
03|2013-06|2015	Tutor at TU Wien, student synthesis laboratory course

Die approbierte gedruckte Originalversion dieser Dissertation ist an der TU Wien Bibliothek verfügbar.
The approved original version of this doctoral thesis is available in print at TU Wien Bibliothek.
TU Bibliothek Your knowledge hub WIEN

Awards and Fellowships

09|2019	Poster prize at International International Sol-Gel Conference, RU
01|2019	Christiana-Hörbiger Fellowship
09|2016	Award for best master thesis of Gesellschaft Österreichischer Chemiker
08|2016	Fellowship of BMVIT for attendance of the Forum Alpbach
12|2015	Merit Grant of TU Wien
08|2015	1st poster prize at the Functional Nanomaterials Symposium, CZ

Peer-Reviewed Publications

ORCID: 0000-0002-9136-6811

1. Baumgartner, B., Hayden, J. & Lendl, B. Mesoporous silica films for sensing volatile organic compounds using attenuated total reflection spectroscopy. *Sensors Actuators B Chem.* **302**, 127194 (2020).
2. Loizillon, J., Baumgartner, B., Sinturel, C., Abbarchi, M., Lendl, B. & Grosso, D. In-Depth Study of Coating Multimodal Porosity Using Ellipsometry Porosimetry in Desorption Scanning Mode. *J. Phys. Chem. C* **123**, 23464–23479 (2019).
3. Baumgartner, B., Hayden, J., Loizillon, J., Steinbacher, S., Grosso, D. & Lendl, B. Pore Size-Dependent Structure of Confined Water in Mesoporous Silica Films from Water Adsorption/Desorption Using ATR–FTIR Spectroscopy. *Langmuir* 35, 11986–11994 (2019).
4. Hayden, J., Baumgartner, B., Waclawek, J. P. & Lendl, B. Mid-infrared sensing of CO at saturated absorption conditions using intracavity quartz-enhanced photoacoustic spectroscopy. *Appl. Phys. B* **125**, 159 (2019).
5. Freitag, S., Baumgartner, B., Tauber, S., Gasser, C., Radel, S., Schwaighofer, A. & Lendl, B. An Acoustic Trap for Bead Injection Attenuated Total Reflection Infrared Spectroscopy. *Anal. Chem.* **91**, 7672–7678 (2019).
6. Baumgartner, B., Hayden, J., Schwaighofer, A. & Lendl, B. *In Situ* IR Spectroscopy of Mesoporous Silica Films for Monitoring Adsorption Processes and Trace Analysis. *ACS Appl. Nano Mater.* **1**, 7083–7091 (2018).
7. Leimhofer, L., Baumgartner, B., Puchberger, M., Prochaska, T., Konegger, T. & Unterlass, M. M. Green one-pot synthesis and processing of polyimide-silica hybrid materials. *J. Mater. Chem. A* **5**, 16326–16335 (2017).
8. Baumgartner, B., Svirkova, A., Bintinger, J., Hametner, C., Marchetti-Deschmann, M. & Unterlass, M. M. Green and highly efficient synthesis of perylene and naphthalene bisimides in nothing but water. *Chem. Commun* (2016). doi:10.1039/c6cc06567h
9. Baumgartner, B., Puchberger, M. & Unterlass, M. M. Towards a general understanding of hydrothermal polymerization of polyimides. *Polym. Chem.* **6**, 5773–5781 (2015).
10. Baumgartner, B., Skrinjar, P., Bojdys, M. J., Unterlass, M. M., Skrinjar, P. & Unterlass, M. M. Design Strategies in Hydrothermal Polymerization of Polyimides. *Macromol. Chem. Phys.* **217**, 485—500 (2016).
11. Baumgartner, B., Bojdys, M. J. & Unterlass, M. M. Geomimetics for green polymer synthesis: highly ordered polyimides via hydrothermal techniques. *Polym. Chem.* **5**,

Die approbierte gedruckte Originalversion dieser Dissertation ist an der TU Wien Bibliothek verfügbar.
The approved original version of this doctoral thesis is available in print at TU Wien Bibliothek.
TU Bibliothek Your knowledge hub WIEN

3771–3776 (2014).

12. Maurer, C., Baumgartner, B., Pabisch, S., Akbarzadeh, J., Peterlik, H. & Schubert, U. Porous titanium and zirconium oxo carboxylates at the interface between sol–gel and metal–organic framework structures. *Dalt. Trans.* **43**, 950–957 (2014).

Conference Proceedings

13. Zhao, H., Raza, A., Baumgartner, B., Clemmen, S., Lendl, B., Skirtach, A. & Baets, R. Waveguide-Enhanced Raman Spectroscopy Using a Mesoporous Silica Sorbent Layer for Volatile Organic Compound (VOC) Sensing. in *Conference on Lasers and Electro-Optics* STh1F.7 (OSA, 2019). doi:10.1364/cleo_si.2019.sth1f.7

Patents

M. M. Unterlass, B. Baumgartner: "*Verfahren zur Herstellung von Polyimiden*"; Patent: WO, Nr. PCT/AT2016/050140; submitted: 13.05.2016.

Conference Contributions

§.. Presenting Author

1. B. Baumgartner§, J. Hayden, J. Loizillon, D. Grosso, B. Lendl: " *Studying Water Adsorption on Mesoporous Silica Films by ATR-IR Spectroscopy: Determination of Porosity and Structure of Adsorbed Water*"; Poster: 20th International Sol-Gel Conference, St. Petersburg; 25.09.2019 - 30.09.2018. Awarded with a poster prize.
2. F. Pilat§, B. Schwarz, H. Detz, A. M. Andrews, B. Baumgartner, B. Lendl, G. Strasser, B. Hinkov: "*μ-fluidic sensing with a quantum cascade lab-on-a-chip*"; Talk: Gemeinsame Jahrestagung in Zürich ÖPG, SPS, Zürich; 26.08.2019 - 30.08.2019.
3. B. Baumgartner§, J. Hayden, A. Schwaighofer, B. Lendl: "*Ordered Mesoporous Silica Films combined with in situ IR spectroscopy: A powerful tool for monitoring adsorption processes and trace analysis*"; Poster: 6th ISGS Summer School, Alghero; 16.09.2018 - 19.09.2018.
4. B. Baumgartner§, J. Hayden, A. Schwaighofer, B. Lendl: "*Ordered Mesoporous Silica Films for Sensing of Organic Contaminants in Water and Gas Phase by ATR-IR Spectroscopy*"; Poster: 8th International Quantum Cascade Laser School and Workshop, Cassis; 02.09.2018 - 07.09.2018.
5. B. Baumgartner§, J. Hayden, A. Schwaighofer, B. Lendl: "*Ordered Mesoporous Silica Films for Mid-IR Evanescent Field Spectroscopic Sensing of Organic Contaminants in Water*"; Poster: FLAIR 2018, Assisi; 10.09.2018 - 14.09.2018.
6. B. Baumgartner§, J. Hayden, B. Lendl: "*A Versatile Porous Enrichment Layer for Monitoring Organic Contaminants in Water via ATR Spectroscopy*"; Poster: Euroanalysis 2017, Stockholm; 28.08.2017 - 01.09.2017.
7. B. Baumgartner§, M. M. Unterlass: "*Towards Understanding Hydrothermal Polymerization of Polyimides: Reaction Pathways and Their Effect on Crystallinity*"; Poster: STEPI 10 - 10th Polyimides & High Performance Polymers Conference, Montpellier, FR; 05.06.2016 - 08.06.2016.
8. B. Baumgartner§, M. M. Unterlass: "*Highly Crystalline Polyimides by Hydrothermal Polymerization: A Mechanistic Study*"; Poster: Makromolekulares Kolloquium 2016, Freiburg; 24.02.2016 - 26.02.2016.
9. B. Baumgartner§, M. M. Unterlass: "*Highly Crystalline Polyimides via Hydrothermal*

Die approbierte gedruckte Originalversion dieser Dissertation ist an der TU Wien Bibliothek verfügbar.
The approved original version of this doctoral thesis is available in print at TU Wien Bibliothek.
TU Bibliothek Your knowledge hub WIEN

Polymerization"; Poster: 16. Österreichische Chemietage, Innsbruck; 21.09.2015 - 24.09.2015.

10. B. Baumgartner§, M. M. Unterlass: "*Geomimetic Synthesis for Highly Crystalline Polymers: High-Performance Polyimides by Hydrothermal Polymerization*"; Poster: Functional Nanomaterials Symposium (FuNMat) 2015, Prague, Czech Republic; 30.07.2015. Awarded with a poster prize.
11. B. Baumgartner§, M. M. Unterlass: "*Geomimetic Polymer Synthesis: Highly Crystalline Polyimides by Hydrothermal Polymerization*"; Poster: Vienna Young Scientists Symposium, Wien; 25.06.2015 - 26.06.2015.
12. B. Baumgartner§, M. Bojdys, M. M. Unterlass: "*Geomimetic Polymer Synthesis: Hydrothermal Polymerization of Polyimides*"; Poster: Polymer Physics Gordon Research Conference (GRC), Mount Holyoke College, South Hadley, MA, USA; 13.07.2014 - 18.07.2014.

Die approbierte gedruckte Originalversion dieser Dissertation ist an der TU Wien Bibliothek verfügbar.
The approved original version of this doctoral thesis is available in print at TU Wien Bibliothek.
TU Bibliothek Your knowledge hub WIEN